UNIVERSITY OF CALGARY

Assessing attenuation, fractures, and anisotropy using logs, vertical seismic profile, and three-component seismic data: heavy oilfield and potash mining examples

by

Zimin Zhang

A THESIS

SUBMITTED TO THE FACULTY OF GRADUATE STUDIES

IN PARTIAL FULFILMENT OF THE REQUIREMENTS FOR THE

DEGREE OF DOCTOR OF PHILOSOPHY

DEPARTMENT OF GEOSCIENCE

CALGARY, ALBERTA

October 2010

UNIVERSITY OF CALGARY

FACULTY OF GRADUATE STUDIES

The undersigned certify that they have read, and recommend to the Faculty of Graduate Studies for acceptance, a thesis entitled " Assessing attenuation, fractures, and anisotropy using logs, vertical seismic profile, and three-component seismic data: heavy oilfield and potash mining examples" submitted by Zimin Zhang in partial fulfilment of the requirements of the degree of Doctor of Philosophy.

Supervisor, Dr. R. R. Stewart
Department of Earth and Atmospheric Sciences, University of Houston

---

Co-Supervisor, Dr. D. C. Lawton, Department of Geoscience

Dr. G. Margrave, Department of Geoscience

Dr. L. R. Lines, Department of Geoscience

Internal / External Examiner, Dr. R. Wong, Department of Civil Engineering

---

External Examiner, Dr. D. Schmitt, Department of Physics, University of Alberta

---

Date

Abstract

Integrated geophysical studies in two areas (the Ross Lake heavy oilfield, Saskatchewan, and a Saskatchewan potash mine) are described in this thesis. Multicomponent seismic processing and interpretation, rock physics modeling, and well log analysis are carried out to develop detailed descriptions of a heavy oil reservoir and fractures which can pose problems in potash mining.

In the Ross Lake oilfield, the VSP data provide a reliable time-depth correlation, image around the borehole, and real amplitude AVO gather for delineating the sand channel reservoir. The relationship between seismic wave attenuation and rock properties is investigated for shale and sandstone using zero-offset VSP data. Interval Q values from VSP data for the P wave and shear wave correlate interestingly with petrophysical variables. Q values increase with P- and S-velocities and decrease with Vp/Vs and porosity. Shaly sandstone shows more attenuation than pure shale and sandstone.

Simulation of fractures in the rocks overlying the potash ore displays a significant velocity decrease and anisotropy for both P- and S-velocities. Seismic interpretation of the time-lapse 3C-3D surveys indicate noticeable amplitude changes and push-down effects at the Dawson Bay Formation and underlying formations in 2008 survey compared with 2004 survey, especially on radial data. Vp/Vs and seismic curvature attributes also outline the fractured zones. The analysis on anisotropic modeling seismic data suggests that by searching for seismic anisotropy, shear-wave splitting on the multicomponent seismic data, we may also be able to delineate the fracture orientation and intensity in the potash mining area.

Acknowledgements

I sincerely thank my supervisor, Dr. Rob Stewart, for his guidance and his encouragement throughout my PhD studies. The discussion with him was a great help in developing my understanding of the research topics. I also want to give my co-supervisor, Dr. Don Lawton, big thanks for his constant support for my research.

I would like to thank the directors, staffs and students of the CREWES Project at the University of Calgary for various help, especially Rolf Maier for proofreading this dissertation, Carlos Montaña for help with the VISTA processing software, Kevin Hall, and Hanxing Lu for varied assistance.

I am grateful for GXT/ION, Dr. James Gaiser and Jim Simmons for help with anisotropic numerical modeling.

I thank Boyd PetroSearch, especially Mr. John Boyd for the help in providing the time-lapse 3C-3D seismic data and engaging in valuable discussions.

Finally, I would like to sincerely thank my wife, Bona, for her patience, support, and encouragement during my study.

Dedication

To my wife, Bona, my son, Victor and my parents

Table of Contents

List of Tables

List of Figures and Illustrations

List of Symbols, Abbreviations and Nomenclature

AGC	Automatic gain control
AVO	Amplitude versus offset
CDP	Common depth point
HTI	Horizontal transverse isotropy (transverse isotropy with horizontal symmetry)
K	Bulk modulus
M	P-wave modulus
m	Meter
ms	Millisecond
P-wave	Compressional wave
PP, PS	Reflected pure compressional / compressional-to-shear reflection
Q	Quality factor (attenuation)
Qp, Qs	Quality factor of P wave / shear wave
RMS	Root mean square
SH wave	A shear wave that is polarized so that its particle motion and direction of propagation are contained in a horizontal plane.
SV wave	A shear wave that is polarized so that its particle motion and direction of propagation occur in a vertical plane.
S/N	Signal-to-noise ratio
S-wave	Shear wave
Vp, Vs	P-wave / S-wave velocity
VSP	Vertical seismic profile
λ	Lamé parameter
μ	Shear modulus (rigidity)
3C	Three-component
3D	Three-dimensional

Chapter One: Introduction

1.1 Motivation and objectives

It is well known that the exploration for subtle hydrocarbon reservoirs and detailed description of them are becoming more and more important. Multicomponent seismic data have increased in numbers since the 1980's. The introduction of shear waves into seismic exploration provides valuable information for imaging and rock property prediction of reservoirs. In the Ross Lake oilfield and at a Saskatchewan potash mining site, multicomponent VSP data and time-lapse multicomponent surface seismic data were acquired. The first part of this thesis undertakes a detailed description of sandstone heavy oil reservoir using multicomponent VSP data and well log data. In the second part, time-lapse multicomponent seismic interpretation, rock physics modeling, and anisotropy analysis are carried out to assess the significance of fractures which may pose problems to potash mining. The objectives of this dissertation are to: 1) delineate heavy oil reservoirs using multicomponent VSP data; 2) further understand seismic wave propagation and investigate seismic attenuation utilizing the benefit of VSP geometry; and 3) delineate fractures by time-lapse multicomponent seismic data for potash mining.

1.2 Vertical seismic profile (VSP)

A VSP is recording a seismic signal generated at the surface of the earth with motion sensors secured at various depths in a well (Hardage, 1983, 2001; Toksöz and Stewart, 1984; Stewart, 2001). With a VSP geometry, both downgoing and upgoing seismic events can be recorded in time and depth (Figure 1.1). Therefore, VSP data give insight into some of the fundamental properties of propagating seismic waves. These insights, in turn, can improve the structural, stratigraphic, and lithological interpretation of surface seismic recordings (Hardage, 1983, 2001; Stewart, 2001). The VSP plays four important roles in assessing the rock and fluids close to the borehole (Stewart, 2001): 1) it provides in situ rock properties in depth, particularly seismic velocity (Stewart, 1984), impedance, anisotropy, and attenuation; 2) it assists in understanding seismic wave propagation (e.g., source signatures, multiples, and conversions); 3) it provides its own seismic reflection image; and 4) all of the above assist in further surface seismic data processing and interpretation.

1.2.1 Seismic attenuation

Energy absorption is a fundamental feature associated with the propagation of seismic waves in all real materials, and as a result, the shape of transient waveforms will evolve with propagation distance or time (Kjartansson, 1979). Numerous physical mechanisms have been proposed to interpret the attenuation including frictional dissipation due to relative motions at grain boundaries and across crack surfaces (Walsh, 1966); dissipation in a fully saturated rock because of the relative motion of the frame with respect to fluid inclusions (Biot, 1956a, b); inter-crack fluid flow (also known as "squirt" flow) (Mavko and Nur, 1975); and partial saturation effects such as gas-pocket squeezing (White, 1975). Nonlinear friction is commonly assumed to be the dominant attenuation mechanisms, especially in crustal rocks (Johnston et al., 1979). In real materials, we expect that multiple mechanisms of attenuation are present, each having its own characteristic frequency and magnitude (Figure 1.2).

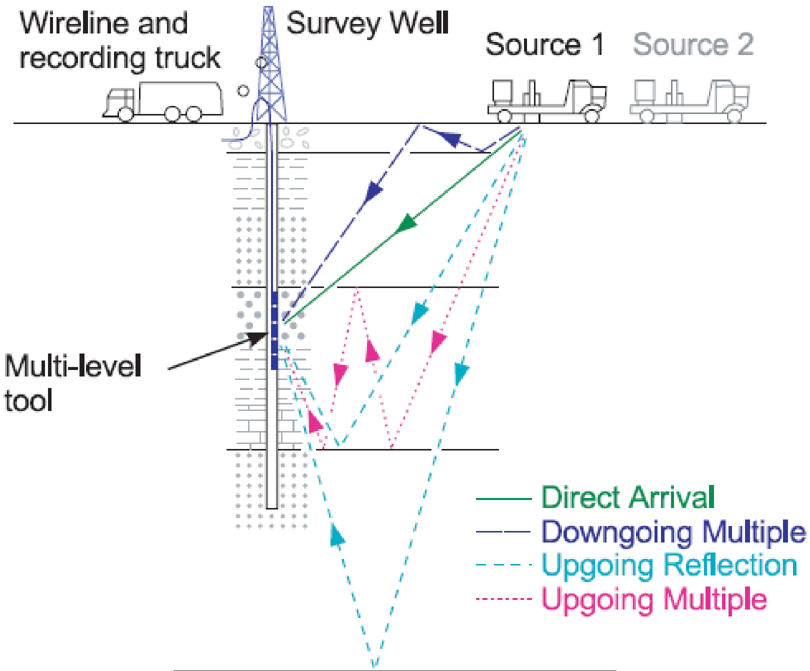

Figure 1.1 Schematic diagram of a VSP survey (from DiSiena et al., 1984).

In these mechanisms, attenuation is assumed to be related to matrix anelasticity, pore fluid, relative motion between matrix and pore fluid, or the fluid phase in the pore space. As one of the basic seismic attributes of waves propagating in the earth, understanding the causes of attenuation as well as the relationship between the attenuation of seismic data and rock properties is important in the acquisition, processing and interpretation of seismic data. Using attenuation measured on rock samples and well logs, a number of authors (e.g., Klimentos and McCann, 1990; Best et al., 1994; Koesoemadinata and McMechan, 2001) examined the relationship between lab measured attenuation and rock properties for sandstones. Since each of the multiple mechanisms of attenuation have their own characteristic frequency and magnitude, understanding the relationship between attenuation estimated directly from seismic wave and rock properties may be of more importance in seismic exploration. The VSP is particularly valuable in the study of seismic attenuation because reliable seismic attenuation can be measured due to the special geometry of a VSP survey.

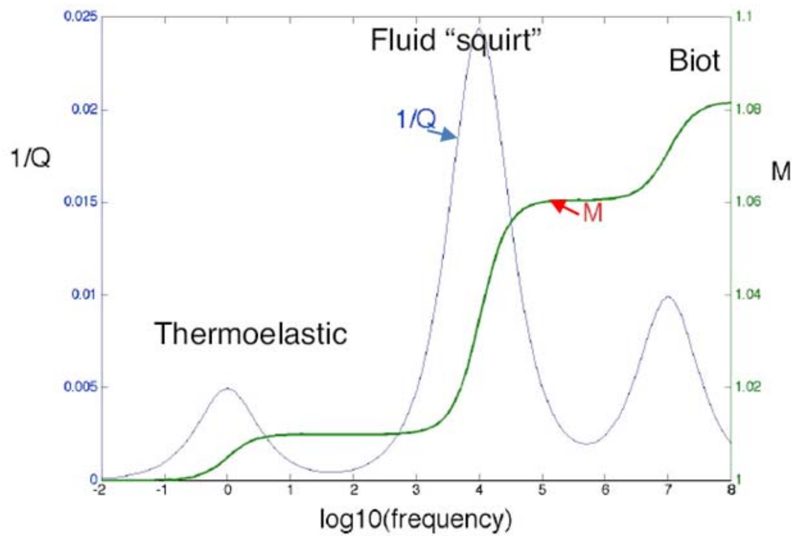

Figure 1.2 Superposition of multiple attenuation mechanisms (from Mavko, 2006). In real materials, multiple mechanisms of attenuation are present, each having its own characteristic frequency and magnitude (Mavko, 2006). The modulus M (green line) tends to increase with frequency in most rocks. The highest attenuation (the attenuation is plotted as blue line) tends to be in frequency range where M is increasing most rapidly. Three mechanisms of attenuation, thermoelastic, squirt flow, and Biot's relative motion of the frame with respect to fluid inclusions, are labeled at their corresponding characteristic frequencies.

1.2.2 Study area and objectives

The Ross Lake heavy oilfield (owned and operated by Husky Energy Inc.) is located in south-western Saskatchewan (Figure 1.3). The producing reservoir is a Cretaceous channel sand in the Cantuar Formation of the Mannville Group. The produced oil is about 13° API gravity. In June 2003, the CREWES Project, Husky Energy Inc., and Schlumberger Canada conducted a multi-offset VSP survey for the well 11-25-13-17W3, including a zero-offset VSP survey using both vertical and horizontal vibrators as sources, two far-offset VSP surveys and a walkaway VSP survey.

The objectives of the VSP data sets were to:

1. improve the characterization of a Cretaceous channel sand;
2. study the AVO effect of the reservoir using walkaway VSP;
3. study the relationship between seismic attenuation and rock properties.

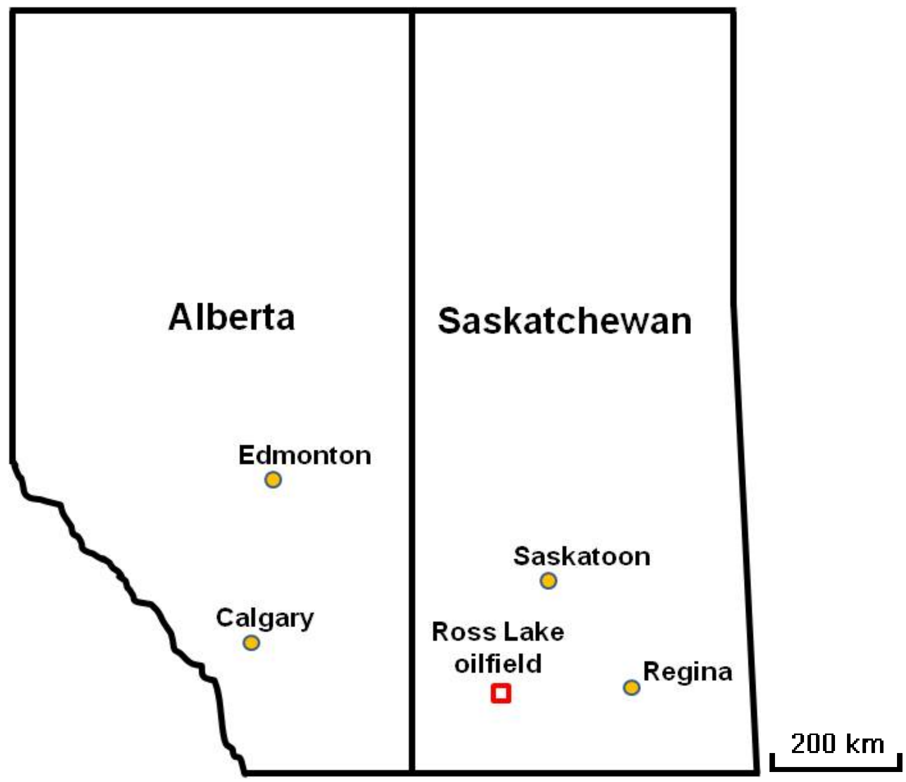

Figure 1.3 Location of the Ross Lake oilfield, Saskatchewan.

1.3 Fracture and brine inflow problems in potash mining

Cracks in rocks can be caused by geochemical interactions or thermal loading and may appear as small thin intra- or inter-granular defects. Their dimensions range from microns up to several millimeters. A typical aspect ratio for cracks ("thickness-to-length ratio") is 0.001 to 0.1 (Macbeth, 2002). Natural fractures are complicated macroscopic planar discontinuities in the rock, generally caused by physical diagenesis or deformation. They may appear as shear fractures that have displacements parallel to their surfaces, or as joints that have experienced tensional/extensional displacement perpendicular to the fracture surface. The apertures of joints are generally on the millimeter scale, and a shear displacement can have an effective hydraulic aperture several orders of magnitude lower. Fracture characterization is of great practical importance in hydrocarbon recovery, mining, well stability, CO_2 sequestration, and nuclear waste isolation. In hydrocarbon exploration and production, fractures are generally favourable because fractures can increase the porosity and permeability of the rock. In particular, significant amounts of hydrocarbon are trapped in tight reservoirs, where natural fractures are the main factors controlling fluid flow. However, fractures are a problem in potash mining operations. Any natural or induced fractures of normally impermeable rocks can create reservoirs and/or provide migrating pathways from subsurface aquifers to potash deposits, thus causing a brine inflow problem. It will not only cause ore loss but also create problems for the mining operations (Gendzwill, 1969).

The large contrast in electrical conductivity between dry and wet salt (dry salt is electrically resistive, with apparent resistivity ranging from 100-100,000 Ω·m, but becomes very conductive when wet, with resistivity on the order of 0.01-10 Ω·m) makes the use of ERI (electrical resistivity imaging) an attractive method for detecting water inflows (Eso et al., 2006). Underground GPR method (Annan et al., 1988) was applied to estimate the salt thickness and condition of the evaporite. Seismic techniques (Pesowski and Larson, 2000; Prugger et al., 2004) have been successfully used for risk analysis and mine planning by mapping the collapse features in the underground potash mining environment.

Due to quality improvements in conventional seismic data and multicomponent data, fracture induced anisotropy began to be widely used for fracture characterization during the last 25 years (Helbig and Thomsen, 2005). In potash mining, the induced fractures which can bring brine from an aquifer to a mine may be a good candidate for seismic monitoring techniques.

Studied area and objective

To monitor the brine inflow problem, seven 3D seismic surveys, including five 3C surveys were recorded from 2003 to 2008 in a Saskatchewan potash mining area. The objective of this study in the potash mining area was to integrate rock physics, seismic modeling and interpretation, and time-lapse multicomponent seismic techniques for characterizing fractures in areas where potash mining occurs.

1.4 Software

The codes for rock physics modeling, well log analysis, and seismic attenuation estimation were developed using the Matlab programming language. The other software or programs used in the thesis include:

1.4.1 Modeling software

The SYNGRAM program from the CREWES Project was used to generate synthetic seismograms. SYNGRAM creates primaries-only synthetic seismograms for PP and PS reflections from well logs, including trace gathers for a horizontally layered earth showing the variation of amplitude with offset as well as the stacked response. The reflection amplitudes, and optional transmission losses, are calculated from the Zoeppritz equations (no approximation) and are therefore appropriate for plane-wave incidence. Traveltimes and incidence angles are calculated by ray tracing.

A layer-matrix method computed in the frequency-wavenumber domain (by GX Technology) was used for anisotropic numerical modeling. It models seismic waves in flat-layer media for any type of anisotropy. Prestack synthetic seismograms are generated by a reflectivity method, where plane waves are propagated downward through the flat-layered earth model using Kennett's recursion relations, anisotropic vertical slownesses are calculated numerically, and the anisotropic eigenvectors are then obtained from the Christoffel equations. The modeling data used in Chapter 6 was done by Dr. James Gaiser, formerly of GX Technology. The modeling data include interbed multiples over the zone of input model, but free-surface multiples is not included.

1.4.2 Processing and interpretation software

VISTA Seismic Processing package is donated to the University of Calgary by GEDCO, and it was used to process the 3C VSP data and 3C-3D numerical modeling seismic data. Seismic interpretation and time-lapse attribute analysis were performed using SeisWare International Inc.'s SeisWare software and CGGVeritas Hampson-Russell's Geoview software.

1.5 Thesis outline

Chapter Two includes the processing and interpretation of offset VSP data, and AVO processing of walkaway VSP data at the Ross Lake heavy oilfield. The interpretive processing workflow used for VSP data and true reflectivity offset gathers analysis from walkaway VSPs are described in detail.

In Chapter Three, the seismic attenuation parameters *Qp* and *Qs* are first estimated from zero-offset VSP data sets acquired with a vertical vibrator and a horizontal vibrator. Then the Q values are compared with rock properties from well log analysis. Considering the advantages of a VSP geometry to study wave propagation, the Ross Lake VSP data were also used to investigate the frequency difference between P- and S-wave data, generally seen on most multicomponent land data.

Fracture detection is one of the major topics of this dissertation. To study fracture effects in the rock, two rock physics models are reviewed in Chapter Four. Naturally or induced fractures may or may not be controlled by a directional stress field; thus the fractures may be randomly or aligned distributed. Therefore, two models, the Kuster-Toksöz model for randomly oriented fractures/cracks and Hudson's model for aligned fractures/cracks were investigated in terms of usage limitation and fracture behaviour in shale, sandstone and carbonates at several field locations.

Chapter Five addresses the brine inflow problem in potash mining. Rock physics and synthetic seismograms are used for a feasibility study for using multicomponent seismic survey to monitor and detect fractures which may cause brine inflow to the mine. Time-lapse 3C-3D seismic surveys are interpreted to look for the seismic signatures of fractures previously seen in the modeling, in the hope of outlining the fractured zones.

Rock physics models suggest that aligned fractures can be related to seismic velocity anisotropy. In Chapter Six, numerical seismic modeling results were used for seismic anisotropy and shear-wave splitting analysis. The purpose was to determine whether an assumed amount of aligned fractures in the study formation could be detected by seismic velocity anisotropy, and shear-wave splitting caused by velocity anisotropy.

Chapter Two: Processing and interpretation of 3C VSP data from Ross Lake heavy oilfield, Saskatchewan

2.1 Introduction

The Ross Lake heavy oilfield (operated by Husky Energy Inc.) is located in south-western Saskatchewan. The regional stratigraphy in this area is shown in Figure 2.1. The exploration target is the Cretaceous channel sand in the Dimmock Creek member of the Cantuar Formation of the Mannville Group. The Mannville Group sandstones and shales unconformably overlie Jurassic sediments, and underlie the Joli Fou Formation of the Colorado Group. The Cantuar Formation of the Mannville Group is composed mostly of sediment developed within ancient valley systems (Christopher, 1974), which carved into the Success Formation and the Upper Jurassic Vanguard Group (Figure 2.2). The Cantuar Formation is further subdivided into the McCloud, the Dimmock Creek, and the Atlas members (Figure 2.2, Christopher, 1974). The channel sands in the Dimmock Creek member have high porosities, of about 30%, and very high permeability (up to the 3 Darcy range). The produced oil is about 13° API gravity.

Due to its acquisition geometry, VSP data can be used to improve the structural, stratigraphic, and lithological interpretation of surface seismic recordings (Hardage, 1983; Stewart, 2001). At the same time, VSP data also play important roles in assessing the rock and fluids close to the borehole (Stewart, 2001). For detailed mapping of the Cantuar Formation channel reservoir, the CREWES Project, Husky Energy Inc., and Schlumberger Canada conducted a multi-offset VSP survey in well 11-25-13-17W3 in June 2003, to enhance the interpretation of surface 3C-3D seismic survey acquired in 2002. Table 2.1 shows the acquisition parameters for the VSP survey; the locations of the

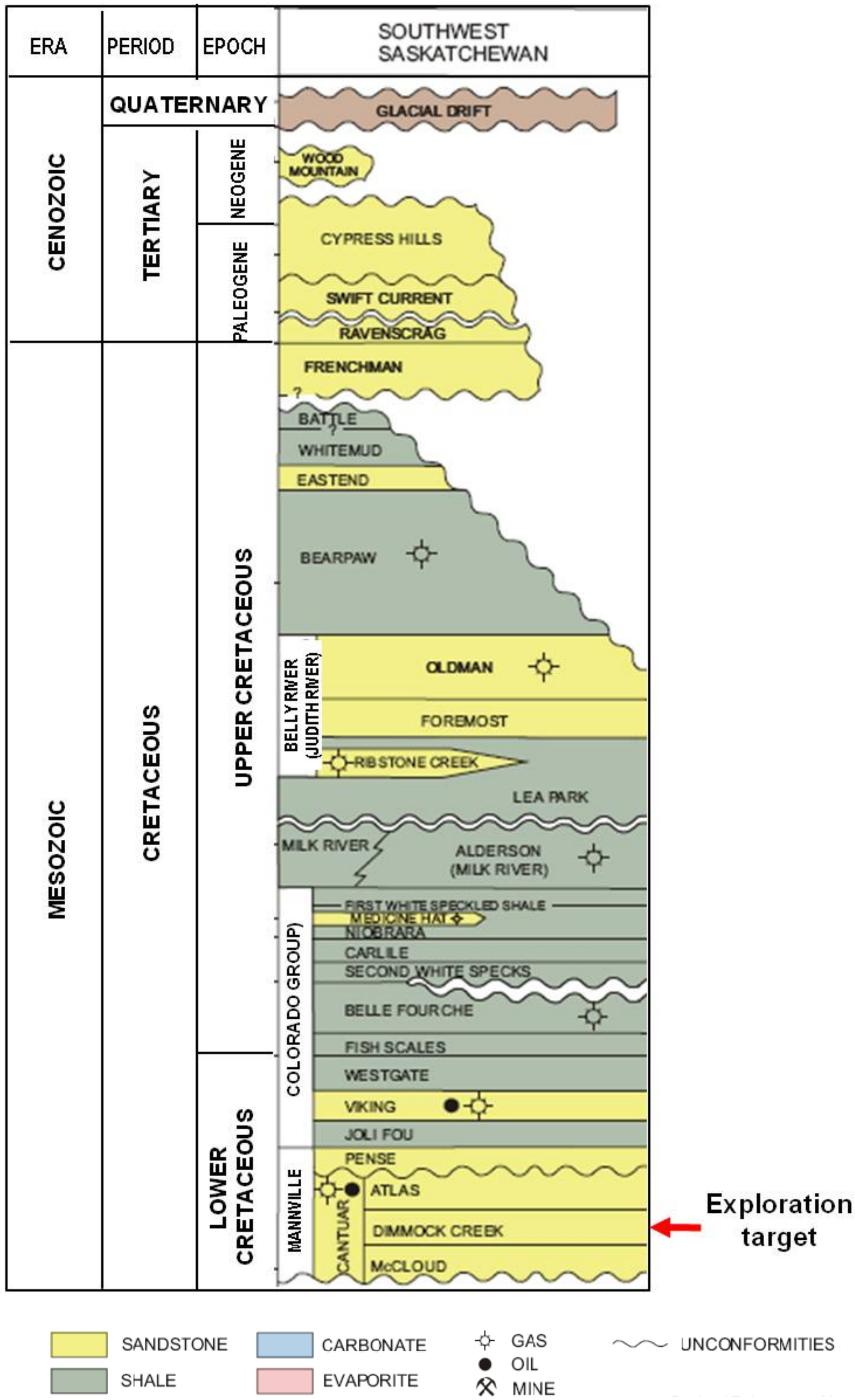

Figure 2.1 Generalized regional stratigraphic chart in southwest Saskatchewan (from Saskatchewan Industry and Resources, 2006).

VSP source and the well are shown in Figure 2.3. All the surveys were conducted with a downhole five-level, three-component VSP tool. The zero-offset VSP survey used both vertical and horizontal (inline) vibrators as sources. A vertical vibrator only was used for the far-offset VSP surveys, and the walkaway VSP surveys. The zero-offset VSP data were processed to provide a reliable correlation between borehole and surface seismic data; far-offset VSP data were processed for improved seismic imaging around the well, and amplitude versus offset (AVO) effects of the reservoir were assessed using the walkaway VSP data.

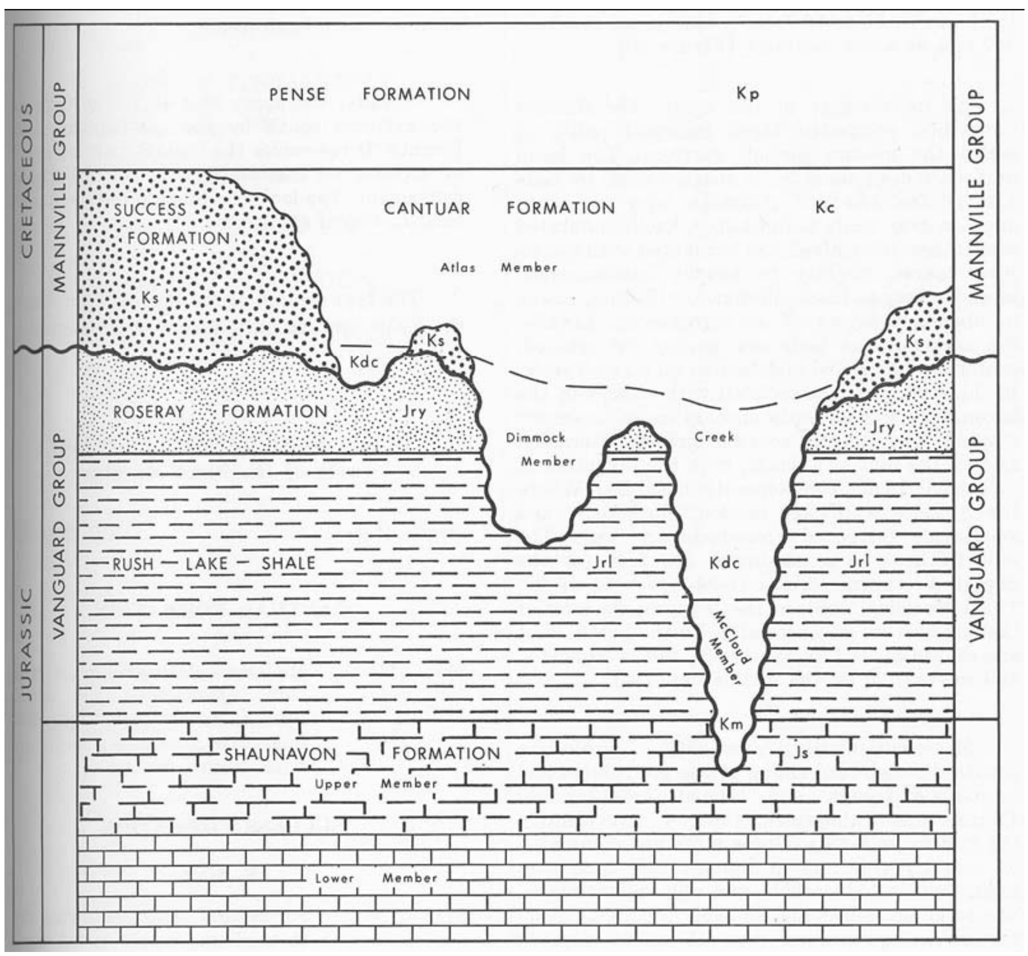

Figure 2.2 Stratigraphic relationship of the upper Jurassic and Lower Cretaceous sediments from southwestern Saskatchewan (from Christopher, 1974).

Table 2.1 Acquisition parameters of the Ross Lake VSP surveys.

Survey Type	**Zero-offset VSP**	**Far-offset VSP**		**Walkaway VSP**			
Offset	53.67 m	399.12 m	698.72 m	149.99 m	250.66 m	558.08 m	996.8 m
Source Elevation	856.1 m	867.7 m	861.2 m	856.3 m	856.7 m	860.7 m	859 m
Source Azimuth	16.3°	337.2°	301.5°	336.2°	337.6°	310.5°	319.5°
Source Type	Litton 315 P-vibe: sweep = 8-180Hz, 12 s linear sweep IVI S-MINI-vibe (inline): Sweep = 5 - 100 Hz; 12 s linear sweep	Litton 315 P-vibe: sweep = 8 - 180 Hz 12 s linear sweep		Litton 315 P-vibe: sweep = 8 - 180 Hz, 12 s linear sweep			
Top Level	197.5 m	197.5 m		954 m			
Bottom level	1165 m	1165 m		1165 m			
Number of Levels	130	130		14			
Receiver Spacing	7.5 m	7.5 m		15 m			
Reference Datum	KB=871.6 m						

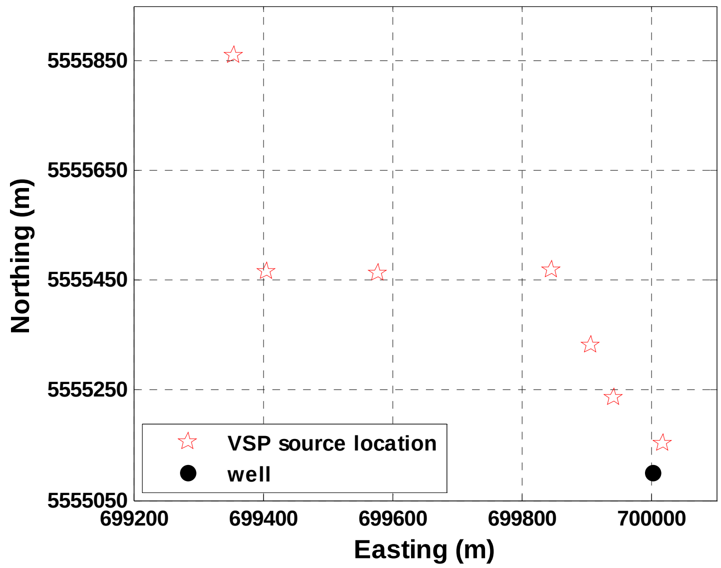

Figure 2.3 Locations of the well and VSP sources.

2.2 Zero-offset and far-offset VSP processing

To avoid processing artifacts which may lead to mis-interpretation as a result of inappropriate choice of processing parameters, a methodology called interpretive processing was followed (Hinds and Kuzmiski, 1996, 2001). The interpretive processing enables the interpreter to examine each step of the processing flow. More importantly, it allows the interpreter to fully examine the VSP data in the same manner as quality control procedure for surface seismic data processing. Compared with surface seismic data, a VSP dataset is smaller. Therefore such an examination is not only effective but easily applicable. The processing flows used for zero-offset and far-offset VSP data are shown in Table 2.2.

Table 2.2 Processing flow for zero-offset (left) and far-offset VSP data (right).

Zero-offset	Far-offset
1. Load geometry	1. Load geometry
2. First arrival picking and velocity inversion	2. Horizontal rotation
3. Horizontal rotation*	3. Amplitude recovery
4. Amplitude recovery	4. Wavefield separation
5. Wavefield separation	5. Time-variant rotation
6. Deconvolution	6. Deconvolution
7. Corridor stack	7. VSP-CDP transform
* This step may not always be necessary.	

2.2.1 Zero-offset VSP data processing

The zero-offset VSP surveys used both vertical and horizontal vibrators as sources. They were processed for PP and SS waves respectively.

Vertical vibrator source zero-offset VSP

In the case of the zero-offset VSP survey with vertical vibrator, energy will be mostly recorded by the vertical (Z) component. However, some energy can still be recorded by horizontal receivers. Figure 2.4 shows the horizontal radial (Hmax, the horizontal channel in the source-receiver plane), horizontal transverse (Hmin, the horizontal channel normal to the source-receiver plane) and vertical (Z) components of the vertical vibrator zero-offset VSP (refer to the processing coordinates in Appendix A). Hmax and Hmin result from a rotation of X and Y components (Appendix A). Various wave types, including transmitted, reflected and direct S-waves are recorded on horizontal components (Figure 2.4a, b). The reason for the generation of S-waves can be imperfect verticality of the source, horizontal heterogeneity of the near surface structure, or perhaps azimuthal anisotropy. On the horizontal radial component, weak direct P waves can also be seen. In the vertical component, direct and reflected P-waves can be easily spotted (Figure 2.4c). Downgoing multiples can also be clearly recognized. Besides, small amount of direct S-waves can also be seen at shallow receivers from 600 ms – 900 ms.

Considering that the P-waves are mostly recorded by the vertical component and the upgoing S-waves are very weak, the vertical component was processed for PP waves. The processing started with assigning the geometry for the VSP data. Then the first arrivals were picked and traveltime inversion for velocity was conducted based on the first arrival time. The resultant velocities will be used for NMO processing (especially for far-offset VSP data) and sonic log calibration. The sonic log and velocity estimated from the VSP are similar with the sonic values usually somewhat higher (Figure 2.5).

A mean scale gain function was calculated in a 100 ms window along the first arrival time and then applied to entire traces to balance the amplitude between each trace. A $t^{1.6}$ gain was also used for amplitude recovery.

The upgoing and downgoing waves were then separated using a 13-trace median filter. First the data were aligned by the first arrival time, and the downgoing waves were estimated by the median filter. The upgoing waves were then estimated by subtracting the downgoing wave from the whole wavefield.

Since the downgoing wavefield is also recorded in the VSP survey, a deterministic waveshaping deconvolution operator can be designed from downgoing P waves and applied to upgoing waves. After deconvolution, the resolution was improved correspondingly. A comparison between the upgoing wavefield before and after

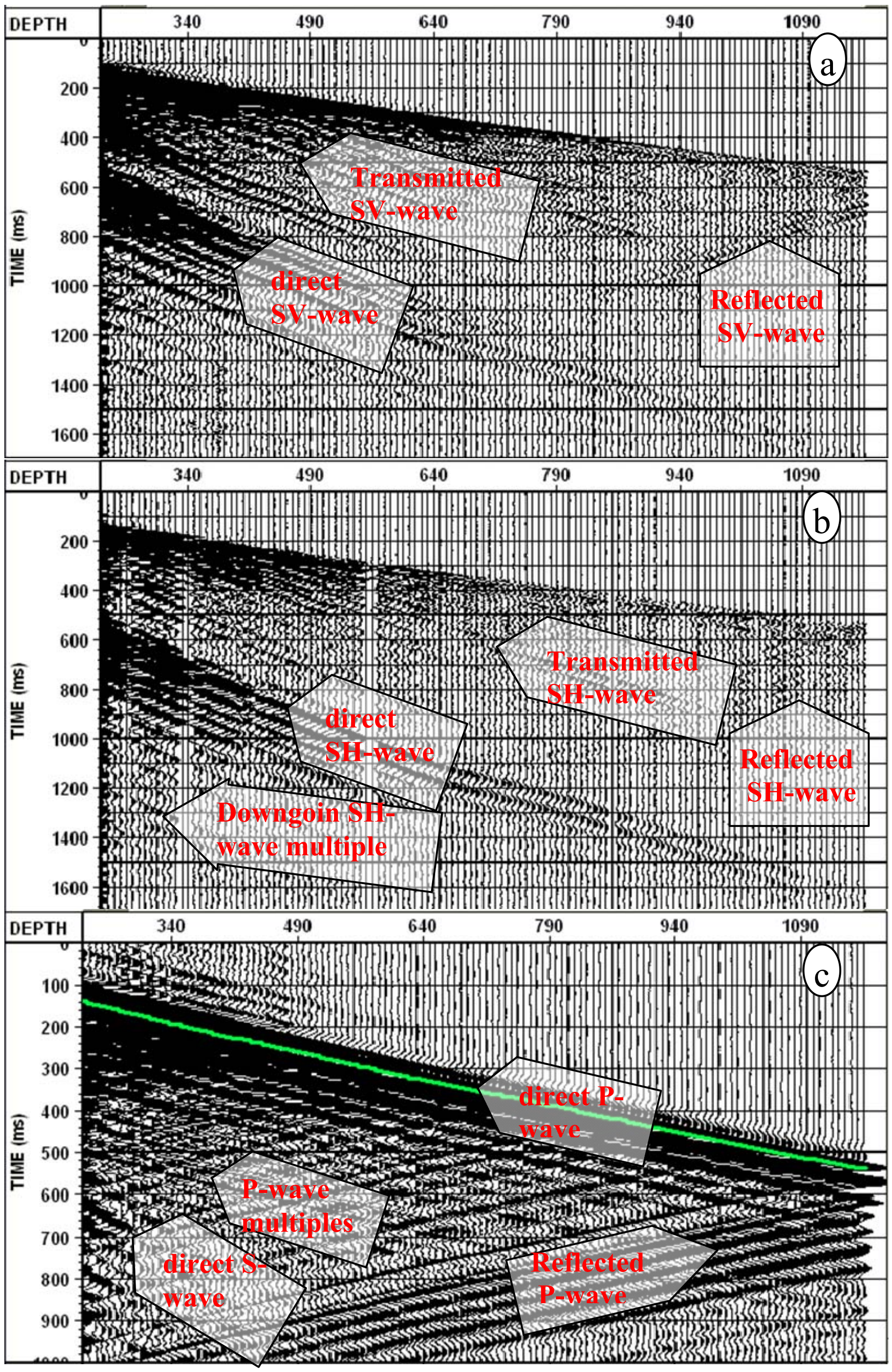

Figure 2.4 Hmax (horizontal radial, a), Hmin (horizontal transverse, b), and Z (c, the green line is first arrival picking) components of zero-offset VSP (54m, vertical vibrator). Hmax and Hmin are from a horizontal rotation of X and Y components.

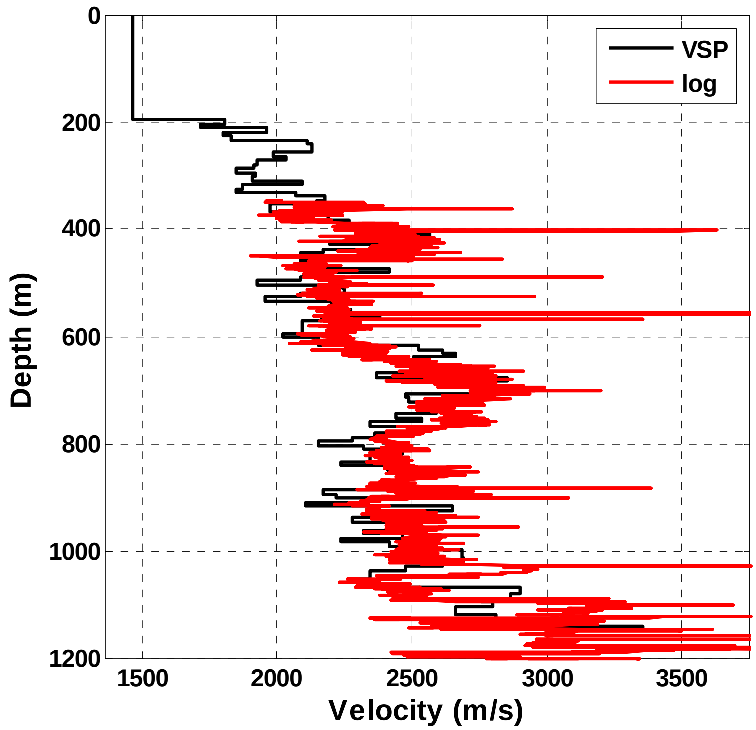

Figure 2.5 P-wave velocity (black line) estimated from zero-offset VSP (vertical vibe) first arrival time. The red line represents P-velocity from the sonic log.

deconvolution is shown as Figure 2.6. Due to the velocity difference between P and S-waves, the downgoing SV waves are not removed by wave separation using median filter. It can be found at shallow receivers from 500 ms to 1200 ms (Figure 2.6), and should be attenuated before stack.

The data was then shifted to two-way traveltime by applying first-arrival time statics (Hardage, 1983). Considering the time lag of multiples, the upgoing wavefield recorded close to reflectors is assumed to be largely noise free. Therefore, before stack, a 50 ms corridor mute was applied to the data to remove multiples and other noise. By comparing the stack with and without a corridor mute, we see that the corridor stack has a higher resolution (Figure 2.7). The corridor stack result of a zero-offset VSP provides a multiple-free trace with frequency bandwidth from 10 Hz to 95 Hz. Compared with the corridor stack trace, residual multiples can be determined by event discrepancies. Multiples can be estimated by subtracting the corridor stack from the non-corridor stack (Figure 2.7e). The multiples can cause event delay, at 1000 ms and 1100 ms, or amplitude change at 1150 ms, and sometimes decrease the seismic resolution, at 750 ms, 900 ms, and 1100 ms. Since the multiples are very difficult to recognize on surface seismic data in some cases, the VSP data can be very helpful in the interpretation of surface seismic data.

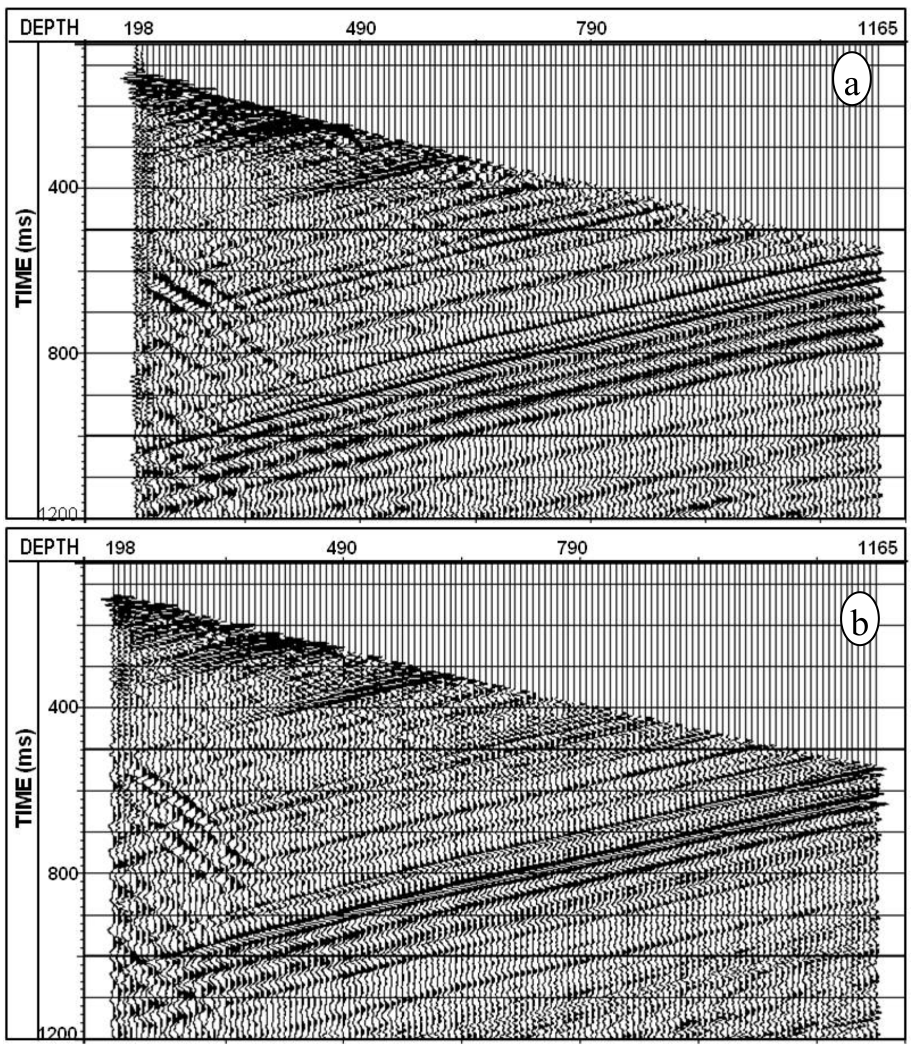

Figure 2.6 Upgoing wave (with mute) before (a) and after (b) deconvolution (source offset 54 m). The downgoing SV waves can be found at shallow receivers from 500 ms to 1200 ms.

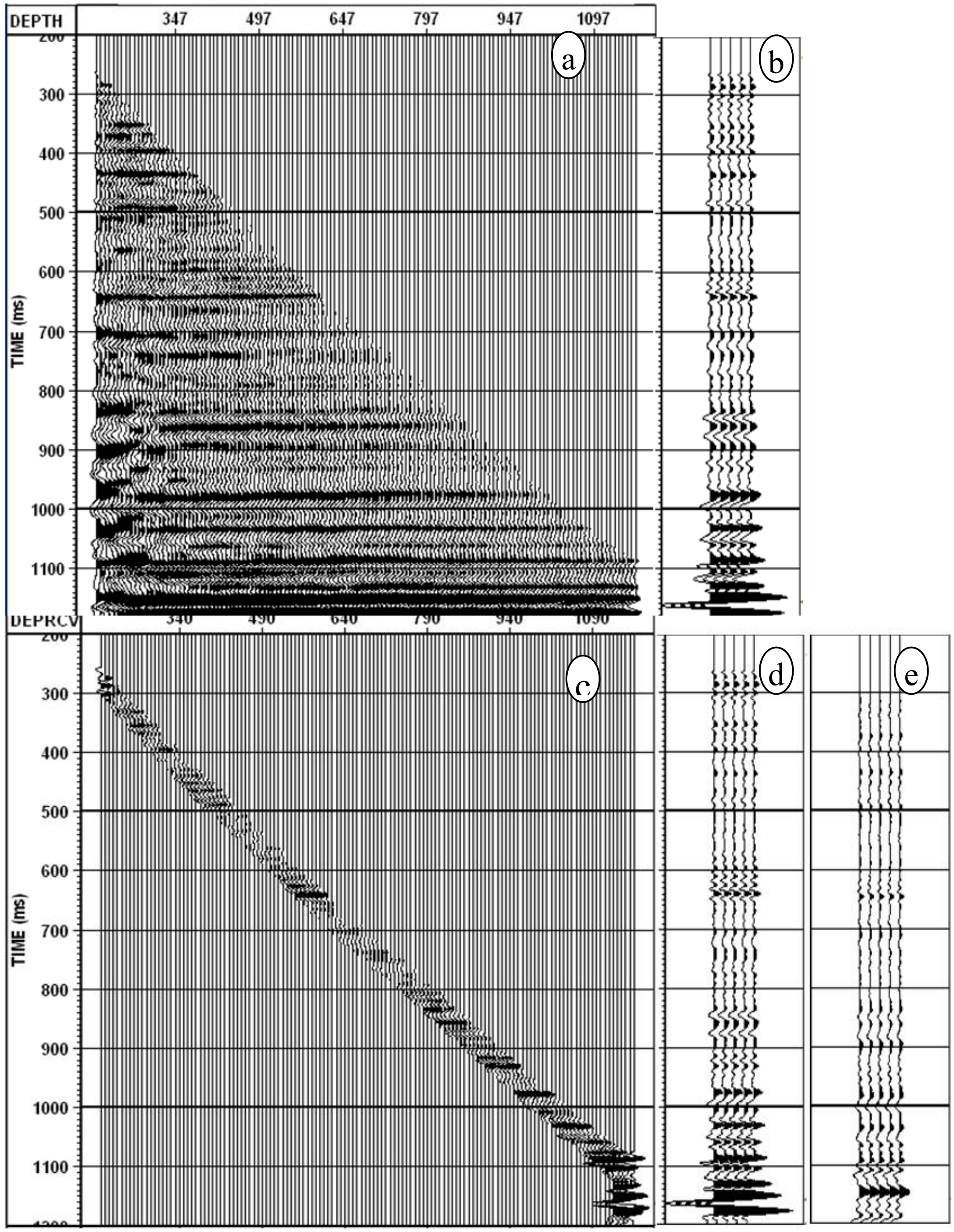

Figure 2.7 Zero-offset VSP data before corridor mute (a) and the corresponding stack trace (b, duplicated 5 times), and after corridor mute (c) as well as the corridor mute stack trace (d, duplicated 5 times). (e) is the difference between corridor stack (d) and non-corridor stack (b).

Horizontal vibrator source zero-offset VSP

The processing of the horizontal vibrator source zero-offset VSP data is similar to that of vertical vibrator source zero-offset VSP data. Figure 2.8 displays the horizontal radial (Hmax), horizontal transverse (Hmin), and vertical (Z) components of the horizontal vibrator zero-offset VSP. Both downgoing and upgoing S-waves can be seen on the radial component, Hmax. The upgoing S-waves are comparatively weak on the transverse component, Hmin. On the vertical component, downgoing P-waves, upgoing P-waves, and direct S-waves can be seen. Figure 2.9 shows the shear velocity estimated from S-wave direct arrival. The sonic values are usually higher than the velocity estimated from the VSP due to velocity dispersion (Stewart et al., 1984).

Both the horizontal radial component Hmax, and the horizontal transverse component Hmin, are processed for SS wave images. The processing follows the same sequence as that for vertical vibrator VSP. The processed Hmax, Hmin (before corridor stack) and corresponding SS corridor stack traces are shown in SS time as Figure 2.10. Hmax displays a higher S/N (signal-to-noise ratio) than Hmin. The stack traces from Hmax and Hmin have similar reflection character.

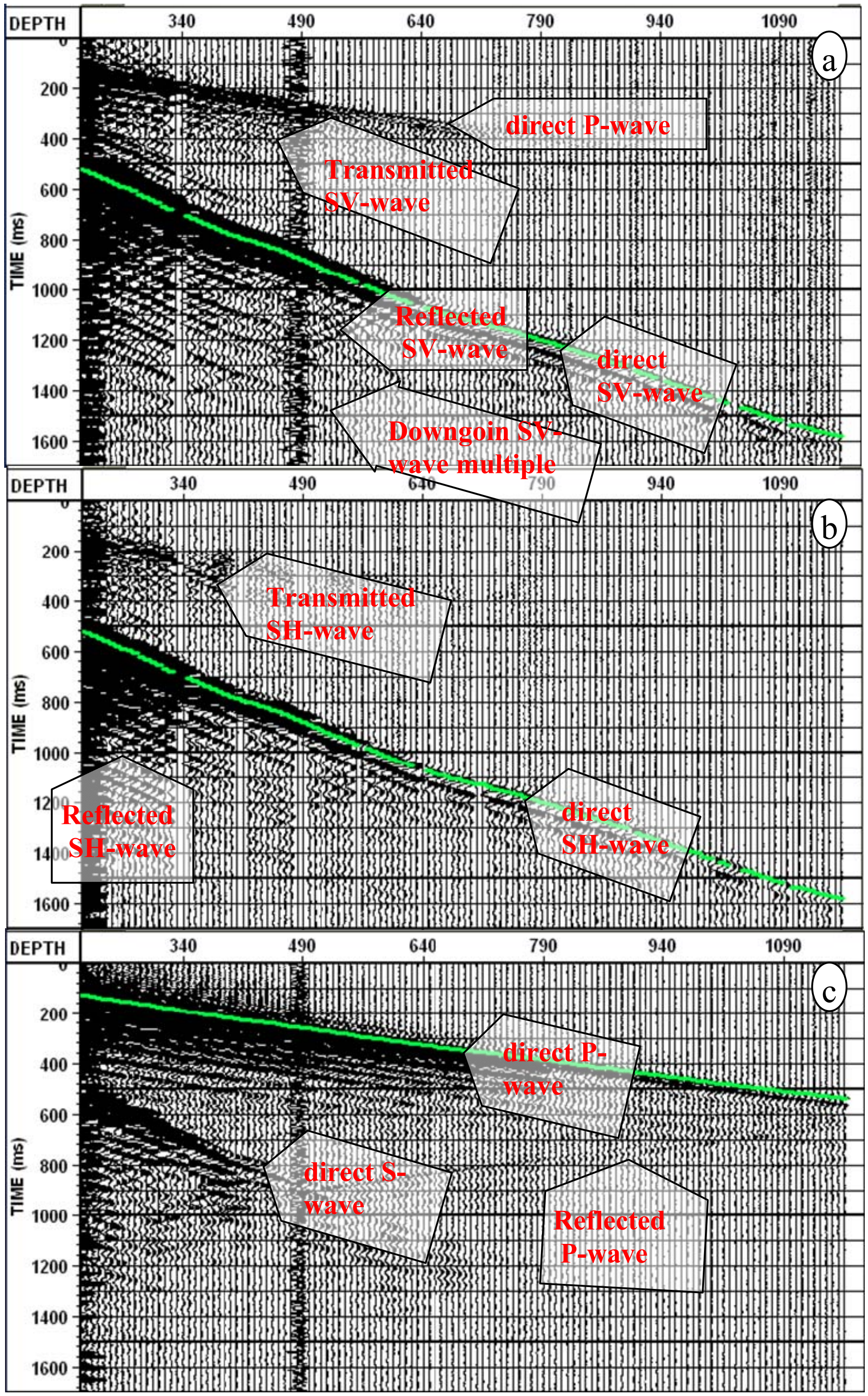

Figure 2.8 Hmax (horizontal radial, a), Hmin (horizontal transverse, b), and Z (c) components of zero-offset VSP (54m, horizontal vibrator). Hmax and Hmin are obtained from a horizontal rotation of X and Y components.

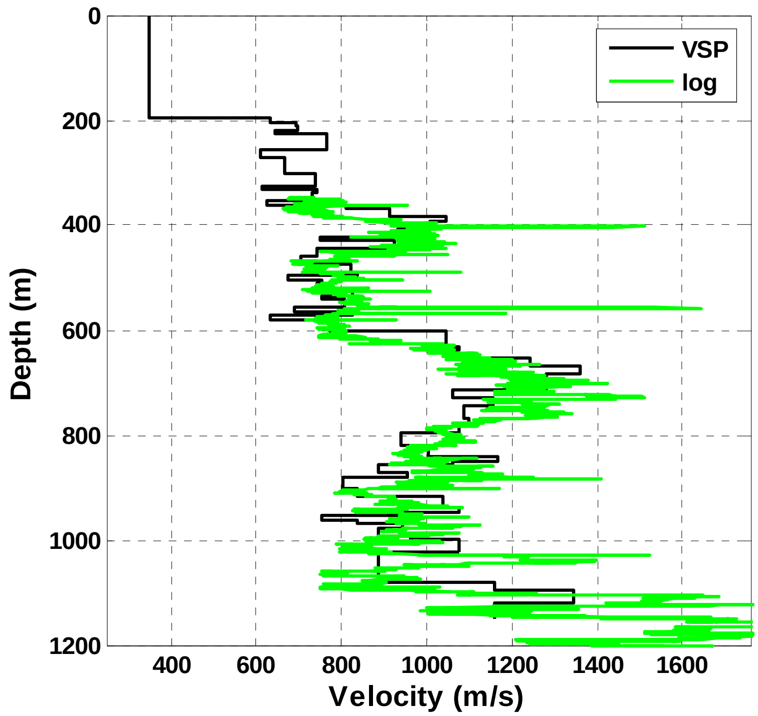

Figure 2.9 S-wave velocity (black line) from S-wave first arrival time inversion of zero-offset VSP (horizontal vibe). The green line represents velocity from the sonic log.

2.2.2 Far-offset VSP data processing

The far-offset VSP data were processed using a 3C processing flow. Vertical and horizontal components are processed for PP and PS images, respectively. Compared with zero-offset VSP, some different processing steps are required for the far-offset VSP. Here, mainly the techniques different from the zero-offset VSP processing flow will be discussed. One of the indispensable processing steps is that the wave polarization must be determined for the far-offset VSP (it is required for zero-offset VSP too, however, it is not necessary for vertical component processing especially when the offset is very small). Hodogram analysis (Appendix A) can be used to determine the polarization of the various wave modes. Figure 2.11 displays the hodogram analysis in an analysis window

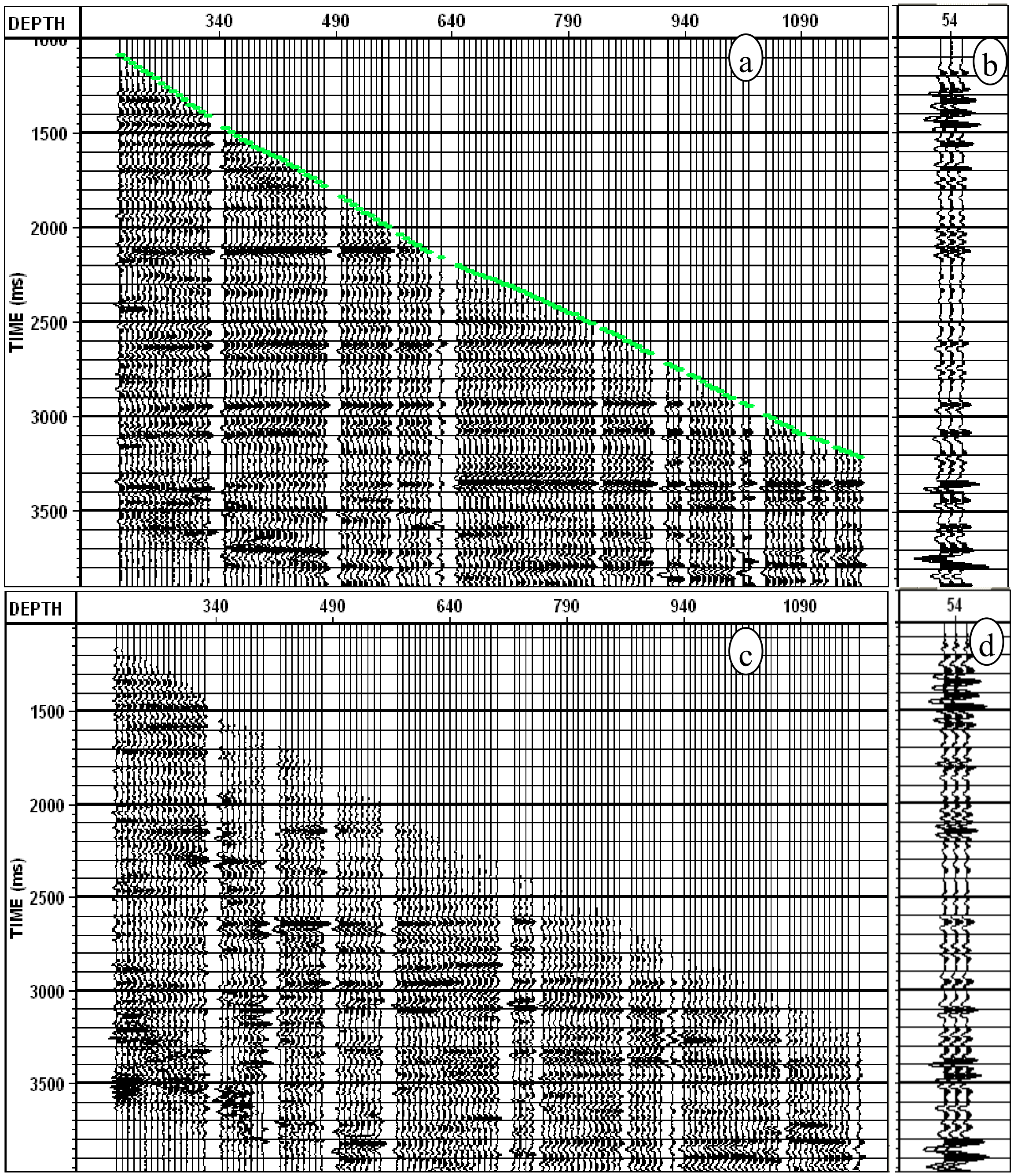

Figure 2.10 Horizontal components processing results of horizontal vibe zero-offset VSP (AGC applied for display). a: processed Hmax (horizontal radial) before stack; b: corridor stack trace of Hmax (duplicated for 3 times); c: processed Hmin (horizontal transverse) before stack; d: corridor stack trace of Hmin (duplicated for 3 times).

of one period/cycle after the first arrival, and the comparison between the horizontal channel data before and after rotation (Appendix A) at a depth level of 234 m. The linearity of the polarization is quite good. There is no distinct amplitude difference between the x and y data on raw data, while most energy is redistributed to Hmax (horizontal radial, the horizontal channel in the source-receiver plane) after data rotation. A polarity reversal is found at the depth level of 302 m (Figure 2.11), and it is corrected after hodogram analysis and data rotation. Random orientation can also be found on the x and y components of offset 399 m VSP data (Figure 2.12), very little coherent signal can be seen on the raw x and y data. After data rotation, most of the P and SV energy was redistributed to Hmax. Both the downgoing and upgoing waves become clearer after data rotation. There is very little P energy on Hmin (the horizontal channel orthogonal to source-receiver plane), but some shear energy exists on Hmin (Figure 2.13). It is thought to be created by imperfect verticality of the source, horizontal heterogeneity of the near surface structure, or perhaps azimuthal anisotropy. Since the upgoing SH waves are very weak on Hmin, only the Z component and Hmax were processed for P and SV wave images.

To unravel the upgoing P waves and upgoing SV waves, the upgoing wavefields were first separated from both channel Z and Hmax. By a time-variant rotation (Appendix A) of the two data sets, the upgoing P and upgoing SV wave can be separated as shown in Figure 2.14.

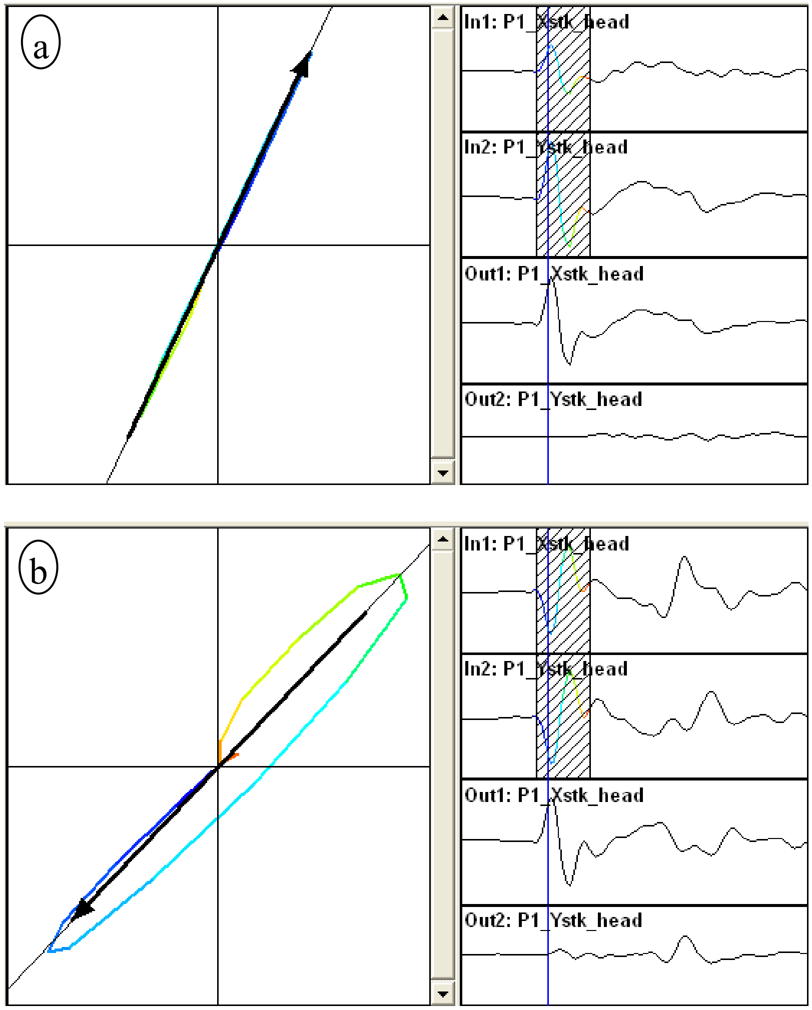

Figure 2.11 Hodogram analysis of X and Y components at depth 234m (a) and 302m (b) of the VSP data with source offset 399.1 m. At each depth, In1 and In2 are X and Y components for hodogram analysis; Out1 and Out2 are Hmax (horizontal radial) and Hmin (horizontal transverse) from X and Y rotation.

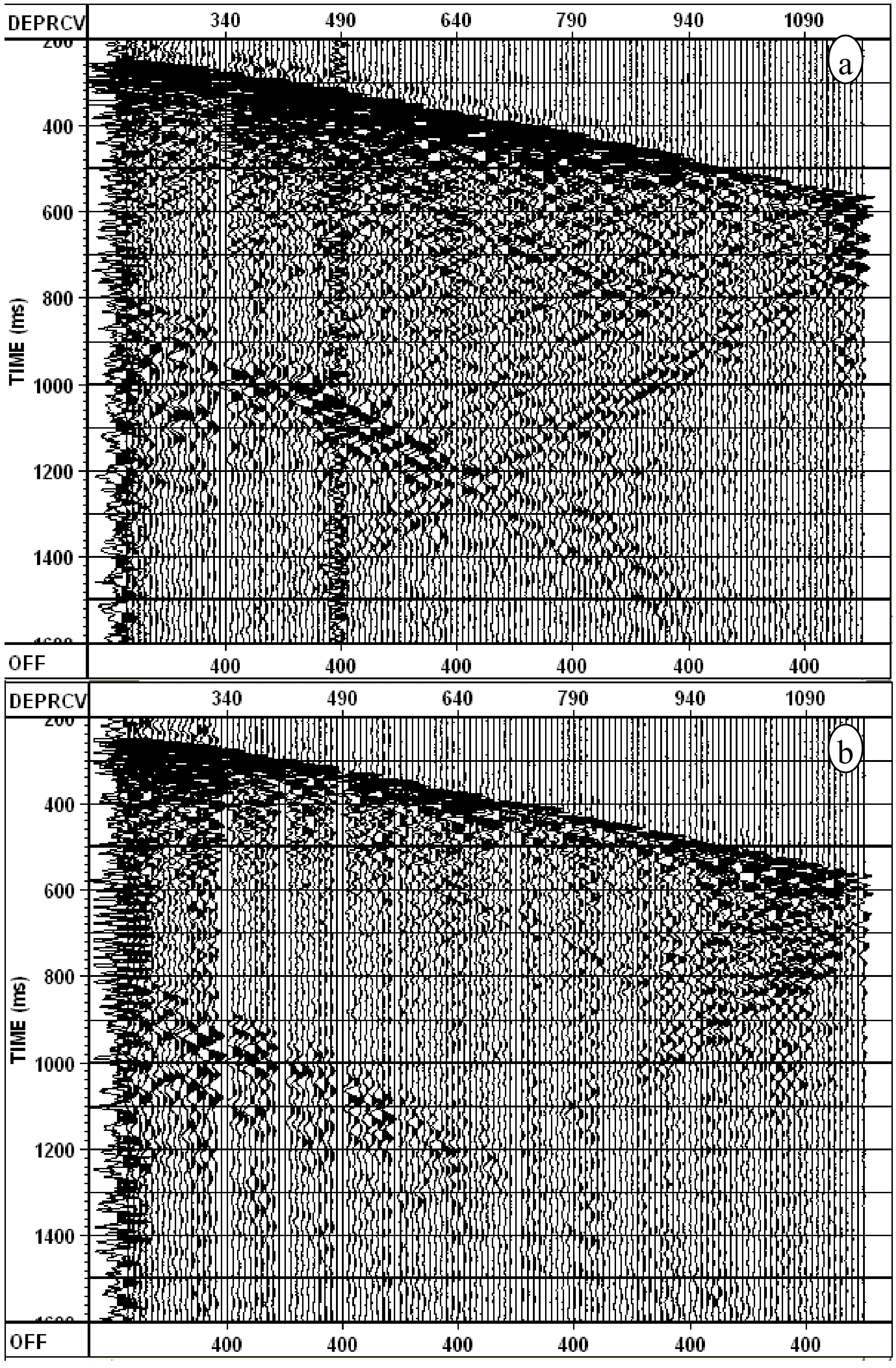

Figure 2.12 X (a) and Y components (b) before rotation (source offset 399.1 m).

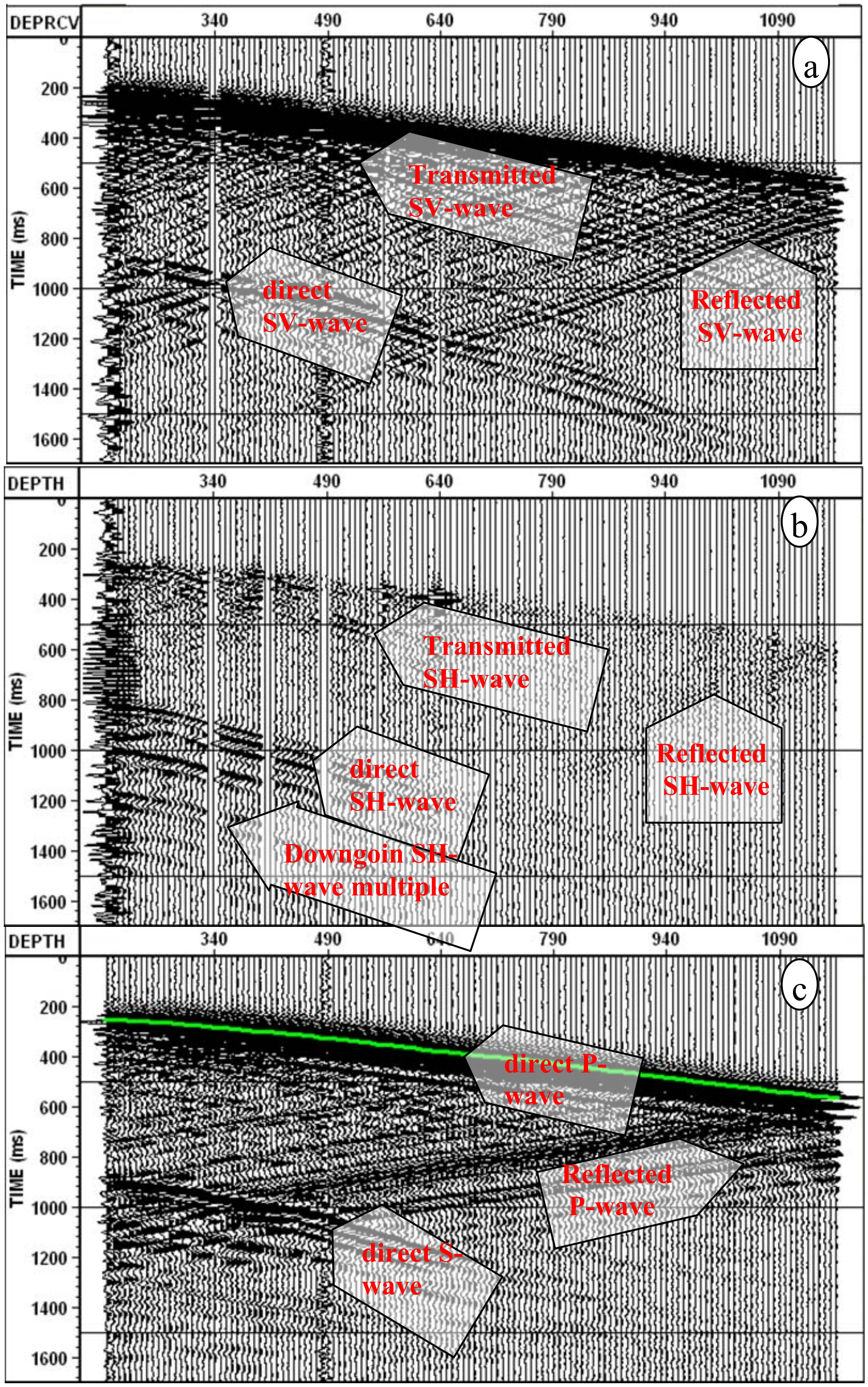

Figure 2.13 Hmax (horizontal radial, a), Hmin (horizontal transverse, b), and Z (c, the green line is first arrival picking) components of far-offset VSP (source offset 399.1m). Hmax and Hmin are from horizontal rotation of X and Y components.

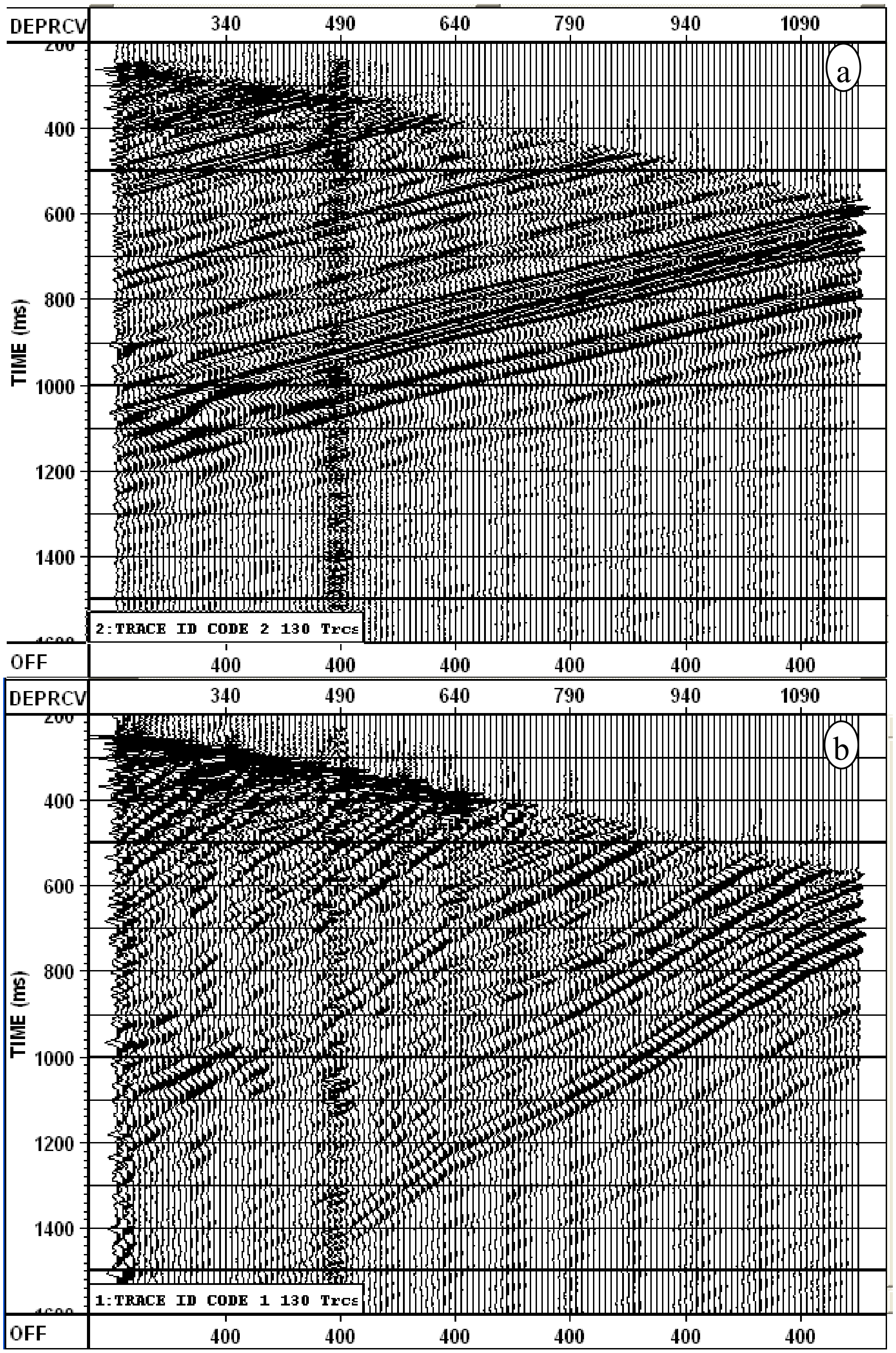

Figure 2.14 Upgoing PP (a) and PS (b) waves from time-variant rotation of upgoing waves from Z and Hmax (source offset 399.1 m).

Most of the rest of the processing resembles that of the zero-offset VSP data. Because of the far offset, there will be a large moveout left if only static shifts are applied to the data, especially for the shallow part. When both NMO and static shift were applied to the data, the reflections were flattened. Finally, a VSP-CDP transform was introduced to map the time- depth domain data into the offset-time domain similar to surface seismic images (Figure 2.15). The frequency bandwidth is 10 Hz to 90 Hz.

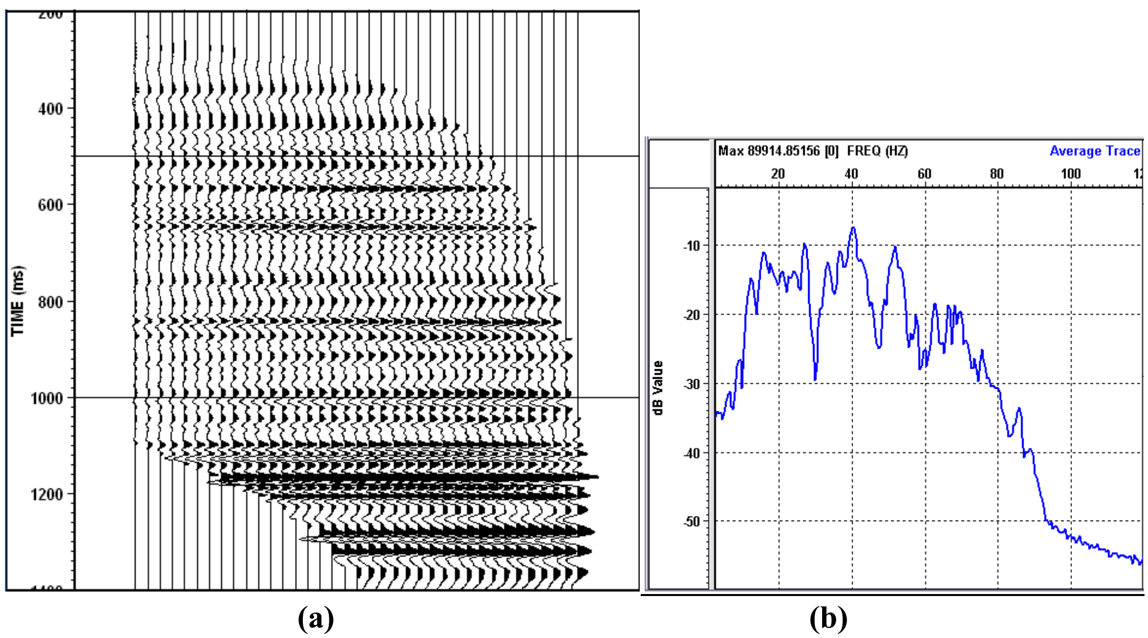

Figure 2.15 VSP-CDP mapping of upgoing P waves (a) and its average amplitude spectrum (b).

2.3 AVO processing of walkaway 3C VSP data

In addition to the near-offset VSP and the far-offset VSPs, a walkaway VSP survey with four shots was also acquired. The source and receiver locations for these VSP shots are listed in Table 2.3. The top receiver of the walkaway VSP is 954m, which is above the Viking Formation and within the Lower Colorado Group. The top of the studied reservoir sand is approximately 1048m from the surface. The bottom receiver of all the VSP shots is in the channel sand.

Table 2.3 VSP surveys for walkaway VSP processing.

Survey Type	Source Offset (m)	Number of Receivers	Top Receiver Depth (m)	Bottom Receiver Depth (m)	Receiver Spacing (m)
Zero Offset	**54**	**130 (14)**	**197 (954.5)**	**1165**	**7.5 (15)**
Offset	**399**	**130 (14)**	**197 (954.5)**	**1165**	**7.5 (15)**
	699	**130 (14)**	**197 (954.5)**	**1165**	**7.5 (15)**
Walkaway	**150**	**14**	**954.5**	**1165**	**15**
	250	**14**	**954.5**	**1165**	**15**
	558	**14**	**954.5**	**1165**	**15**
	997	**14**	**954.5**	**1165**	**15**

Note: the numbers parenthesized in the table are the values actually used for AVO processing.

Due to its geometry, a VSP survey has some advantages for AVO analysis (Coulombe et al., 1996): (1) VSP data generally have a broader bandwidth than comparable surface seismic data due to the short travel path from the source to receiver, especially only one-way through the near surface; (2) the S/N (signal-to-noise ratio) is higher than that of surface seismic data due to the quiet borehole environment; (3) a deterministic waveshaping deconvolution operator can be designed because the downgoing wavefield is also recorded, thus wave-field propagation effects such as multiples and attenuation along the incident travel path can be removed; (4) the downgoing (incident) waves and upgoing (reflected) waves are both recorded near the interface and largely free of undesirable wave propagation effects, thus a good estimate of the reflection coefficient of an interface is relatively easy to obtain. The walkaway VSP geometry is especially suitable for AVO analysis (Figure 2.16). Considering all these advantages, walkaway VSP data were processed for AVO analysis at the reservoir interval. In addition to the four shots of the walkaway survey, the zero-offset VSP and far-offset VSP data were also processed using the same workflow and included in the AVO analysis.

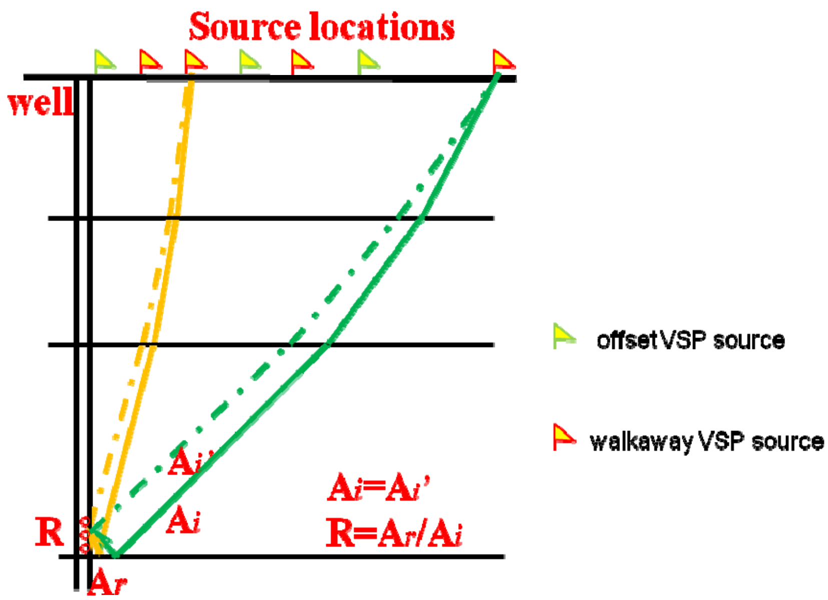

Figure 2.16 Schematic diagram of the advantage of walkaway VSP geometry for AVO processing. Since the receivers are located very close to the reflectors, the incidence wave amplitude *Ai* approximately equal to the downgoing wave amplitude A_i'. Thus the reflectivity *R* can be calculated by dividing the upgoing wave amplitude *Ar* by downgoing wave amplitude A_i. Shots at varied locations give different incidence angles, therefore AVO gather can be built.

The walkaway VSP data were processed using a workflow described by Coulombe et al. (1996, as shown in Figure 2.17). The processing of the 558 m offset will be used as an example to illustrate the processing procedure. Firstly, each shot was processed individually with a workflow similar to that for offset VSP. Horizontal rotation was applied initially to correct for tool spin. The resultant Hmax (horizontal radial direction) and Hmin (horizontal transverse direction) for the 558 m offset VSP are shown in Figure 2.18. Upgoing and downgoing P and SV waves were separated from Hmax and Z component data by “wave-by-wave” algorithm (Blias, 2007). A significant merit of the “wave-by-wave” algorithm compared with a conventional median filter or FK filter methods is that the separated wavefields are largely noise free. Figure 2.19 displays the downgoing and upgoing P waves, and SV waves, derived from the Hmax and Z component data. Then deterministic deconvolution was applied to the upgoing wavefield using the deconvolution operator designed on the downgoing P wave for each shot. Figure 2.20 shows the comparison of the downgoing P wave before and after deconvolution, respectively. After deconvolution, the downgoing P wave was compressed to a real zero-phase wavelet, its corresponding amplitude spectrum was whiter that for the raw data. The deconvolved upgoing P and SV waves using the operator designed form downgoing waves are shown as Figure 2.20.

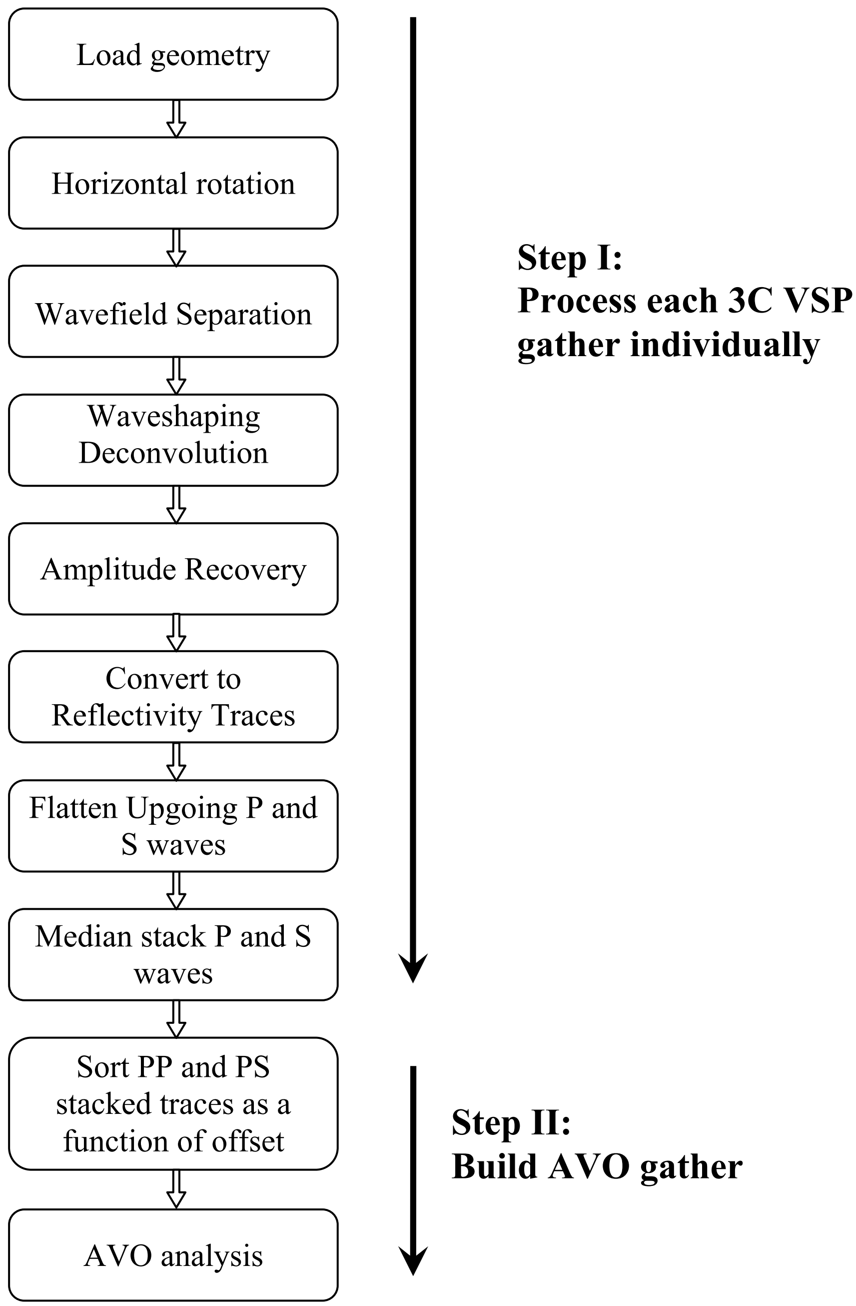

Figure 2.17 The walkaway VSP processing workflow for AVO analysis (modified after Coulombe et al., 1996). Each offset was processed individually to get a reflectivity trace from each shot, and then all shots were combined to form an offset-dependent gather for AVO analysis.

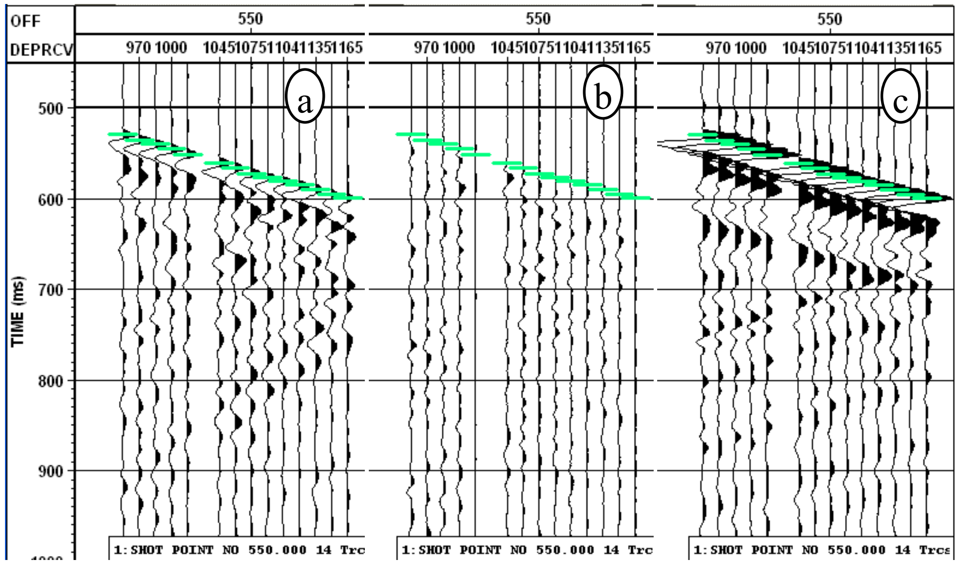

Figure 2.18 Hmax (a, horizontal radial), Hmin (b, horizontal transverse) after a horizontal rotation of X and Y components, and Z component data (c) of the offset 558 m shot (AGC applied, the green line is the first break picks). The waves received in transverse direction (Hmin) are much weaker than those in the radial direction (Hmax).

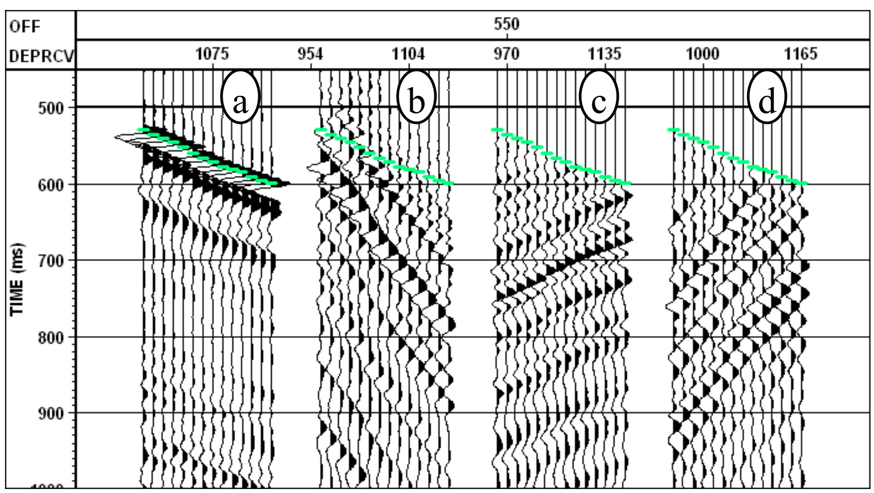

Figure 2.19 Downgoing P waves (a), downgoing SV waves (b), upgoing P waves (c), and upgoing SV waves (d) separated from Hmax and Z data of the offset 558 m shot (AGC applied, the green line indicates the first arrival picks).

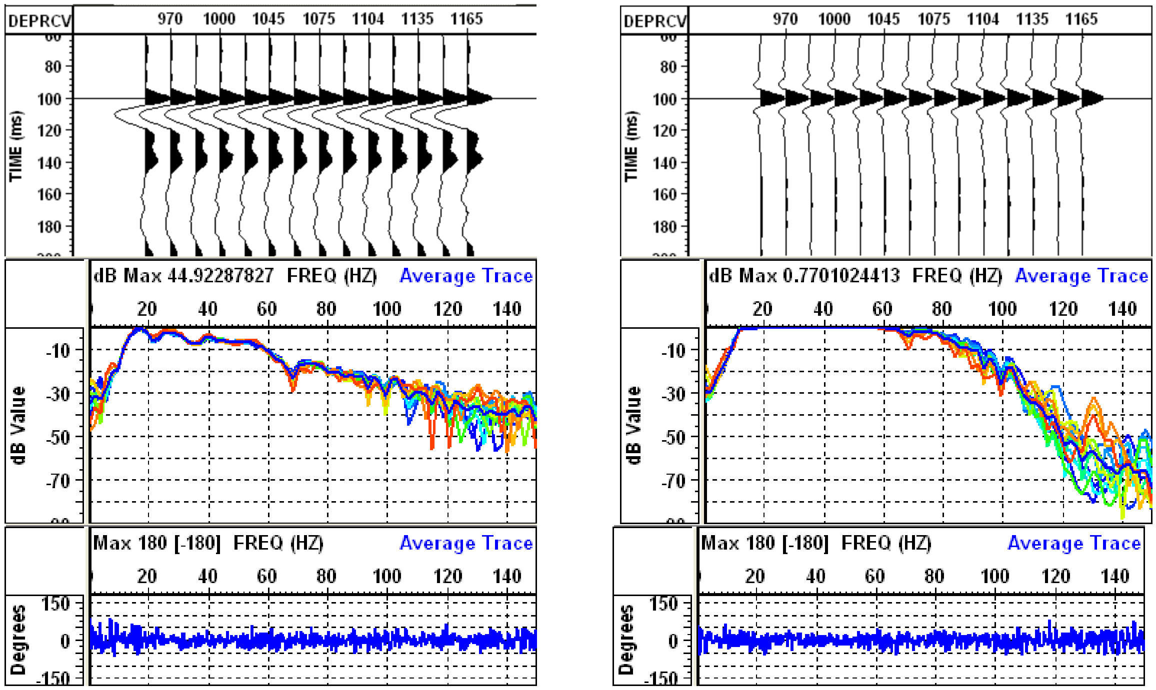

Figure 2.20 Downgoing P waves before (top left) and after (top right) deterministic deconvolution, as well as the corresponding amplitude spectra (the average spectrum is in blue) and average phase spectra (shot offset 558 m).

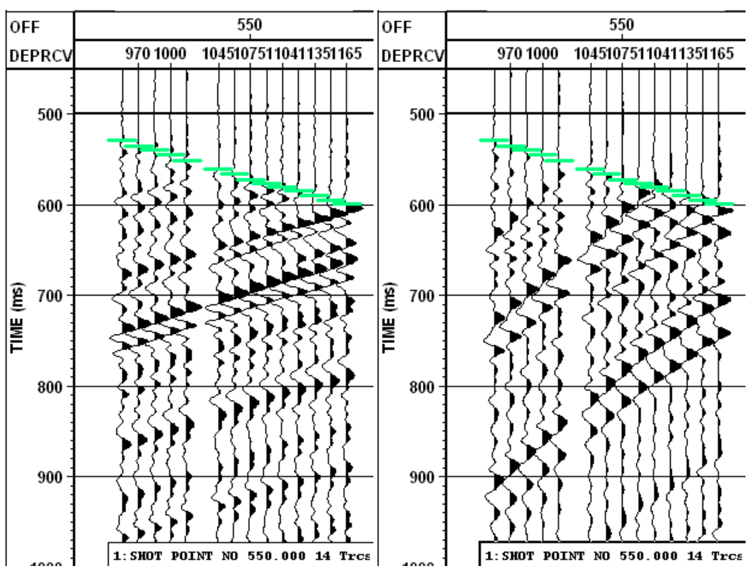

Figure 2.21 Upgoing P and SV waves after a deterministic deconvolution with operator derived from downgoing P waves (shot offset 558 m, the green line indicates first arrival picks).

To recover the true amplitudes for the P- and S-waves, scale factors were first calculated by normalizing the downgoing P waves and applied to the upgoing P and shear wavefields. This processing compensates for the energy decay during the downward propagation; thus the incident waves will be at the same relative amplitude level at each depth level. Figure 2.22 displays the mean scaling of downgoing P waves. Before scaling, the P wave amplitude decreases with depth but after mean scaling over a window from 90 ms to 110 ms, the downgoing P wave at each receiver depth was normalized to the same amplitude. Then a $t^{1.6}$ gain was used to correct spherical divergence losses. The final step for amplitude processing was dividing the upgoing wavefield by the peak amplitude of the downgoing P wave to get the reflectivity traces. Figure 2.23 displays the upgoing P and SV offset-dependent reflectivity gather at a receiver depth 1075 m, from the seven VSP shots.

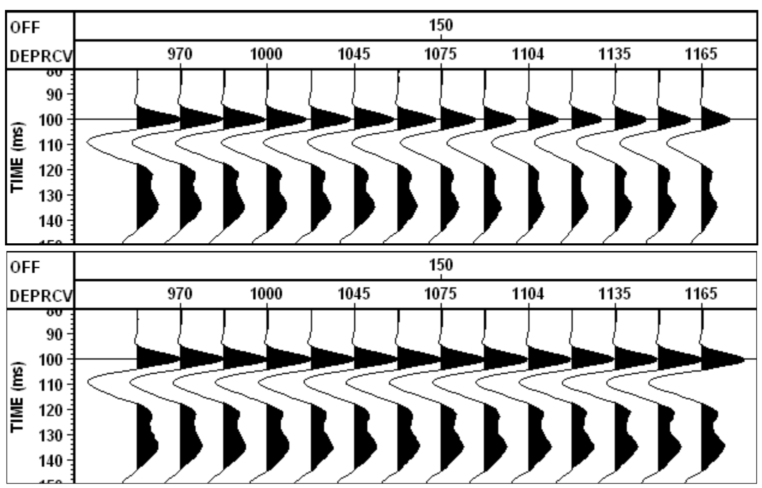

Figure 2.22 Downgoing P waves before and after mean scaling (flattened to 100 ms, shot offset 558 m). Note amplitude decay of direct P waves with increasing receiver depth before scaling.

After amplitude processing, NMO correction was applied to each shot. Also the traces were flattened to the reflection time of a specific event to remove the effect of small time shifts between each trace due to source statics. Here the reflection of the base of the sand channel was chosen, considering that it is close to the reservoir and its reflection is strong and easy to pick. The two-way P wave traveltime was determined after applying NMO correction and first-arrival time flattening of the upgoing P wavefield of the zero-offset VSP. This process will also correct the static due to source elevation and near surface velocity variation between each shot. The reflection of the same horizon, the base of sand channel was corrected to 1096 ms for every VSP shot and the results are shown as Figure 2.24.

Finally, the upgoing P and S waves from each shot were stacked as one trace to improve the signal-to-noise ratio, and were then sorted into offset-dependent gathers for AVO analysis. Figure 2.25 shows the offset gather from common shot stack of the upgoing wavefield, flattened to the reflection time of the base of the sand channel. NMO exists between the shots at different offset locations. The PP reflection time difference on stacked traces between offset 54 m and 699 m is 10 ms for the high-amplitude peak at about 1.15 s. The PS time difference for the same horizon is about 12 ms at about 1.2 s. Combining NMO and channel base reflection flattening, the time shift between different offset locations was removed (Figure 2.24). Figure 2.26 show the stack P and SV traces sorted in the order of source offset. Compared with the results shown in Figure 2.25, the time shift between traces caused by NMO is basically removed not only for the reflection of the channel sand base but for the reflections of other interfaces, too.

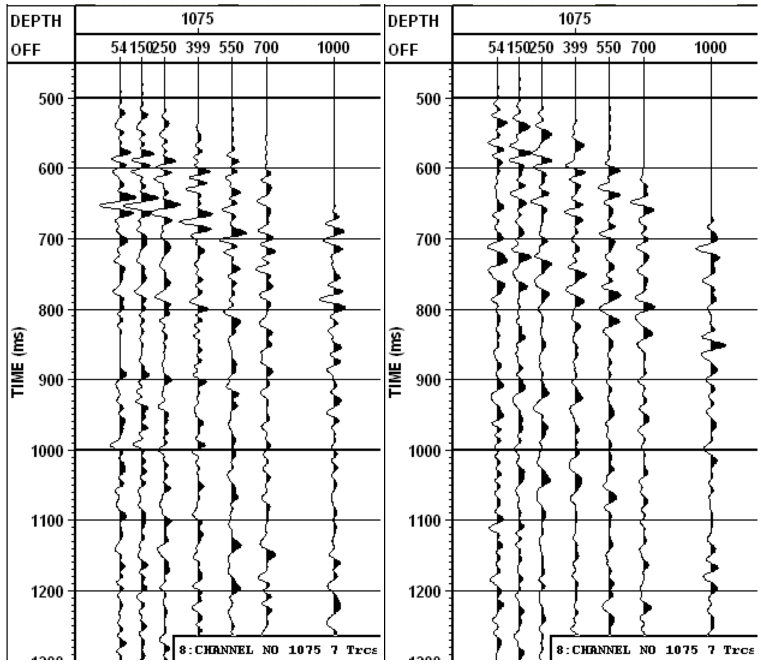

Figure 2.23 Upgoing P and SV offset-dependent reflectivity gather at a receiver depth of 1075 m.

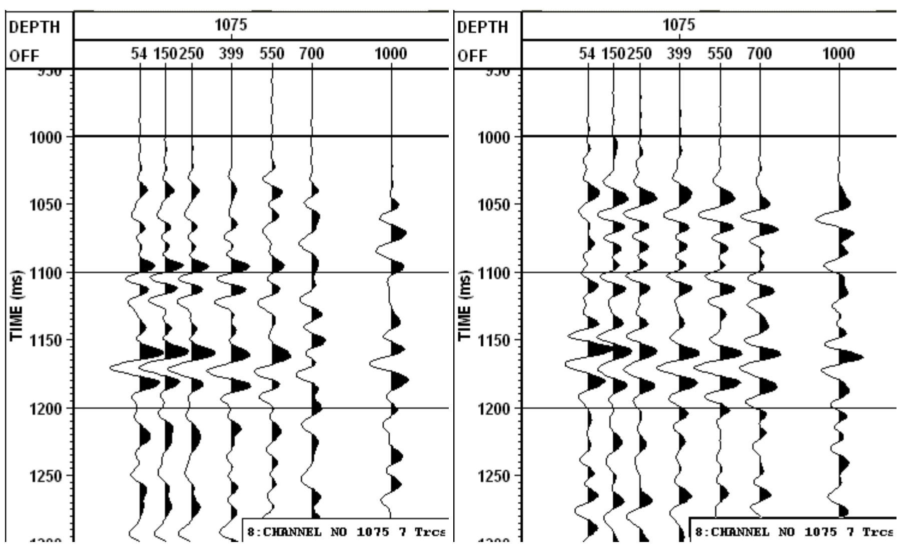

Figure 2.24 NMO and static correction (by flattening the 1096 ms event) applied to an upgoing P and SV offset-dependent reflectivity gather at a receiver depth of 1075 m.

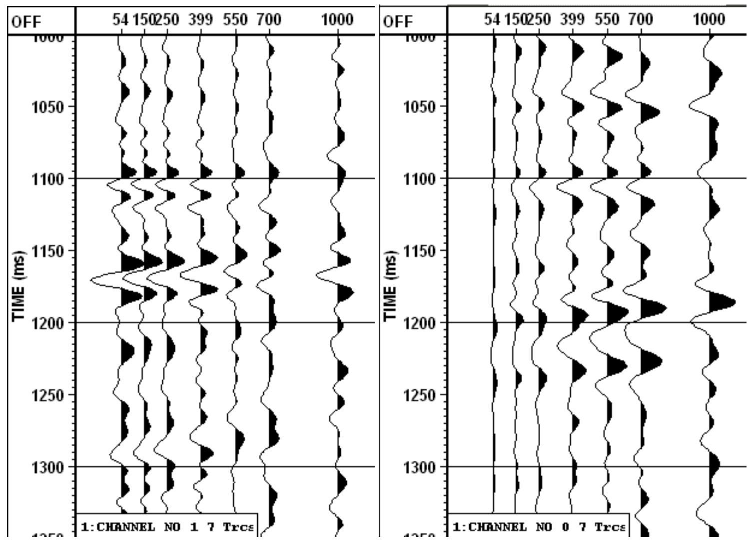

Figure 2.25 Offset gathers of upgoing P and upgoing SV waves from the common shot stack of 1096 ms event flattened gathers (no NMO correction). Note that only the 1096 ms reflection was exactly flattened, the other reflections were all dipping toward 1096 ms event.

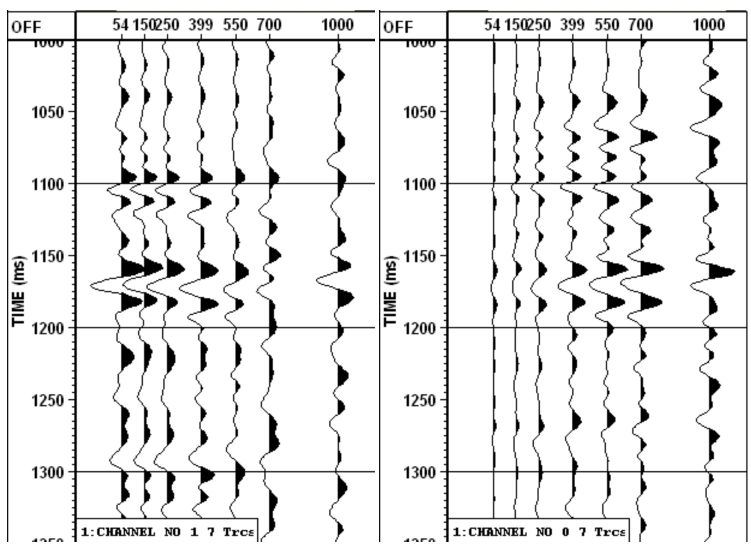

Figure 2.26 Offset gathers of upgoing P and upgoing SV waves from the common shot stack after NMO and static correction (by flattening the 1096 ms event). SV wavefield (P-SV) was also converted to PP reflection time.

Mean scaling factors calculated from the downgoing P wave were applied to the upgoing wavefields to account for incident wave amplitude decay due to increasing propagation distance. However, it is only accurate for the reflections recorded at the receivers very close to the reflectors. Furthermore, spherical divergence and transmission losses were also very difficult to be fully compensated. However, for reflections recorded by receivers close to reflectors, the amplitude recovery measures used are effective and accurate. Therefore a corridor stack will yield more reliable reflectivity traces. Figure 2.27 displays the corridor mute of upgoing P and SV waves. We find that the amplitude of each event on the corridor muted traces is fairly consistent at different depths. Then, each shot was stacked and sorted to offset-dependent gathers for AVO analysis (the P and SV offset-dependent reflectivity traces are shown in Figure 2.28).

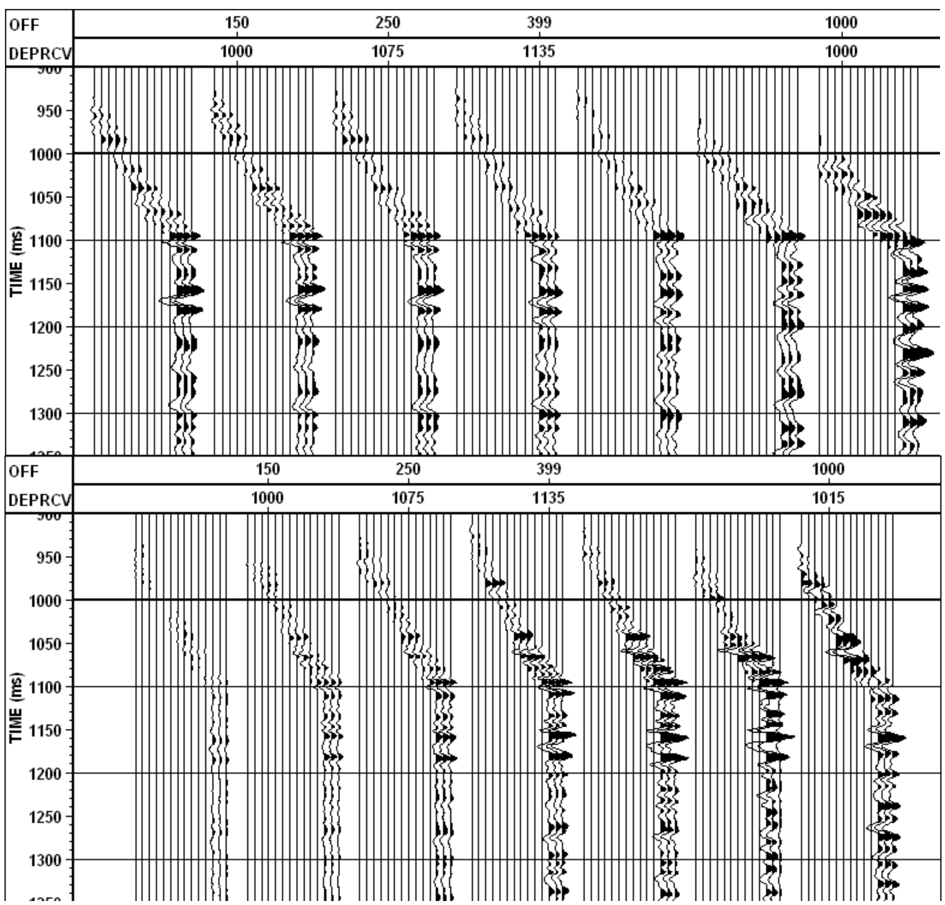

Figure 2.27 A 50 ms corridor mute to depth 1115m of upgoing P and upgoing SV waves.

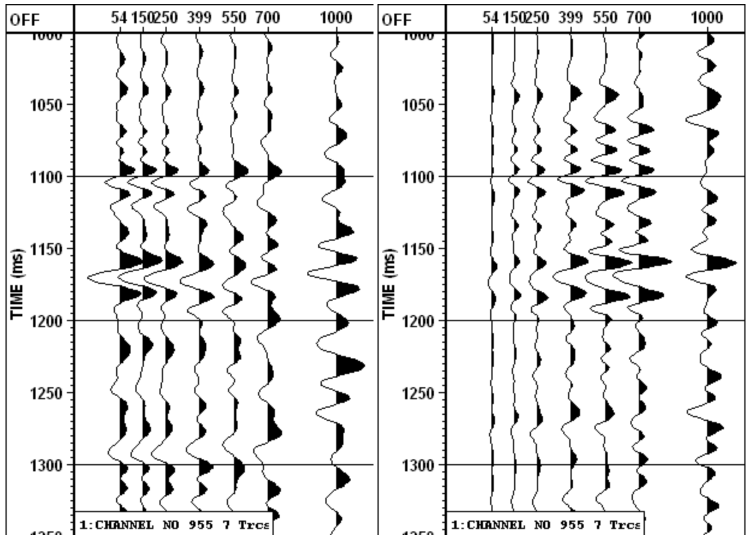

Figure 2.28 Offset-dependent gathers of upgoing P and upgoing SV waves from corridor stack of each shot.

2.4 Results and interpretation

2.4.1 Well log analysis

Figure 2.29 displays well log curves with formation tops of well 11-25-13-17W3 from the Ross Lake oilfield. Clay content in the rock was estimated from the gamma-ray curve by linear scaling between its minimum and maximum values. The total porosity was calculated from the average of density-porosity and neutron-porosity logs. Effective porosity was estimated from the average of the shale-corrected density-porosity and neutron-porosity. Water saturation in this well was calculated from the resistivity curve based on Simondoux model (Crain, 2005). The results are plotted in Figure 2.30. A PE (photoelectric) log was unavailable for this well. According to the neutron-density porosity difference and regional geology in southwest Saskatchewan, the lithologies in this well are mostly shale, shaly sandstone and sandstone.

There are two clean sand intervals with good permeability at 1148 m-1160 m and 1164 m-1180 m respectively (Figure 2.30), which are interpreted to be sand channels in the Cantuar Formation. The rock properties of the two sand intervals are list in Table 2.4. The porosity of the channel sand is quite high, about 30%. There is about 12 m of oil pay of the upper sand, whereas the lower sand is wet. The Vp/Vs value for the upper channel sand (reservoir) is about 1.8. The wet lower channel sand also has a Vp/Vs value of 1.8. Between the upper and lower sand, there is a tight formation with low porosity, about 7%. Here, Vp/Vs value is 1.66.

For the shallow sector (above Milk River Formation) in this well, the rocks have a shale content of more than 50%, although the calculated porosities are quite high. The total porosity is approximately 40%. The effective porosity is about 20%. To investigate the reason for such high porosity in high shale content rocks, a crossplot between total porosity and P-wave velocity was created (Figure 2.31). From the characteristics of the well log curve, the P-wave velocity and total porosity are separated into three parts: from 198 m to 617 m (data in blue), from 617 m to 781 m (the data in red), and from 781 m to the bottom of the well (data in green). These three groups distribute differently in the crossplot of Vp and total porosity. According to the model described by Mukerji and Mavko (2006), this perhaps indicates diagenetic differences of these three depth ranges. The data in the shallow part are mostly around the suspension line and display poor cementation. The compaction and diagenesis of the rock are poor in the shallow part of this well. The rock below the Milk River Formation displays much greater diagenesis. Clean sand tends to be within a narrow region and relatively far from the suspension line. Shaly sand and sandy shale are generally located on the left side of clean sand.

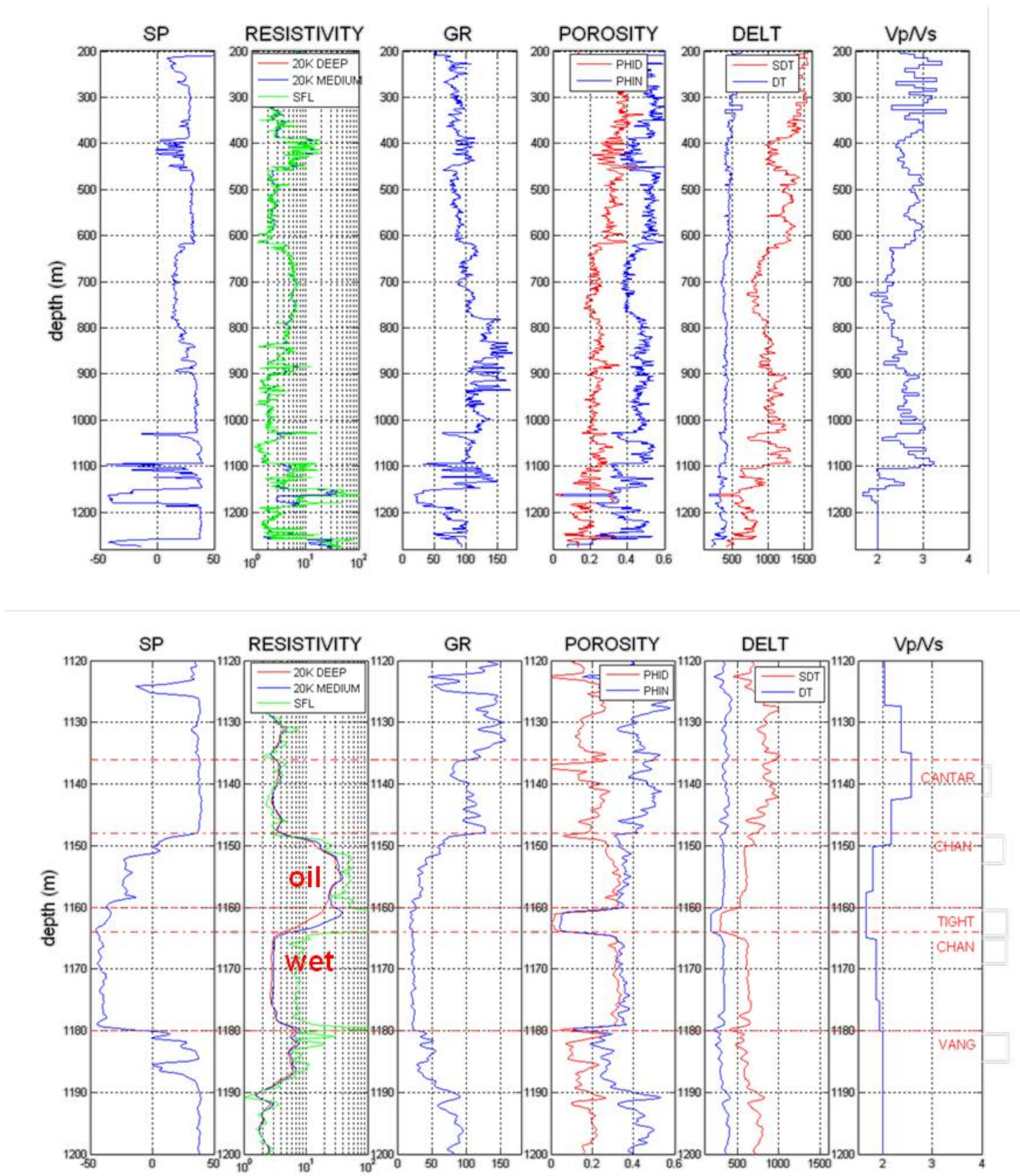

Figure 2.29 Well log curves for the Well 11-25-13-17W3. Top: From left to right - spontaneous potential (SP); resistivity (deep measurement in red, medium measurement in blue and shallow tools in green); gamma-ray (GR); density porosity (red, sandstone-scale) and neutron porosity (blue, sandstone-scale); Slowness (shear wave in blue, and P wave in red); and Vp/Vs. The bottom plots are the same as the top plots focusing on the channel sand portion of the well.

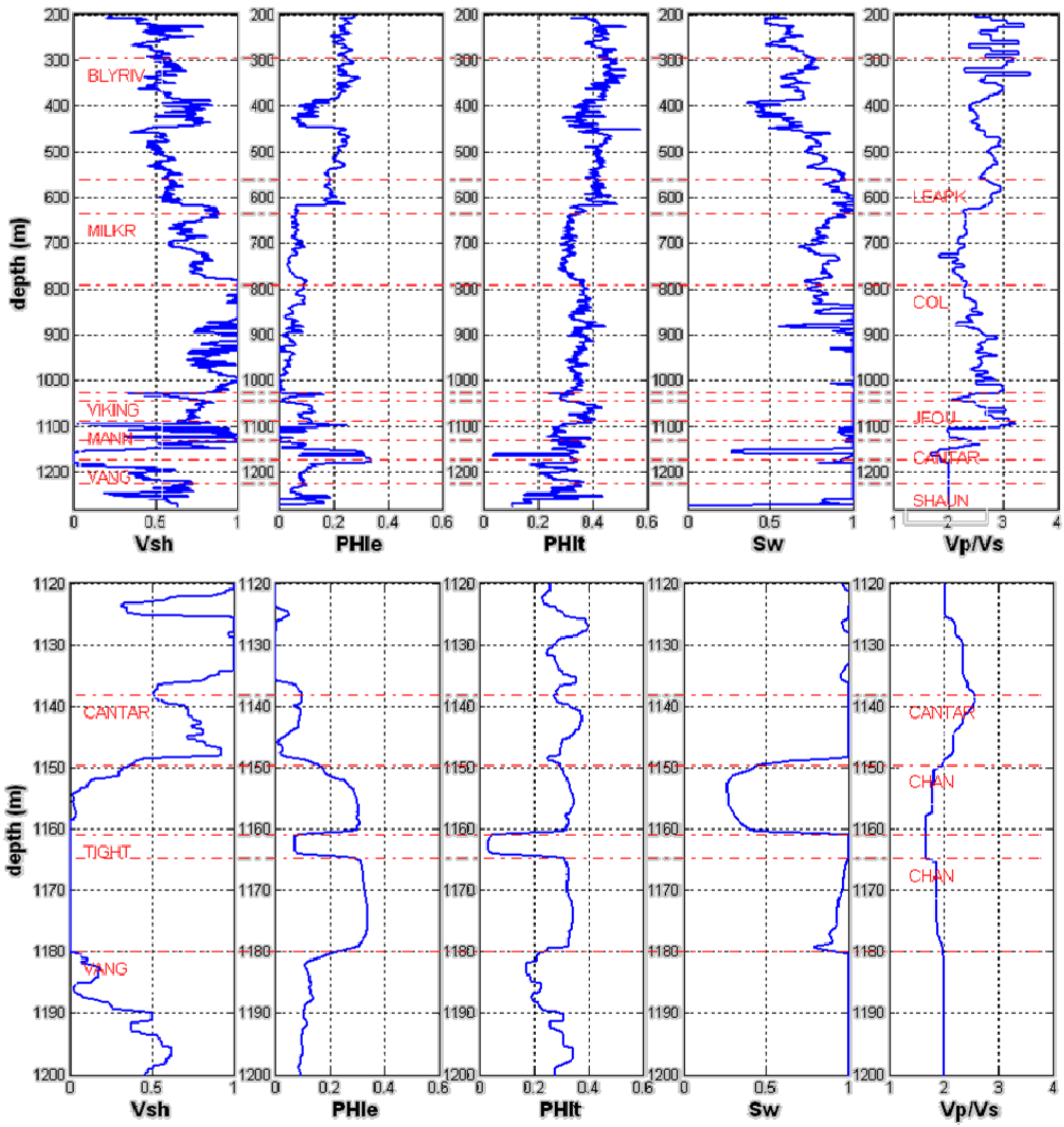

Figure 2.30 Top, rock properties from well log data, from left to right: shale volume, effective porosity, total porosity, water saturation, and Vp/Vs. Bottom, rock properties from the top, focusing on the channel sand part of the well.

Table 2.4 Rock properties of the two sand intervals.

	Thickness/depth (m)	Vp (m/s)	Vs (m/s)	Density (kg/m^3)	Porosity (%)	Vp/Vs
Upper sand (oil)	12 /1148-1160	3010	1660	2130	28	1.8
Lower sand (wet)	16/1164-1180	2980	1630	2130	32	1.8

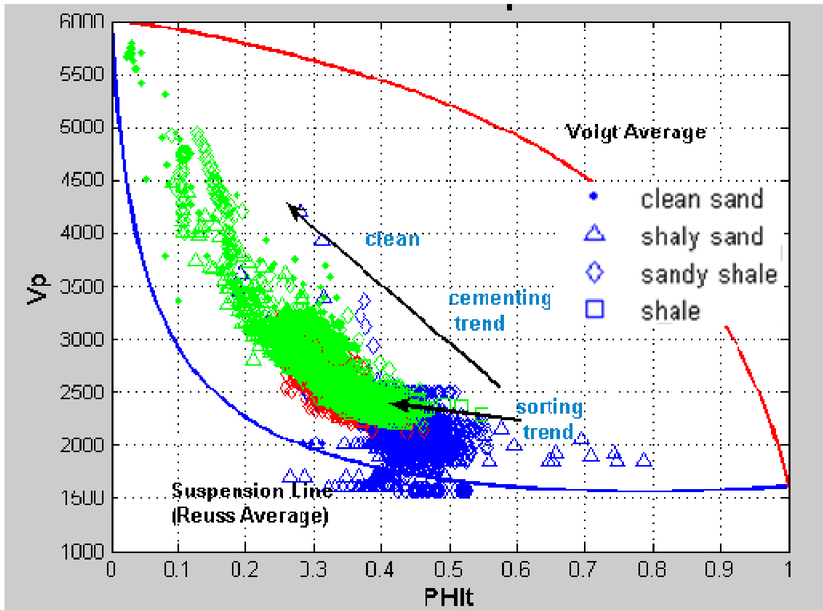

Figure 2.31 Crossplot between Vp and total porosity. Blue: 198 m-617 m (above the Milk River); red: 617 m-781 m (from the Milk River to the Colorado Group); green: 781 m-1276 m (the Colorado Group and below).

2.4.2 Velocity inversion from VSP data

Figure 2.32 displays the P- and S-wave velocities estimated from zero-offset VSP first-arrival time (plotted in blue) and the velocities from dipole sonic logs (plotted in green. The sonic log velocities are blocked to the same depth location as those from the VSP). The sonic log and velocity estimated from the near-offset VSP are similar but with the sonic values somewhat higher (Figure 2.32). It is considered to be caused by velocity dispersion (Stewart et al., 1984). The shear velocities from the shear wave first-arrival time inversion range from 500 m/s to 1360 m/s (Figure 2.32b). The Vp/Vs values from VSP traveltime inversion are close to that from dipole sonic logs. According to well logs analysis, above the upper Cretaceous unconformity (refer to the generalized stratigraphic chart in southwest Saskatchewan shown as Figure 2.1; the unconformity locates between the Lea Park Formation and the Milk River Formation, at a depth of 600 m). Above the unconformity, the rocks display poor cementation and compaction. The Vp/Vs values are generally higher, averagely 2.85. Below the upper Cretaceous unconformity, the Vp/Vs values are relatively lower, averaging 2.2 for sandier rocks from depth 600 m to 900 m, and 2.6 for shaly formations from depth 900 m to the bottom receiver level of the VSP (Figure 2.32).

The P wave velocity difference from near-offset VSP and well logs also displays fairly good correlation with the Vp/Vs, generally a lower value of Vp/Vs correlates to a low velocity difference between VSPs with different source offset locations. It can also be rephrased that lower Vp/Vs correlate with smaller P velocity dispersion. The shear velocities display a similar general trend.

2.4.3 VSP processing results

Zero-offset VSP data yields a time-depth correlation between seismic reflections from VSP data and well logs. Compared with synthetic seismograms from well logs, the measurement frequency of VSP data is fairly close to that for surface seismic data, thus the drift between the VSP and surface seismic is negligible. A composite plot (Stewart and DiSiena, 1989) of the zero-offset corridor stack, flattened shot gather and well logs is shown in Figure 2.33. The correlations between well logs and seismic signatures of chosen geological markers are marked by red lines. Figure 2.34 shows the detailed correlation between zero-offset VSPs and well logs focusing on the reservoir part. The synthetic seismogram (by SYNGRAM) generated from well log data (after VSP calibration) ties the VSP processing results very well. The P and S-wave velocities from the sonic log increase at the top of the Mannville Group and the Cantuar Formation, and the corresponding events on PP and SS data of zero-offset VSP data is a peak. For the

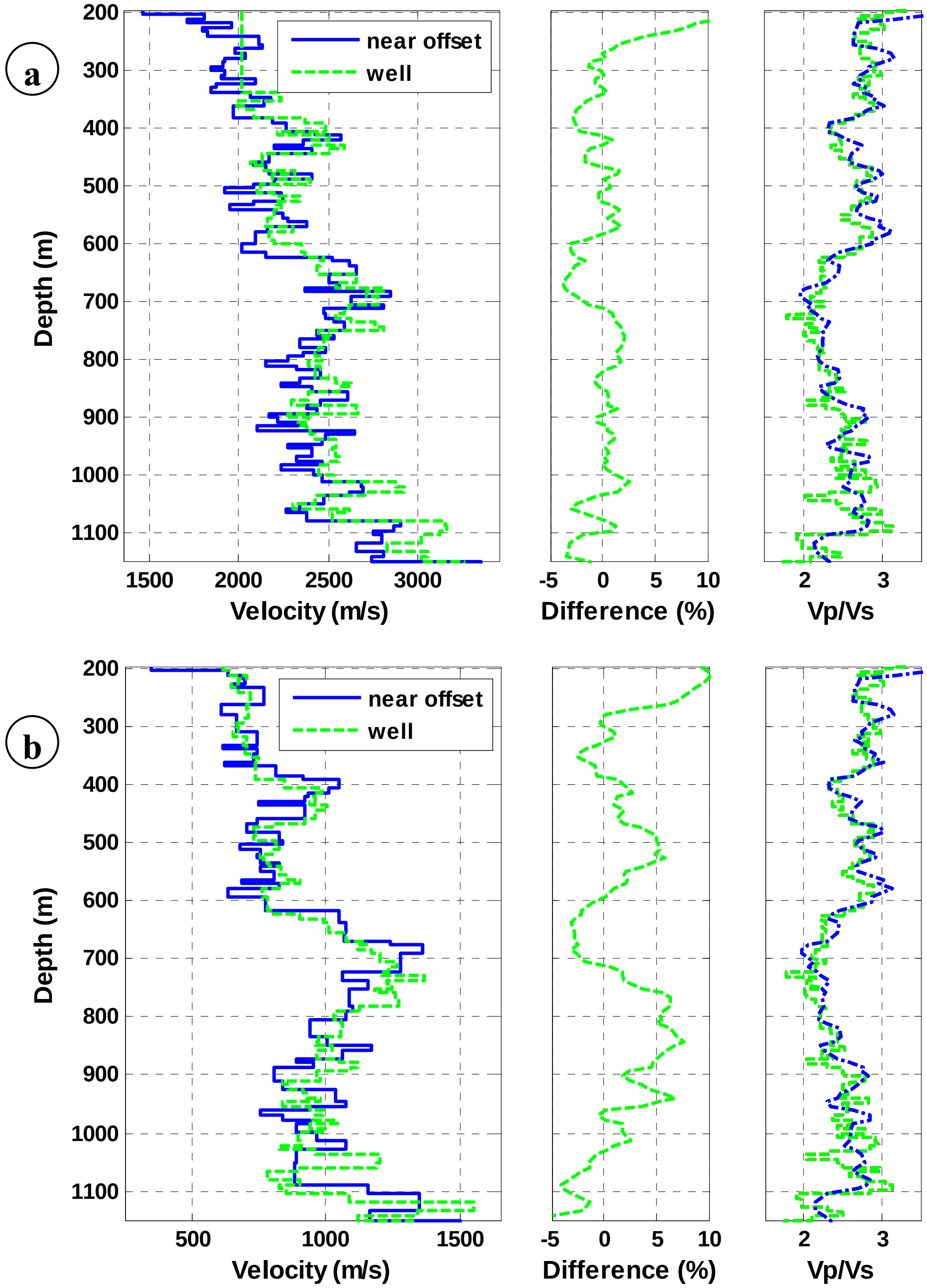

Figure 2.32 Comparison of the P (a) and shear (b) velocities from VSP first-arrival time inversion and sonic logs. The differences between sonic log and near-offset VSP (middle plots), are also displayed by applying an 11-point median filter. The Vp/Vs values are from zero-offset VSP first-arrival time inversion (blue line) and sonic log (green line), and a 3-point median filter was applied.

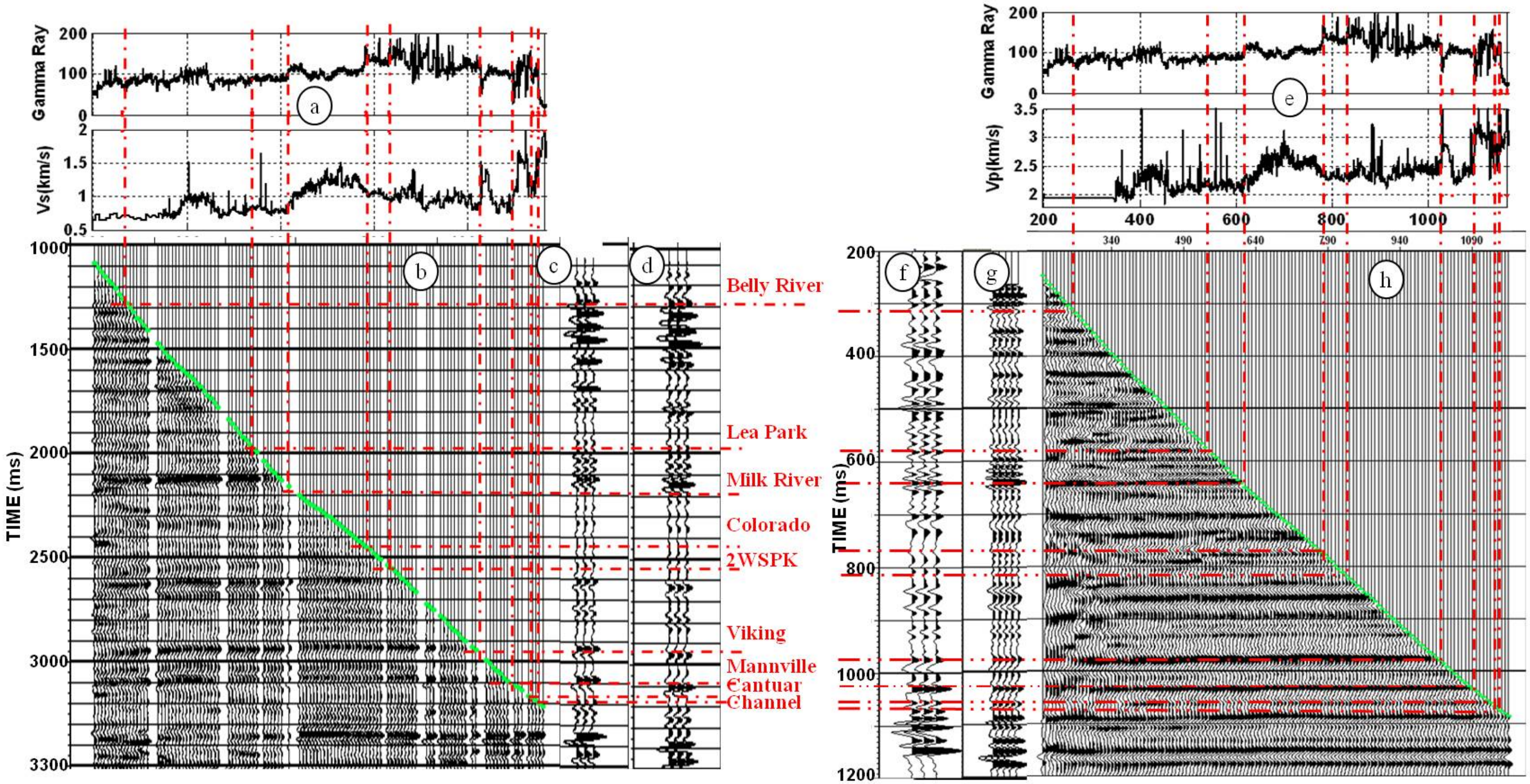

Figure 2.33 Correlation between well logs and zero-offset VSPs. a: Gamma-Ray and Vs logs; b: Hmax of horizontal vibrator zero-offset VSP in two-way SS time (applied statics and NMO correction); c: Hmax corridor stack of horizontal vibrator zero-offset VSP; d: Hmin corridor stack of horizontal vibrator zero-offset VSP; e: Gamma-Ray and Vp logs; f: synthetic P wave seismogram from VSP-calibrated well logs; g: vertical component corridor stack of vertical vibrator zero-offset VSP; h: vertical component of vertical vibrator zero-offset VSP in two-way PP time (applied statics and NMO correction).

channel sand (reservoir), the velocities increases at the top. However the P wave seismic signature on the VSP data is a trough, the SS seismic response is a zero-crossing (the reason is thin bed tuning, as there are several layers above the sand with only several meters layer thickness); at the bottom of the channel sand, the P and S velocity again increases and the corresponding seismic event is a peak on both PP and SS VSP data.

A good correlation is also found for the VSP results and an intersecting surface seismic section (Figure 2.35). The correlations between VSP data and surface seismic data for P wave and shear wave (displayed in PP time) are shown in Figure 2.35. The surface seismic section is extracted from a 3-D volume described by Xu and Stewart (2003).

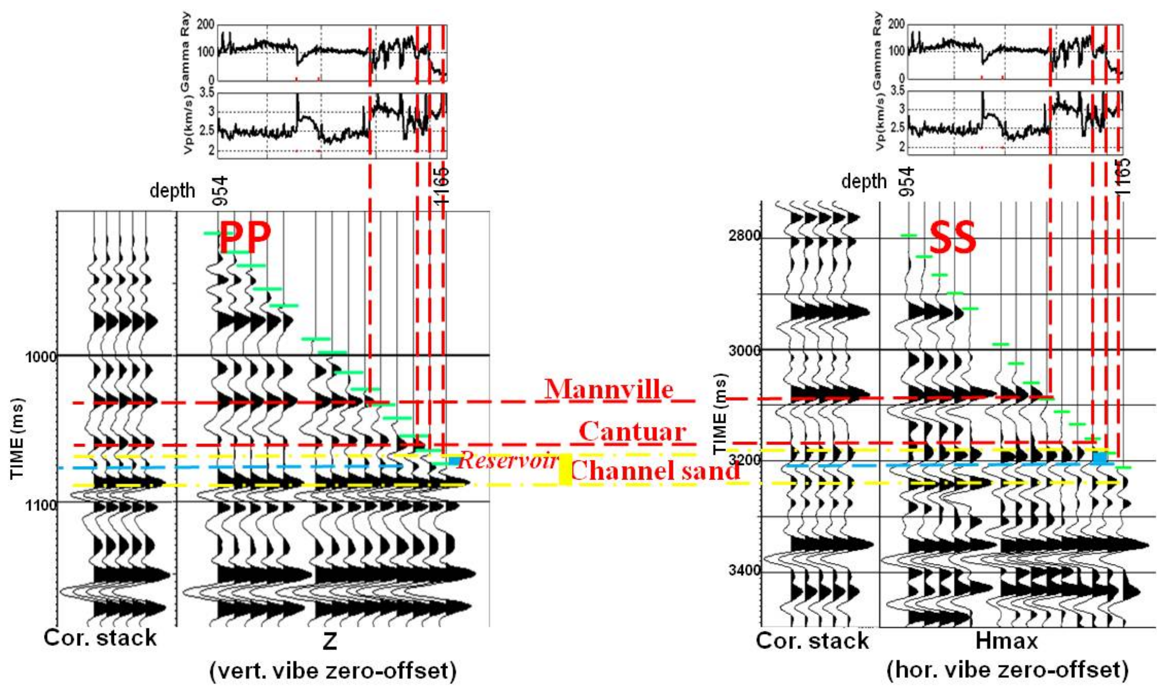

Figure 2.34 Correlation between well logs and zero-offset VSPs focusing on the reservoir part. The PP and SS data are from the processing results of zero-offset VSP acquired with vertical vibe and horizontal vibe, respectively.

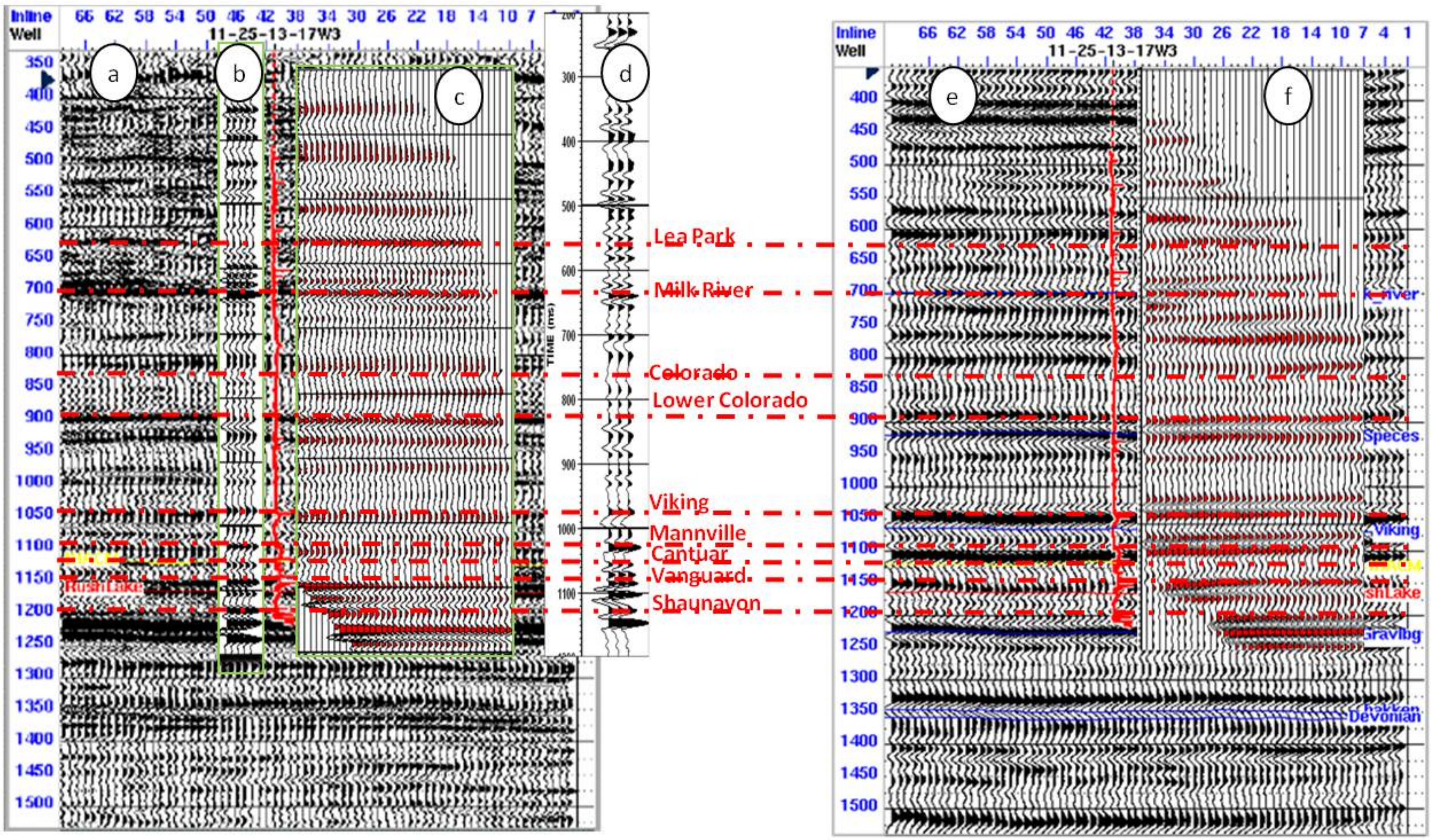

Figure 2.35 Correlation between surface seismic, VSP, and synthetic seismogram from well logs. A: surface PP seismic data with the sonic log at the well location (from Xu and Stewart, 2003); b: vertical component corridor stack of zero-offset VSP(repeated five times); c: PP wave VSP-CDP mapping from the offset 399 m VSP; d: synthetic PP seismogram from sonic and density well logs (repeated three times); e: surface PS seismic data tied in PP time (from Xu and Stewart, 2003); f: PS wave VSP-CDP mapping (PP time) of the offset 399 m VSP.

Event mismatch can be found between the corridor stack traces of Hmax and Hmin of the horizontal vibrator VSP data in Figure 2.33. Figure 2.36a shows the comparison between the two corridor stack traces. Positive time shift can be found on the Hmin stack trace compared with the Hmax stack trace. It is possibly caused by S-wave velocity anisotropy. Cross-correlations between the two traces were calculated for the whole trace, and five 1000 ms windows (Figure 2.36b). The time shift changes a little with time, from 18 ms for shallow window, 1000-2000 ms, to 25 ms for deeper window, 3000-4000 ms (Table 2.5). The time shift from the whole trace cross-correlation is similar, 20 ms. The results suggest that if the time shift between the stack traces of Hmax and Hmin is caused by velocity anisotropy, it should be mostly in the near surface. The velocity in S-N direction is faster than that in E-W direction. Below depth 198 m, which is the depth of the shallowest receiver, no obvious velocity anisotropy is observed from the zero-offset VSP data.

2.4.4 AVO interpretation

The composite plots shown in Figure 2.37 and Figure 2.38 display the detailed (compared to Figure 2.35) correlation between well logs (gamma ray and velocity as examples) and upgoing P (PP) and upgoing shear (PS) waves from VSP data (the PP data was from the near-offset VSP, the PS data was from the 558 m walkaway VSP shot) within the walkaway VSP receiver depth range. The geological markers for correlation are the top of the Mannville Group, the Cantuar Formation, and the channel sand (the reservoir is in the upper porous sand of the channel). The tops of the Mannville Group and the Cantuar Formation both correlate to peak reflection on PP and PS data on the VSP data. The top of the reservoir appears as a trough on PP reflection, and zero-crossing point (negative to positive) on PS reflection. The bottom of the reservoir expressed as a weak peak reflection on PP data and a zero-crossing point (positive to negative) on PS data.

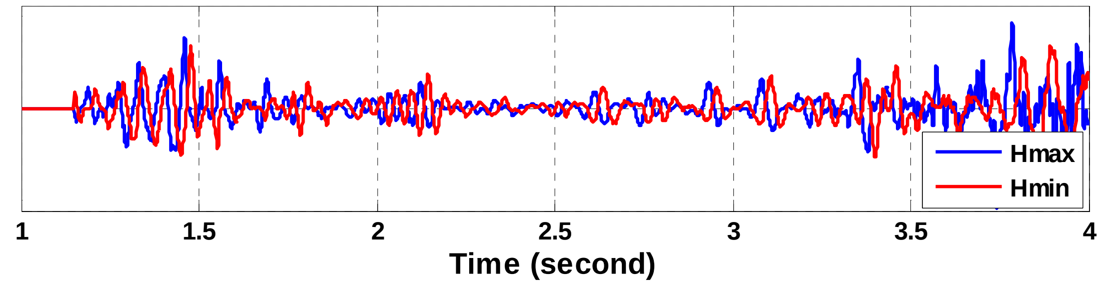

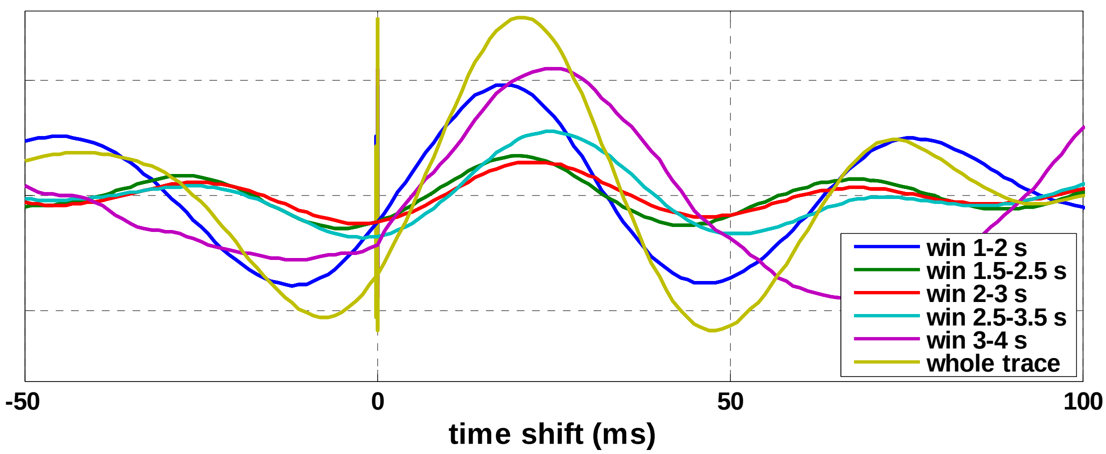

Figure 2.36 Comparison of the corridor stack of Hmax and Hmin of the horizontal vibrator zero-offset VSP (in SS time) and the cross-correlation of the two traces. The cross-correlations are calculated using five 1000 ms window data and the whole trace data.

Table 2.5 Time shift calculated from the cross-correlations between corridor stack traces of Hmax and Hmin of the horizontal vibrator zero-offset VSP.

Window	Whole trace	1 – 2 s	1.5 – 2.5 s	2 –3 s	2.5 – 3.5 s	3 – 4 s
Time shift (ms)	20	18	20	22	25	25

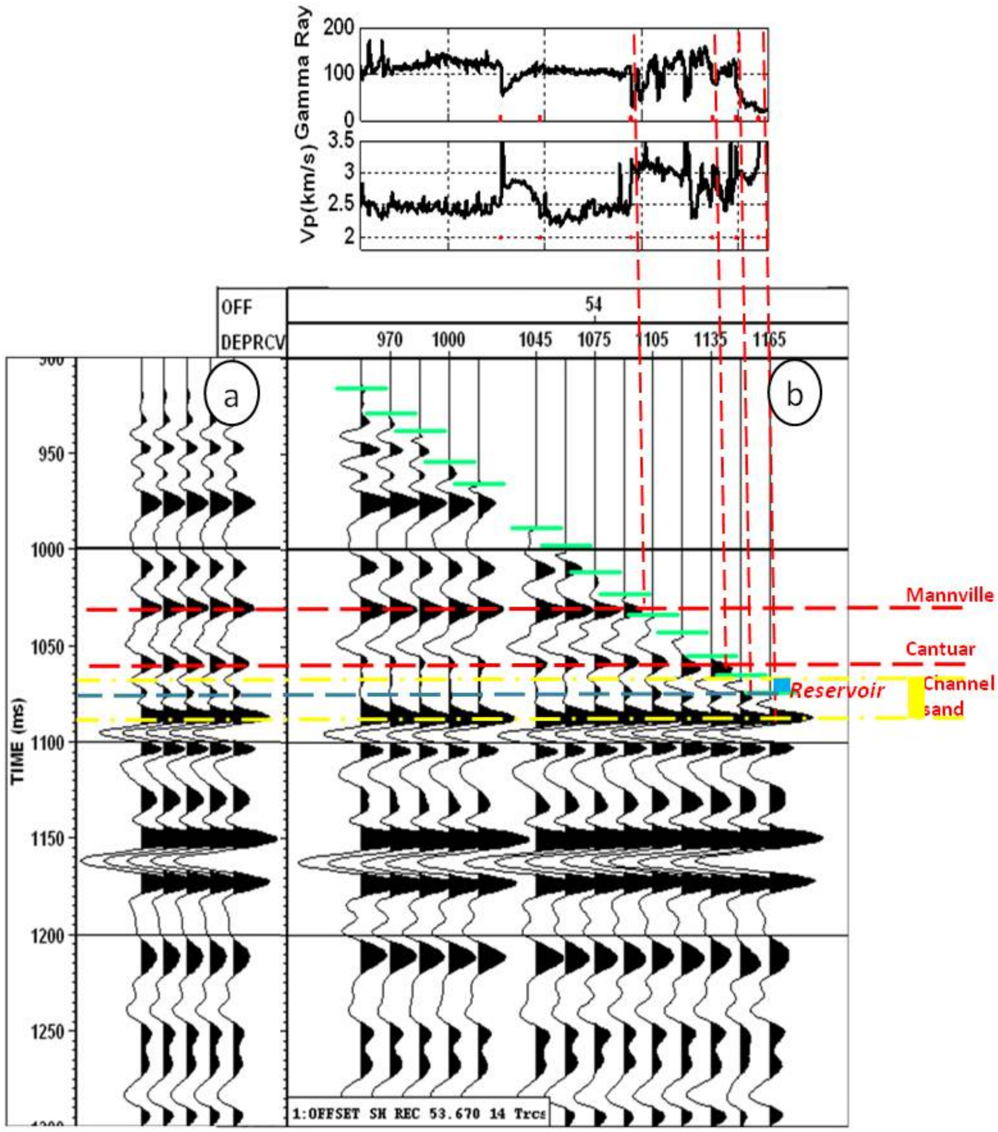

Figure 2.37 Correlation between well logs and zero-offset VSP within walkaway VSP receiver depth range. a: upgoing P wave corridor stack; b: upgoing P wave in two-way P traveltime (applied NMO and first-arrival time flattening).

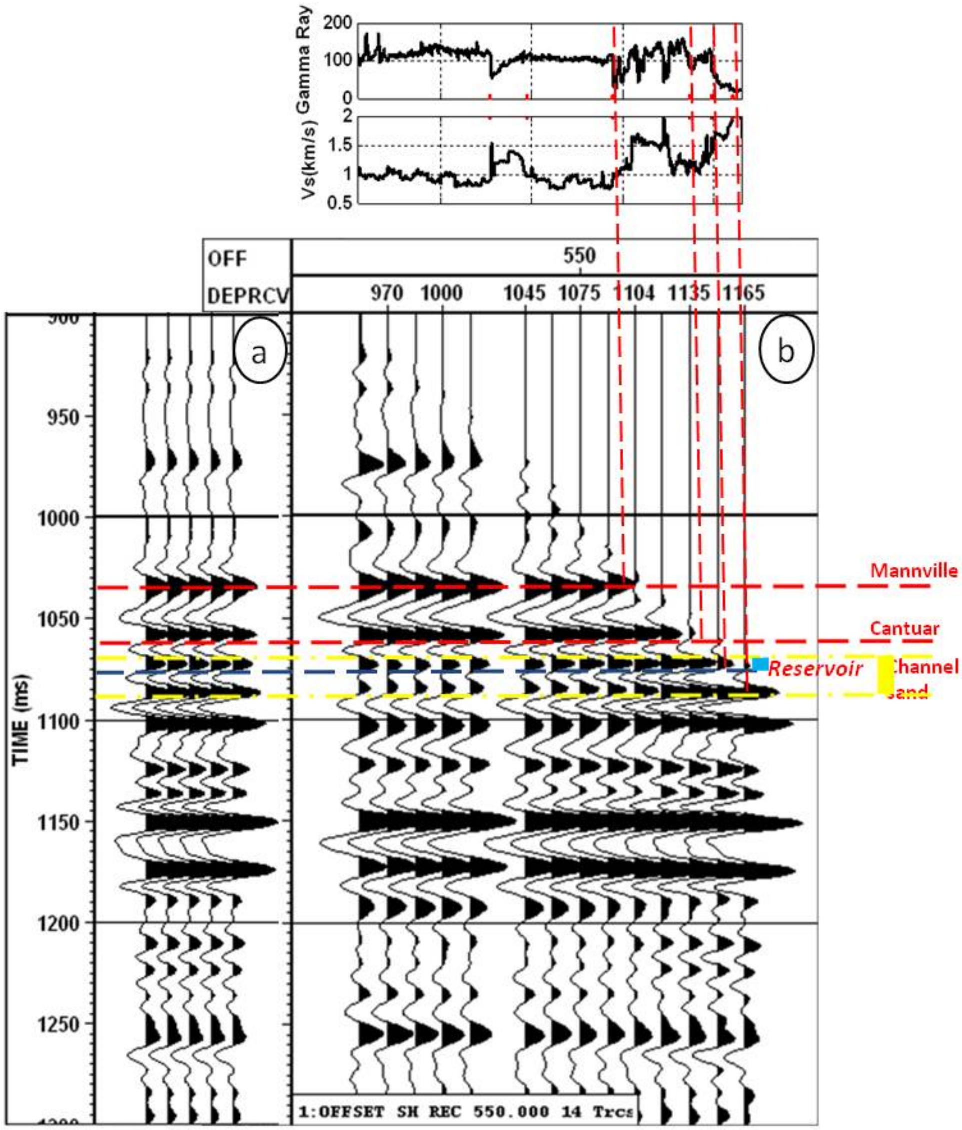

Figure 2.38 Correlation between well logs and source offset 558 m VSP within walkaway VSP receiver depth range. a: upgoing PS wave corridor stack; b: upgoing PS wave in two-way P traveltime (applied NMO and first-arrival time flattening).

The PP and PS VSP data were then correlated to the synthetic seismograms. Figure 2.39 displays the correlation of PP data from walkaway VSP data and synthetic seismograms. The synthetic seismograms were generated with VSP calibrated well logs. The corridor stack (Figure 2.39a) of zero-offset VSP data correlates to the stack trace (Figure 2.39d) of the synthetic seismogram very well. They display very good event matches, however, there are still amplitude differences between the real and synthetic data. Although the stack was based on the reflection of the base of the channel (1096 ms on PP data), good correlations can still be seen on the reflections of the top and the base of the reservoir. On the synthetic gather (Figure 2.39c), the top of the reservoir displays an amplitude increase (negative amplitude, here the change means the absolute value variation trend) with offset. The offset gather (Figure 2.39b) resulting from the walkaway VSP processing displays the same trend except for the trace at offset 1000 m. At the bottom of the channel sand the VSP offset gather and synthetic gather display the same amplitude decrease (peak) with offset.

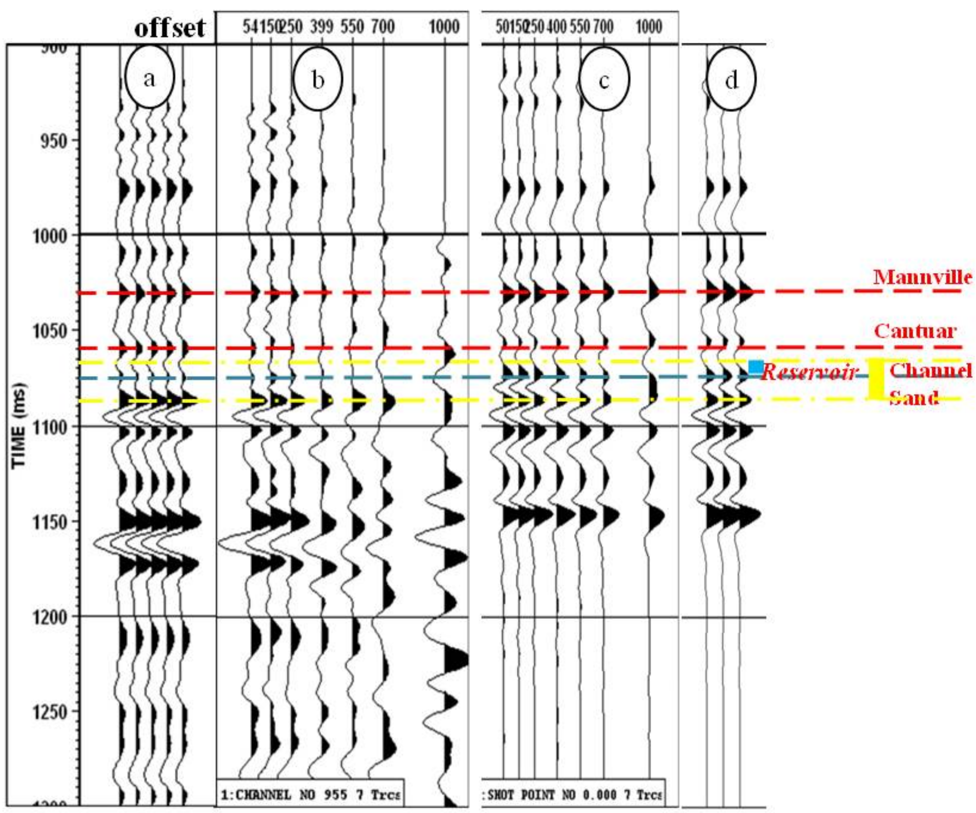

Figure 2.39 Comparison of PP offset gathers from walkaway VSP processing and PP synthetic seismogram from sonic and density logs. a: upgoing P wave corridor stack of the zero-offset (54 m) VSP (repeated five times); b: PP offset gather from walkaway VSP; c: PP synthetic offset gather; d: stacked traces of the PP synthetic seismogram (repeated three times).

The correlation of PS data from walkaway VSP data and synthetic seismograms is shown as Figure 2.40. It also displays good correlation between the PS corridor stack (Figure 2.40a) of offset (558 m) VSP data and the stack trace (Figure 2.40d) of the PS synthetic seismogram. As found for PP data, good event matches, while amplitude differences between the real and synthetic data are observed. At the top of the reservoir, both the synthetic gather (Figure 2.40c) and the offset gather (Figure 2.40b) resulting from the walkaway VSP processing are zero-crossings. At the bottom of the channel sand the VSP offset gather and synthetic gather display the same amplitude increase (peak) with offset.

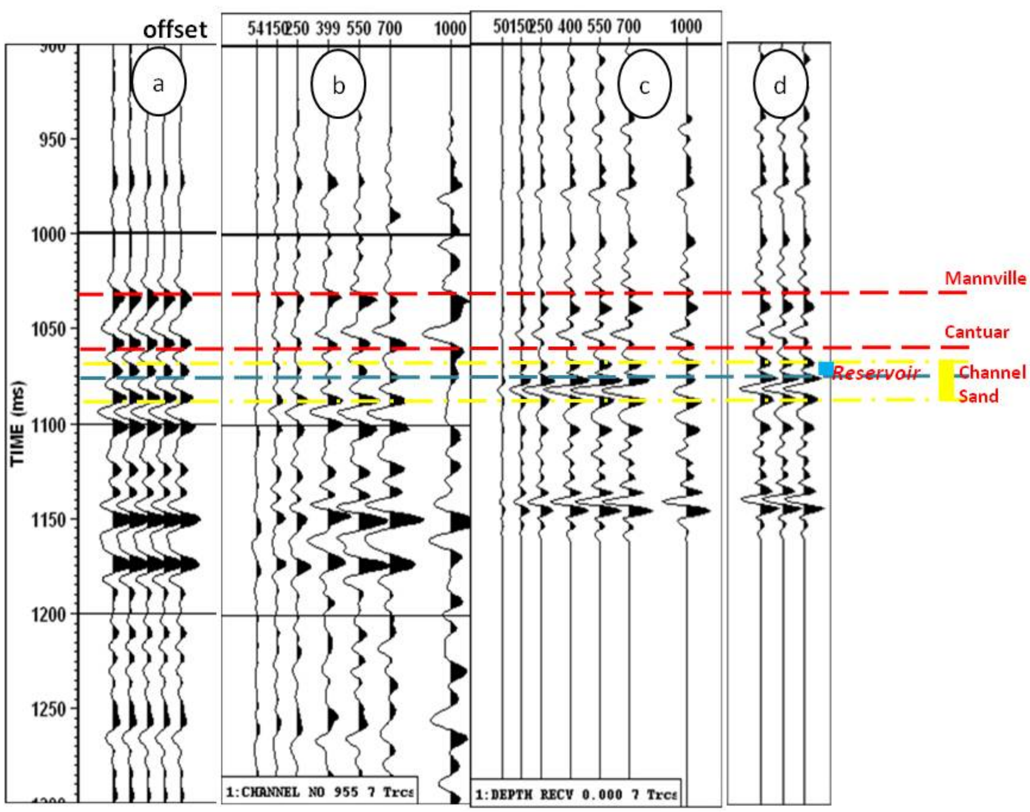

Figure 2.40 Comparison of the PS offset gather from walkaway VSP processing and PS synthetic seismograms from sonic and density logs. a: upgoing PS wave corridor stack of offset (558 m) VSP (repeated five times); b: PS offset gather from walkaway VSP; c: synthetic PS offset gather; d: stacked traces of the synthetic seismogram (repeated three times). All PS data are plotted in two-way P wave traveltime.

Figure 2.41 displays the comparison of amplitude versus offset at the base of the channel sand between walkaway VSP data and synthetic seismograms. The amplitudes of synthetic seismograms were scaled to those of the VSP data by multiplying factors deriving from the ratio of average amplitudes of VSP data to those of synthetic data. Both the PP and PS data display similar variation trends of amplitude versus offset. The amplitude differences at each offset are small for both PP and PS data. The mean amplitude difference is 0.2% for PP data, and -0.1% for PS data (Table 2.6). These results give us promise of rock properties inversion using AVO gather from walkaway VSP.

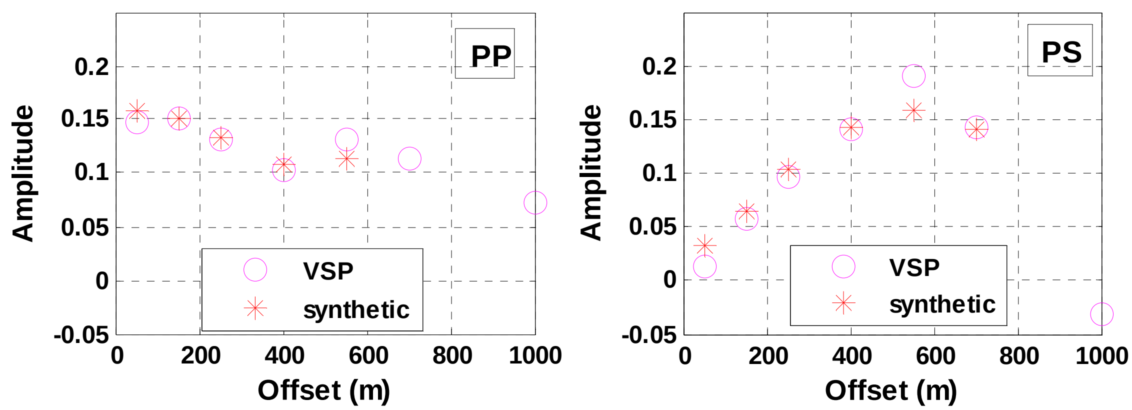

Figure 2.41 Comparison between the amplitude at the base of the channel sand from walkaway VSP and synthetic seismograms (generated by Syngram) for PP and PS data. The amplitude of synthetic data were scaled to the average amplitude level of VSP data.

Table 2.6 Amplitude of offset gathers from walkaway VSP data and synthetic seismograms at the base of the channel sand base and their difference.

Amplitude \ Offset (m)		50	150	250	400	550	700	1000
PP	VSP	0.147	0.15137	0.13118	0.10217	0.1313	0.11317	0.07217
	synthetic	0.1577	0.1510	0.1323	0.1082	0.1138	-	-
	mean difference (%)	0.18					-	
	standard deviation (%)	8.45					-	
PS	VSP	0.01303	0.05671	0.09677	0.14156	0.19037	0.14256	-0.0308
	synthetic	0.0326	0.0640	0.01035	0.1428	0.1578	0.1402	-
	mean difference (%)	-	-0.13					-
	standard deviation (%)	-	11.6					-

Chapter Three: Seismic attenuation analysis from zero-offset VSP data

Attenuation is one of the basic seismic attributes of waves propagating in the rock. Understanding the causes of attenuation as well as the relationship between seismic attenuation (*Q*) and rock properties is important in the acquisition, processing and interpretation of seismic data. A number of authors (e.g., Klimentos and McCann, 1990; Koesoemadinata and McMechan, 2001) have examined the relationship between lab measured attenuation and rock properties. In this chapter, the relationship between seismic attenuation and rock properties is studied in shale and sandstone using well logs and VSP data from well 11-25-13-17W3 at the Ross Lake heavy oilfield, Saskatchewan. Seismic attenuation was derived from zero-offset VSP data. The rock properties were calculated from well logs. Based on this study, attenuation characteristics of seismic data are expected to provide information helpful to seismic interpretation and reservoir characterization. Since the attenuation derived from VSP data is in seismic frequency range, it is of more importance in seismic exploration. Considering the advantages on studying the wave propagation by VSP geometry, attenuation effects on P and shear waves were also studied using the Ross Lake 3C VSP data.

3.1 Q value estimation

A variety of methods have been developed to estimate the Q values from VSP data. Tonn (1991) compared these methods and concluded that none of these approaches is significantly better than the others in all situations. In noise-free cases, the spectral ratio method (Hauge, 1981; Toksöz and Johnson, 1981) is optimal. Considering the high signal-to-noise ratio of the VSP data, especially downgoing waves, the spectral ratio method should be appropriate for Q value estimation in this study.

Supposing first arrival wavelets, $g_1(t)$ and $g_2(t)$ are recorded at depths Z_1 and Z_2. The amplitude spectra, $G_1(f)$ and $G_2(f)$, of these two geophone responses are plotted as a function of frequency. In such a case,

$$\boldsymbol{G_2(f) = kG_1(f)e^{-Af}},$$

(3-1)

where f is the frequency and k is a frequency independent factor that accounts for amplitude effects such as spherical divergence, variations in recording gain, and changes in source and receiver coupling. The exponent, A, is the cumulative seismic attenuation between depths Z_1 and Z_2, and it is assumed to be independent of frequency. This equation can be rewritten as

$$\ln\left[\frac{\boldsymbol{G}_2(\boldsymbol{f})}{\boldsymbol{G}_1(\boldsymbol{f})}\right] = -\boldsymbol{Af} + \ln(\boldsymbol{k}),$$

(3-2)

The left-hand side of this equation is the log spectral ratio of the VSP data recorded at two depths, Z_1 and Z_2. The cumulative attenuation value, A, is determined by the slope of the best straight line fit to this spectral ratio trend. The average Q value, Q_{ave}, between depths Z_1 and Z_2 can be calculated from cumulative attenuation A,

$$\boldsymbol{Q_{ave} = \pi(t_2 - t_1)/A},$$

(3-3)

where t_2 and t_1 are the first arrival time at depths Z_1 and Z_2.

Both vertical vibrator and horizontal vibrators were used for the Ross Lake zero-offset VSP survey, Qp and Qs values were derived from the two zero-offset VSP data separately. To estimate the Q values, downgoing P waves and shear waves should be extracted from vertical vibrator data and horizontal vibrator zero-offset VSP data, respectively.

Although the source-well distance of the zero-offset VSP data is fairly small, the seismic waves are still not propagating vertically at the receivers even when the earth is an ideally layered medium. Thus it is impossible that the P waves were only recorded by the vertical component, the horizontal component will also record part of the P wave energy. For the same reason, the vertical component will also record some shear waves. Thus hodogram analysis based 3C rotation (Appendix A.2) of the zero-offset VSP data was carried out to isolate the primary downgoing wavelet. Hmax' (in the source-receiver direction, shown as Figure 3.1a) instead of vertical component of vertical vibrator zero-offset VSP data, and Z' (normal to the source-receiver direction, Figure 3.1b) instead of Hmax component of horizontal vibrator zero-offset VSP data were used for downgoing P and shear wave separations. Down-going P- and shear waves (Figure 3.2) were then extracted using F-K filter from these two data respectively. It is clear that shear waves were attenuated much more severely than P waves. Then, the amplitude spectra for all the levels were calculated using a 500 ms window (Figure 3.3). Considering the signal-to-noise ratio, frequency bands from 20 Hz to 120 Hz for P waves and 20 Hz to 40 Hz for shear waves were chosen to build the cumulative attenuation curves for Q value estimation. To avoid unreasonable Q values, the cumulative attenuation curves were smoothed using a 7-point smoothing window before calculating average Q values from the surface to each depth. Using the surface sweep signal as reference, average Q values at each receiver depth were calculated.

To examine the relationship between attenuation and rock properties, interval Q values are necessary. The interval Q values (Q_{int}) for a layered medium are estimated from the average Q values (Q_{ave}) using a method by Bale and Stewart (2002),

$$\frac{1}{Q_{int}(n+1)} = \frac{1}{T(n+1)-T(n)}\left(\frac{T(n+1)}{Q_{ave}(n+1)} - \frac{T(n)}{Q_{ave}(n)}\right), n = 1, 2, 3, \dots, N-1 \tag{3-4}$$

where $T(n)$ is the first arrival time at the n^{th} depth level, $Q_{ave}(n)$ is the average Q value between the reference depth and the n^{th} receiver depth, $Q_{int}(n+1)$ is the interval Q value between the n^{th} and $(n+1)^{th}$ receivers.

Using equation (3-4), attenuation-depth structures for P waves and shear waves were determined from smoothed average Q values using a 21-point window (the right curves of Figure 3.3). The Qp values are from 20 to 120, and Qs values range from 10 to 80. All of them are in reasonable range. They are also comparable to average Q values by Haase and Stewart (2004), which are 67 for the P-wave and 23 for the shear-wave over an interval of 200 m to 1200 m.

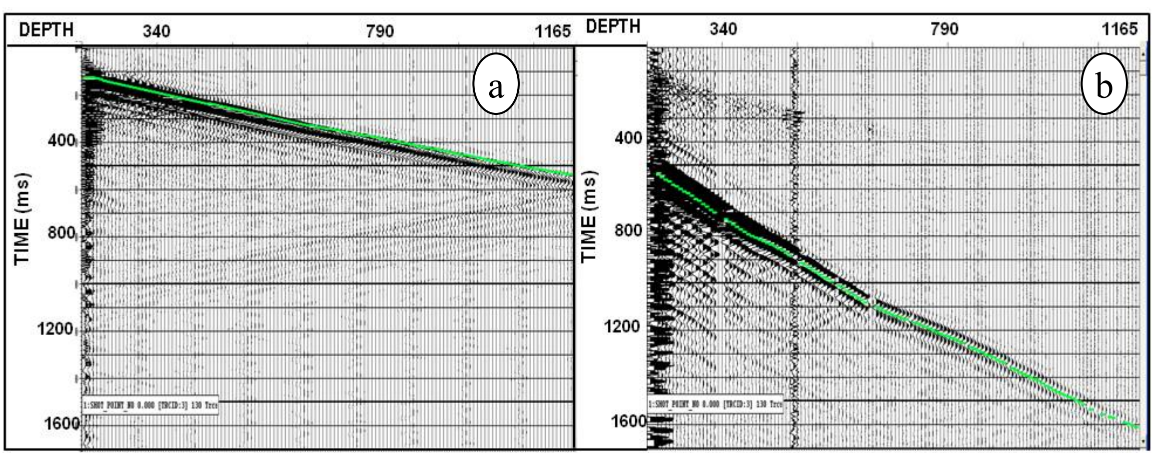

Figure 3.1 Hmax' (in the direction of source-receiver) of vertical vibrator VSP data (a), and Z' (in the direction perpendicular to source-receiver direction) of horizontal vibrator VSP data (b).

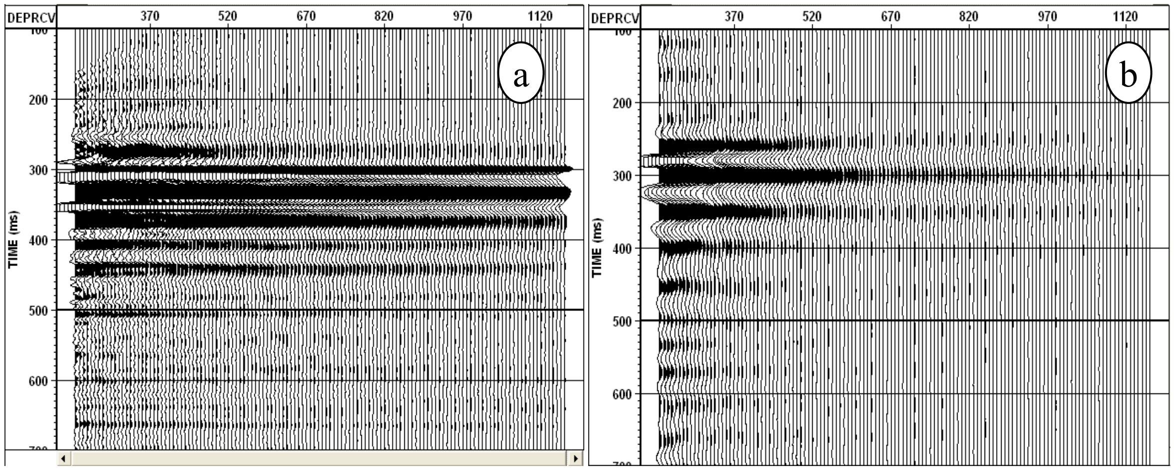

Figure 3.2 Flattened down-going P waves (a) and shear waves (b) separated from the Hmax' and Z' shown in Figure 3.1.

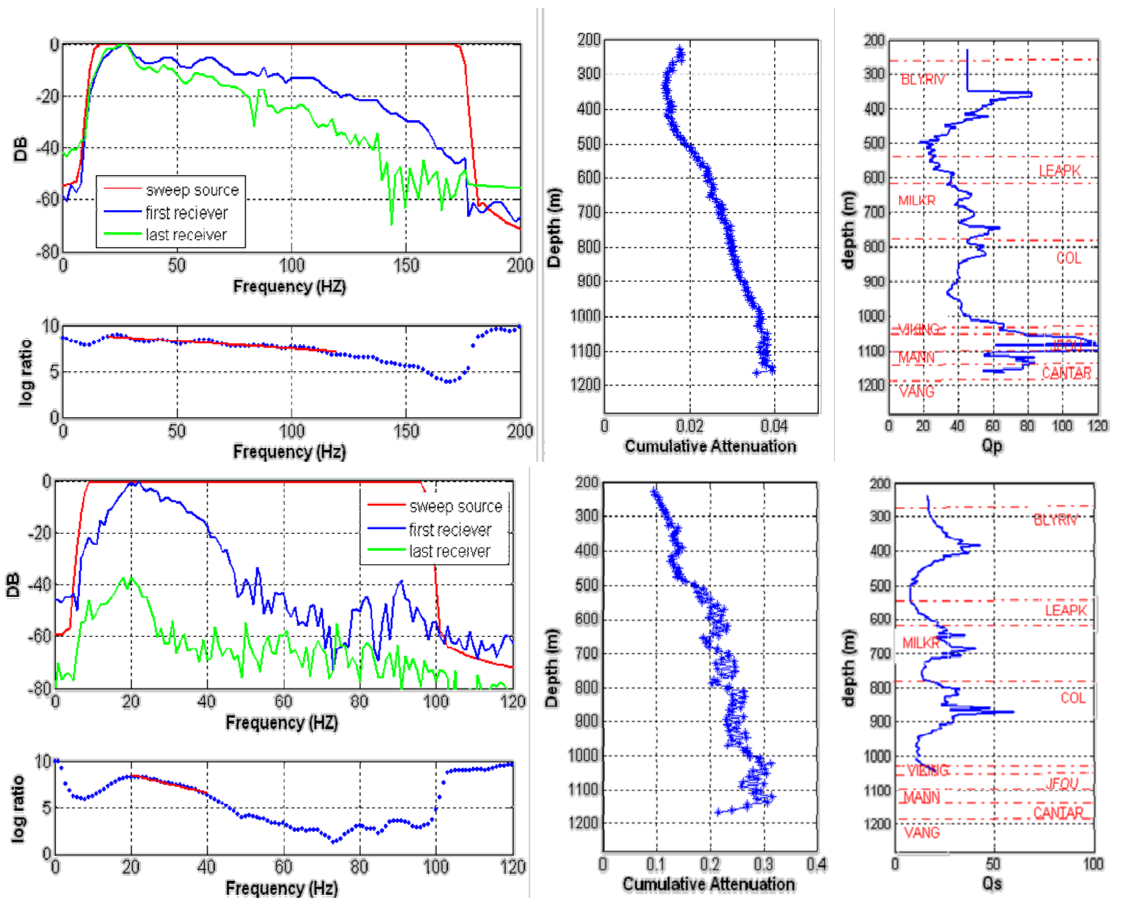

Figure 3.3 Top, from left to right: amplitude spectrum (sweep source in red, the first depth level in blue and the bottom receiver in green) as well as spectral ratio at the first receiver, cumulative attenuation from the spectral ratio method, and estimated interval Q values of the P wave. The lower plots are for the shear wave.

3.2 Q value and rock properties

The cumulative attenuation curves in Figure 3.3 show that the values gradually increase with depth from 400 m to 1050 m. The Q values for P waves are considered reliable for this interval. For shear waves, since the frequency bandwidth for Q estimation was narrow, the cumulative attenuation at each depth level was more scattered. A decreasing cumulative attenuation was found over some scattered intervals and the bottom part of the well, which means the interval Q value will be negative (not physically reasonable). Therefore, the following analysis will focus on the depth intervals with reliable Q values.

Figure 3.4 displays Q values for the P- and shear-wave data, and rock properties from the well log analysis. Some correlations between Q values and rock properties can be seen from these curves. Generally high attenuation corresponds to low velocity, high porosity and high Vp/Vs, and vice versa. From the crossplot between *Qp* values and P- and S-wave velocities (Figure 3.5), we see that *Qp* values increase approximately linearly with P and shear velocities. A similar variation is also observed for Qs values and velocities, although the correlation is not as compelling (Figure 3.6). Decreasing quasi-linear relationships are found between Q values and Vp/Vs (Figure 3.7).

From the crossplot between Q value and shale volume (Figure 3.8), the maximum P-wave attenuation was found in shaly sandstones. The attenuation of P-wave was lower in clean sand and shale. However, it is generally observed that Vp/Vs increases with shale content. However, this is not obvious in our current case. The Q vs. Vp/Vs relationship and the Q vs. shale volume relationship seem to be contradictory here.

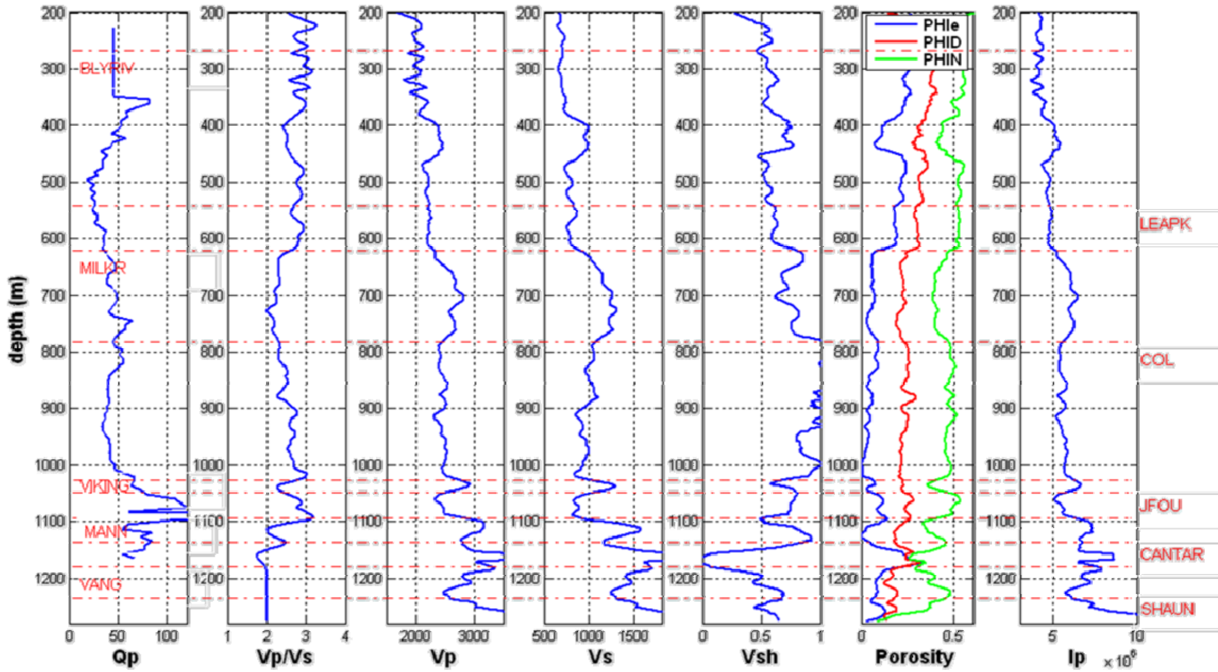

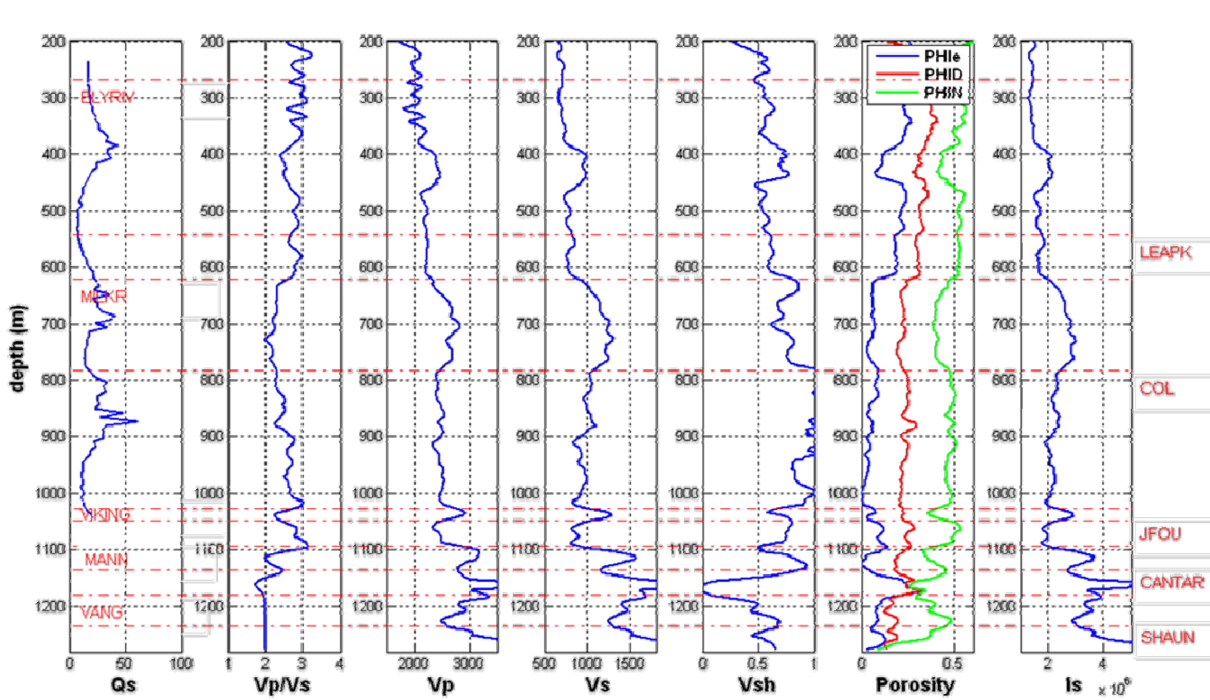

Figure 3.4 Top, from left to right: *Qp*, Vp/Vs, Vp, Vs, shale volume, porosity (effective porosity in blue, density porosity in red and neutron density in green), and P-wave impedance. The bottom plots are for the S wave (the right frame is shear-wave impedance). Well log data were smoothed using a 15m window.

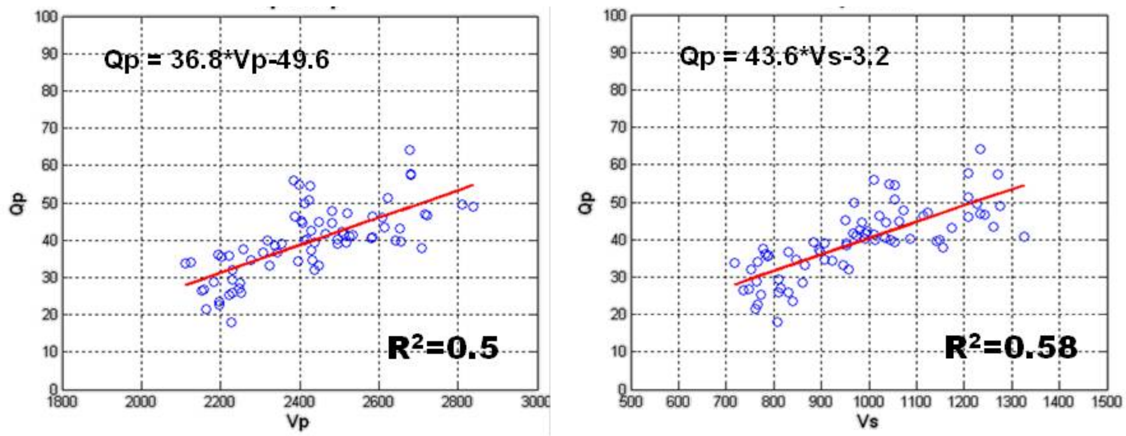

Figure 3.5 Crossplot between Qp and P velocity (left), and crossplot between *Qp* and shear velocity (right). The red lines are linear regression lines. In the equations, the velocity unit is km/s.

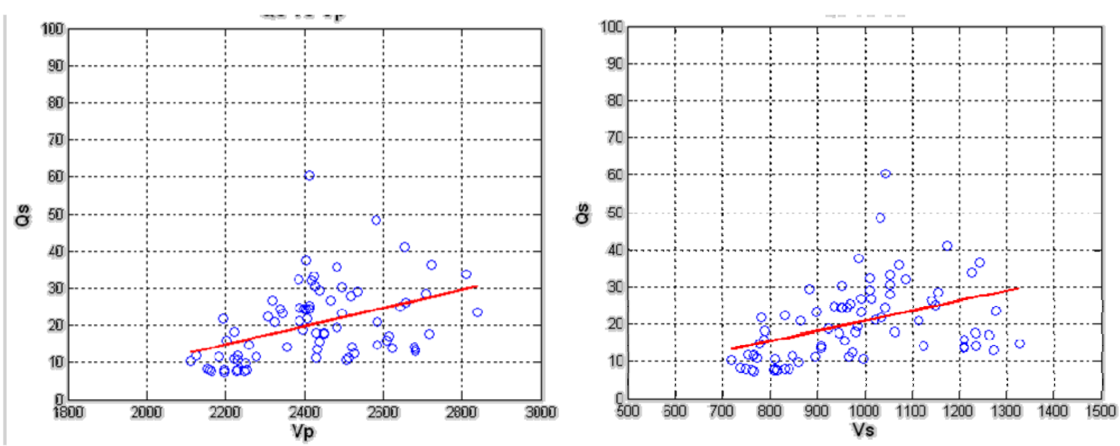

Figure 3.6 Crossplot between *Qs* and P velocity (left), and crossplot between *Qp* and shear velocity (right). The red lines are linear regression lines.

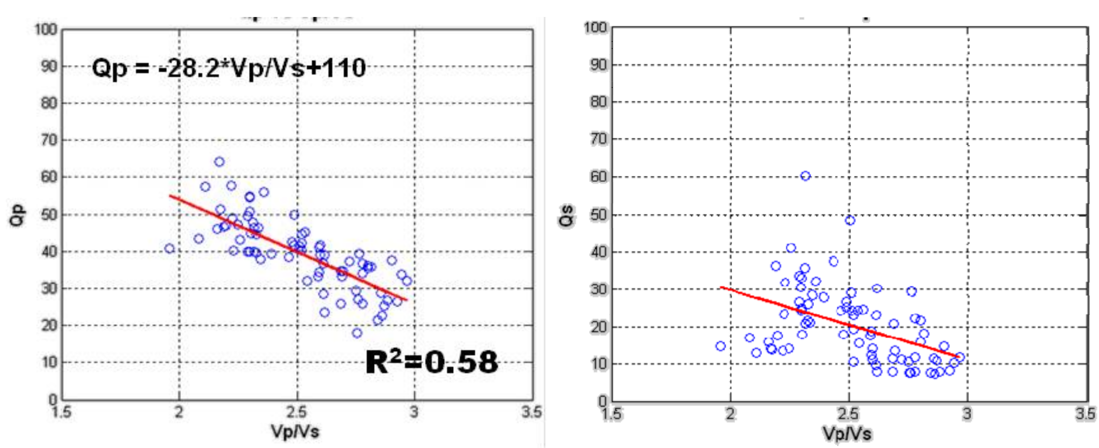

Figure 3.7 Crossplot between *Qp* and Vp/Vs (left), and crossplot between *Qs* and Vp/Vs (right). The red lines are linear regression lines.

According to the relationship between attenuation and fluid, it is possible that the interaction between mobile water in the pores and clay-bound water generates a large P-wave attenuation. To investigate this idea, a crossplot between Q values and clay-bound water was created (Figure 3.9). Neutron porosity responds to the total water volume in the rock, which includes clay-bound water and free water. Thus, the clay-bound water volume was estimated from the difference between neutron porosity and effective porosity and normalized by neutron porosity. When the water is 100% bound to clay, the attenuation seems small. When part of the water is free and the other is bound to clay, a larger attenuation seems to be measured. For the shear waves, a similar relation is observed, although it is less distinct, because the S-wave does not mobilize the free water as much.

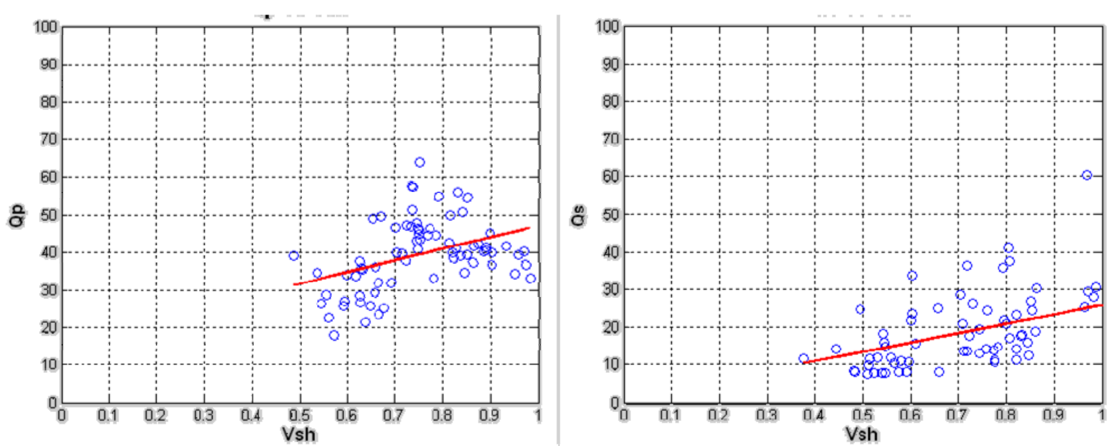

Figure 3.8 Crossplot between *Qp* and shale volume (left), and *Qs* vs. shale volume (right). The red lines are linear regression lines.

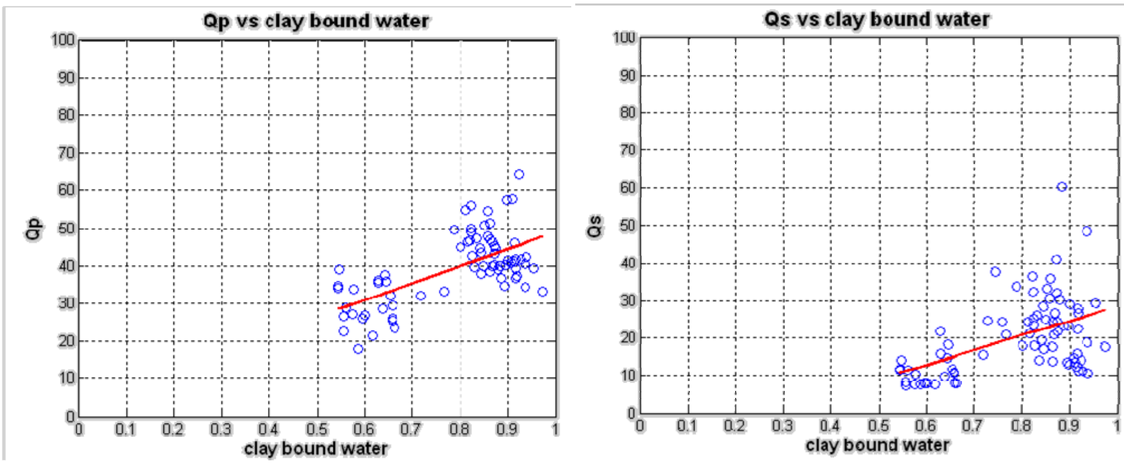

Figure 3.9 Crossplot between *Qp* and clay-bound water (left), and *Qs* vs. clay-bound water (right). The red lines are linear regression lines.

Since there are correlations between the Q values and the rock properties, empirical equation can be used to approximately calculate Q values from rock properties. Assuming linear relationship between the Q values and the rock properties in the studied well, firstly each single rock property is used to predict the Q value using least-square regression method (Appendix B). The purpose is to see which rock property is the most effective for Q estimation. Figure 3.10 shows the fit between the actual *Q* values and predicted *Q* values from Vp, Vs, P modulus, shear modulus, Vp/Vs, shale volume, effective porosity, and density. The *Qp* correlates more with velocities and Vp/Vs, while the Qs influence more by Vp/Vs and shale volume. Then least-square regression for multiple rock properties is also implemented. The results indicate that moduli are better than velocities for *Qp* prediction, while velocities are a little better for *Qs* prediction. To test the sensitivity of each rock property on the prediction accuracy, one rock property is excluded from the calculation each time. The results are shown as Figure 3.11 for both *Qp* and *Qs*. The prediction using all the testing rock properties is also displayed (the far right-end bar) for comparison. Compared with estimating Q value with one rock property, multiple rock properties yield better results (higher R^2 value). No exclusion of one rock property has much influence on the result for *Qp*. Relatively, density and shear moduli have the least influence. The *Qs* values seem to be affected more by shale volume and porosity.

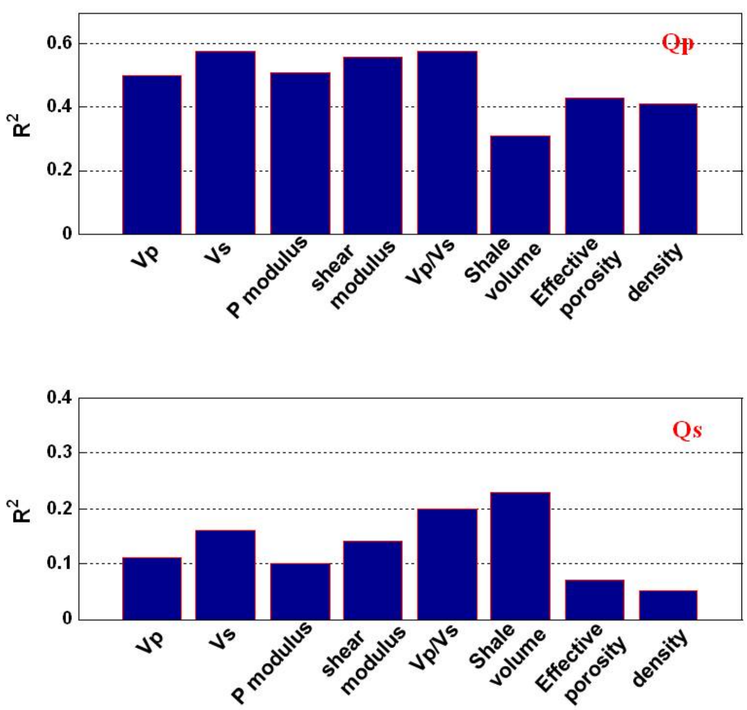

Figure 3.10 Correlation between real Q values and the Q value from single rock property values. The prediction of Q value is from linear regression equation including only one rock property. The higher R^2 value indicates higher correlation.

According to the analysis, P modulus, Vp/Vs, effective porosity, and shale volume are chosen to build empirical equation for *Q* prediction using multiple parameter least-square regression method (Appendix B). The equations for *Qp* and *Qs* are:

$$Qp = 1.95 * M - 13.63 * \frac{Vp}{Vs} + 37 * \emptyset + 21 * Vsh + 28.6$$

$$Qs = 66.4 * M - 13.38 * \frac{Vp}{Vs} + 285 * \emptyset + 101 * Vsh - 210$$

(3-5)

where M is P wave modulus, unit: GPa; ϕ is effective porosity; Vsh is shale volume. The comparison between the real and predicted Q values using equation (3-5) is shown as Figure 3.12. It shows better prediction quality of Qp (R^2=0.65) than Qs (R^2=0.48).

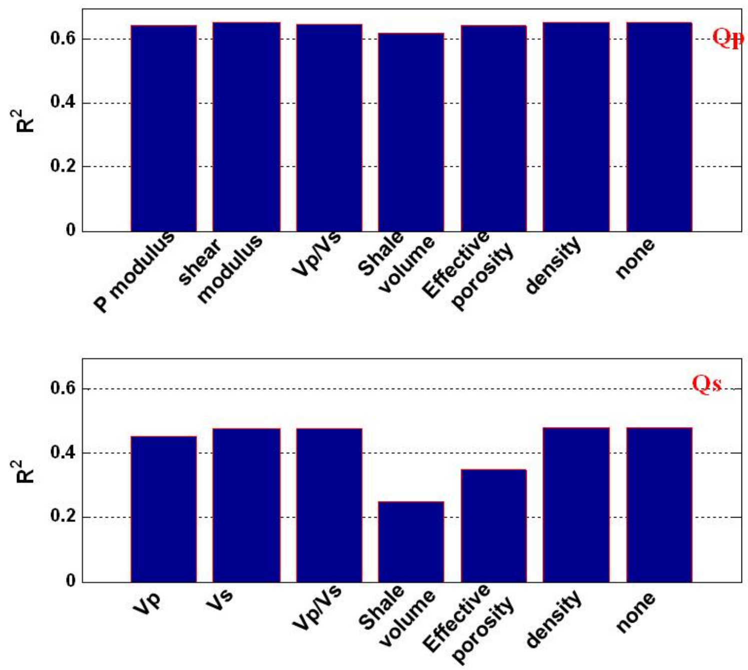

Figure 3.11 The influence of a single rock property value on prediction accuracy of Q value from rock properties. The prediction of Q value is from linear regression equation including all the rock properties listed at the bottom of each plot, except for the one right below the bar plot. "None" in the figure indicates that all the previous six values are used for linear regression calculation.

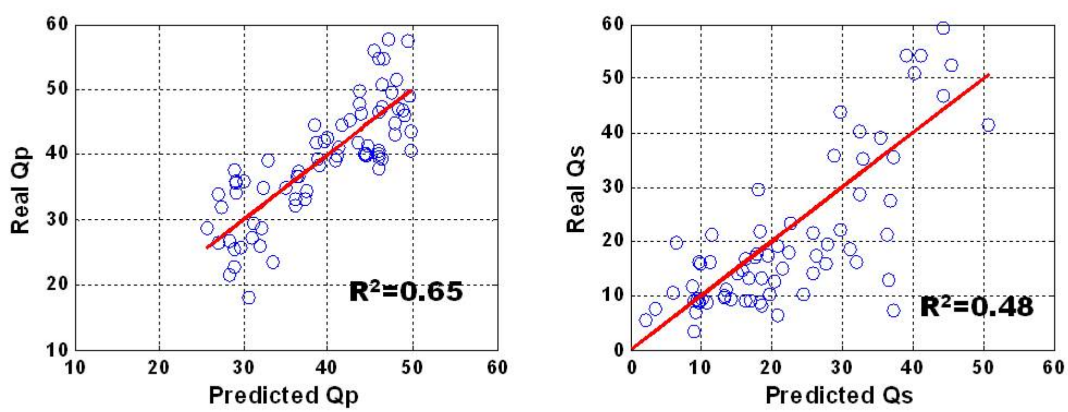

Figure 3.12 Comparison between real and predicted *Qp* and *Qs* values using equation (3-5).

3.3 Frequency analysis of Ross Lake 3C VSP data: does attenuation account for the frequency difference of PP and PS waves?

In multicomponent seismic exploration, the frequency content of the PP and PS waves are often found to be different. At the reflector where wave-mode conversion occurs, if there is no variation of the amplitude relationships (defined by the Zoeppritz equations, Aki and Richard, 1980) between P and S waves with frequency, the frequency content of P and S waves should be equivalent at the interface. When the waves leave the interface, they will diminish in amplitude as a result of several factors, such as spherical divergence, transmission losses, energy mode conversions, and dissipation. Some of these factors will not affect the frequency content. Others, such as dissipation, will have different frequency effects on P and shear waves. Due to its particular source-receiver geometry, a VSP records the different wave modes close to the interface besides the reflected waves which propagate some distance from the interface (which are the wave types recorded by surface seismic data). Therefore, VSP offers us an opportunity to gain a better understanding about seismic wave propagation, and the analysis of frequency relationships between different wave modes at or close to the reflector and some distance from the reflector becomes to be convenient.

3Cfar-offset VSP data, with source offset 399 m, is used for frequency analysis. The frequency analysis was implemented on both raw and attenuation compensated PP and PS waves to analyze the frequency content, and the reason for the frequency difference that we generally see between P and shear waves in multicomponent seismic exploration.

3.3.1 Frequency analysis of PP and PS waves on raw data

Frequency analysis was first undertaken on the raw PP and PS data. Two windows were designed for the frequency analysis on the same traces. One window is designed along the first arrival (Figure 3.13, outlined by red dot-dashed lines). The purpose of a frequency analysis in this window is to investigate the frequency relationship between PP and PS waves close to the reflectors. We assume that in the short window from the first arrival the waves travel for just a short distance from the interface, the attenuations for both PP and PS waves are comparatively small and the frequency relationship should be similar to that at the interface. Figure 3.13 shows the amplitude spectra of the upgoing PP wave and PS wave in the 300 ms window starting from the first arrival. The frequency components of PP waves and PS waves are similar. The frequency bandwidth of the PS wave is generally narrower than that of the PP wave at each trace. The amplitude spectra at depths 700 m, 900 m, and 1100 m (Figure 3.13e) show more attenuation of the high frequency content of PS waves than for PP waves. The frequency bandwidth of the PP wave decreases with depth (Figure 3.13c), and the PS wave displays a similar trend (Figure 3.13d).

The second window (Figure 3.14, outlined by yellow dot-dashed lines) is along the reflections. The aim is to study the frequency relationship between PP and PS data at different distances from the reflectors. The window is 400 ms for PP data, and the window length for the PS data is calculated based on the average Vp/Vs in order to include the same reflections as in the PP data. Figure 3.14 display the analysis windows for PP and PS data and the corresponding amplitude spectra. The frequency difference between PP and PS data is much larger in this case than in the window along the first

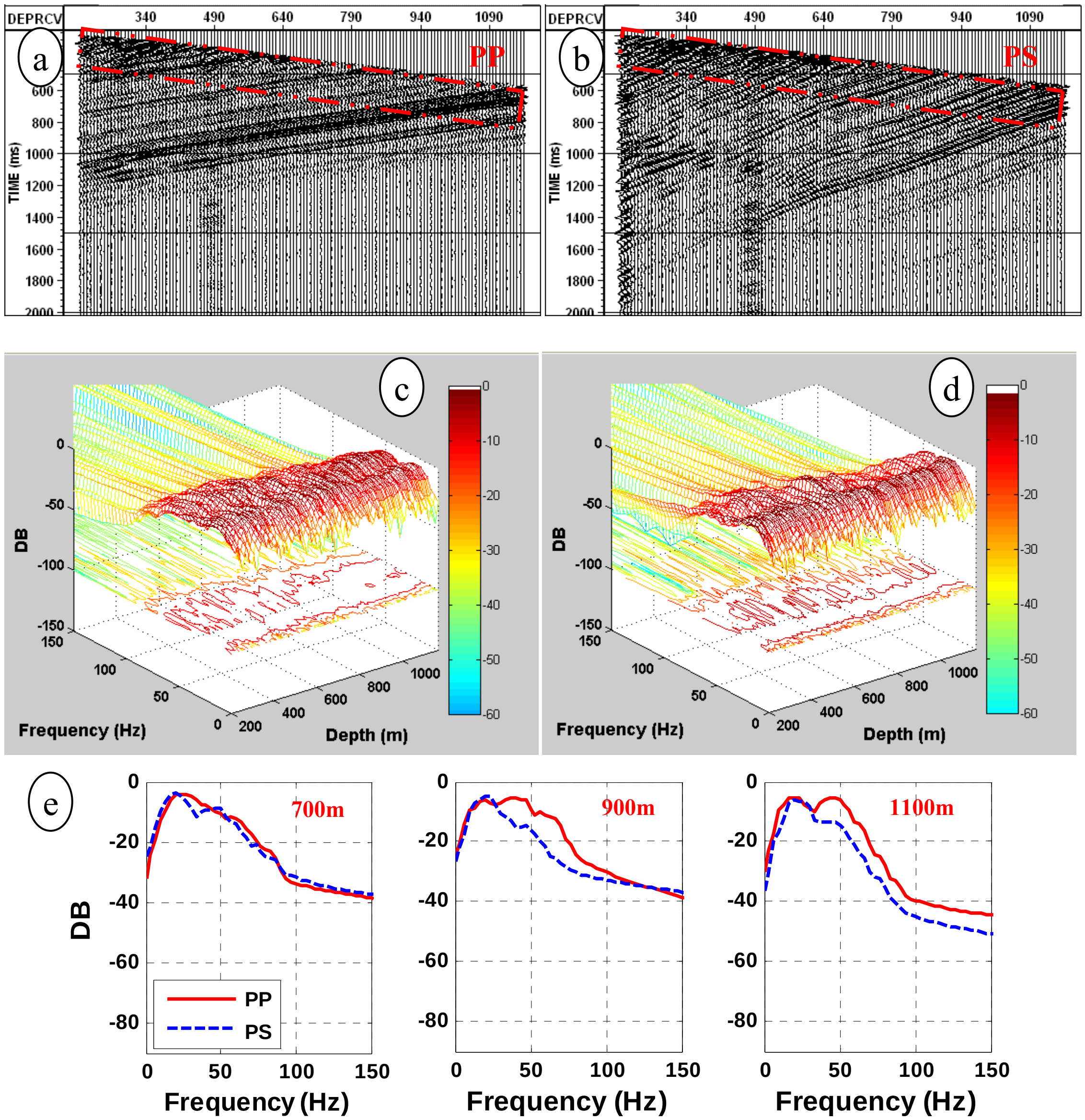

Figure 3.13 Frequency analysis of raw PP and PS data in a 300 ms window (VSP offset 399 m). The red dot-dashed lines in figures a and b outline the analysis windows for PP and PS data, respectively. The amplitude spectra of PP and PS data at each receiver are shown as c and d. The amplitude spectra at depths of 700 m, 900 m, and 1100 m are average spectra of the traces within 30 m from each chosen depth.

arrival. The high frequency content of PS waves also shows much more attenuation than that of PP waves. The amplitude spectra chosen at depths 700 m, 900 m, and 1100 m show the frequency difference increasing with distance from the reflector. At depth 1100 m, the reflections are relatively close to the reflectors, therefore the frequency content difference between PP and PS waves is small. At depths of 700 m and 900 m, the difference gets larger when the reflections travel further from the reflectors.

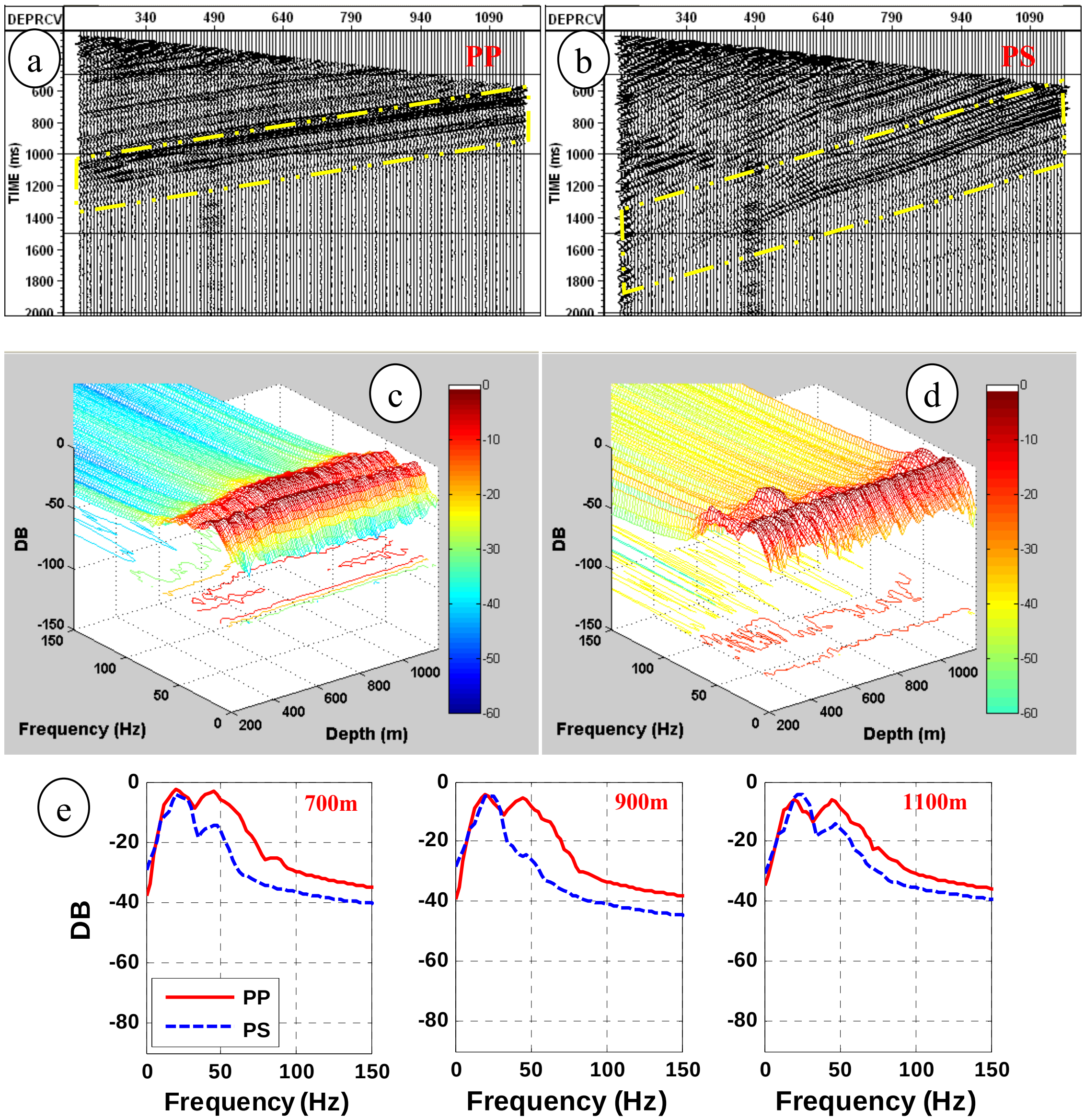

Figure 3.14 Frequency analysis of raw PP and PS data in a window along the reflections (VSP offset 399 m). The yellow dot-dashed lines in figures a and b outline the analysis windows for PP and PS data, respectively. The window for PP data is 400 ms, the window length for PS data is calculated assuming an average Vp/Vs 2.4. The amplitude spectra of PP and PS data at each receiver are shown as c and d. The amplitude spectra at depths of 700 m, 900 m, and 1100 m are average spectra of the traces within 30 m from each chosen depth.

The analysis on raw data shows that the frequency contents of PP and PS waves are similar close to the reflector, and the difference between PP and PS waves relates to the distance from the reflectors. Thus the difference might be caused by different attenuation of P and shear waves. If it is possible to compensate for the attenuation of the different type of waves, then it should be possible to recover a similar frequency content.

3.3.2 Frequency analysis of PP and PS waves after attenuation compensation

From the Q value estimated from zero-offset, the attenuation of P and S waves changes with depth. So time-variant inverse Q filters were used to remove the attenuation effect of P wave and S wave. However, the algorithm of the inverse Q filter is designed for surface seismic, and the Q values are given according to downgoing P wave time, therefore, the Q compensation is basically valid close to the first arrival. For the waves travel further from the reflector, they will be under-compensated.

After applying inverse Q filters to the data, frequency analysis is executed following the same idea as aforesaid: a window along the first arrival for frequency relationship close to the reflectors and a window along reflections for traveling distance effect on the PP and PS wave frequency content. The amplitude spectra of upgoing PP wave and PS wave in the 300ms window starting from the first arrival are shown as Figure 3.15. The frequency content of PP wave and PS wave are almost the same after applying inverse Q filter. The amplitude spectra at depth 700m, 900m, and 1100m (Figure 3.13c) shows that PP and PS wave have almost the same frequency bandwidth. The frequency bandwidth variation with depth is very small for both the PP and PS wave.

Figure 3.16 displays the frequency analysis in the window along the reflections (the analysis windows are outlined by yellow dot-dashed lines). The frequency difference between PP and PS data get smaller comparing with that without attenuation compensation. It can also be found that the variation of frequency bandwidth with travel distance also decreases after applying inverse Q filter. Since the Q compensation is

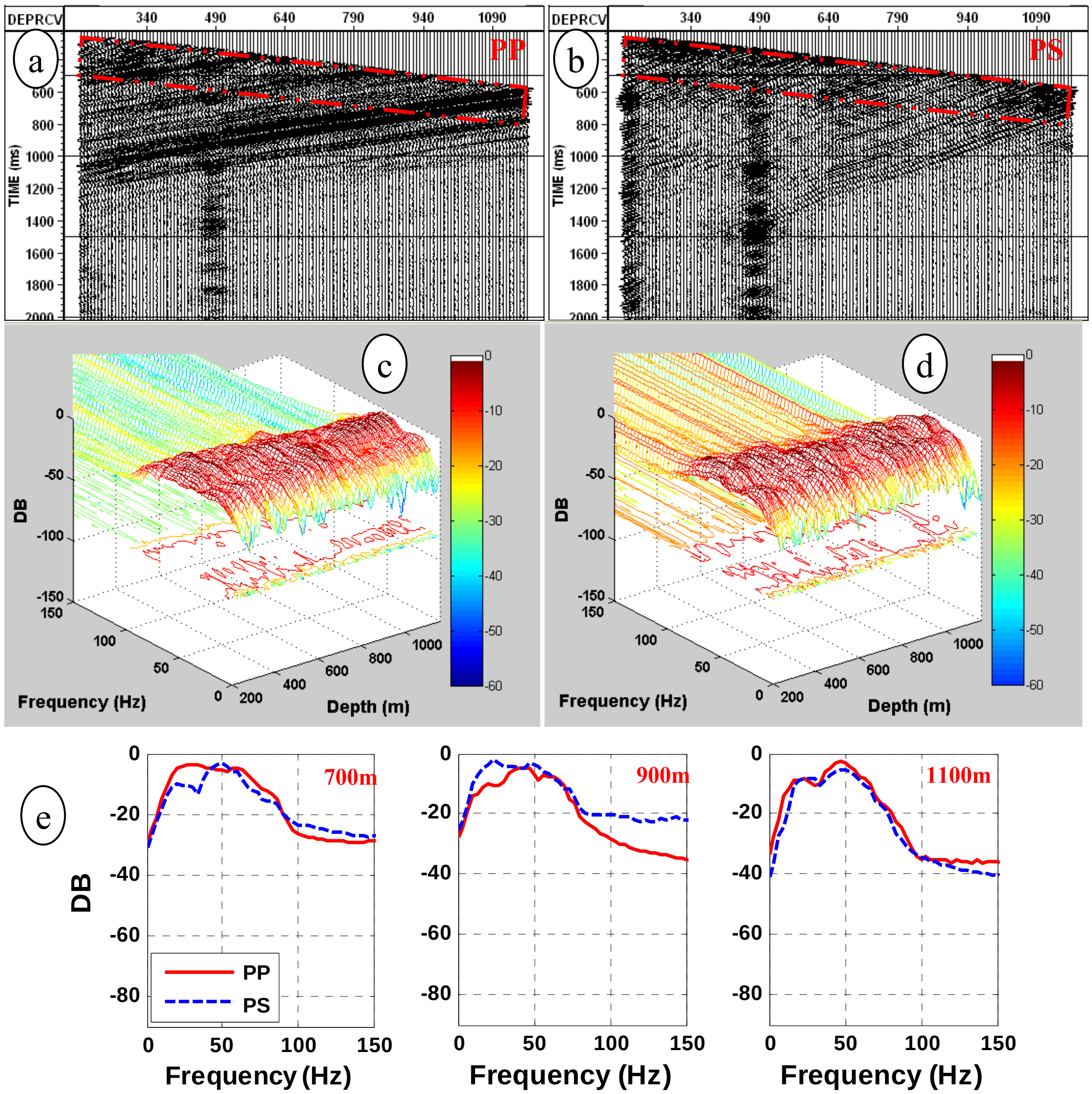

Figure 3.15 Frequency analysis after attenuation compensation in a 300 ms window (offset=399.1 m). The red dot-dashed lines in figures a and b outline the analysis windows on PP and PS data. The amplitude spectra of PP and PS data at each receiver are shown as c and d, respectively. The amplitude spectra at depths of 700 m, 900 m, and 1100 m are average spectra of the traces within 30 m from each chosen depth.

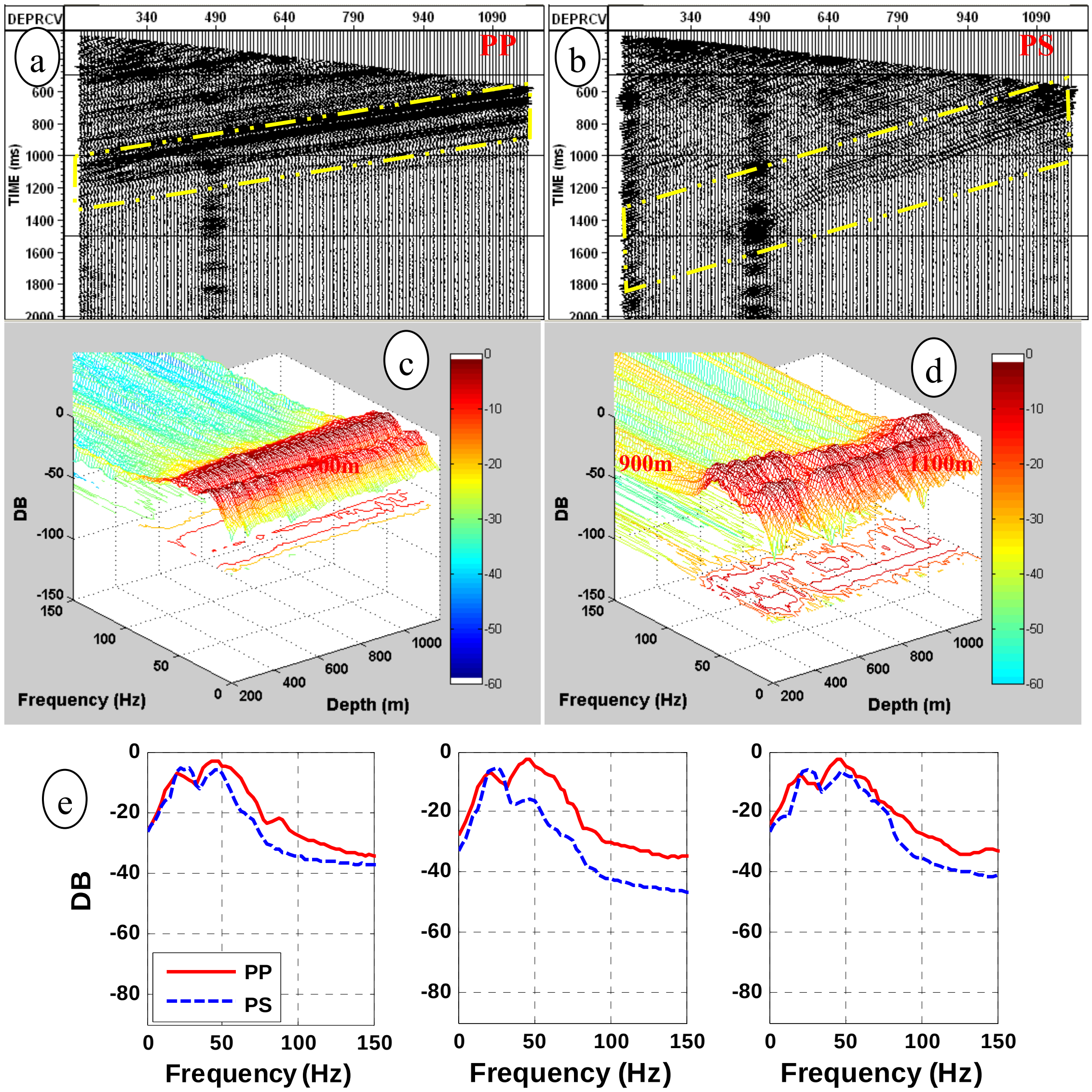

Figure 3.16 Frequency analysis after attenuation compensation in a window along the reflections (VSP offset 399 m). The yellow dot-dashed lines in figures a and b outline the analysis windows for PP and PS data, respectively. The window for PP data is 400 ms, the window length for PS data is calculated assuming an average Vp/Vs 2.4. The amplitude spectra of PP and PS data at each receiver are shown as c and d, respectively. The amplitude spectra at depth 700m, 900m, and 1100m are average spectra of the traces with 30 meters from the chosen depths.

inadequate in the analysis window, especially the PS wave, the PP and PS wave still display apparent difference at the high frequencies.

From the above analysis, we found that the frequency difference often showing on the field data might be caused by different attenuation of P and S waves. If we can accurately account for such attenuation in data processing, the frequency content of PP and PS should be similar.

3.4 Summary

Well log analysis indicates the studied depth interval contains mainly shale and sandstone. An interesting correlation between the Q values and rock properties was found over a reliable Q estimation interval. Generally, increasing P- and S-velocities accompany a decreasing attenuation of P- and S-waves. Greater pore space in the rock and higher Vp/Vs values coincide with low *Qp* and *Qs* values. Interestingly, attenuation was found to decrease with clay content for clay-rich sandstone. Clean sand in this well shows less attenuation of P and S-waves than shaly sandstone. The crossplot between *Qp* and clay-bound water indicates more attenuation of shaly sandstone possibly caused by the interaction between mobile water and clay-bound water.

Since the attenuation data over the reservoir and wet sand interval in this well were not obtained in this study, the effect of different pore fluids on attenuation was not addressed. If reliable attenuation data could be acquired from surface seismic data, then attenuation variation with different pore fluids could possibly be studied. Thus, we might be able to use the attenuation characteristics of seismic data to differentiate hydrocarbons from water in the reservoir.

To understand the reason for the frequency difference generally found in multicomponent seismic exploration, especially in surface seismic data, frequency analysis was undertaken on the 3Cfar-offset VSP data. The results revealed that: 1) the frequency contents of PP and PS data are similar near the reflector; 2) the difference between the frequency of PP and PS becomes larger when the waves travel farther from the reflector; 3) the differences are mostly explained by attenuation, and the frequency contents of PP and PS data are similar after attenuation compensation.

Chapter Four: Rock physics model for cracked/fractured media

4.1 Introduction

Cracks and fractures are commonly caused by stress exceeding the rock strength. They are generally produced as strain due to natural stress on the rock. Cracks and fractures are important as they relate to flow characteristics of fluids in the rock. Furthermore, cracks and fractures contribute no more than a few percent to overall porosity (Macbeth, 2002), and hence have a very small effect on the bulk density of the rocks. However, they can introduce large changes in seismic velocity. Aligned cracks/fractures can also cause velocity anisotropy, in which the velocity parallel to fractures is larger than the velocity perpendicular to fractures (Thomsen, 1986).

Several theoretical models have been developed to predict the effective elastic moduli of a mixture of grains and pores. These models can be used to model the cracks/fractures in the rocks. The Kuster-Toksöz model (Kuster and Toksöz, 1974; Berryman, 1980) calculates the effective moduli of randomly distributed cracks/fractures based on scattering theory, assuming that the cavities are isolated with respect to flow. The Hudson's model (1980, 1981) predicts the effective moduli for aligned cracks/fractures, assuming the cracks/fractures in the rock to be thin and penny-shaped. Cheng (1993) proposed a model for the effective moduli of transversely isotropic rocks, which is valid for arbitrary aspect ratios.

In this chapter, two rock physics models for cracked media are examined to investigate the velocity effects of crack/fractures in the rocks: the Kuster-Toksöz model for randomly oriented cracks/fractures and Hudson's model for aligned cracks/fractures. Since there are some limitations on the use of these two rock physics models, the effects of crack/fracture shape, aspect ratio, and crack/fracture density are also discussed, using rock properties from several field locations: the Ross Lake, Saskatchewan, the Violet Grove, Alberta, and a Saskatchewan mining area.

4.2 Rock physics models for seismic velocities of cracked/fractured media

4.2.1 Kuster-Toksöz Model

Based on a long-wavelength, first-order scattering theory, Kuster and Toksöz (Kuster and Toksöz, 1974; Berryman, 1980) derived a method to calculate effective moduli for randomly distributed inclusions. A generalization of the expressions for the effective moduli K^* and μ^* can be written as (Kuster and Toksöz, 1974; Berryman, 1980):

$$(K_m - K^*)\frac{K_m + \frac{4}{3}\mu_m}{K^* + \frac{4}{3}\mu_m} = \sum_{i=2}^{N} c_i(K_m - K_i)P^{mi}, \tag{4-1}$$

$$(\mu_m - \mu^*)\frac{\mu_m + F_m}{\mu^* + F_m} = \sum_{i=2}^{N} c_i(\mu_m - \mu_i)Q^{mi}, \tag{4-2}$$

and

$$\rho_1 - \rho^* = \sum_{i=2}^{N} c_i(\rho_1 - \rho_i), \tag{4-3}$$

where,

- $c_i = \Omega_i/\Omega$ is the volume concentration of each inclusion type, and $\sum_{i=1}^{N} c_i = 1$, Ω

  : volume;
- K_i, μ_i: bulk and shear moduli of inclusion;

  K_m, μ_m: bulk and shear moduli of matrix;

  $k = \rho v_p^2 - \frac{4}{3}\rho v_s^2$, $\mu = \rho v_s^2$;

- $F_m = (\mu_m/6)[(9K_m + 8\mu_m)/(K_m + 2\mu_m)]$;
- P^{mi},Q^{mi}: coefficients describing the effect of an inclusion of material *i* in a background medium m (Table 4.1);
- ρ_1, ρ_i,ρ^*: density of matrix, inclusion, and effective density.

Table 4.1 Coefficients $\mathbf{P^{mi}}$ and $\mathbf{Q^{mi}}$ for four types of inclusion. $\boldsymbol{F = (\mu/6)[(9K + 8\mu)/(K + 2\mu)]}$, $\boldsymbol{\gamma = \mu[(3K + \mu)/(3K + 7\mu)]}$, $\boldsymbol{\beta = \mu\big[\big(3K + \mu/(3K + 4\mu)\big)\big]}$, $\boldsymbol{\alpha}$ is the aspect ratio. The expressions for spheres, needles, and disks were derived assuming $\mathbf{K_i/K_m \ll 1}$ and $\boldsymbol{\mu_i/\mu_m \ll 1}$.

Inclusion shape	***P^mi***	***Q^mi***
Spheres	$\dfrac{K_m + \frac{4}{3}\mu_m}{K_i + \frac{4}{3}\mu_m}$	$\dfrac{\mu_m + F_m}{\mu_i + F_m}$
Needles	$\dfrac{K_m + \mu_m + \frac{1}{3}\mu_i}{K_i + \mu_m + \frac{1}{3}\mu_i}$	$\dfrac{1}{5}\left(\dfrac{4\mu_m}{\mu_m + \mu_i} + 2\dfrac{\mu_m + \gamma_m}{\mu_i + \gamma_m} + \dfrac{K_i + \frac{4}{3}\mu_m}{K_i + \mu_m + \frac{1}{3}\mu_i}\right)$
Disks	$\dfrac{K_m + \frac{4}{3}\mu_m}{K_i + \frac{4}{3}\mu_m}$	$\dfrac{\mu_m + F_i}{\mu_i + F_i}$
Penny cracks	$\dfrac{K_m + \frac{4}{3}\mu_i}{K_i + \frac{1}{3}\mu_i + \pi\alpha\beta_m}$	$\dfrac{1}{5}\left(1 + \dfrac{8\mu_m}{4\mu_i + \pi\alpha(\mu_m + 2\beta_m} + 2\dfrac{K_i + \frac{2}{3}\mu_i + \frac{2}{3}\mu_m}{K_i + \frac{4}{3}\mu_i + \pi\alpha\beta_m}\right)$

4.2.2 Hudson's model

The Hudson's model (1981) is based on a scattering theory analysis of the mean wavefield in an elastic solid with aligned thin, penny-shaped ellipsoidal cracks or inclusions. The effective moduli c_{ij}^{eff} are given by:

$$c_{ij}^{eff} = c_{ij}^{0} + c_{ij}^{1} + c_{ij}^{2}, \tag{4-4}$$

where c_{ij}^{0} are the isotropic background moduli, and c_{ij}^{1}, c_{ij}^{2} are the first- and second- order corrections, respectively.

$$c^0 = \begin{bmatrix} \lambda + 2\mu & \lambda & \lambda & 0 & 0 & 0 \\ \lambda & \lambda + 2\mu & \lambda & 0 & 0 & 0 \\ \lambda & \lambda & \lambda + 2\mu & 0 & 0 & 0 \\ 0 & 0 & 0 & \mu & 0 & 0 \\ 0 & 0 & 0 & 0 & \mu & 0 \\ 0 & 0 & 0 & 0 & 0 & \mu \end{bmatrix} \tag{4-5}$$

where $\lambda = \rho(v_p^2 - 2v_s^2)$, $\mu = \rho v_s^2$.

For a single fracture set with the fracture normal aligned with the 3rd axis (Figure 4.1), the fractured medium exhibits transversely isotropic symmetry as equation (4-6), and the corrections are,

$$c = \begin{bmatrix} c_{11} & c_{12} & c_{13} & 0 & 0 & 0 \\ c_{12} & c_{11} & c_{13} & 0 & 0 & 0 \\ c_{13} & c_{13} & c_{33} & 0 & 0 & 0 \\ 0 & 0 & 0 & c_{44} & 0 & 0 \\ 0 & 0 & 0 & 0 & c_{44} & 0 \\ 0 & 0 & 0 & 0 & 0 & c_{66} \end{bmatrix}, c_{66} = \frac{1}{2}(c_{11} - c_{12}) \tag{4-6}$$

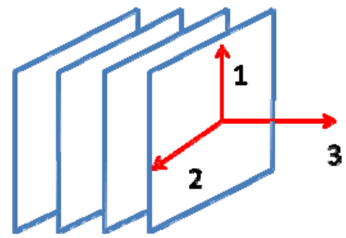

Figure 4.1 Schematic diagrams of aligned fractures (shown in blue).

- $c_{11}^{1} = -\frac{\lambda^2}{\mu}\varepsilon U_3$
- $c_{13}^{1} = -\frac{\lambda(\lambda+2\mu)}{\mu}\varepsilon U_3$
- $c_{33}^{1} = -\frac{(\lambda+2\mu)^2}{\mu}\varepsilon U_3$
- $c_{44}^{1} = -\mu\varepsilon U_1$
- $c_{66}^{1} = 0$

The second-order corrections are

- $c_{11}^{2} = -\frac{q}{15}\frac{\lambda^2}{(\lambda+2\mu)}(\varepsilon U_3)^2$
- $c_{13}^{2} = -\frac{q}{15}\lambda(\varepsilon U_3)^2$
- $c_{33}^{2} = -\frac{q}{15}(\lambda + 2\mu)(\varepsilon U_3)^2$
- $c_{44}^{2} = -\frac{2}{15}\frac{\mu(3\lambda+8\mu)}{\lambda+2\mu}(\varepsilon U_1)^2$
- $c_{66}^{2} = 0$

where

- $q = 15\frac{\lambda^2}{\mu^2} + 28\frac{\lambda}{\mu} + 28, \lambda = \rho(v_p^2 - 2v_s^2), \mu = \rho v_s^2;$
- $\epsilon = \frac{N}{V}a^3 = \frac{3\phi}{4\pi a}$ = crack/fracture density.

The isotropic background elastic moduli are λ and μ, ϕ is the porosity, while a and α are the fracture radius and aspect ratio (Appendix C), respectively. The corrections c_{ij}^1, c_{ij}^2 obey the usual symmetry properties for transverse isotropy or hexagonal symmetry. The term U_1 and U_3 depend on the fracture conditions.

For dry fractures

$$U_1 = \frac{16(\lambda + 2\mu)}{3(3\lambda + 4\mu)}, \qquad U_3 = \frac{4(\lambda + 2\mu)}{3(\lambda + \mu)}$$

For "weak" inclusions

$$U_1 = \frac{16(\lambda + 2\mu)}{3(3\lambda + 4\mu)} \frac{1}{(1 + M)}, \qquad U_3 = \frac{4(\lambda + 2\mu)}{3(\lambda + \mu)} \frac{1}{(1 + \kappa)}$$

where

$$M = \frac{4\mu'}{\pi\alpha\mu} \frac{(\lambda + 2\mu)}{(3\lambda + 4\mu)}, \qquad \kappa = \frac{[K' + (\frac{4}{3})\mu'](\lambda + 2\mu)}{\pi\alpha\mu(3\lambda + 4\mu)}$$

K' and μ' are the bulk and shear moduli of the inclusion material, respectively. The criterion for an inclusion to be "weak" depends on its shape or aspect ratio α as well as on the relative moduli of the inclusion and matrix material. Dry cavities can be modeled by setting the inclusion moduli to be zero. Fluid-saturated cavities are simulated by setting the inclusion shear modulus to be zero.

Both models assume no fluid flow between spaces, thus they simulate high-frequency, saturated-rock behaviour. At low frequencies, when there is time for wave-induced pore pressure increments to flow and equilibrate, dry-rock moduli should first be calculated from the two models. Then, Gassmann (1951, Appendix D) fluid substitution for isotropic media, and Brown and Korringa's (1975, Appendix D) fluid substitution for anisotropic media can be used to predict saturated rock properties.

The overall effect of randomly distributed inclusions in a rock from the Kuster-Toksöz method is an isotropic medium. The overall effect of the aligned fractures from the Hudson's model is an anisotropic medium.

4.3 Parameter test on rock physics models for cracked/fractured media

The assumptions for both fracture models indicate that there are some limitations on the fracture parameters including fracture shape, aspect ratio, and fracture density. Several rock types were selected to provide values for numerical tests: a Cretaceous-aged, high-porosity (about 30%) channel sand, and a tight sand from the Ross Lake heavy oil field, another Cretaceous-age low-porosity (about 12%) sandstone from Violet Grove, Alberta, and a Devonian carbonate and a shale from a potash mining area in Saskatchewan. These rock properties are listed in Table 4.2. The porous channel sand and tight sand from Ross Lake area were used for various parameter tests with the Kuster-Toksöz model and Hudson's model. For this modeling, the Hashin-Shtrikman bounds (Appendix E) were also calculated for comparison. These bounds are the narrowest constraints when the geometries of the constituents are not known. Fractured rock properties are then calculated for all the chosen rocks, assuming penny-shaped fractures, with a fractional fracture porosity of 0.01 and an aspect ratio 0.01. For all the tests, the void spaces are filled with brine with a density of 1100 kg/m^3 and a velocity of 1430 m/s.

4.3.1 Kuster-Toksöz Model

Figure 4.2 and Figure 4.3 display the results for randomly oriented inclusions in the porous channel sand of the Ross Lake heavy oil field calculated by the Kuster-Toksöz model. Dry moduli were calculated first by assuming that both the bulk and shear moduli of the porosity are 0 (air filled), then the Gassmann equations were used to calculate the effective moduli when the void space is filled with brine. As shown in Figure 4.2a, the velocities decrease significantly, depending on the inclusion shape. Smaller aspect ratios yield larger decreases of velocities. The velocities of the sphere pore shape are coincident with the Hashin-Shtrikman upper bound. The sphere inclusion shapes give the same results from the Kuster-Toksöz (1974) formula and a generalized formula (Berryman, 1980). The effective velocities of the small aspect ratio shapes approach the Hashin-Shtrikman lower bound at a smaller volume fraction of pores. Except for the spherical shaped inclusions, all other inclusion shapes have a limitation on volume fraction values for reasonable effective velocity values. The concentration value limitations decrease with aspect ratio. For needle shape inclusions, there is no dependence on aspect ratio. The results are valid for a large range of concentration values. The same calculation was carried out for the tight sand of the Ross Lake heavy oil field (Figure 4.2b). The concentration limitations for each inclusion shape are quite similar to those of the porous sand.

Table 4.2 Rock properties for numerical tests of fractured media.

	Ross Lake		Violet Grove	Sask. mining	
Lithology	Sandstone	Sandstone	Sandstone	Carbonate	shale
Depth	1148m	1160m	1605m	970m	1006m
Vp (m/s)	3026	5689	3778	5538	3765
Vs (m/s)	1721	3413	2237	2954	2074
Density (kg/ m^3)	2133	2630	2420	2695	2326
Porosity	30%	2%	12%	3%	<5%

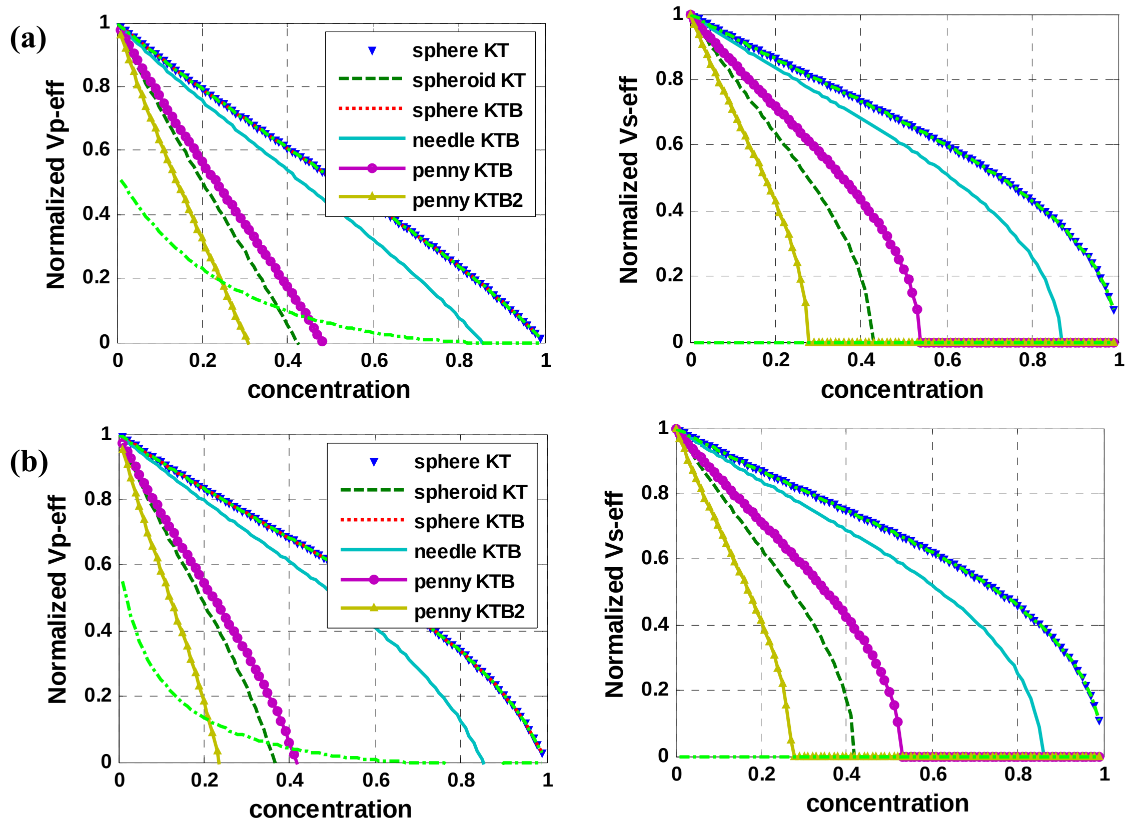

Figure 4.2 Variation of effective velocities with the volume concentration of inclusions for several fracture shapes from the Kuster-Toksöz model. All the velocity values are normalized to the range from fluid to unfractureed rock velocities. The aspect ratio value for the oblate spheroid shape is 0.1. For the penny shapes, an aspect ratio of 0.1 (noted as penny KTB) and 0.05 (noted as penny KTB2) are used. KT: results from the Kuster-Toksöz formula for sphere and oblate-spheroid pores; KTB: results from the generalized Kuster-Toksöz model by Berryman. The green dash-dot lines are Hashin-Shtrikman bounds (Appendix E). a. Ross Lake porous channel sand; b. Calculations as in Figure 1a, for the Ross Lake tight sand.

Figure 4.3 shows the variation of effective velocities with aspect ratio α for spheroid and penny shape pores. The volume fraction porosity, c, of the pores was set to be 0.1. When the aspect ratio is too small, the assumption of no fluid flow cannot be satisfied, thus the model can't give reasonable results. When the aspect ratio increases, velocity drops will decrease. The results of spheroid shapes will approach those of the sphere. For penny-shaped fractures, the aspect ratio cannot be too large, otherwise, the predicted velocities will exceed the upper bound.

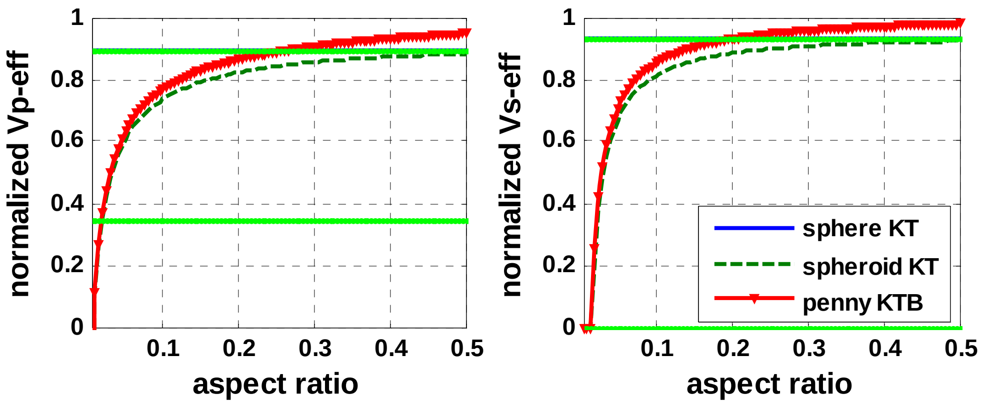

Figure 4.3 Ross Lake porous channel sand: the variation of effective velocities (from the Kuster-Toksöz model) with fracture shape and aspect ratio. All the values are normalized to the range from fluid to unaltered rock velocities. The volume fraction of the fractures c is 0.1. The green dash-dot lines are the Hashin-Shtrikman bounds (Appendix E). KT: results from the Kuster-Toksöz formula; KTB: results based on the generalized Kuster-Toksöz model by Berryman.

The results displayed in Figure 4.3 indicate that there are limits for the α/c value to ensure the predicted velocities falling within the Hashin-Shtrikman bound. To investigate the value range, a test of the α/c values with different c values (0.01, 0.05, and 0.25) was carried out, and the results are shown in Figure 4.4a for the Ross Lake porous channel sand. The velocity values in Figure 4.4a were normalized by the Hashin-Shtrikman upper and lower bounds. For various c values, both P- and S-velocity results indicate relatively stable minimum α/c values of approximately 0.2. However, for penny-shaped inclusions, the maximum α/c values for reasonable velocities change drastically with respect to the fracture concentration value c. Small c values will still have reasonable effective velocities for large α/c values. The P-velocities are less dependent on the α/c values than the S-velocities. For spheroid inclusions there is no upper limitation on the α/c value. However, the effective velocities approach the upper bound quickly for larger c values. Calculation carried out for the tight sands of the Ross Lake heavy oil field (Figure 4.4b) yields a similar conclusion.

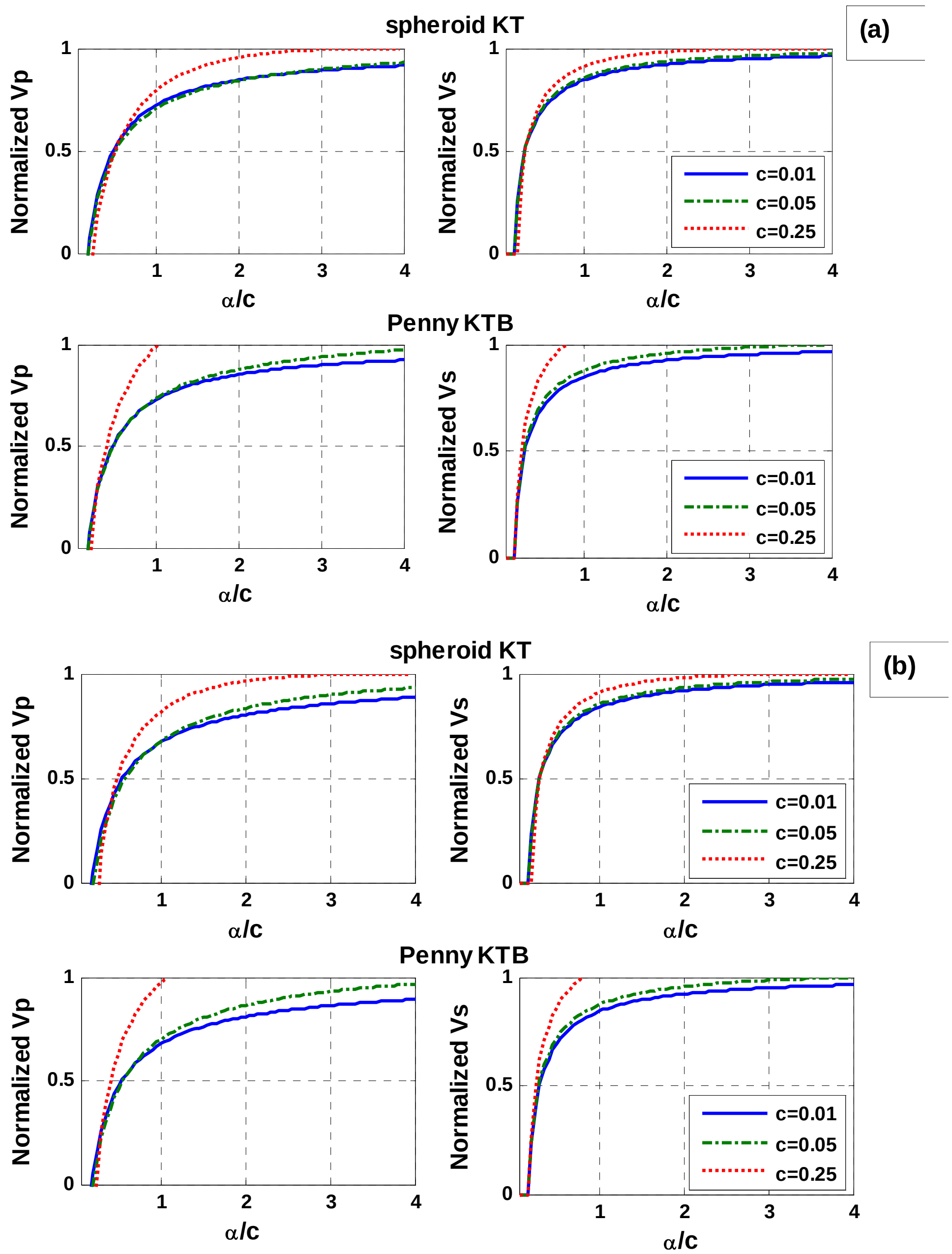

Figure 4.4 Variation of effective velocities (from the Kuster-Toksöz model) with α/c (aspect ratio/volume concentration). All the values are normalized to the range of Hashin-Shtrikman bounds (Appendix E). a. Ross Lake porous channel sand; b. Calculations as in Figure 3a, for the Ross Lake tight sand.

4.3.2 Hudson's model

Figure 4.5a display the modeled P- and S-velocity variations with fracture density for the Ross Lake porous channel sand from Hudson's model for penny-shaped fractures, with three aspect ratios (α): 0.002, 0.01, and 0.05. When the rock contains fractures aligned in one direction, it will appear transverse anisotropy with respect to the axis along the normal to the fractures. The P-velocity drops very little when the waves travel parallel to the fracture plane, but will display a distinct decrease when the wave travels normally to the fractures. For SV waves, the velocity will change the same amount whether it travels normal to the fractures or across the fracture plane. Fractures with an aspect ratio of 0.05 were also modeled by the Kuster-Toksöz model for penny-shaped fractures. The effective P velocities from the Kuster-Toksöz model are between the P velocities from Hudson's model along the fracture normal and fracture plane.

For given aspect ratio fractures, when the fracture density exceeds a certain limit, the velocities will display an abnormal increase with fracture density value, especially for Vs. This is about 0.05 (0.1% fracture porosity) for fractures with an aspect ratio of 0.002, and 0.2 (around 1% fracture porosity) for fractures with an aspect ratio of 0.01.

From the modeling results for tight sand from the Ross Lake area (Figure 4.5b), the P-velocity variations with fracture density show an apparent dependence on the properties of the unfractured rock, whereas the S-velocity displays a similar variation with crack density for the two different rock samples. Reasonable fracture density ranges for each aspect ratio are still the same due to the similar variation of S-velocity with fracture density.

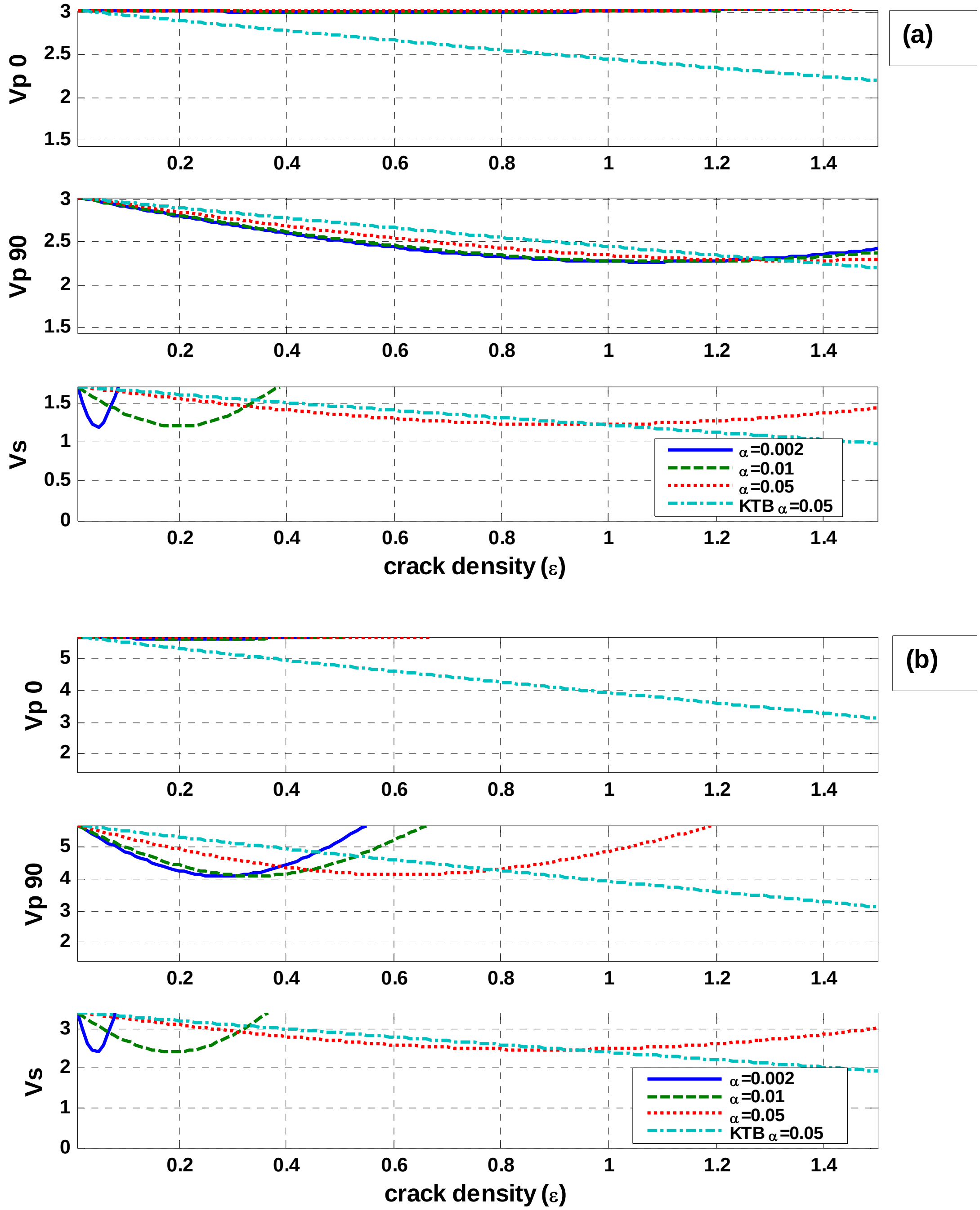

Figure 4.5 Variation of effective velocities of fractured rock from Hudson's model with fracture density ε. The velocity plot range are from the velocities of fluid and isotropic unfractured rock, respectively. KTB denotes the effective velocities from the Kuster-Toksöz model. a. Ross Lake porous channel sand; b. Calculations as in Figure 4a, for the Ross Lake tight sand.

4.4 Seismic velocity changes associated with cracks/fractures

Assuming a 1% fracture porosity induced by penny-shaped fractures with an aspect ratio of 0.01, the effective P- and S-velocities from Kuster-Toksöz and Hudson's model are plotted in Figure 4.6 for sample 1) the Ross Lake porous sand, sample 2) the Saskatchewan mining shale, sample 3) the Violet Grove sand, sample 4) the Saskatchewan mining carbonate, and sample 5) Ross Lake tight sand. The findings are:

1. These fractures can produce up to a 22% velocity decreases in Hudson's model, a P-velocity decrease of 16% and an S-velocity decrease of 11% using the Kuster-Toksöz model;
2. The changes (in percentage) of P-velocity along fracture planes from Hudson's method and S-velocity from both models have almost no dependence on unfractured rock properties;
3. The changes (in percentage) of S-velocity along fracture normal are very similar from Hudson's method without or with fluid substitution;
4. The change trends (in percentage) of P-velocity (P-velocity along the fracture normal for Hudson's model results) are consistent with the values of unfractured rocks from the Kuster-Toksöz model and Hudson's model without fluid substitution.

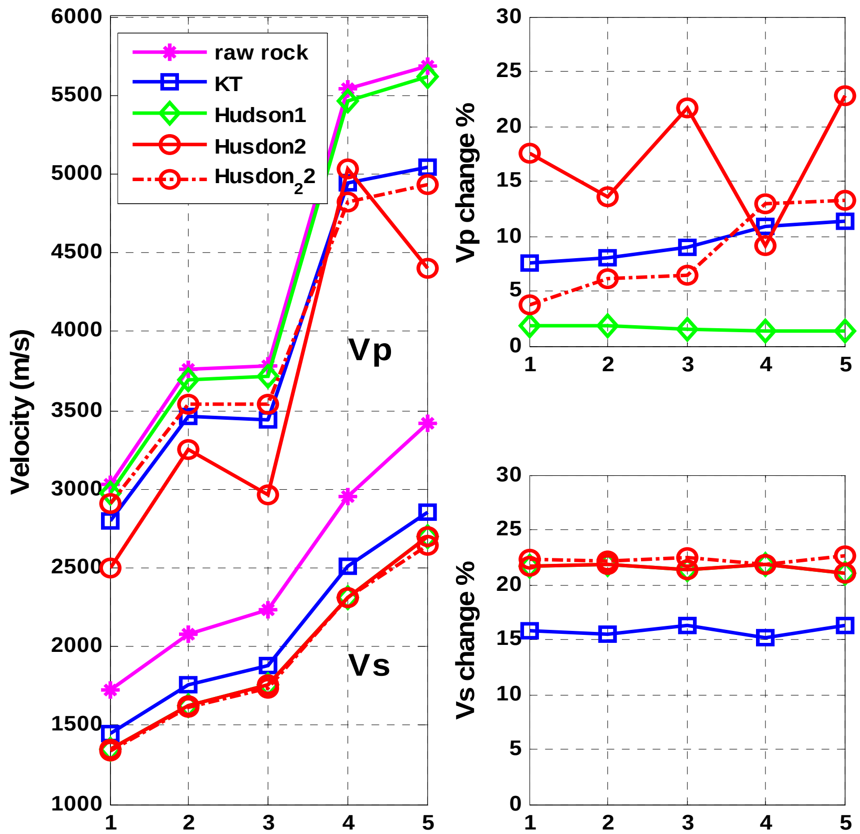

Figure 4.6 Modeled effective P- and shear velocities for selected rocks (rock samples number 1 through 5) assuming penny shape fractures with aspect ratio of 0.01 and a fracture density of 0.01. KT: velocities from Kuster-Toksöz model. Hudson 1: velocities along the fracture plane; Hudson 2: velocities along fracture normal; Hudson$_2$ 2: velocities along fracture normal without fluid substitution. The plots on the right are percentage changes with respect to the original velocity.

4.5 Summary

Two rock physics models, Kuster-Toksöz and Hudson's model for fractured media are discussed. When the assumptions of the models are satisfied, the Kuster-Toksöz and the Hudson's methods can predict rock properties for randomly oriented fractures and aligned fractures, respectively.

The results of the Kuster-Toksöz model indicate that the rock properties depend largely on the pore shape. Generally, the smaller aspect ratios yield a larger decrease of moduli and velocities. For both spheroid and penny shaped pores, α/c values should not be smaller than about 0.4 (equivalent to c<2.5α). For penny-shaped inclusions, the valid maximum α/c values change drastically with respect to the concentration value c. Small c values will still give reasonable effective moduli for large α/c values.

For the Hudson's model, smaller aspect ratio fractures have a smaller valid fracture density range, especially for Vs, approximately 0.05 (for a fracture porosity of about 0.1%) for fractures with aspect ratio 0.002, and 0.2 (equivalent to about 1% fracture porosity) for fractures with aspect ratio 0.01.

The modeling results for several rocks assuming 1% fracture porosity, and penny-shaped fractures with an aspect ratio of 0.01 indicate: the percentage changes of the S-velocity from both models, and the P-velocity along fracture planes from Hudson's method have almost no dependence on unfractured rock properties. The percentage changes of the P-velocity (P-velocity along fracture normal for Hudson's model results) are consistent with the property values of unfractured rocks for the Kuster-Toksöz model and Hudson's method without fluid substitution; anisotropic fluid substitution introduces a higher percentage of P-velocity changes and similar S-velocity changes.

Chapter Five: Seismic detection of cracks/fractures associated with potash mining

5.1 Introduction

The middle Devonian Elk Point Group contains the largest volume of salt deposits preserved in the Western Canada Sedimentary Basin. These deposits (Figure 5.1) extend from the USA northward for more than 1900 km (1200 miles) to Canada's Northwest Territories (DeMille *et al*., 1964). In the study area (outlined by the dashed line in Figure 5.1), the most widely developed deposit is that within the Prairie Evaporite Formation, which is present through much of the Williston Basin region. Its thickness ranges from 0 m to about 220 m. Potash (*the common name for potassium carbonate* (K_2CO_3) *and various mined and manufactured salts that contain the element potassium in water-soluble form*, http://en.wikipedia.org/wiki/Potash) ore (used as fertilizer and other products) is situated 20-30 m below the top of a 100-200 m thick salt unit, approximately 1000 m below the ground surface. Mining is undertaken using a long room and pillar method (The rooms here refer to the tunnels cut into the ore body, the pillars are the material around the rooms left standing to hold up the rock ceiling for roof support in the mining. The description of the mining method can be found at *http://en.wikipedia.org/wiki/Room_and_pillar.*). The ore body is 30m thick on average with a typical composition of 55% halite, 40% sylvite, 4% carnallite and 1% insoluble matters (Maxwell et al., 2005). A generalized stratigraphic column around the mining interval for the area is shown as Figure 5.2.

A major potential problem for potash mining in this area is brine inflow. This may cause ore loss, operational problems, or danger to personnel. There are two situations associated with brine movement: flows or dissolution before mining and

Figure 5.1 Areal distribution of potash-bearing rocks in the Elk Point Basin (from Fuzesy, 1982).

inflows during mining. The existence of brine prior to mining can cause disruption to the normal Phanerozoic stratigraphy by way of collapse structures. Collapse structures are localized regions of considerable, sometimes complete, removal of original geological layers and resultant overlying collapse. These features are thought to result from the dissolution of Prairie Evaporite salts, with associated brecciation and collapse of the overlying strata (mostly carbonate, then shale) into the washout caverns (e.g. Gendzwill and Lundberg, 1989). Collapses are often assumed to take the shape of sub-vertical cylinders, 100m to 1000m in diameter, extending from a depth of over 1000m possibly to the surface. Mining into one of these collapse zones results in cost increases for the mining operation at best, and in some instances the loss of the mine (Prugger et al., 2004).

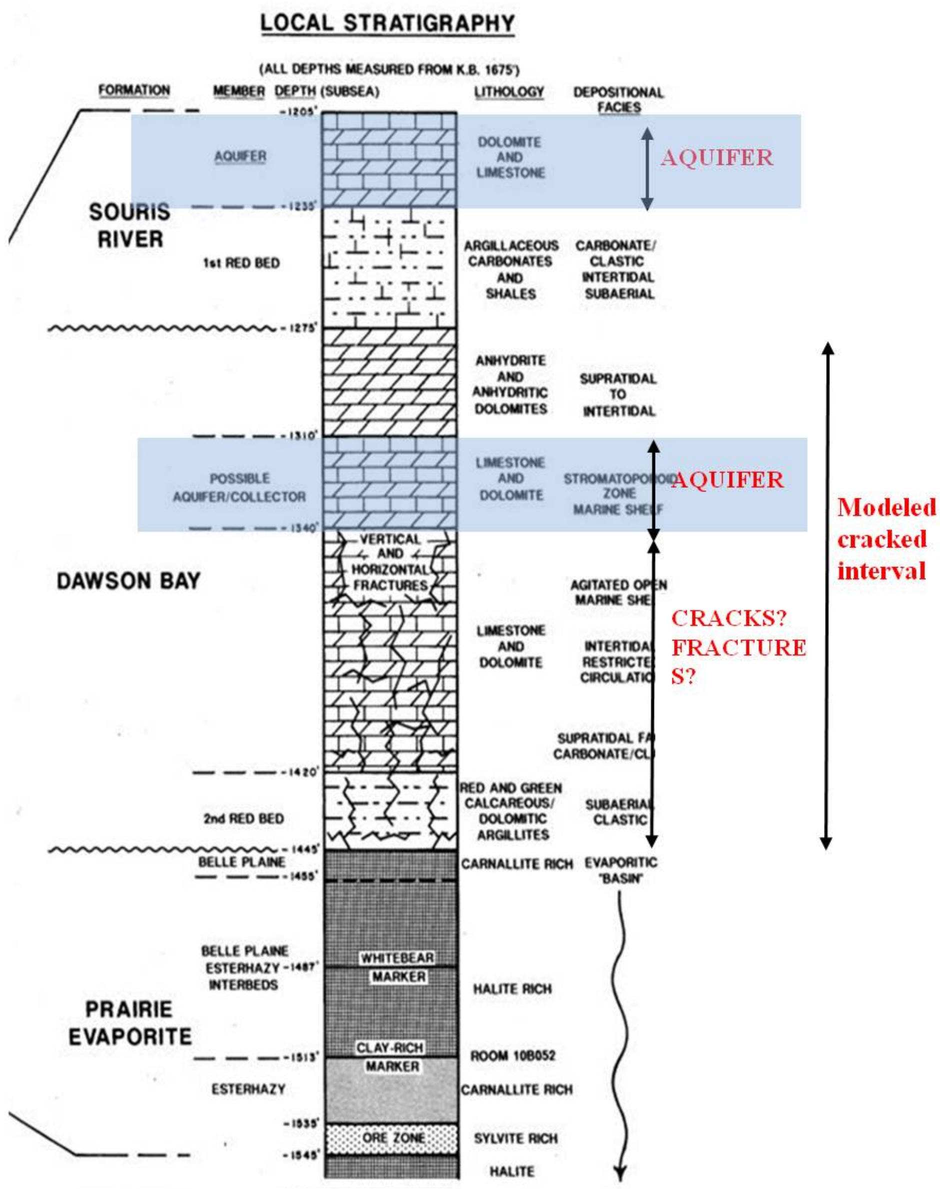

Figure 5.2 Local stratigraphy of Prairie Evaporite and overlying formations in the mining area. The Dawson Bay carbonates, dolomites, and shales can host fractures (from R. Edgecombe, personal communication, 2008).

The use of the long-room and pillar mining method may cause subsurface stress fields to change, thus potentially inducing fractures. In the potash mining area, there are two aquifers, one is near the base of the Souris River Formation, the other aquifer is at the top part of the Dawson Bay Formation (Figure 5.2). Between the aquifers and ore zone, the formation is composed of shale, dolomite and dolomitized limestone. All these rocks are apt to be fractured. Any fracturing of normally impermeable carbonate rocks could create a brine inflow path that might compromise potash mining operations.

An effective way to mitigate the risk posed by brine flows is to map and predict the volume and location of potentially affected areas prior to mining. 3D seismic surveys have been used successfully to map the subsurface, including collapse structures (Gendzwill, 1969; Hamid et al., 2004; Prugger et al., 2004). To predict fractures induced by mining processes, multicomponent and repeated (time-lapse) seismic methods might be useful. In this study, rock physical modeling of fractured media was used to assess the feasibility of detecting fractures by multicomponent and time-lapse seismic methods. Kuster-Toksöz modeling (Kuster and Toksöz, 1974; Berryman, 1980; Mavko et al., 1998) was first undertaken to simulate randomly oriented and distributed fractures, whereas Hudson's model (Hudson, 1980, 1981) was used for studies of aligned fractures. In this study, data and results from two wells are shown: Well A and Well B. Well A is particularly useful as it penetrates to the Cambrian. Well B is within the studied mining area.

5.2 Well log analysis and properties of potash ore

Table 5.1 shows the well log properties of the minerals for some of the lithologies involved in the study. The essential wireline logs to differentiate the potash ore from other lithologies are the spectral gamma ray and neutron logs. Potash ore displays high radioactivity due to the potassium-40 isotope existing in sylvite (KCl). Sylvite's gamma ray value is about 730 API. Additionally, the ore will display a slightly higher neutron-porosity compared with pure sylvite due to presence of water in carnallite (KCI, $MgCI_2$, $6H_2O$). For a typical composition, the gamma ray of the potash ore is about 290 API, the neutron porosity will be in the vicinity of 0%.

Table 5.1 Well log properties of selected minerals (from Crain, 2005)

	Neutron-porosity (fractional)	DENSITY (kg/m^3)	Acoustic slowness (μs/m)	PE
Clean Quartz	-0.028	2650	182	1.82
Calcite	0	2710	155	5.09
Dolomite	0.005	2870	144	3.13
Anhydrite	0.002	2950	164	5.08
Fluorite	-0.006	3120	150	6.66
Halite	-0.018	2030	220	4.72
Sylvite	-0.041	1860	242	8.76
Carnallite	0.584	1560	256	4.29

Figure 5.3 shows logs from Well A, the shear log is of poor quality over the shallow part of the well, about above 580 m. The Prairie Evaporite is about 150m thick, at a depth of 1010m. The Prairie Evaporite displays overall low neutron-porosity (-5%) and high density-porosity (40%). The ore interval is situated at about 10m from the top of Prairie Evaporite Formation and is composed of several thin ore beds, and it is about 50m thick. The ore beds display high radioactivity. On the neutron-porosity log, the ore beds generally show a slightly higher value. Deviation of the neutron- porosity values from the normal trend might be caused by the variation of carnallite content in the ore:

carnallite-rich ores related to a higher neutron-porosity and vice versa (Figure 5.3 b). Sonic velocities in the Paleozoic interval are in the area of 5000m/s for P waves and 2900m/s for S-waves. Vp/Vs values are typically around 1.8.

Figure 5.4 displays the log curves of well B, which is within the mining area under investigation. The Prairie Evaporite is overlain by the 2nd Red Bed Shale of the Dawson Bay Formation, which is largely dolomite and dolomitized limestone. Above the Dawson Bay lies the 1st Red Bed shale and a porous zone which belongs to the Souris River Group and is saturated by water. This aquifer is about 15m thick, with quite high porosity, about 20%. In the upper Dawson Bay is another aquifer, approximately 10m thick with a porosity about 16%. The rock layers between the aquifer and the Prairie Evaporite consist of shale, dolomite and dolomitized limestone. They are all likely to be fractured. Both horizontally and vertically aligned fractures may exist in the Dawson Bay Formation. If fractures occurred in these formations prior to or during mining process, brine in the aquifer could flow into the mining interval. Thus, it is necessary to identify if fractures occur and where the fractures are located.

(a)

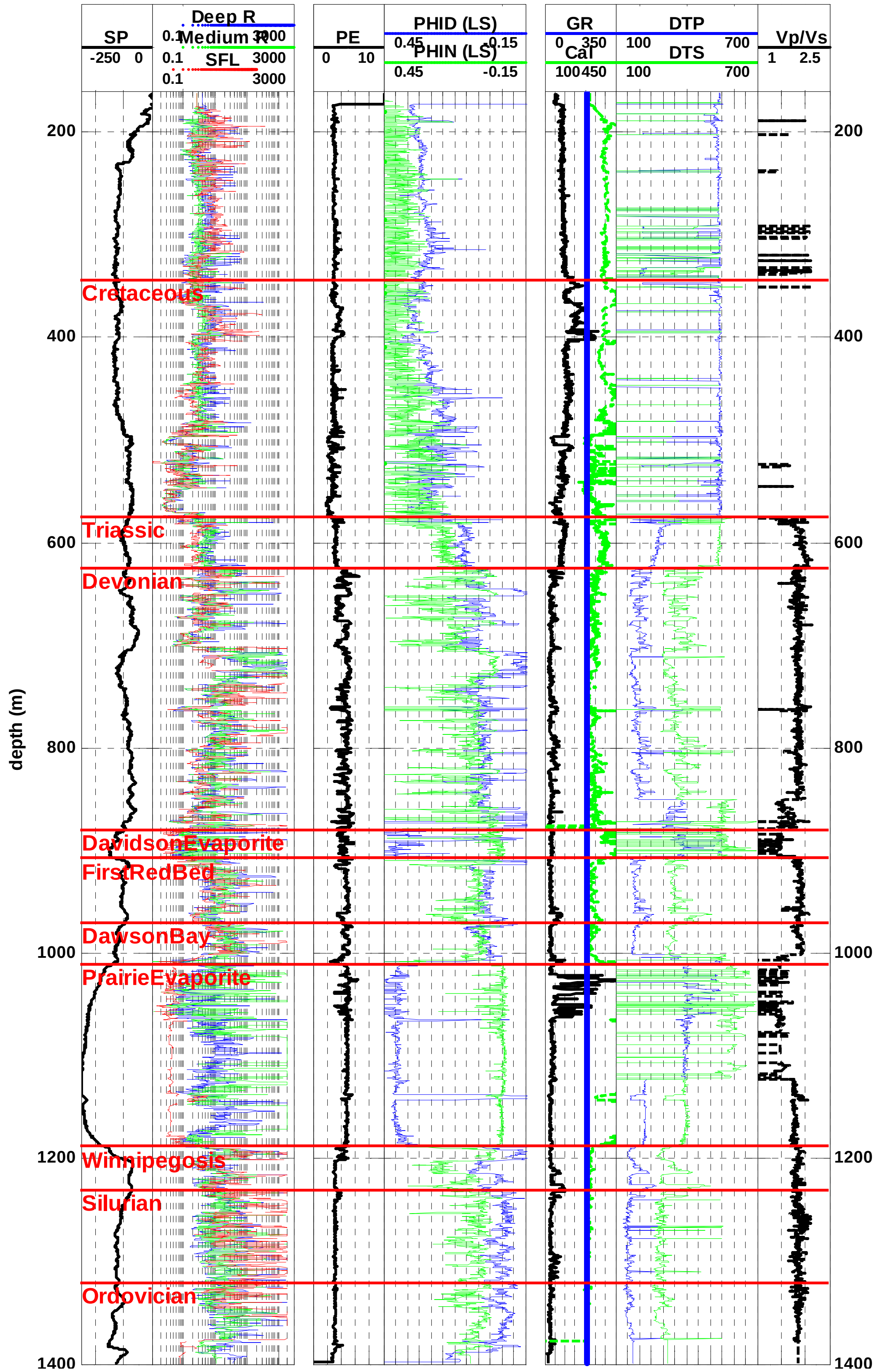
SP
-250 0
Deep R
0.1 3000
Medium R
0.1 3000
SFL
0.1 3000
PE
0 10
PHID (LS)
0.45 -0.15
PHIN (LS)
0.45 -0.15
GR
0 350
Cal
100 450
DTP
100 700
DTS
100 700
Vp/Vs
1 2.5
depth (m)
200
400
600
800
1000
1200
1400
Cretaceous
Triassic
Devonian
DavidsonEvaporite
FirstRedBed
DawsonBay
PrairieEvaporite
Winnipegosis
Silurian
Ordovician

(b)

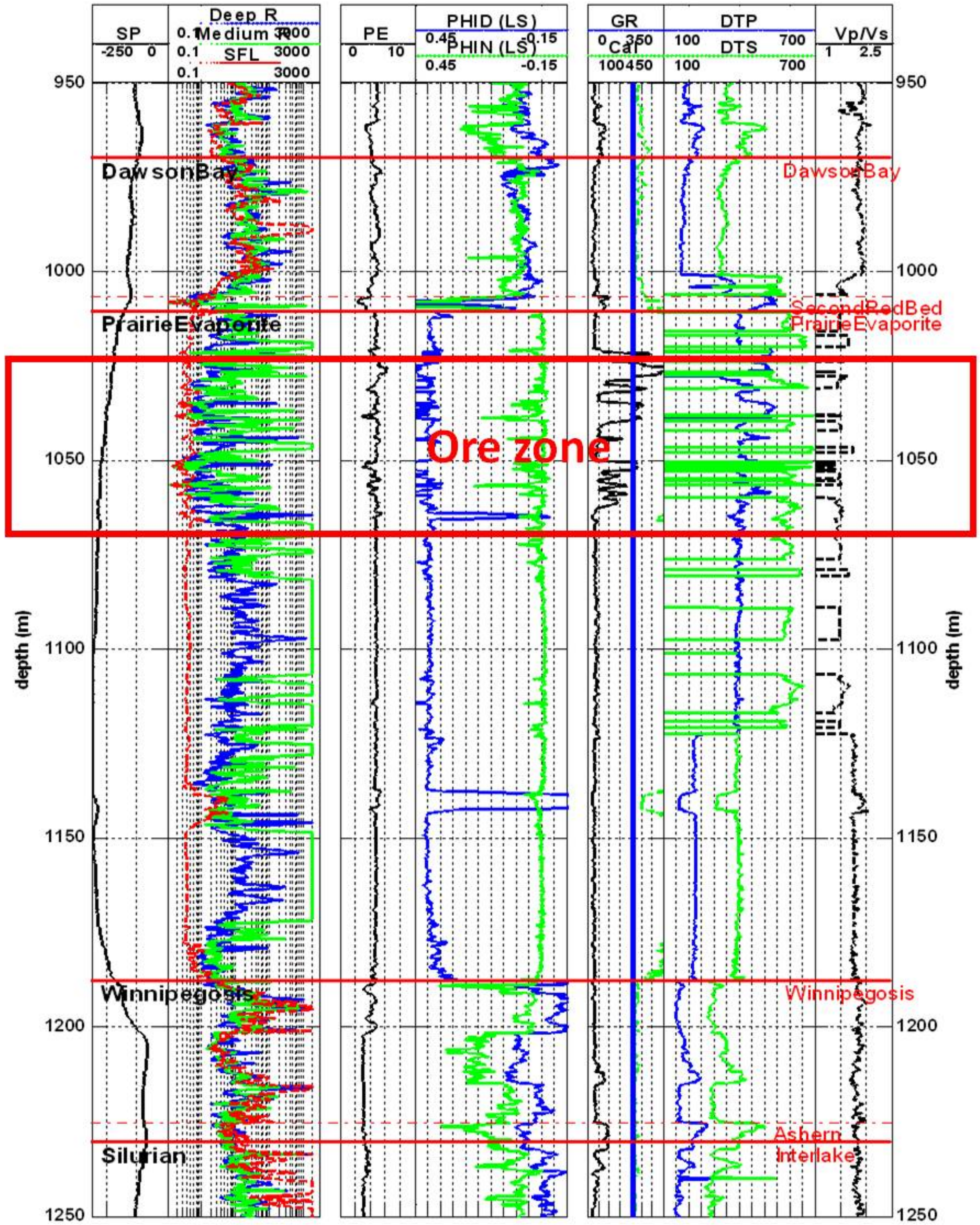

Figure 5.3 a: Log curves with the layer tops of Well A; b: Log curves of Well A focusing on the Prairie Evaporite Formation. The second track of the well logs includes deep (blue), medium (green) resistivity measurement, and spherically focused log (red).

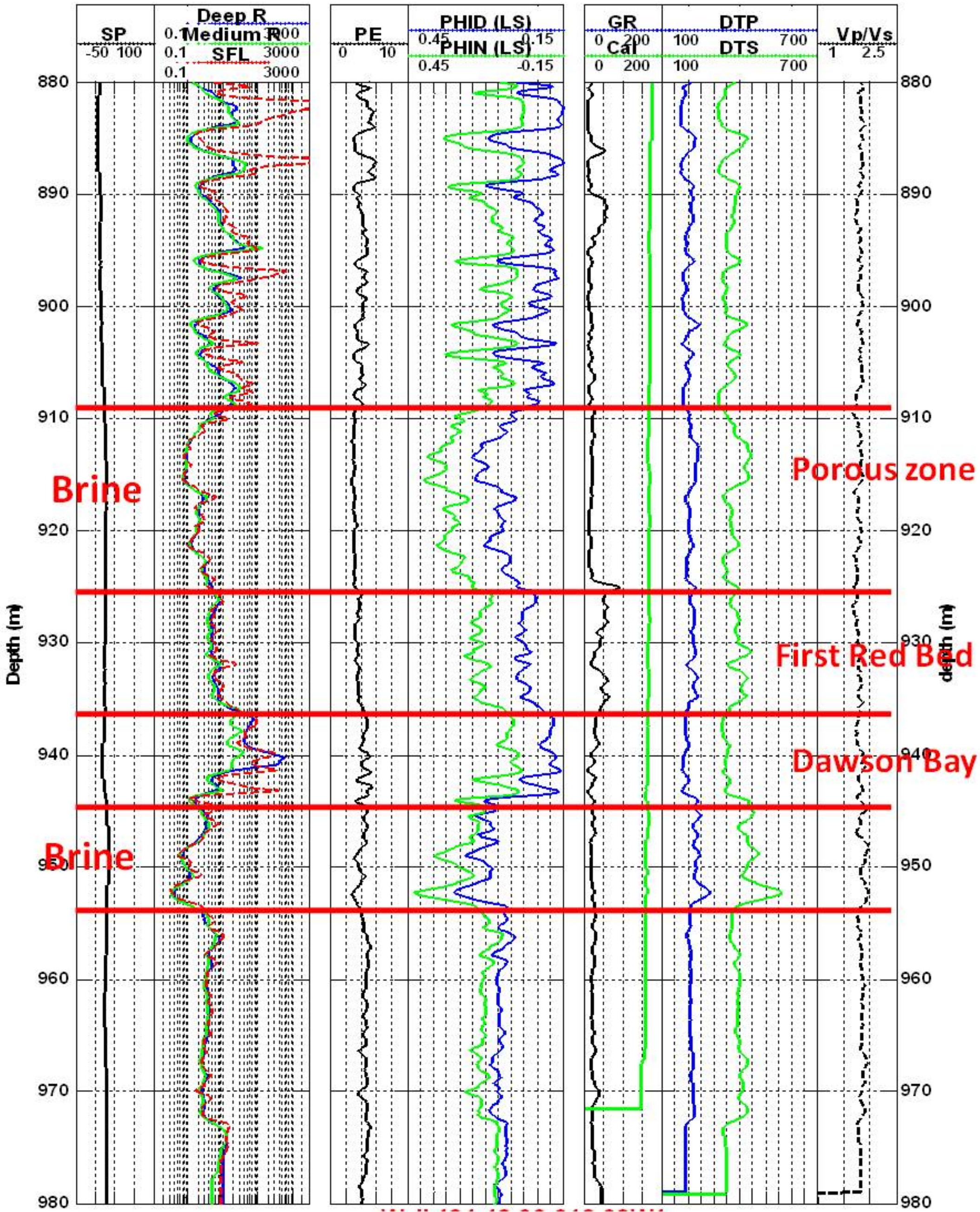

Figure 5.4 Logs with the layer tops for Well B. The two porous acquifers are about 908 – 925m, and 944 – 953 m. The second track of the well logs includes deep (blue), medium (green) resistivity measurement, and spherically focused log (red).

5.3 Modeling cracks/fractures in the rock overlying the potash ore interval

In the potash mining area, an aquifer exists in the Souris River Formation (Figure 5.2). Just below the aquifer lies the First Red Bed Shale and the Dawson Bay Formation. All these formations, together with the Second Red Bed Shale above the Prairie Evaporite Formation, may be fractured. To investigate possible elastic changes caused by fractures in these formations, rock physics modeling for cracked media was applied to the full Dawson Bay Formation, including the Second Red Bed shale. In Well A, this amounts to a 40 m interval whereas in the Well B area, it is 43 m thick. The Kuster-Toksöz (Kuster and Toksöz, 1974; Berryman, 1980) method was used for randomly oriented fractures, and Hudson's (1980, 1981) model was used for aligned fractures. The randomly oriented fractures display overall isotropy, while aligned fractures introduce azimuthal anisotropy. Both the Kuster-Toksöz and Hudson's methods assume isolated fractures, thus they are valid only at high-frequencies. For low-frequency (seismic frequency range) moduli calculation, dry moduli were first predicted using effective moduli theory for fractured media. Then, the saturated moduli were calculated through fluid substitution using the Gassmann (1951) equations for randomly distributed fractures. Since aligned fractures induce anisotropy, the effective saturated moduli were calculated using Brown and Korringa's (Brown and Korringa, 1975) low-frequency relationships.

The sequence for modeling fractures and fractures is:

1. Edit the well log values (especially shear logs);
2. Predict shear logs using P-velocity and density logs where the shear log is not reliable;

3. Model dry fractures using the Kuster-Toksöz method and undertake fluid substitution using Gassmann's equation for randomly oriented fractures;
4. Model dry fractures using Hudson's theory and fluid substitution using Brown-Korringa's low frequency relation for aligned fractures;
5. Calculate P- and S-velocities for the fractured media.

5.3.1 Predicting shear velocity from density and P-velocity

Before modeling the fractured media with values from well logs, it is necessary to investigate the quality of those logs. In Figure 5.3, poor S-wave data are evident in the shallow part of the well, the Davidson Evaporite, and the Prairie Evaporite Formations. The P-wave velocity and density logs are of reasonable quality. Utilizing the relationship proposed by Han and Batzle (2004), the S-wave modulus can be predicted from P-wave velocity and density. The coefficients in equation (5-1) were calculated using the data over the interval with reasonable shear log values (positive shear velocity values from depths 600m to 1378m):

$$\mu = 0.0 * M^2 + 0.2687 * M + 1.7864 \tag{5-1}$$

where, μ is the shear modulus and M is the P modulus ($M = \rho v_p^2$. ρ: density, g/cm^3; ν_p: P velocity, km/s.).

Figure 5.5 displays the cross-plot between actual shear velocity from the dipole sonic log and the predicted shear velocity from equation (5-1). A reasonable correlation can be seen (with a correlation coefficient of 0.99). Figure 5.6 also shows the predicted and actual shear velocity logs and their differences, which are mostly within ±200m/s.

All the shear velocities over the questionable intervals will be replaced by the values predicted by equation (5-1).

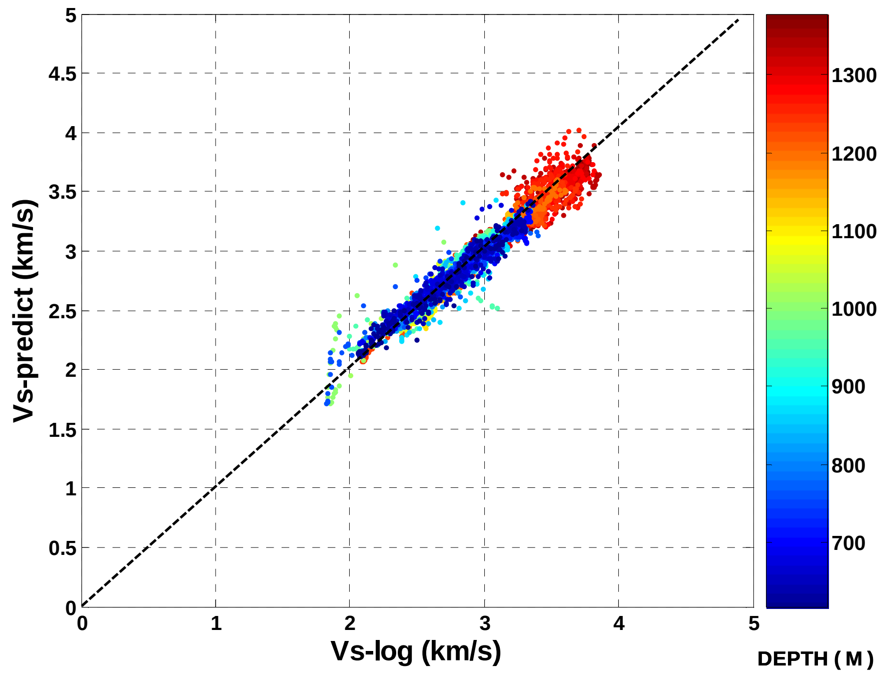

Figure 5.5 Comparison of predicted and actual *Vs* (using M from *Vp* and ρ) for Well A (over depths 600m-1378m with positive velocity values).

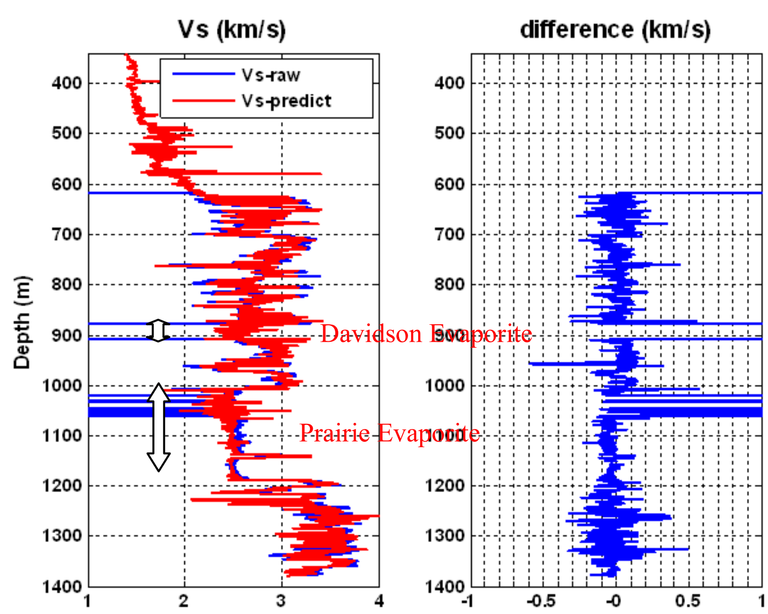

Figure 5.6 Predicted (red) and actual *Vs* (blue) and their difference for Well A.

5.3.2 Modeling randomly oriented fractures

We first used the Kuster-Toksöz theory (Kuster and Toksöz, 1974; Berryman, 1980) to calculate the effect of fractures on velocities. Some basic definitions of fractures are outlined in Appendix A. For fracture modeling, we assumed that the porosity introduced by fractures is 1%, the aspect ratio is 0.01, and the fractures are penny-shaped. Figure 5.7 displays the modeled logs of Well A using the Kuster-Toksöz model for randomly oriented brine saturated fractures. The density and P-velocity of brine are set to 1100 kg/m^3 and 1430 m/s respectively. The P-velocity drops about 0.7 km/s (12.5%), and the shear velocity decreases by 0.6 km/s (20%). For a 40m fractured interval, this amounts to about a 2 ms delay in P-wave reflection times and a 3.5 ms delay in PS reflection traveltime.

5.3.3 Modeling vertical aligned fractures

If the fractures are aligned with specific directions (see Figure 5.8), the elastic properties of the rock can be modeled by Hudson's (1981) theory, and the rock will display azimuthal anisotropy.

Figure 5.9 shows the modeled logs of Well A assuming vertically aligned fractures in the formations overlying the mining interval. The rock displays transverse isotropy with respect to the x direction, or azimuthal anisotropy in the x-y plane. The P-velocity along the vertical direction shows a small decrease, less than 0.2 km/s (3.5%), while the SV-velocity propagating vertically drops significantly, about 0.8 km/s (26%). For horizontally traveling waves, the P-velocity decreases by about 0.75 km/s (13.5%) and the SV-velocity decreases by the same amount as for the vertical propagation.

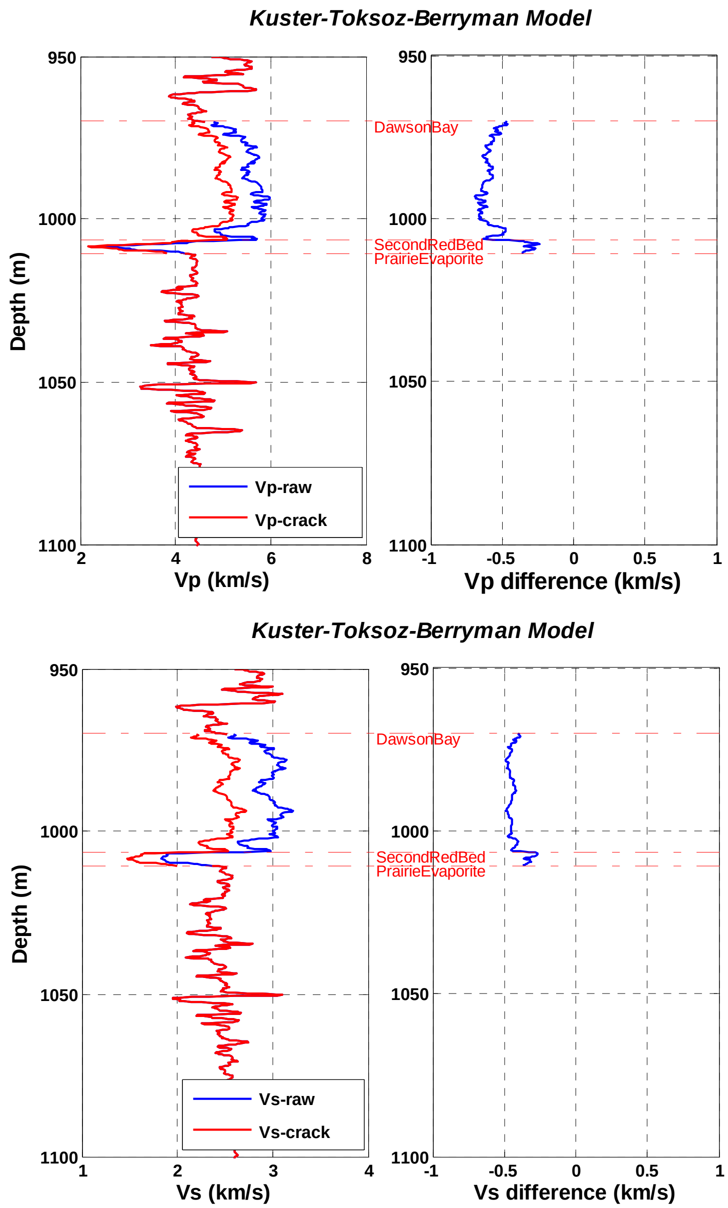

Figure 5.7 Velocity of fractured media from the Kuster-Toksöz model, and velocity difference between unfractured (blue curve) and fractured (red curve) rock for Well A. Top: P-wave velocity; bottom: shear-wave velocity.

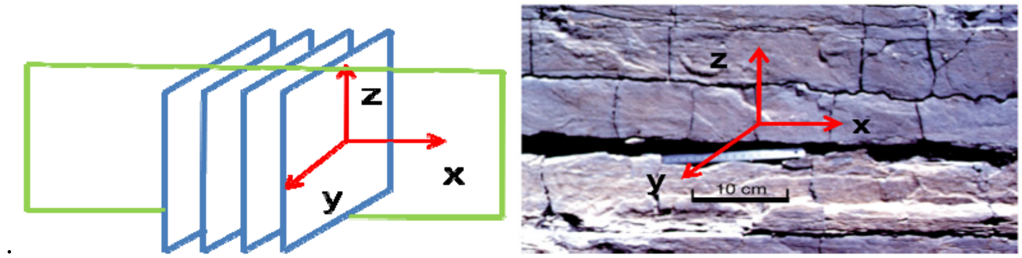

(a) (b)

Figure 5.8 Schematic diagrams of vertical fractures (a, shown in blue, velocities are modeled assuming waves travel in the green plane.), and vertically and horizontally aligned fractures (b:www.nature.com/.../n6771/images/403753aa.2.jpg)

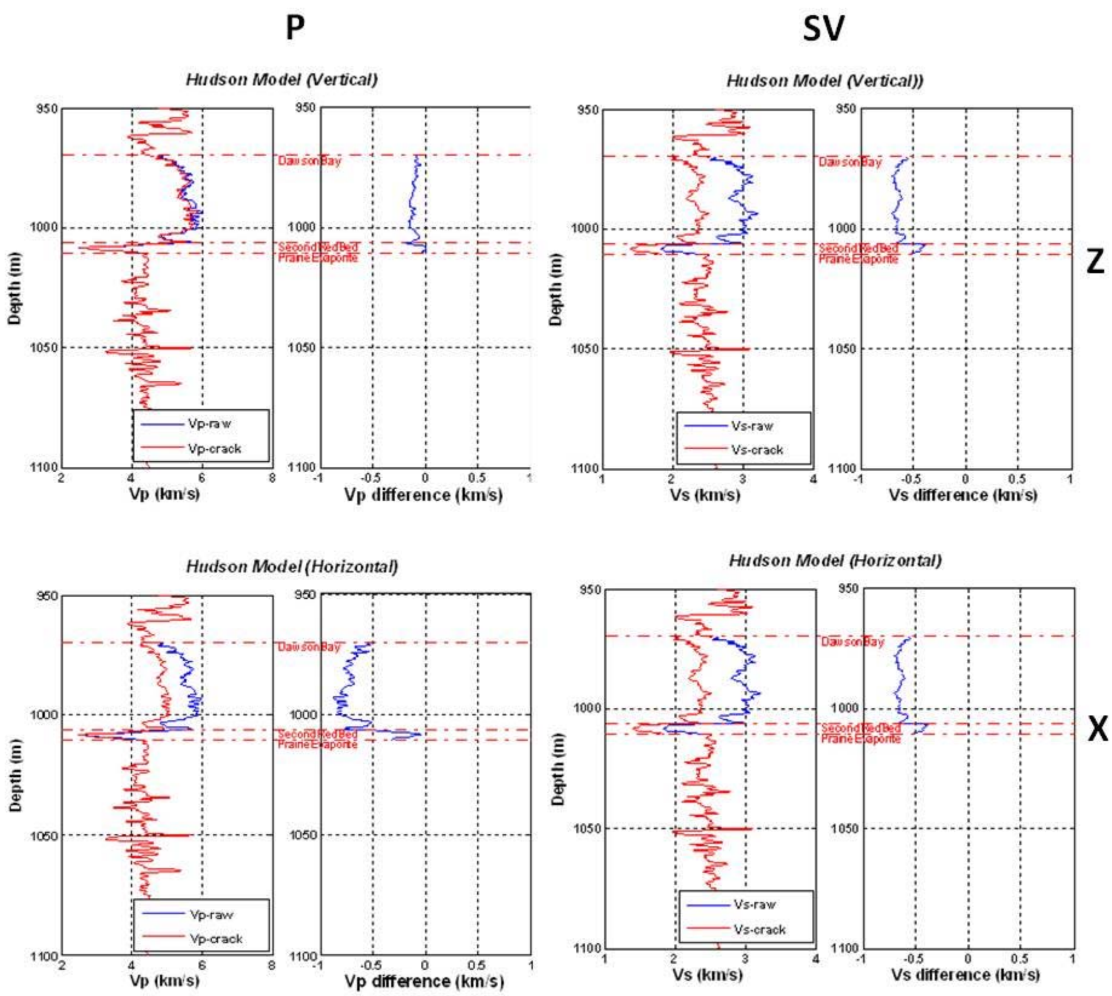

Figure 5.9 a: vertical propagation velocity of a vertically fractured medium from Hudson's model and the velocity difference between unfractured and fractured rock (Left: P wave; right: S-wave) for Well A. b: the same plots for horizontally propagating waves through a vertically fractured medium.

Figure 5.10 shows the velocity variation with angle from the symmetry axis (the x axis). The P-velocity will gradually drop at small incidence angles from 0° to 45°, and then increase for incidences from 45° to 90°. The SV-wave velocity reaches its minimum at 0 and 90° incidences, and peaks at a 45° incidence. The SH-wave velocity drops gradually from vertical to horizontal propagation.

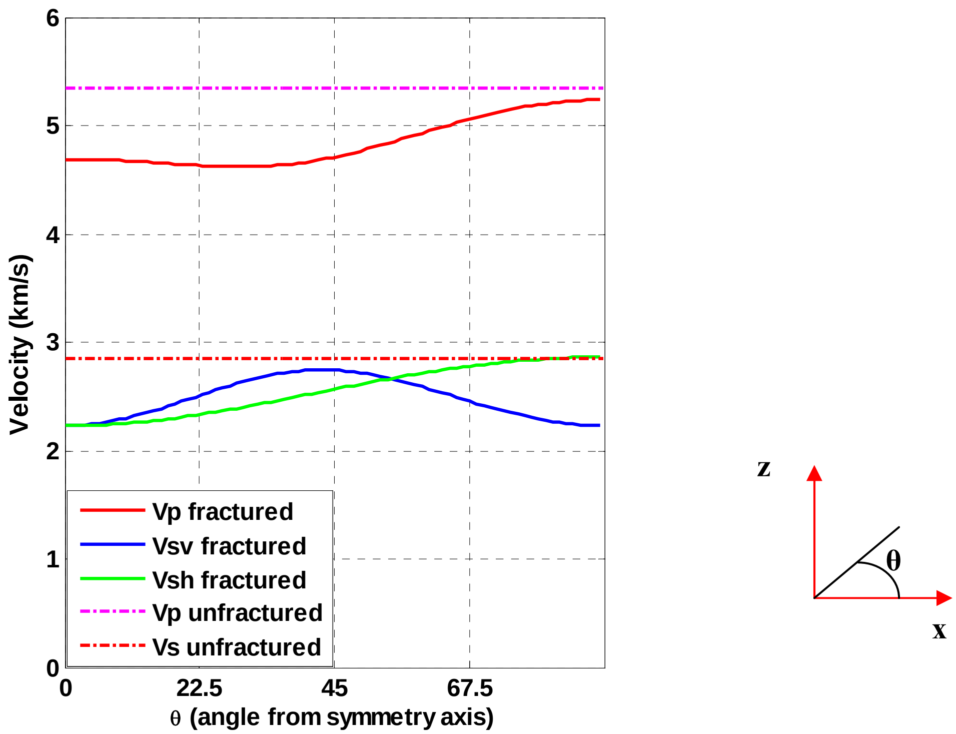

Figure 5.10 P- (red), SV- (blue) and SH- (green) velocity variation with angle (θ) from the symmetry axis (x-axis) for the fractured medium. The rock properties of unfractured media (velocities shown by the dashed line) are the average over the Dawson Bay Formation (including the Second Red Bed Shale) of Well A.

5.3.4 Modeling vertically and horizontally aligned fractures

There could be two sets of fractures in the rocks of the Dawson Bay Formation, one of which is aligned in the vertical direction and the other is in a horizontal direction (see Figure 5.8b). This orthogonal symmetry fracture system can be modeled with

Hudson's theory and will display azimuthal anisotropy. We assume the total porosity induced by these two set of fractures is still 1%, the aspect ratio is 0.01, and the fractures are penny-shaped.

Figure 5.11 shows the modeled P- and S-velocities for Well A. For vertically propagating P- and S-waves, the velocities will decrease significantly (Figure 5.11a). The velocity decrease is about 0.5km/s (about 10%) for the P wave, and 0.75km/s (25%) for the SV wave. The velocities for waves propagating horizontally in the XZ plane are similar to that of vertically travelling waves (Figure 5.11b). However, the horizontal traveling velocities in the YZ plane are quite different (Figure 5.11c). Both the P- and SV-velocities drop less than the previous two cases, 0.2km/s (3.5%) for the P-wave and 0.35km/s (11.5%) for the SV-wave. The velocity variations with incidence angle (from the z-axis) are shown in Figure 5.12. All the velocities show different variations with angle when traveling in the XZ and YZ planes. P- and SV-velocities drop more in the XZ plane than in YZ plane. The SH-velocity shows no anisotropy in the XZ plane, but anisotropy is apparent in the YZ plane.

Table 5.2 gives the values for the Dawson Bay Formation. The matrix values for modeling are the averages of the Dawson Bay Formation from Well A. Three cases of fractures were modeled: randomly oriented fractures, vertically aligned fractures, and vertically plus horizontally aligned fractures. Densities and velocities are calculated for both dry and water-saturated fractures (brine density 1100kg/m^3, P-velocity 1430m/s). There is generally a substantial decrease in P-wave and S-wave velocity with fracturing. In addition, the amount of this decrease can depend significantly on fracture orientation with respect to seismic wave propagation (azimuthal seismic anisotropy).

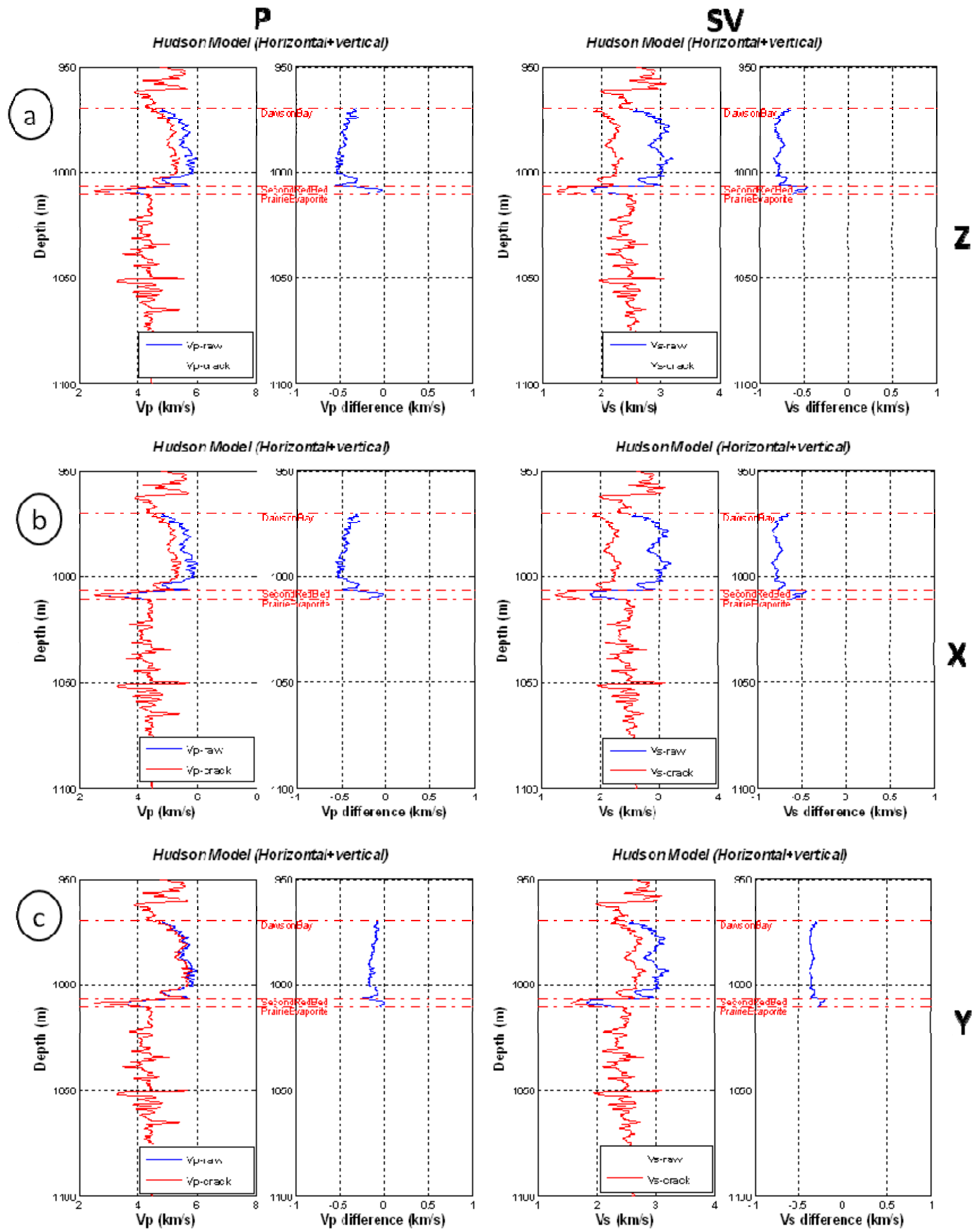

Figure 5.11 Modeled velocities and velocity difference between unfractured and fractured rock for vertically and horizontally aligned fractures (Left: P wave; right: SV wave) for Well A. a: vertically propagating waves; b: horizontally propagating waves in the XZ plane; c: horizontally propagating waves in the YZ plane.

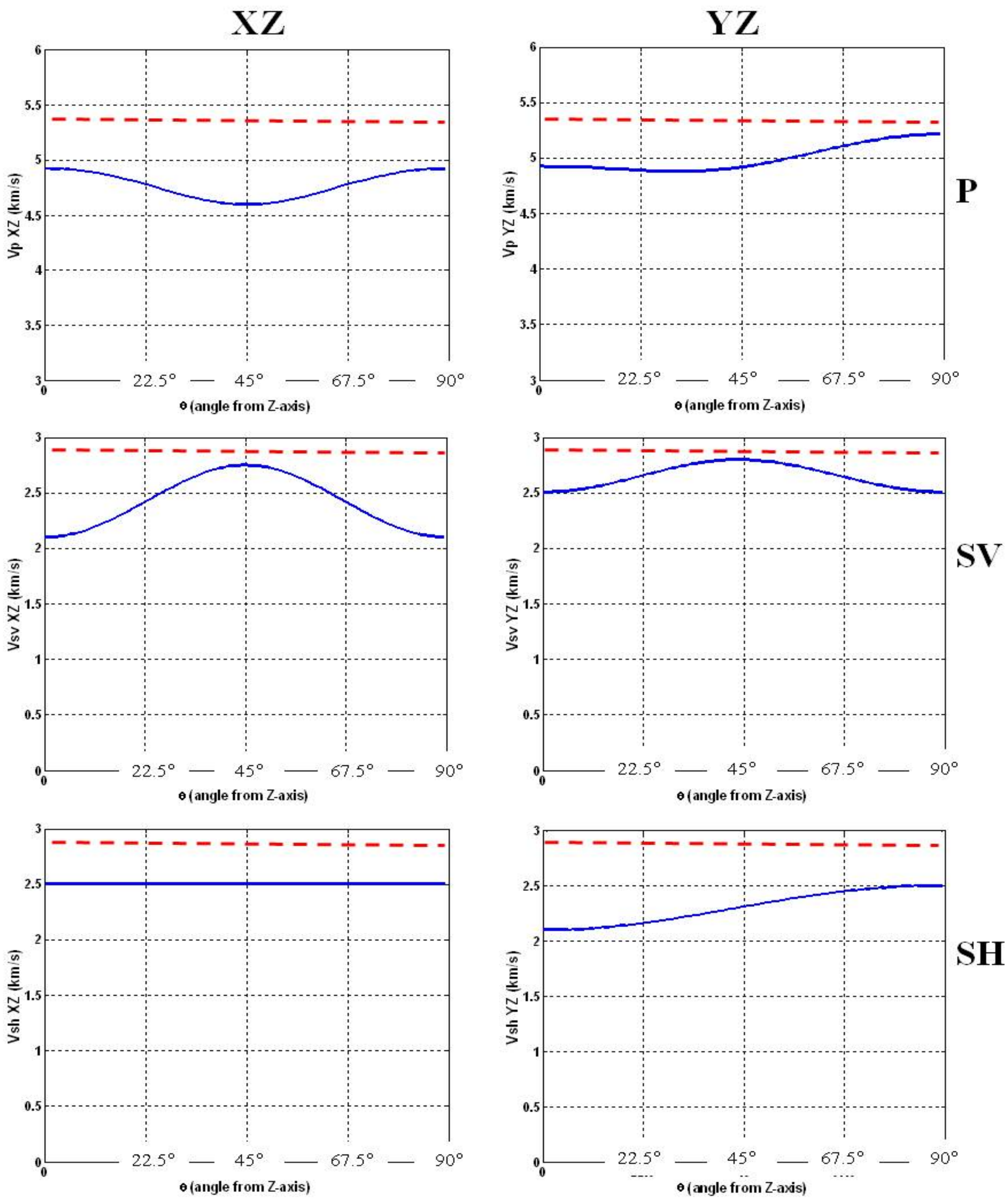

Figure 5.12 P- (top), SV- (middle) and SH- (bottom) velocity variation with angle from the z-axis for media with horizontally and vertically aligned fractures, the left side is for the wave propagating in the XZ plane and the right is for the wave propagating in YZ plane. The rock properties of unfractured media (velocities shown by red line in each plot) are the average over the Dawson Bay Formation (including the Second Red Bed Shale) of Well A. The Z-axis is in the vertical direction, and the X-axis is in the horizontal direction which is normal to vertical fractures.

Table 5.2 Rock properties for unfractured and fractured rocks. The values of the matrix for modeling are the averages over the Dawson Bay Formation in Well A. The density and P-velocity of brine are 1.1g/cm3, and 1430m/s. Vert: vertically propagating waves; Hxz: waves travelling horizontally in the XZ plane; Hyz: waves travelling horizontally in the YZ plane. Random: randomly oriented fractures; Vert.: vertically aligned fractures; Vert.+Hor.: vertically and horizontally aligned fractures.

<table>
<tr><th colspan="3" rowspan="2"></th><th rowspan="2">Matrix</th><th colspan="3">Dry fracture</th><th colspan="3">Water saturated fracture</th></tr>
<tr><th>Random</th><th>Vert.</th><th>Vert.+Hor.</th><th>Random</th><th>Vert.</th><th>Vert.+Hor.</th></tr>
<tr><td rowspan="7">Dawson Bay Formation (970.1-1006.5 m)</td><td colspan="2">Density</td><td>2683.4</td><td colspan="3">2656.6</td><td colspan="3">2667.6</td></tr>
<tr><td rowspan="3">Vp</td><td>Vert</td><td rowspan="3">5514.7</td><td rowspan="3">3980.9</td><td>-</td><td>3851.9</td><td rowspan="3">4926.2</td><td>5437.7</td><td>5069.3</td></tr>
<tr><td>Hxz</td><td>-</td><td>3851.9</td><td>5012.4</td><td>5069.3</td></tr>
<tr><td>Hyz</td><td>-</td><td>5073.9</td><td>-</td><td>5390.7</td></tr>
<tr><td rowspan="3">Vsv</td><td>Vert</td><td rowspan="3">2941.7</td><td rowspan="3">2499.4</td><td>-</td><td>2175.6 (XZ)
2595.6 (YZ)</td><td rowspan="3">2494.2</td><td>2301.1</td><td>2171.1 (XZ)
2590.2 (YZ)</td></tr>
<tr><td>Hxz</td><td>-</td><td>2175.6</td><td>2301.1</td><td>2171.1</td></tr>
<tr><td>Hyz</td><td>-</td><td>2595.6</td><td>-</td><td>2590.2</td></tr>
<tr><td rowspan="7">2nd Red Bed Shale (1006.5-1010.7 m)</td><td colspan="2">Density</td><td>2250.4</td><td colspan="3">2227.9</td><td colspan="3">2238.9</td></tr>
<tr><td rowspan="3">Vp</td><td>Vert</td><td rowspan="3">3609.1</td><td rowspan="3">2650</td><td>-</td><td>2538.2</td><td rowspan="3">3330.1</td><td>3545.2</td><td>3495.0</td></tr>
<tr><td>Hxz</td><td>-</td><td>2538.2</td><td>3125.7</td><td>3495.0</td></tr>
<tr><td>Hyz</td><td>-</td><td>3368.0</td><td>-</td><td>3585.4</td></tr>
<tr><td rowspan="3">Vsv</td><td>Vert</td><td rowspan="3">1984.8</td><td rowspan="3">1681.4</td><td>-</td><td>1460.9 (XZ)
1748.3 (YZ)</td><td rowspan="3">1677.3</td><td>1551.9</td><td>1457.3 (XZ)
1744.0 (YZ)</td></tr>
<tr><td>Hxz</td><td>-</td><td>1460.9</td><td>1551.9</td><td>1457.3</td></tr>
<tr><td>Hyz</td><td>-</td><td>1748.3</td><td>-</td><td>1744.0</td></tr>
</table>

The same work was also carried out for Well B. Figure 5.13 and Figure 5.14 show the modeled well logs of vertically aligned and vertically plus horizontally aligned fractures for Well B, which is located within the mining area. This modeling gives similar results as for Well A.

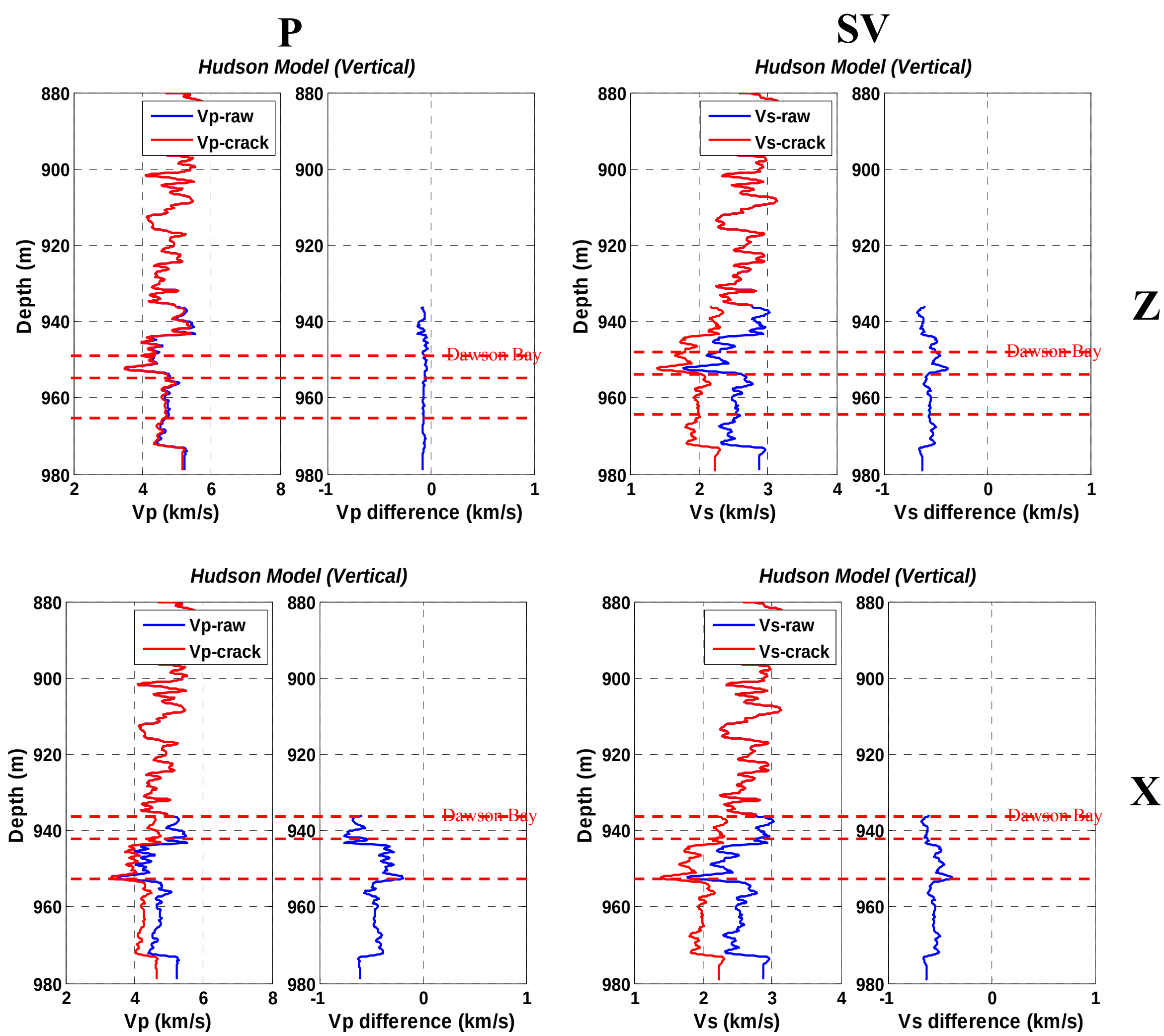

Figure 5.13 Top: vertical propagation velocity from Hudson's model and velocity differences between unfractured and vertically aligned fractures (Left: P wave; right: shear wave) for Well B. Bottom: the same plots for horizontally propagating waves.

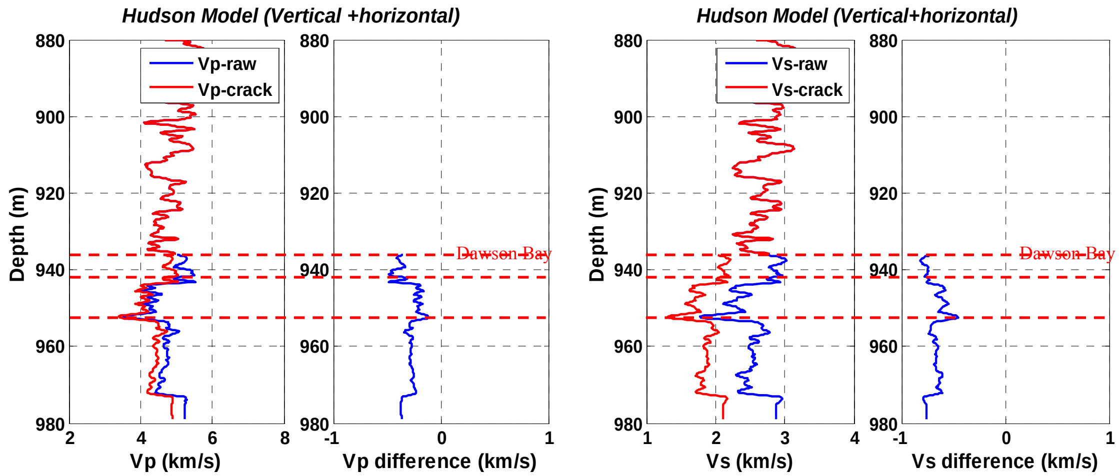

Figure 5.14 Vertical propagation velocity from Hudson's model and velocity differences between unfractured, and vertically and horizontally aligned fractured rocks (Left: P wave; right: shear wave) for Well B.

5.4 Synthetic seismograms for P- and converted waves

We now use these "fractured" (results from Hudson's model) and unfractured logs to generate synthetic seismograms. The purpose of this simulation is to investigate the change in the seismic response caused by the fractures. Figure 5.15 shows the Ricker wavelet used (based on the likely bandwidth of field seismic energy). Synthetic seismograms calculated from our modeled velocities and densities for vertically aligned fractures are illustrated.

The software used for synthetic seismogram generation is the SYNGRAM program from the CREWES Project. It assumes isotropic velocities, so vertical velocities from Hudson's model were used. Figure 5.16 through Figure 5.19 show the original well logs and their accompanying synthetic seismograms along side the "fractured" well logs and their synthetic seismic response.

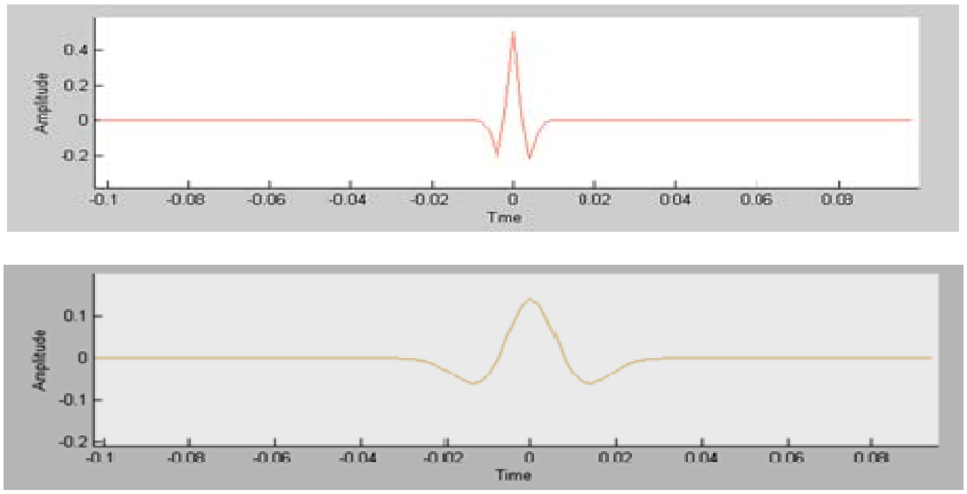

Figure 5.15 Ricker wavelet used for synthetic PP (left, dominant frequency 106Hz) and PS (right, 28.85Hz) seismograms.

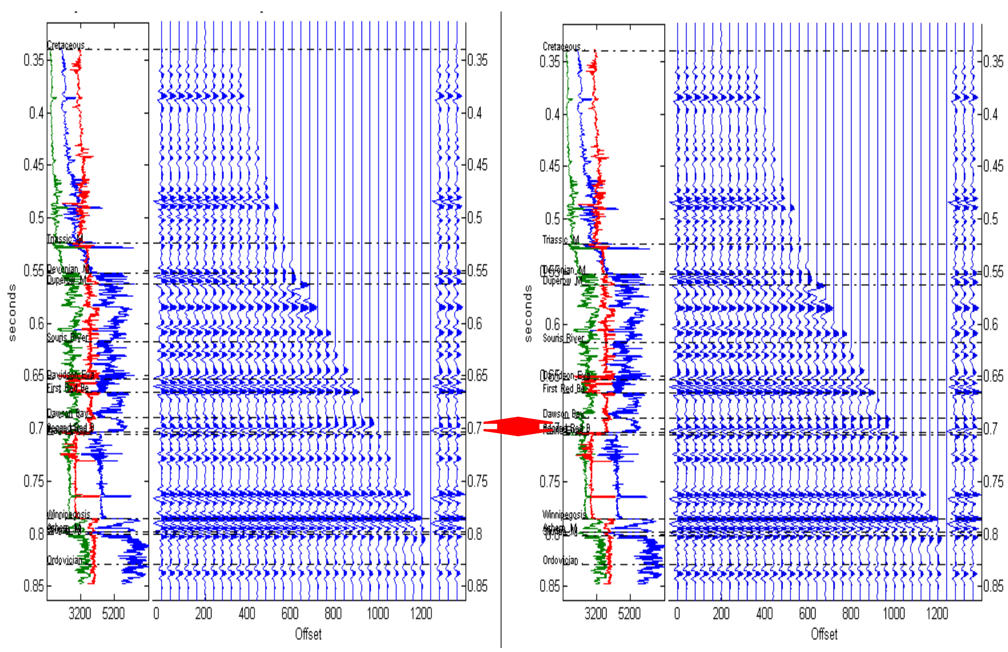

Figure 5.16 Well logs (P velocity in blue, S-velocity in green, and density in red) and PP synthetic seismogram (NMO removed gather and summed response, duplicated three times) for Well A. Left: unfractured rock; right: fractured rock. The red arrow marks the interval containing the fractures.

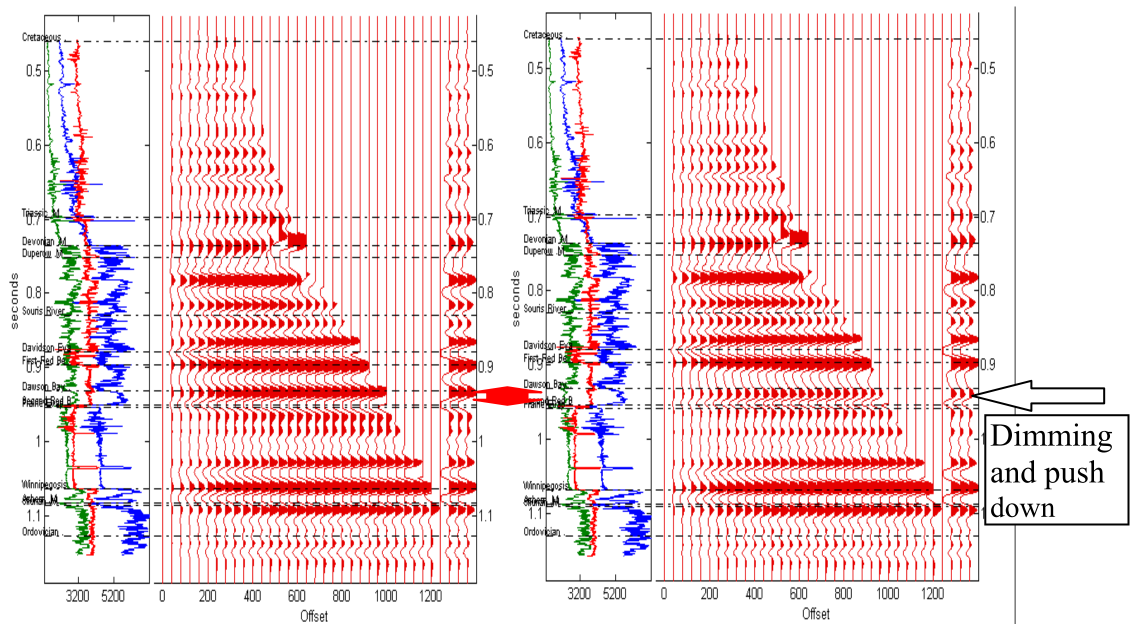

Figure 5.17 Well logs (P velocity in blue, S-velocity in green, and density in red) and PS synthetic seismogram (NMO removed gather and summed response, duplicated three times) for Well A. left: unfractured rock; right: fractured rock. The red arrow marks the interval containing the fractures.

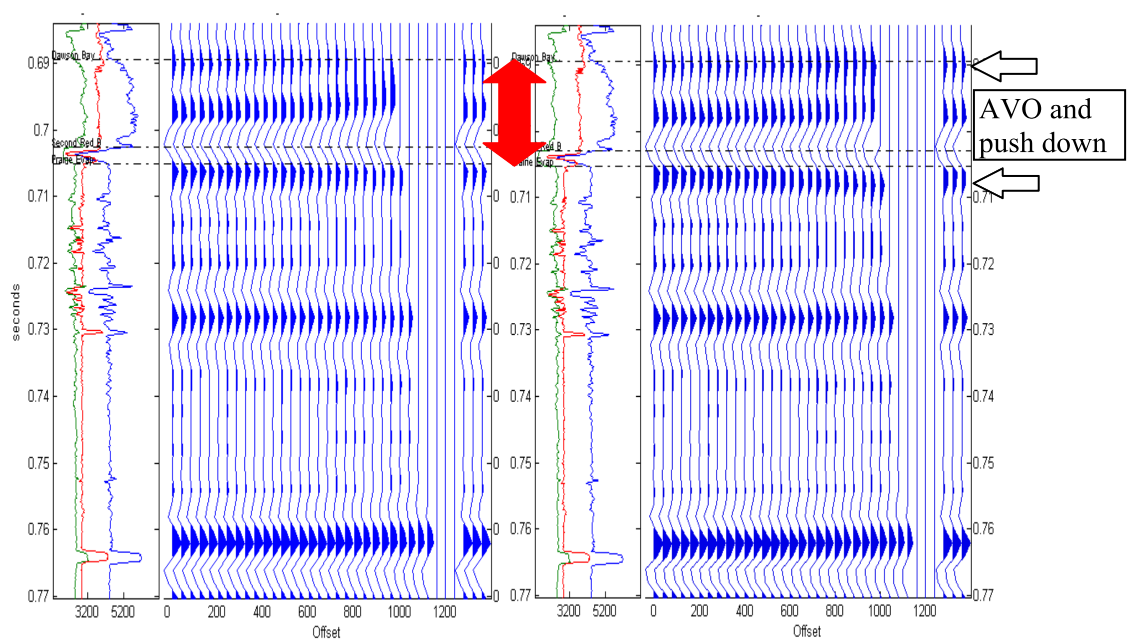

Figure 5.18 Well logs (P velocity in blue, S-velocity in green, and density in red) and PP synthetic seismogram (NMO removed gather and summed response, duplicated three times) focusing on The Dawson Bay Formation (including the Second Red Bed Shale) for Well A. left: unfractured rock; right: fractured rock. The red arrow marks the interval containing the fractures.

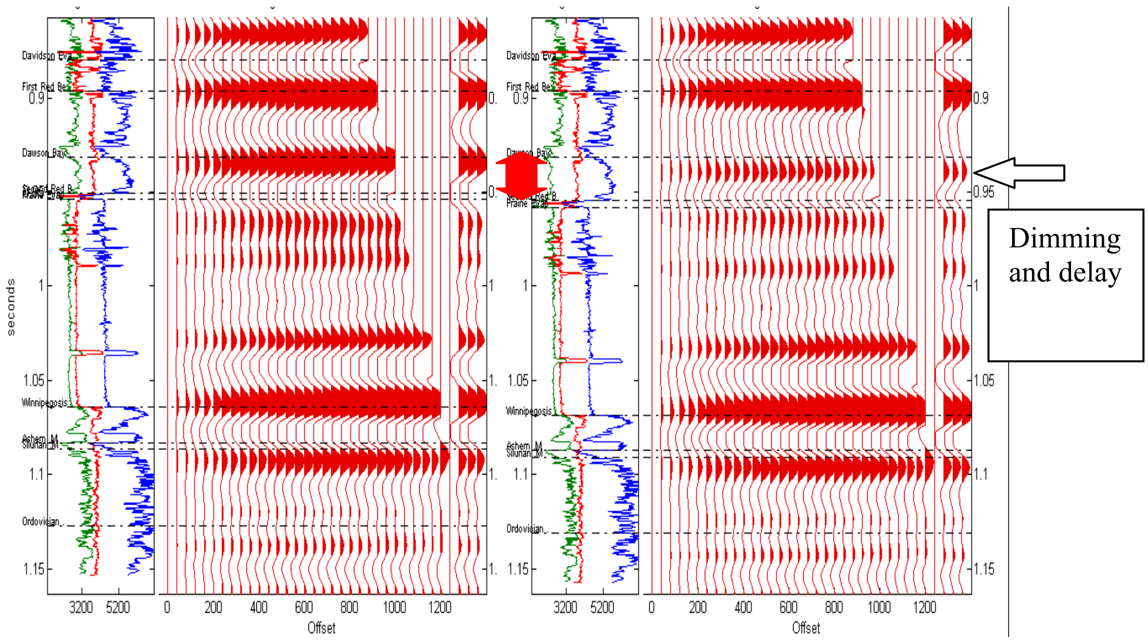

Figure 5.19 Well logs (P velocity in blue, S-velocity in green, and density in red) and PS synthetic seismogram (NMO removed gather and summed response, duplicated three times) focusing on The Dawson Bay Formation (including the Second Red Bed Shale) for Well A. left: unfractured rock; right: fractured rock. The red arrow marks the interval containing the fractures.

From the previous synthetic seismograms for Well A, we observe the following changes caused by fractures in the Dawson Bay Formation:

1) Some delay (time increase) in the PP reflection times and an amplitude versus offset (AVO) effect;
2) Delay and dimming (amplitude loss) in the PS wave;
3) The effects are much stronger on the PS data than PP data.

Small AVO effects on the PP seismogram (Figure 5.20) and reflection character changes in the PS response (Figure 5.21) over the fractured interval are observed in the synthetic seismograms for Well B. Assuming that the PS data have the same frequency content as the PP data, amplitude brightening and time delay can be found in the PS response (Figure 5.22). A strong PS character change is observed.

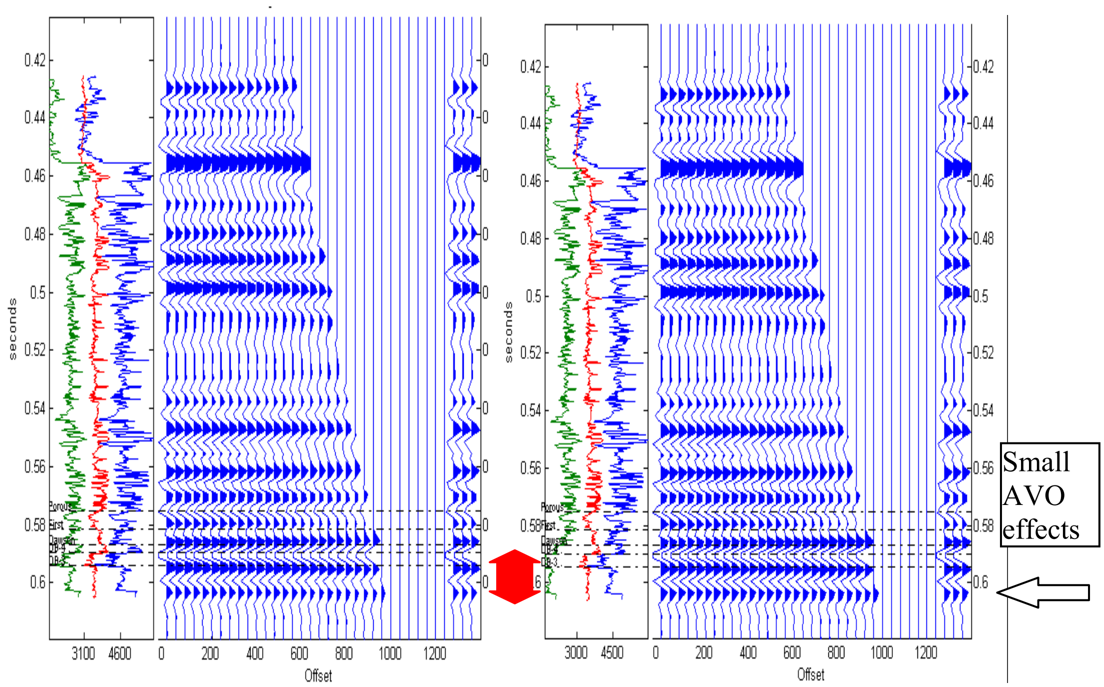

Figure 5.20 Well logs (P velocity in blue, S-velocity in green, and density in red) and PP synthetic seismogram (NMO removed gather and summed response, duplicated three times) for Well B. Left: unfractured rock; right: fractured rock. The red arrow marks the interval containing the fractures.

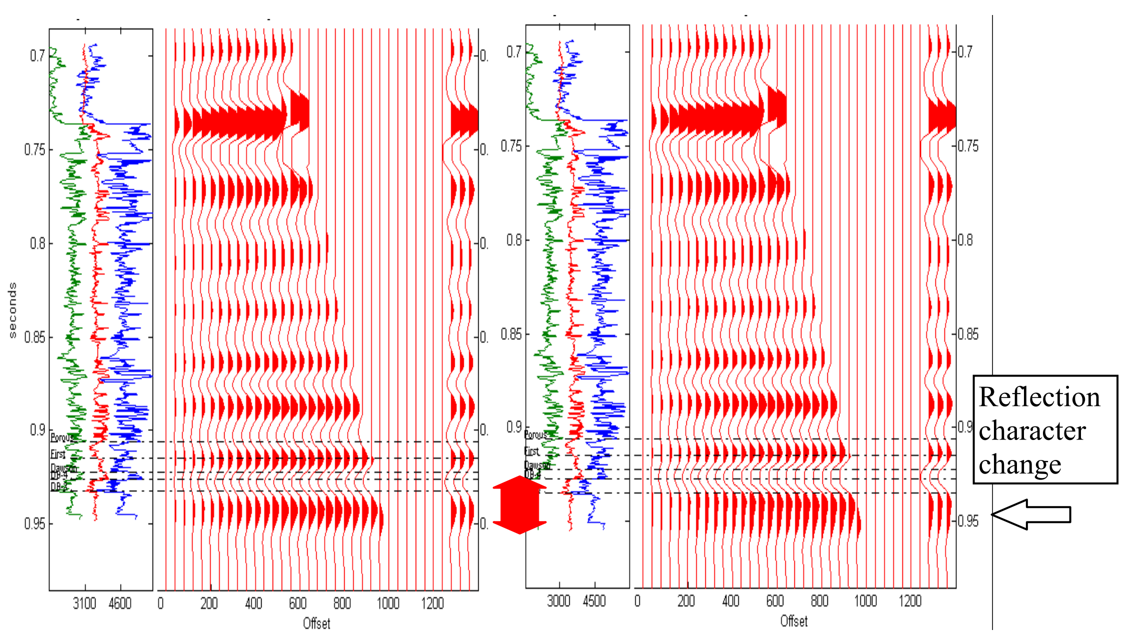

Figure 5.21 Well logs (P velocity in blue, S-velocity in green, and density in red) and PS synthetic seismogram (NMO removed gather and summed response, duplicated three times) for Well B. Left: unfractured rock; right: fractured rock. The red arrow marks the interval containing the fractures.

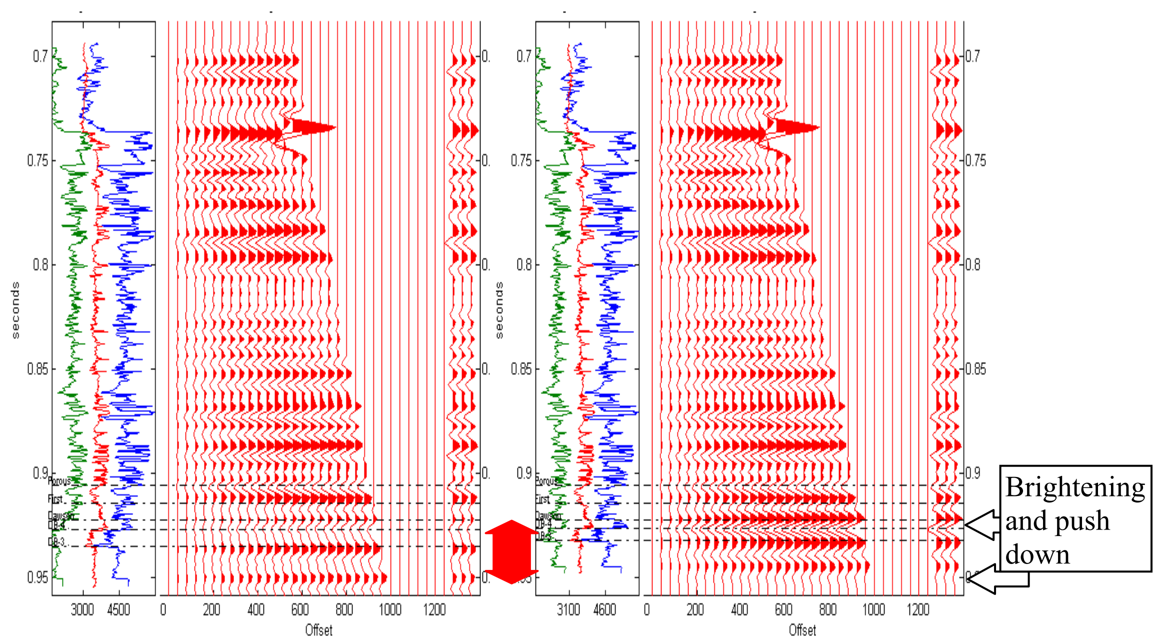

Figure 5.22 Well logs (P velocity in blue, S-velocity in green, and density in red) and PS synthetic seismogram using wavelet with PP frequency content (NMO removed gather and summed response, duplicated three times) for Well B. Left: unfractured rock; right: fractured rock. The red arrow marks the interval containing the fractures.

Because logs in Well A extend the deepest, we preliminarily tie them to the surface seismic data although the two data sources are many kilometres apart. Somewhat surprisingly, there is a reasonable tie between P-wave synthetic seismograms and the PP field seismic section (see Appendix F, Figure F.1). Then, we tie our PS synthetic seismograms to the field PS seismic data (see Appendix F, Figure F.2). Again, a reasonable correlation. We note that there is a strong Dawson Bay reflection in the PS seismic section. This bodes well for measuring changes in it. Finally, we correlate the PP and PS sections (see Appendix F, Figure F.3).

We note that there may also be attenuation changes due to fractures and fluid saturation that would also affect the seismic response.

5.5 Time-lapse 3D surface seismic interpretation

To assess the brine inflow problem, seven 3D seismic surveys including five 3C surveys were shot from 2003 to 2008 in the mining area. In 2009, two 3C-3D surveys, which were acquired in 2004 and 2008, were processed to monitor and characterize the brine inflow. Figure 5.23 shows the location of the processed time-lapse (2004 and 2008) 3C-3D surveys in the mining area. The "trap door" outlined by red line is the main interpreted brine inflow area. The size of the survey is about 6.5 km^2. The processing workflow is shown in Figure 5.24 (Sensor Geophysical).

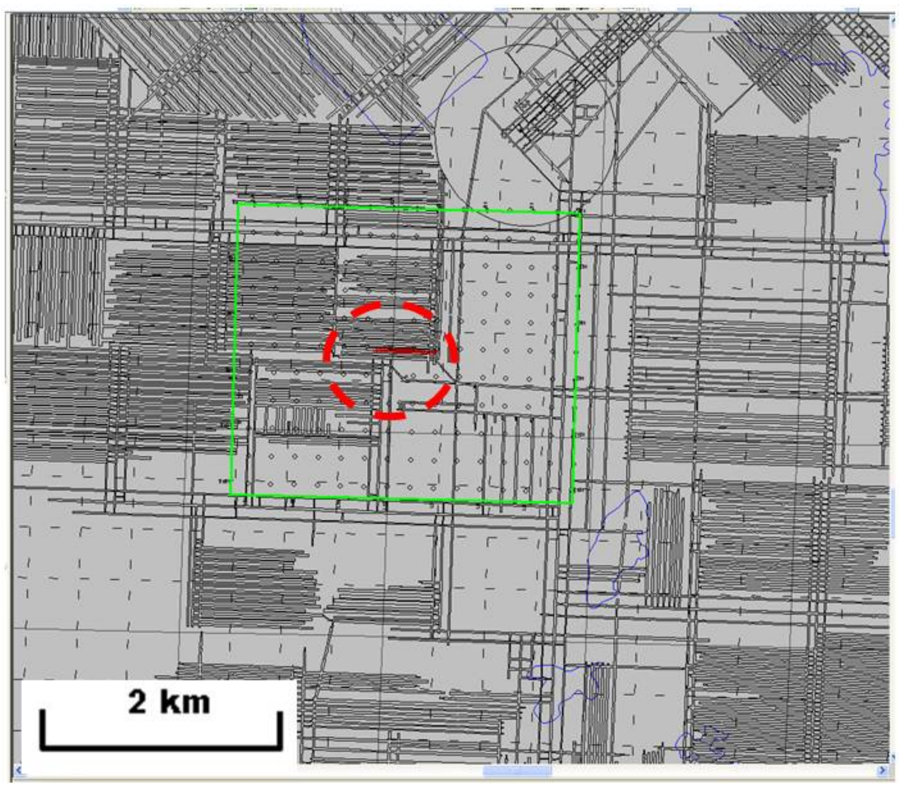

Figure 5.23 The time-lapse 3C-3D survey location within the mining site (shown in the green box), the grey lines are the mining plan (rooms). The red circle outlines the trap door area (where push-downs interpreted from seismic reflections around the mining level were caused by brine inflow) interpreted from previous work (from John Boyd, personal communication, 2009).

```
C01                    *** Field Recording History ***
C02 Area: Brine 3C/3D 2008, Sask. T 19  R 32  W 1 M    Mosaic Company
C03 Recorded by: Conquest, Party 102,  October, 2008
C04 Amplifier:ARAM Aries, 1390 chan, IBM SEG-Y, 3-328 Hz,Notch OUT
C05 Record Length: 3.0 s  Sample Interval: 1 ms
C06 Source: Dyn, single hole, 0.5 Kg at 9 m, N-S 125 m lines, 30 m source int
C07 Sensors: ION SM-7, single 3-comp, 0 degrees, E-W 180 m lines, 25 m int
C08 Typical Patch: 14 lines x 110 stations, 2340 m x 2725 m
C09 RADIAL LAYER STRIPPED FILTERED MIGRATED STACK
C10                    *** Processing History ***
C11 Processed by: Sensor Geophysical Ltd., July, 2009
C12 Reformat: Record length 3.0 s, Sample interval 1.0 ms
C13 Geometry Assignment, Asymptotic 3D Binning, CDP Bin size 12.5 m x 15 m
C14 H1/H2 to Radial/Transverse Rotation: 7 degrees, Trace edits, 60 Hz removal
C15 Amplitude Recovery: Spherical divergence correction, Additional gain 4 dB/s
C16 Surface-Consistent Deconvolution
C17    Resolved: Source, Receiver, Offset  Applied:  Source, Receiver
C18    Operator Type Spiking, Operator length 100 ms, Prewhitening 0.01%
C19    Design window 120-2300 ms at 0 m, 1000-2500 ms at 2170 m offset
C20 Time-Variant Spectral Whitening: 2/6-80/100 Hz, 7 panels, 500 ms operator
C21 Lateral Receiver Statics, Refraction Statics: Datum elev 620m, Repl vel 2000
C22 Surface Consistent Statics: Max shift 24 ms,400-2200 ms, CDP Trim Statics
C23 Anisotropic Normal Moveout Correction: eta 0.1
C24 Front-End Muting: Mute time (ms) 0 400 2300  Offset (m) 300 375 2125
C25 Limited Azimuth Stacks: 10-360(10) degrees, AGC
C26 PS1/PS2 Analysis: 500-900, 900-1250, 1500-1900 ms
C27 RAD/TRS to RAD 3 Layers Stripped Rotation
C28 3D CCP Stack: Effective Vp/Vs = 60% Vertical Vp/Vs, bulk shift 0 ms
C29 Time-Variant Spectral Whitening: 2/6-60/80 Hz, 6 panels, 500 ms operator
C30 Trace Equalization: Mean window 400-3000 ms
C31 F-XY Filtering, 5x5 point operator, 100 ms window, 50 ms taper
C32 Diffusion Filter
C33 Migration: Implicit FD Time, Aperture 65 degrees, 95% smoothed stacking vels
C34 Bandpass Filter, Zero-phase Ormsby, 5/10-30/40 Hz
C35 Time Variant Scaling: mean, centre-to-centre, multiple gates
C36
C37 Grid Bin Center (Inline   1, Crossline   1) = (299448.0, 5615084.0)
C38 Grid Bin Center (Inline   1, Crossline 157) = (299388.4, 5612745.0)
C39 Grid Bin Center (Inline 2
```

CDP Bin size: 12.5m X 15m

Figure 5.24 Processing workflow used for the time-lapse 3C-3D seismic data (from Sensor Geophysical Ltd.).

5.5.1 Well-seismic correlation, and PP and PS data registration

We first proceed to correlate the wells to the 3C-3D seismic data before interpreting the seismic data. Figure 5.25 displays the correlation between the synthetic PP seismogram of well GROUT 59-1 and the migrated PP data of the 2004 survey. The P-wave synthetic seismogram ties fairly well with the PP field seismic section. Then, the PS synthetic seismogram is tied to the field PS seismic data (Figure 5.26). Again, a reasonable correlation is found. Then the PP and PS sections (Figure 5.27 and Figure 5.28) are registered for both 2004 and 2008 surveys. The difference between the frequency bandwidth of the PP data and the PS data is significant. The effective frequency of the P waves is up to 120Hz, while it is only about 60Hz with the PS events. The reflections of the interfaces of porous zone, the Dawson Bay Formation, and the Prairie Evaporite Formation within the target zone can all be recognized (Figure 5.25, Figure 5.26, and Figure F.8 in Appendix F). However, due to the frequency difference, they are not easily picked on radial data individually. Therefore, to pick the PP and PS horizons at exactly the same depth is particularly difficult. However, the structure from PP and PS data can still represent relative features despite of the picking errors.

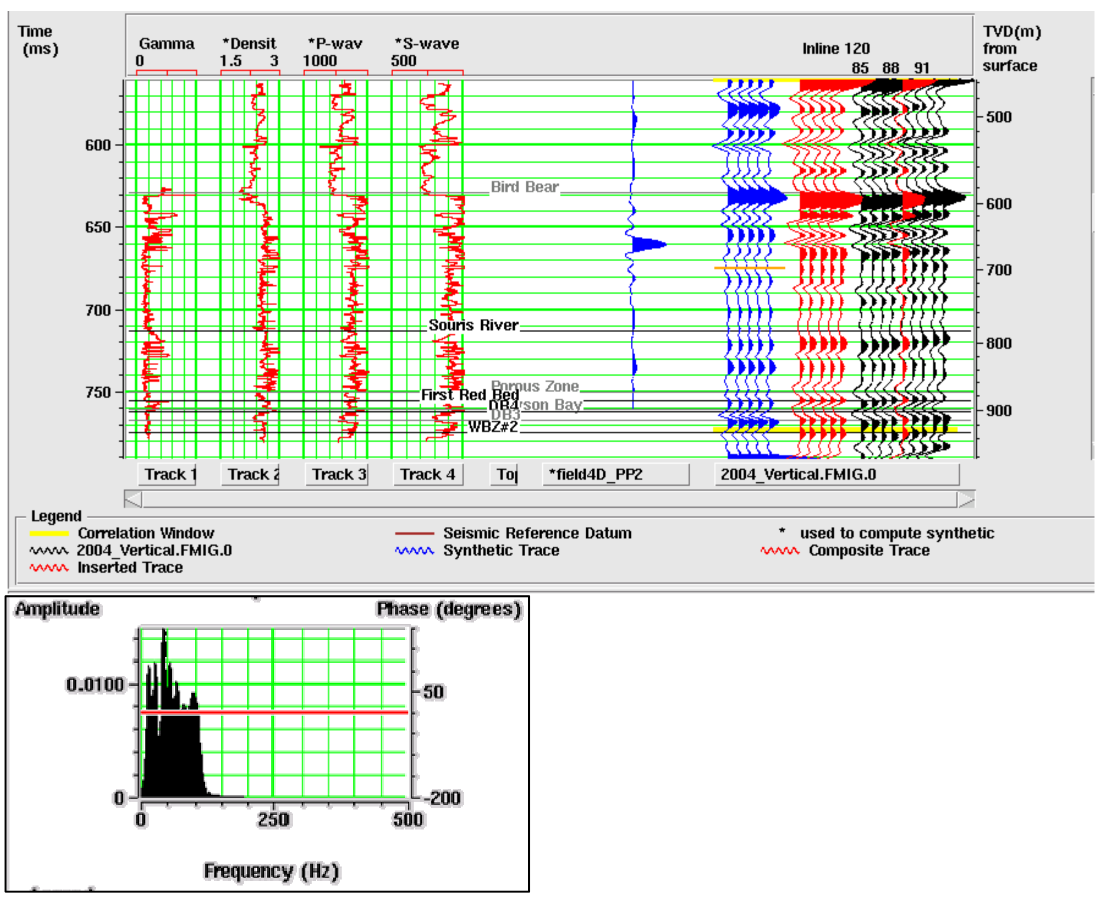

Figure 5.25 Correlation between the synthetic PP seismogram of well GROUT 59-1 and migrated PP data of 2004 survey. The synthetic seismogram is displayed in blue and repeated for 5 times, the seismic traces adjacent to the well are displayed in black. The corresponding frequency spectrum is shown at the bottom.

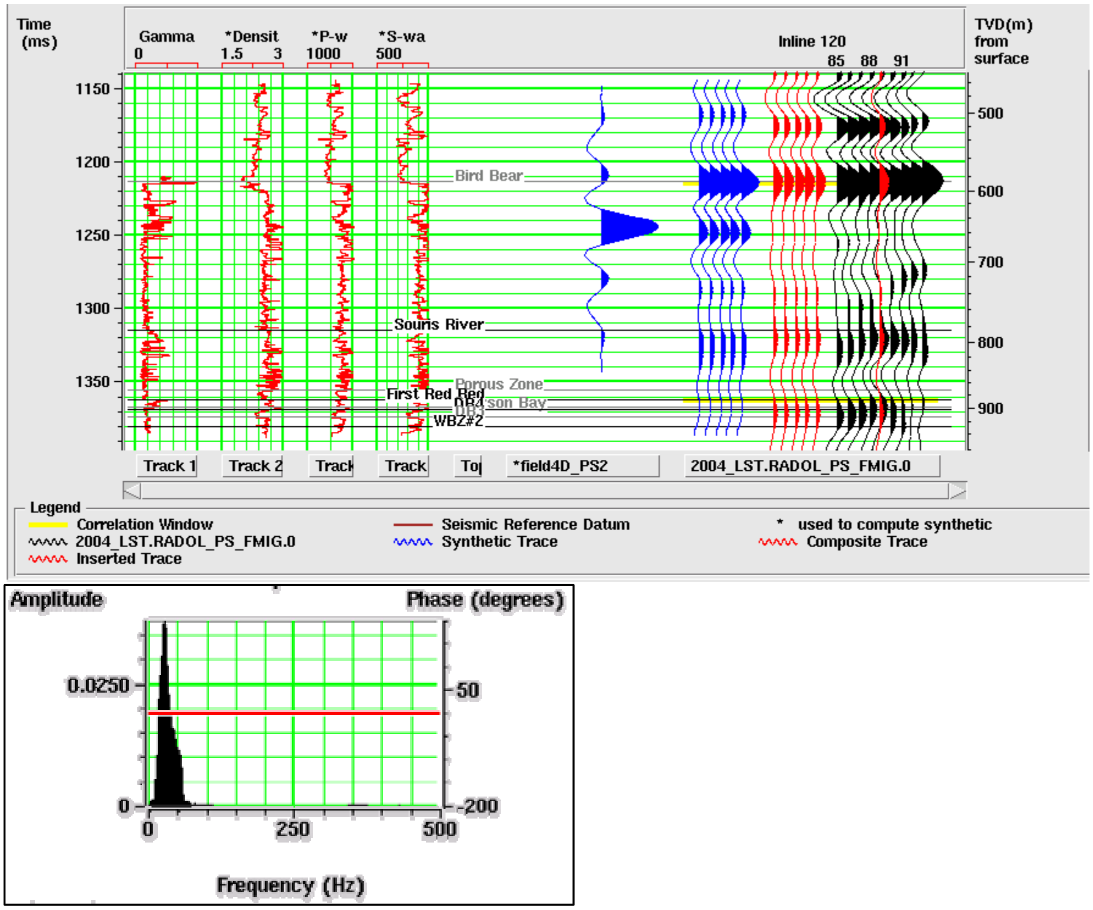

Figure 5.26 Correlation between the synthetic PS seismogram of well GROUT 59-1 and migrated PS data of 2004 survey. The synthetic seismogram is displayed in blue and repeated for 5 times, the seismic traces adjacent to the well are displayed in black. The corresponding frequency spectrum is shown at the bottom.

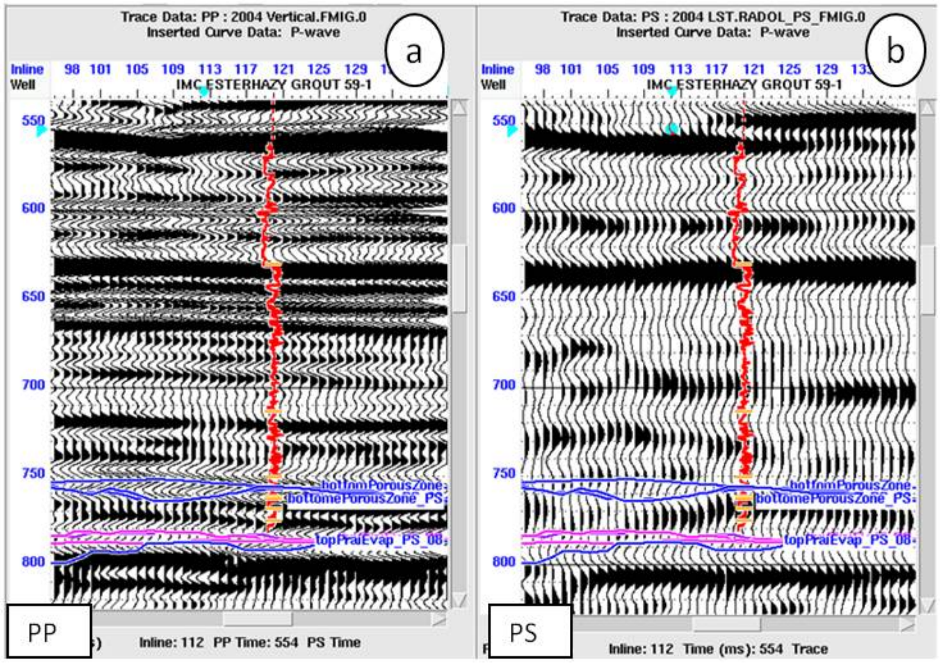

Figure 5.27 Registration of the PP data and PS data of the 2004 survey, both data are in PP time. The picked horizon at about 750ms is the base of the porous zone, and the horizon at about 800ms is approximated the top of Prairie Evaporite Formation. The horizontal bars on the well log curve are the geological markers.

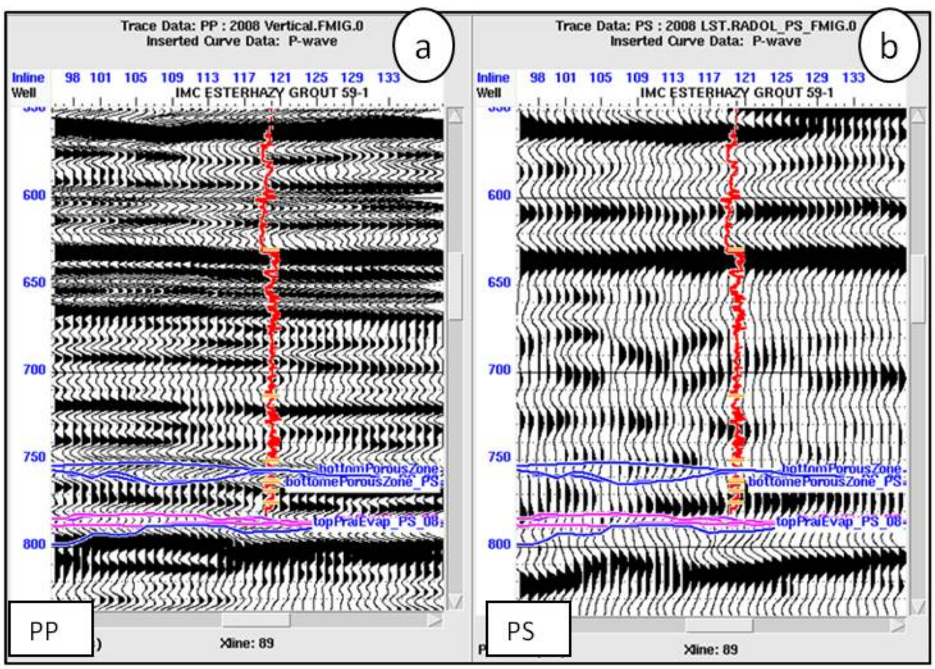

Figure 5.28 Registration of PP data (a) and PS data (b) of the 2008 survey, both data are in PP time. The picked horizon at about 750ms is the base of the porous zone, and the horizon at about 800ms is approximately the top of Prairie Evaporite Formation. The horizontal bars on the well log curve are the geological markers.

5.5.2 Time-lapse interpretation

Figure 5.29 and Figure 5.30 display the PP data and the PS data of a west-east line (line number 76) from the two 3D surveys. There are visible changes such as time shift and amplitude difference on both PP and PS data, especially within the red ellipse in the figures. Both components show apparent push-down effects due to velocity drops between the 2004 and 2008 surveys. Amplitude dimming can be seen at the Dawson Bay Formation in the 2008 PS data compared with the 2004 survey. Difference data between the 2004 and 2008 survey were also calculated after applying a match filter derived in the 420-620 ms widow for PP data, and 600-1250 ms for PS data. The difference is relatively small for PP data. Based on the rock physics modeling result, the reason should be a small P velocity change when fractures exist in the formation. However, in the trap door area some difference can still be found. On the PS data, an apparent difference can be seen below the Dawson Bay Formation (the bottom is approximately the green horizon on the seismic line). All these features are consistent with the modeling results: when fractures exist in the formation, a significantly greater decrease of S-wave velocity will be observed. Figure 5.31 also displays the RMS amplitude difference between the two surveys for the Dawson Bay Formation. There were two main areas where fractures might exist in the Dawson Bay Formation, one is outlined by blue circles and the other is shown in red circles. The area of change (red circle) is also observed on the vertical and PS data in Figure 5.29 and Figure 5.30, respectively. An evident push-down effect can be seen in this region.

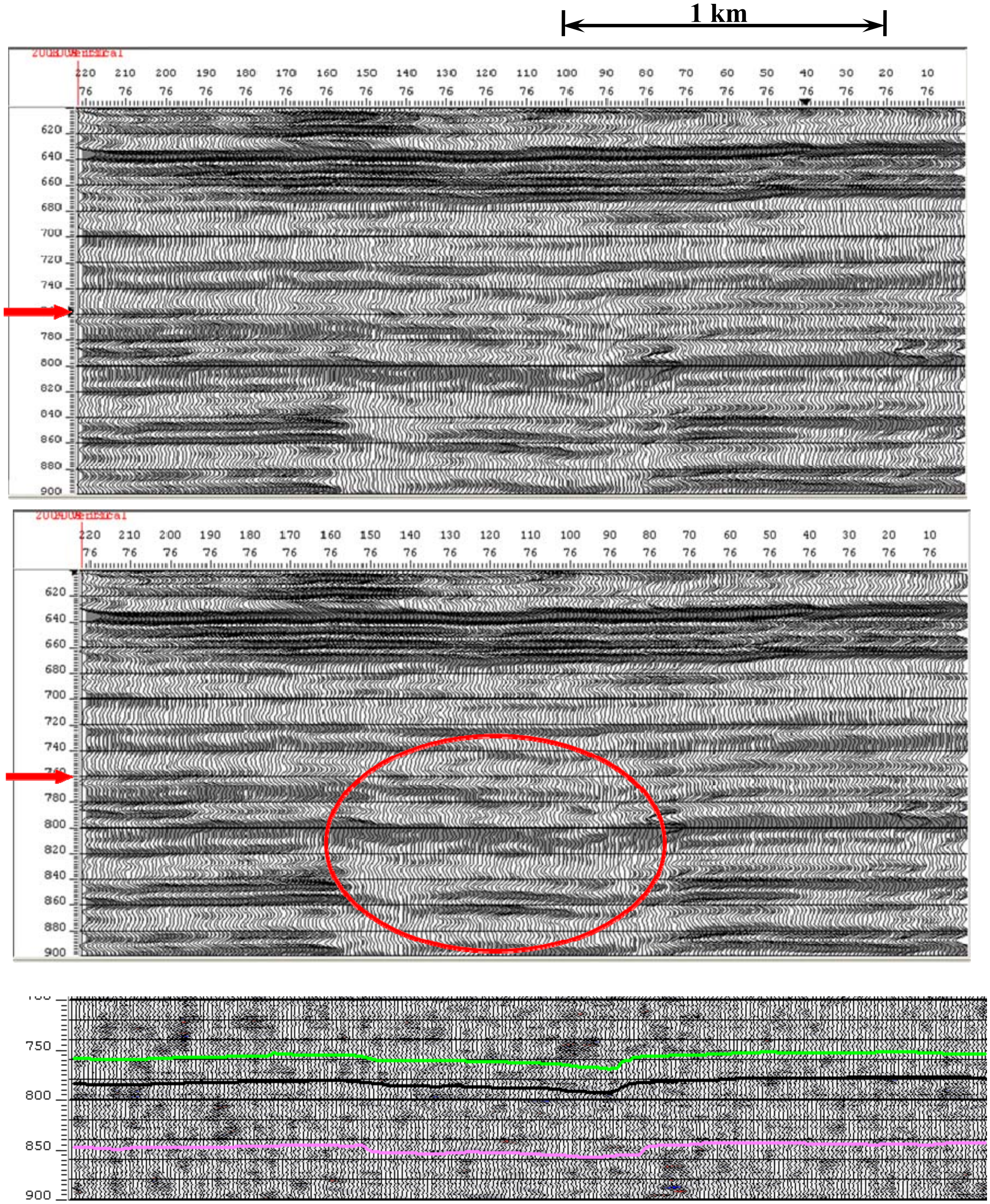

Figure 5.29 PP data of a west-east line (line number 76). Top: 2004 survey; middle: 2008 survey; bottom: difference between the two data sets. The red arrows mark the location of the top of the Dawson Bay Formation. The red ellipse denotes the trap door area.

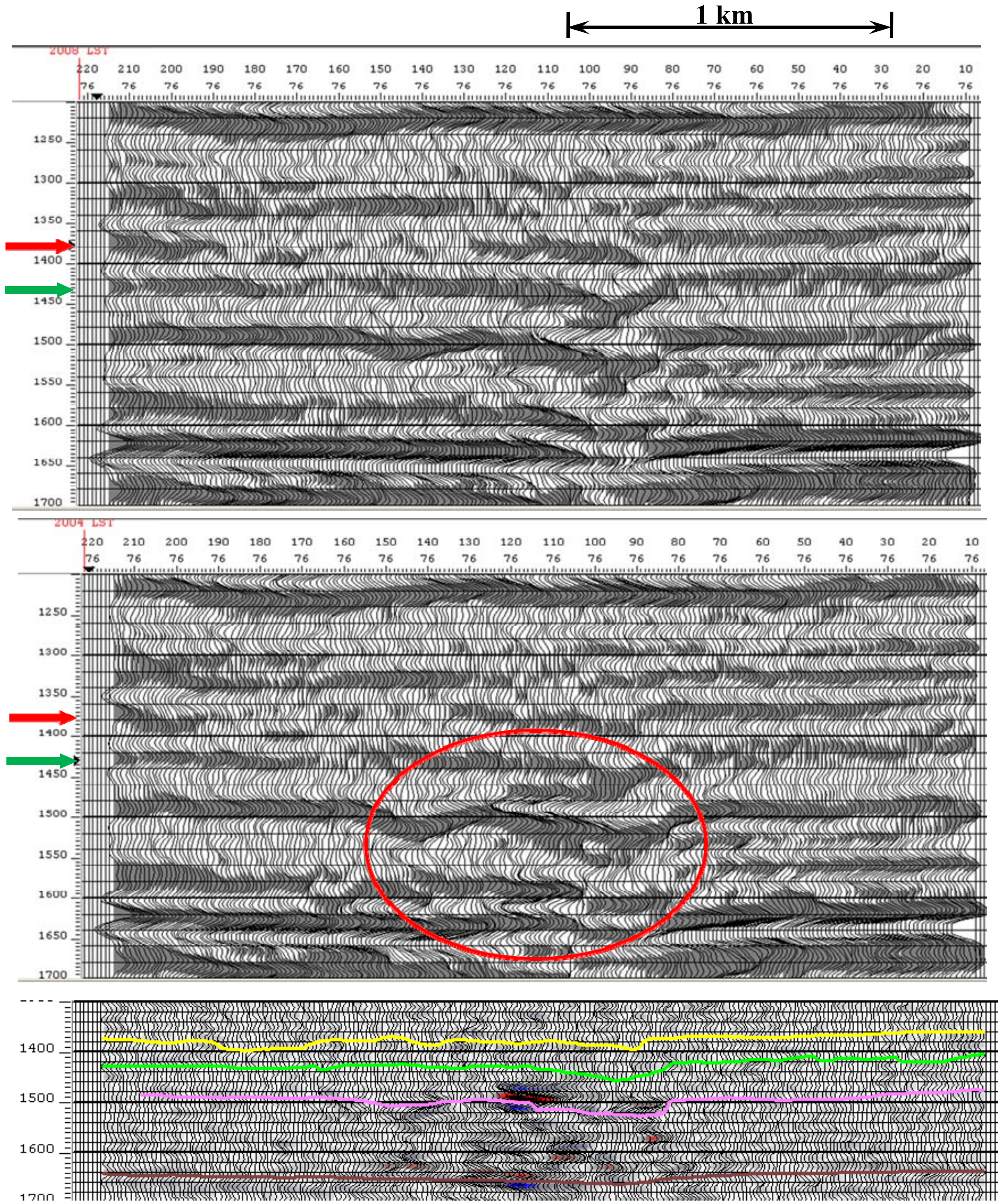

Figure 5.30 PS data of a west-east line (line number 76). Top: 2004 survey; middle: 2008 survey; bottom: difference between the two data sets. The red arrows mark the location of the top of the Dawson Bay Formation. The green arrows are the mining zone. The trap door area is outlined by red ellipse.

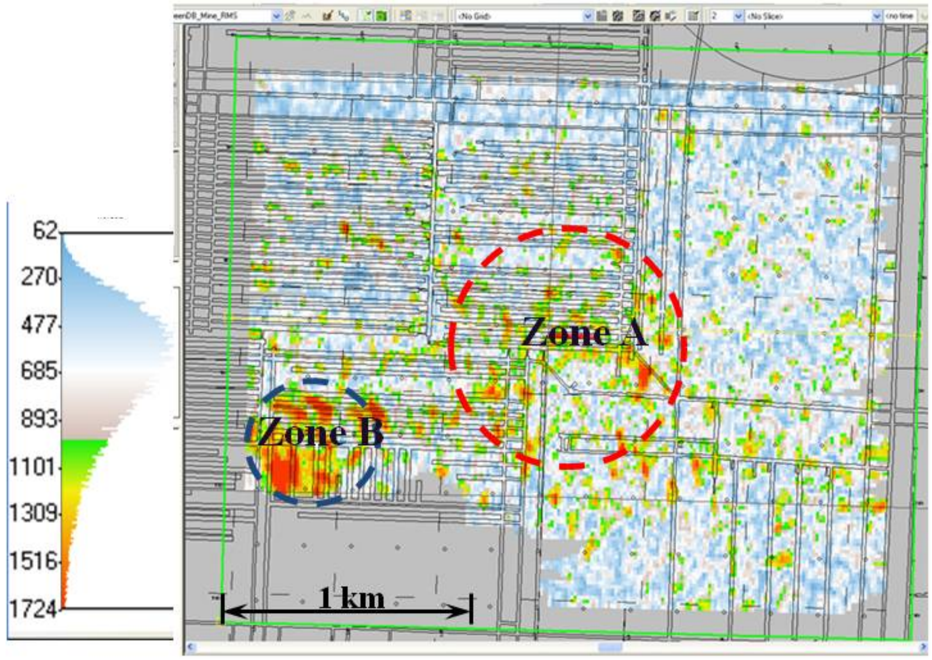

Figure 5.31 RMS amplitude difference of PS data from the Dawson Bay Formation to mine level between 2004 and 2008 survey.

To investigate the time shift caused by the changes in the Dawson Bay Formation, the top and the bottom of the Dawson Bay Formation were picked to see the time structure changes between the 2004 and 2008 surveys. Due to the low frequency of the PS data, however, the base of the Dawson Bay Formation, which is also the top of the Prairie Evaporite Formation, was difficult to pick. Therefore, on the PS data, the mine level will be picked. Figure 5.32 and Figure 5.33 show the time structure on the top of the Dawson Bay Formation. The difference on PP data is fairly small. A visible difference can also be seen on the PS data, pull-up effect appears at the top of the Dawson Bay Formation in the 2008 survey compared with the 2004 survey. Since the difference between the two surveys of the Birdbear Formation is fairly small (refer to Appendix F, Figure F.4 and Figure F.5), it indicates that some changes happened in the formations between Birdbear Formation and the Dawson Bay Formation.

At the bottom of the Dawson Bay Formation, the time structure of the PP data shows mostly of a push-down on the 2008 data (Figure 5.34). However, the time-shift is only up to about 2ms. On the PS data, a significant time-shift (push-down) can be seen at the mining level (Figure 5.35). The time shift can exceed 10ms. The modeling of fractures in the Dawson Bay Formation indicates that the P velocity will decrease less than the S-velocity, so the time-shift of PS data caused by fractures should be much larger than that of the PP data. Considering the time-shift values of the PP and PS data, the rocks between the top of Prairie Evaporite Formation and mine level should also be fractured.

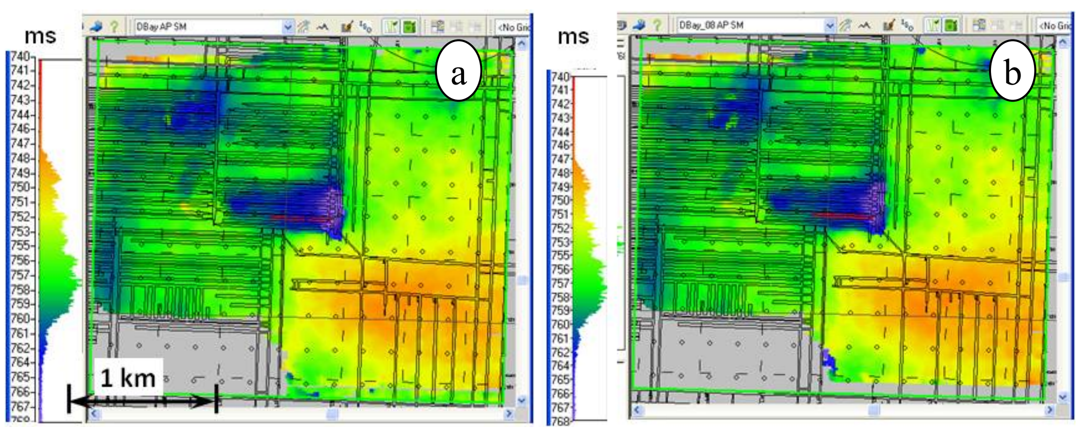

Figure 5.32 Time structure of the top of the Dawson Bay Formation on the PP data. a: 2004 survey; b: 2008 survey.

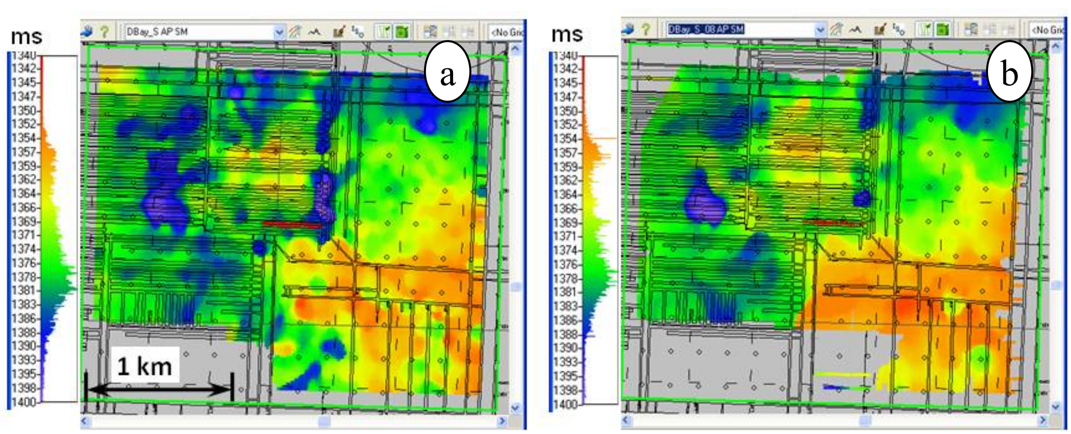

Figure 5.33 Time structure of the top of the Dawson Bay Formation on the PS data, a: 2004 survey; b: 2008 survey.

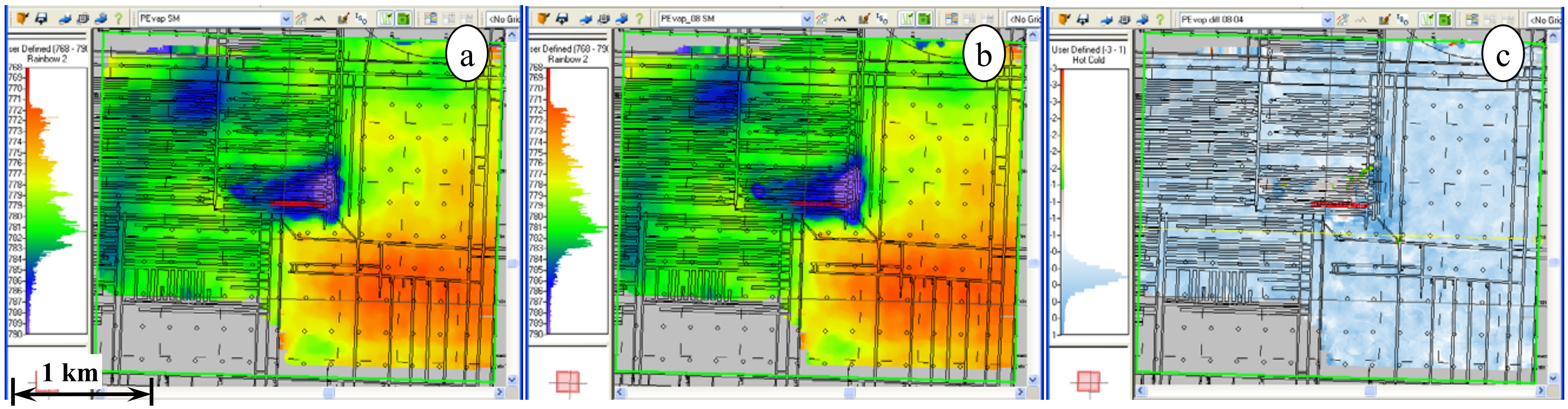

Figure 5.34 Time structure of the top of the Prairie Evaporite Formation on the PP data, a: 2004 survey; b: 2008 survey; c: PP travel time difference at the top of the Prairie Evaporite Formation between 2008 and 2004 survey.

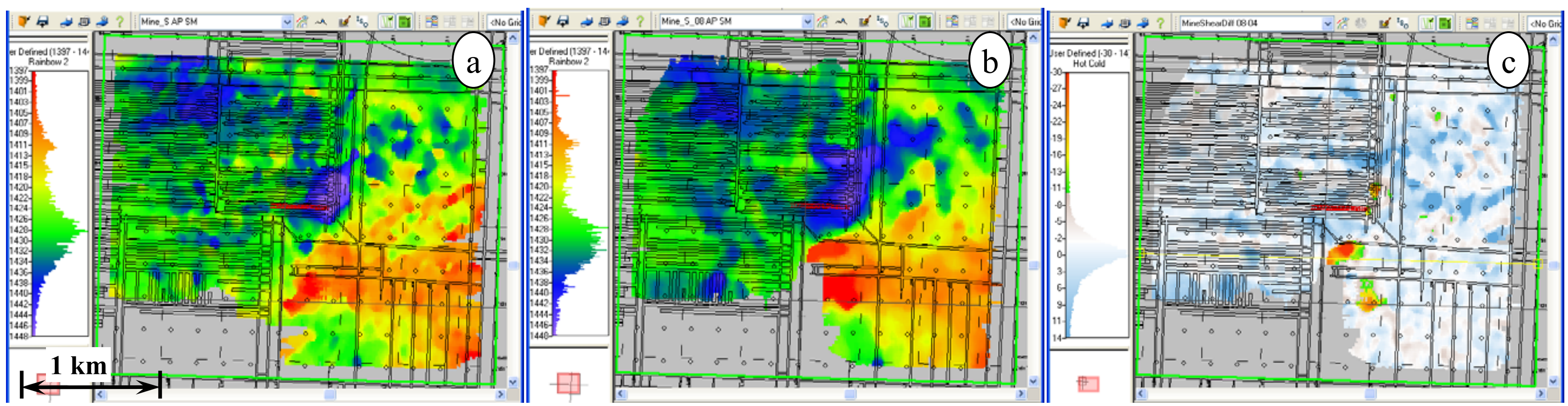

Figure 5.35 Time structure of the mine level on the PS data, a: 2004 survey; b: 2008 survey; c: PS travel time difference at the mine level between 2008 and 2004 survey.

According to the rock physics modeling result, Vp/Vs will increase when fractures are present in the Dawson Bay Formation due to relatively larger shear-wave velocity change. Therefore, interval Vp/Vs map of the Dawson Bay Formation can be used as an indicator of fractures in the formation. The Vp/Vs maps are constructed using the isochron maps from both PP and PS data for the same interval according to the formula (Margrave, et al., 1998),

$$\frac{\boldsymbol{v_p}}{\boldsymbol{v_s}} = \frac{\mathbf{2}\boldsymbol{\Delta t_{ps}} - \boldsymbol{\Delta t_{pp}}}{\boldsymbol{\Delta t_{pp}}} \tag{5-2}$$

where Δt_{ps},and Δt_{pp} are the PS and PP isochron maps for a particular interval.

Considering the difficulty to accurately pick the top and the base of the Dawson Bay Formation as well as robust Vp/Vs calculation, two intervals were chosen for interval Vp/Vs analysis using equation (5-2): interval 1 is from the Birdbear Formation to the Dawson Bay Formation, and interval 2 is from the Birdbear Formation to (approximately) the Shell Lake anhydrite below the Dawson Bay Formation (Figure 5.36). By comparing the Vp/Vs maps of these two intervals, the relative Vp/Vs change trend caused by the Dawson Bay Formation can approximately estimated.

From Figure 5.37, it can be found that there is almost no variation of interval Vp/Vs values between the two surveys from the Birdbear Formation to the Dawson Bay Formation. About 10% Vp/Vs increase is observed within the trap door area (outlined by red ellipse) on the interval Vp/Vs values of 2008 data from the Birdbear Formation to the Shell Lake anhydrite (Figure 5.38). These results indicate that: 1) above the Dawson Bay Formation, there are no fractures created between 2004 and 2008; 2) fracturing process might happen in the strata from the Dawson Bay Formation to the Shell Lake anhydrite between 2004 and 2008. A west-east line across the south edge of the trap door area was chosen for detailed interval Vp/Vs analysis of the Dawson Bay Formation (Figure 5.39). The Vp/Vs values of the Dawson Bay Formation for the 2004 survey are around 2.0. In the 2008 survey, a generally increasing trend of Vp/Vs can be seen, especially from CDP 80 to CDP 140, where is in the trap door area. The Vp/Vs increase suggests a larger S-wave velocity decrease caused by fractures in the formation. However, the Vp/Vs values seem to be too large (Vp/Vs for carbonate is 1.8). It should attribute to the large picking errors of the top and the base of the Dawson Bay Formation on the PS data (which is also the top of Prairie Evaporite Formation) due to their low frequency content. Since the horizon picked on seismic data following distinct wave features, such as peak, trough, or zero crossing, it is unlikely that PP and PS picks will coincide consistently in depth. It will also cause deviation between the Vp/Vs values estimated from seismic data and real values (Margrave, et al., 1998).

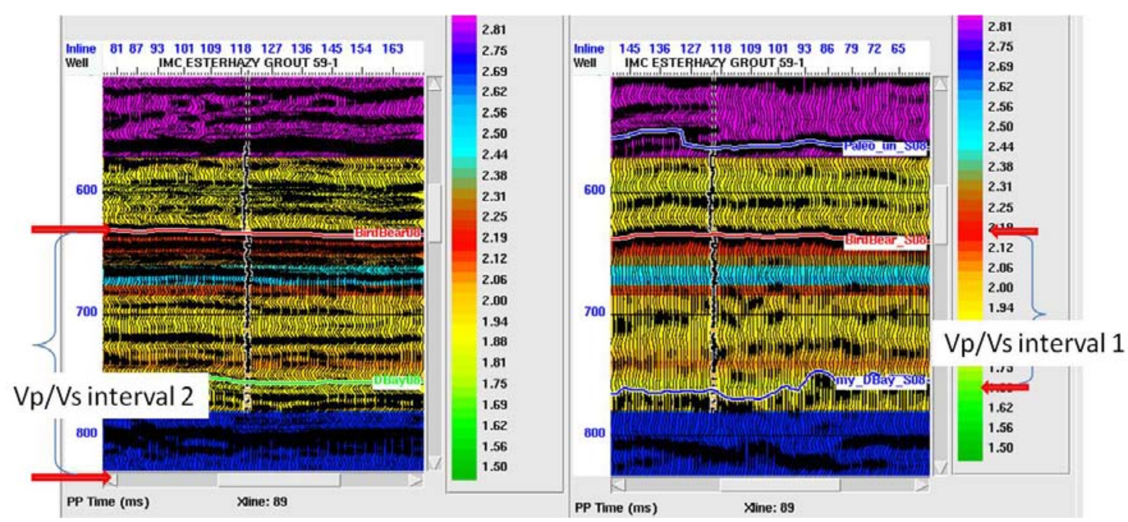

Figure 5.36 The arrow marks the intervals used for interval Vp/Vs calculation. Interval 1 is from the Birdbear Formation to the Dawson Bay Formation; interval 2 is from the Birdbear Formation to (approximately) the Shell Lake anhydrite below the Dawson Bay Formation (Vp/Vs extrapolated from well values superimposed on the seismic sections).

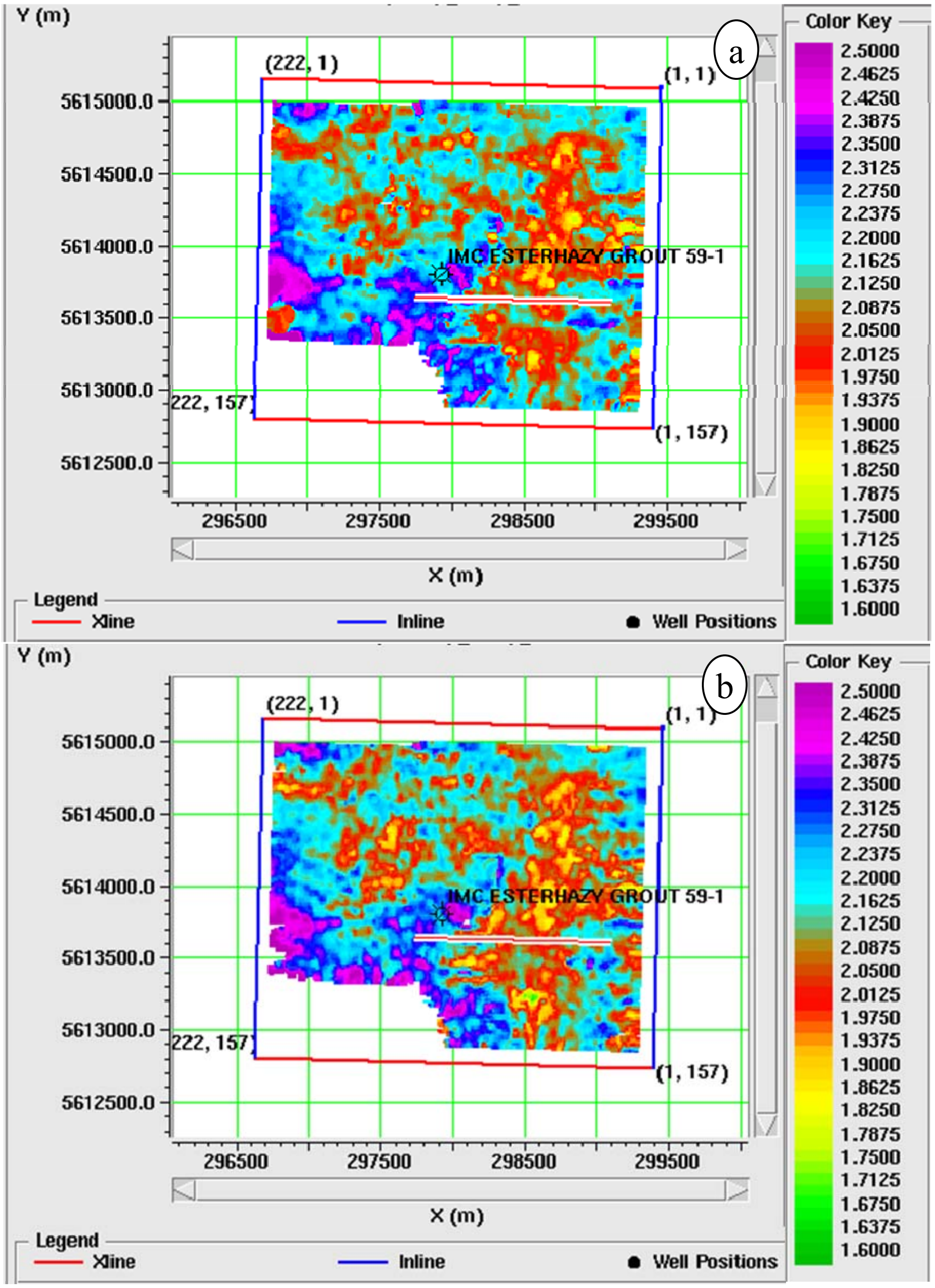

Figure 5.37 Interval Vp/Vs map from the Birdbear Formation to the Dawson Bay Formation. a: 2004 survey; b: 2008 survey.

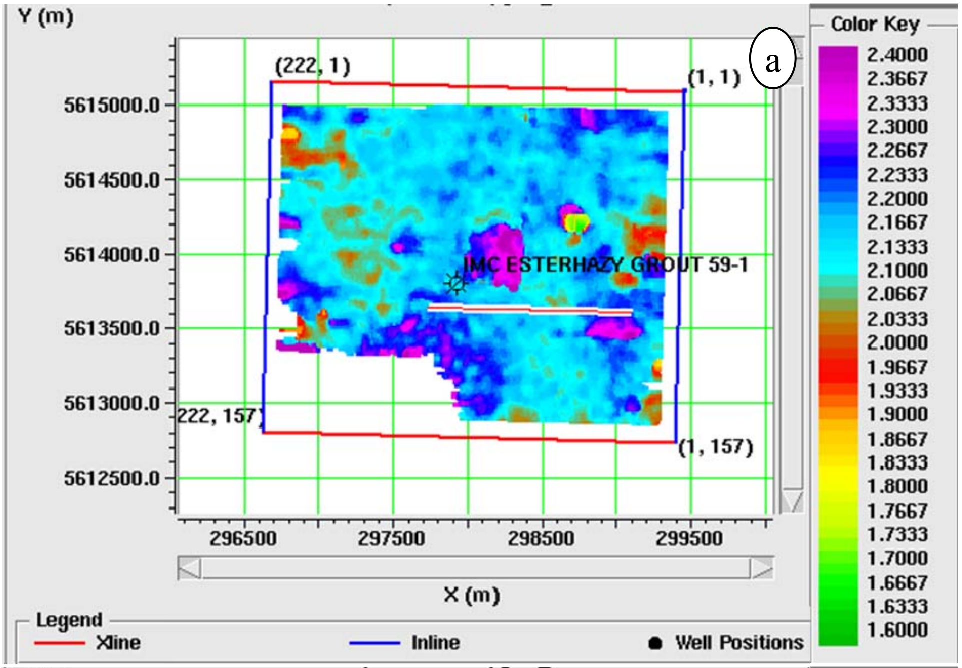

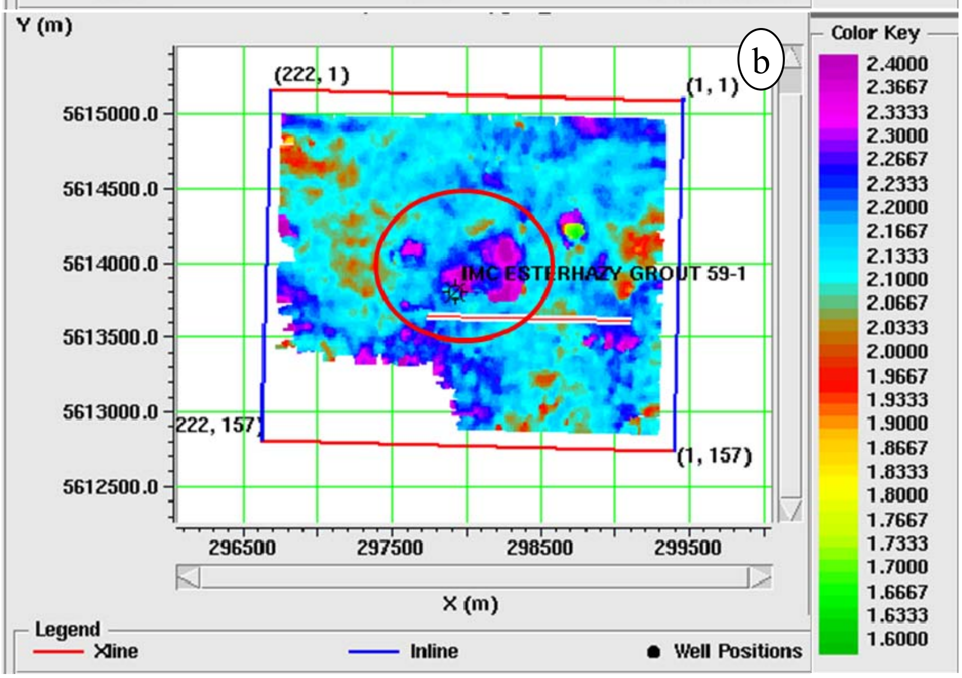

Figure 5.38 Interval Vp/Vs map from the Birdbear Formation to the Shell Lake anhydrite. a: 2004 survey; b: 2008 survey.

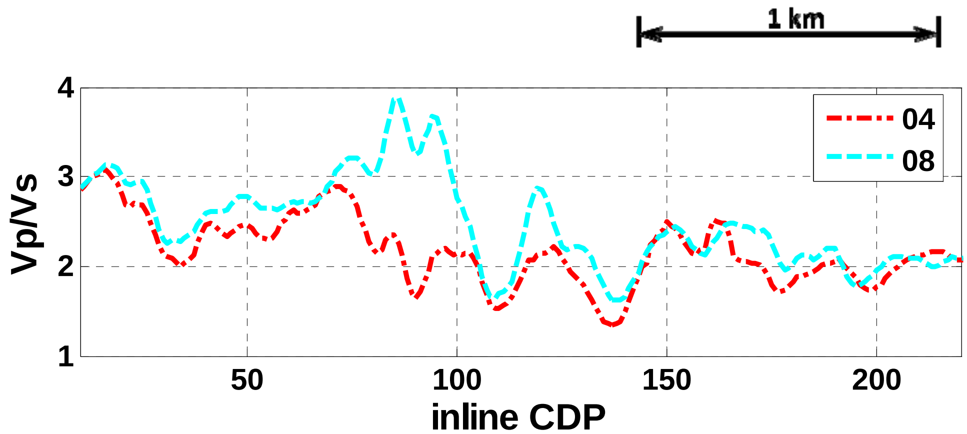

Figure 5.39 Average Vp/Vs values of west-east line 89 between the bottom of the Porous zone and the top of Prairie Evaporite Formation. The red line denotes the values from the 2004 survey, the blue line shows the values of the 2008 survey.

5.5.3 Fracture detection using curvature

Compared with coherency methods, reflector curvature is a seismic attribute relating more directly to fracture distribution (Lisle, 1994; Roberts, 2001). It helps to remove the regional dip effects and emphasizes the small scale features (Ganguly et. al., 2009). It can be used to quantify the distribution of brittle strain in strata and thus can be used to predict fracture orientations and distributions. The most positive and negative curvatures were found to be the most useful for delineating faults, fractures, flexures, and folds (Al-Dossary and Marfurt, 2006). To delineate the fractured zone which could poses a brine inflow problem to potash mining, the curvature attribute is calculated for the top of the Dawson Bay Formation and the mining level on 2008 radial data (Figure 5.40 and Figure 5.41). Compared with the top of the Dawson Bay Formation, the curvature calculated at the mining level shows much more developed fractures. This indicates that above the Dawson Bay Formation, fractures are rare. However, fractures are well developed in the Dawson Bay Formation and mining level. Curvature values also showed the distribution patterns of the fractured zone: around the edge of the trap door area, fractures were well developed; another fractured zone lies at the top right corner of the survey, which can also be easily seen on the time difference map of the mine level between 2004 and 2008 radial component data (Figure 5.35 c).

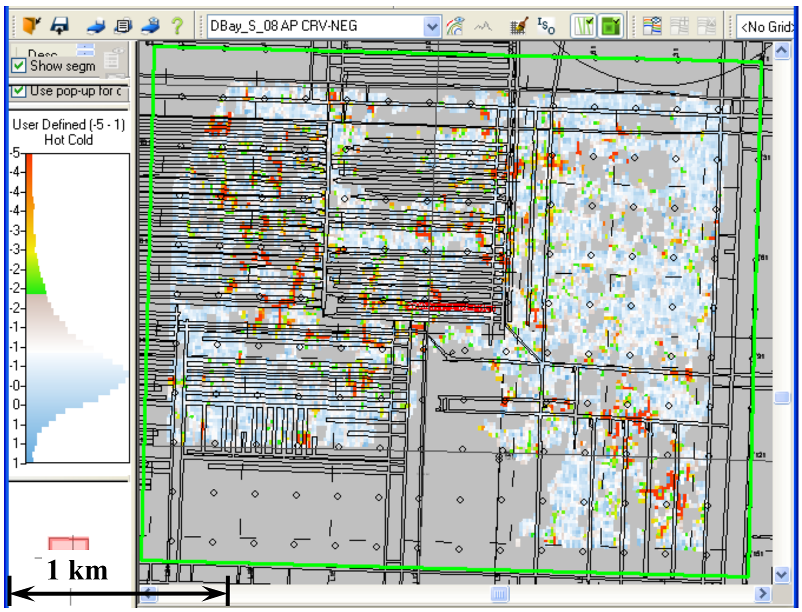

Figure 5.40 Negative curvature of the Dawson Bay Formation on PS data of the 2008 survey.

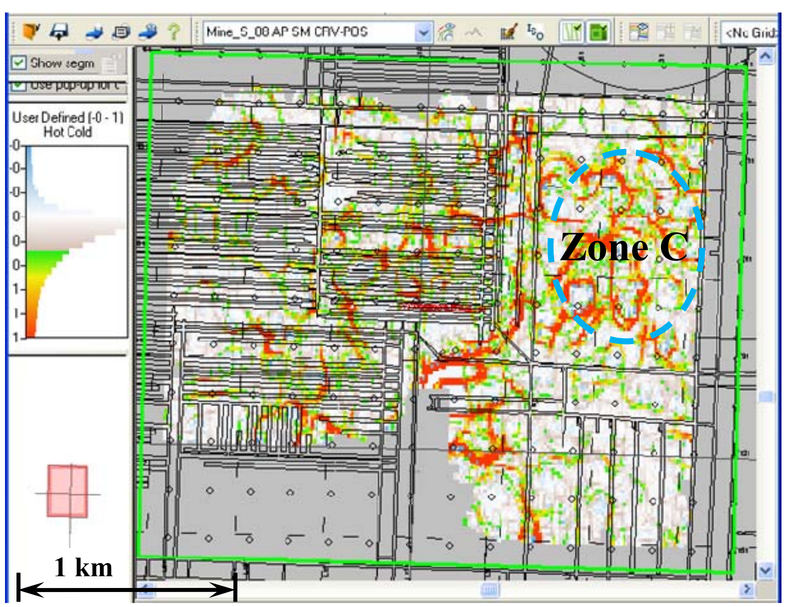

Figure 5.41 Positive curvature of the mine level on PS data of the 2008 survey.

5.5.4 Discussion

The seismic signatures of the fractures can be found on various aspects of the time-lapse 3C-3D seismic survey. However, the overlying differences of the seismic data were not effectively removed for the Dawson Bay Formation. The match filters were derived in a window from 420-620 ms for vertical data, and 600-1250 ms for radial data respectively. From the time shift and amplitude difference, there were also some changes of the strata between the Birdbear Formation and the Dawson Bay Formation. To separate the difference caused by the fractures in the Dawson Bay Formation, the windows for match filter calculations are relatively narrow. It is best to calculate the filter from the top of the Devonian to the top of the Dawson Bay Formation. The reason to exclude the shallow window is accounting for mute parameter difference in the processing.

Curvature has proved to be an effective attribute to delineate the fractures in this study. Since they were only calculated using the full wave-bandwidth data, we are confident on detecting the overall fracture effect. To account for subtle features at different wavelengths, it might be better to examine curvature at various scales.

5.6 Summary

This chapter first presents the results of a petrophysical and seismic simulation study in a potash mining area of western Canada. The goal of the work is to model the effects of fractured rocks in the Dawson Bay Formation on seismic reflection character. Shear-wave sonic logs sometimes display unrealistic values. We can effectively edit these values, in this study, by using P velocity and density logs. Rock physics modeling (from Kuster- Toksöz and Hudson's models) indicates that P-wave and S-wave velocities will decrease (often significantly) with cracks or fractures. These fractured strata may also display various types of anisotropy or velocity variation with direction. Synthetic seismogram calculation using the original log values and those with fractures shows observable changes. Those changes include “push-down” effects or time lags and amplitude variations with offset. The seismic character differences are especially evident in the PS reflections.

Then the interpretation of time-lapse 3C-3D surveys was implemented. The PP and PS synthetic seismograms correlate reasonably well with field time-lapse 3C-3D surface seismic data. This suggests that, by searching for anomalies in multicomponent seismic data or by looking for changes in repeated seismic surveys, we may be able to detect fractures in the Dawson Bay Formation and similar intervals. Seismic interpretation on the time-lapse 3C-3D surveys saw noticeable amplitude changes and push-down effects at the Dawson Bay and underlying formation in the 2008 survey compared with the 2004 survey, especially on radial data. Vp/Vs analysis displayed increasing values on the 2008 survey within the trap door area. Finally, seismic curvature attributes were calculated at the top of the Dawson Bay Formation and the mining level. The curvatures suggest that the fractures are well developed in the Dawson Bay Formation.

Chapter Six: Numerical modeling of shear-wave splitting analysis associating potash mining

Many crustal rocks are found experimentally to be anisotropic (Thomsen, 1986). When aligned cracks/fractures occur in rock, they will cause velocity anisotropy. The rock physics modeling results in chapter 5 showed that 1% vertically aligned fractures in the Dawson Bay Formation bring about measurable azimuthal anisotropy. Gupta (1973a, b) and Crampin (e.g., 1981, 1983) pointed out that azimuthal anisotropy effects are measurable, and two- and three-component seismic data are suitable to measure the corresponding shear-wave splitting thus the orientation and the intensity of fractures can be determined (Helbig and Thomsen, 2005; Pérez et al., 1999). Numerous authors (e.g. Crampin, 1985; Tatham et al, 1992; Slack et al, 1993; Gaiser and Van Dok, 2002; Verdon et al., 2009; Verdon et al., 2010) evaluated the degree of anisotropy from shear-wave splitting. If the anisotropy is due to cracks/fractures, their orientation and intensity can also be determined by analyzing shear-wave splitting (e.g. Tatham et al., 1992).

In Chapter Five, rock physics models and seismic simulation were used to predict the effects and seismic signatures of cracks/fractures in the Dawson Bay Formation. However, the synthetic seismogram modeling program in chapter 5 is for isotropic velocities, seismic signatures of anisotropy caused by aligned fractures can not be seen. The feasibility of using anisotropy analysis of time-lapse 3C seismic data for fracture detection in the Dawson Bay Formation was not evaluated yet. Thus, in this chapter, seismic modeling of 3C data for unfractured (isotropic) and fractured (anisotropic) earth models will be used for shear-wave splitting, seismic velocity anisotropy, and time-lapse seismic signature analysis.

6.1 Acquisition of 3D-3C seismic modeling data

6.1.1 Input earth models

Two laterally homogeneous earth models were input for 3C-3D seismic modeling. The unfractured earth model was built from the blocked well logs from the study area. By replacing rock properties of the full Dawson Bay Formation by the rock physics modeling results of vertically aligned fractures formation, an anisotropic (HTI) earth model was created for seismic modeling.

Figure 6.2 shows the general stratigraphic chart and blocked well logs for the density and velocity models. The shallow parts are shales and sandstones of Cretaceous and Triassic age. The Devonian strata are mainly carbonates with two evaporite intervals: the Davidson Evaporite and the Prairie Evaporite. Underlying the Prairie Evaporite is the Winnipegosis carbonate. The red rectangle denotes the location of the fractured layer, the Dawson Bay Formation. The upper part of it is mostly dolomite or dolomitized limestone, the lower part is the Second Red Bed shale. The rock properties for the Dawson Bay Formation are listed in Table 6.1.

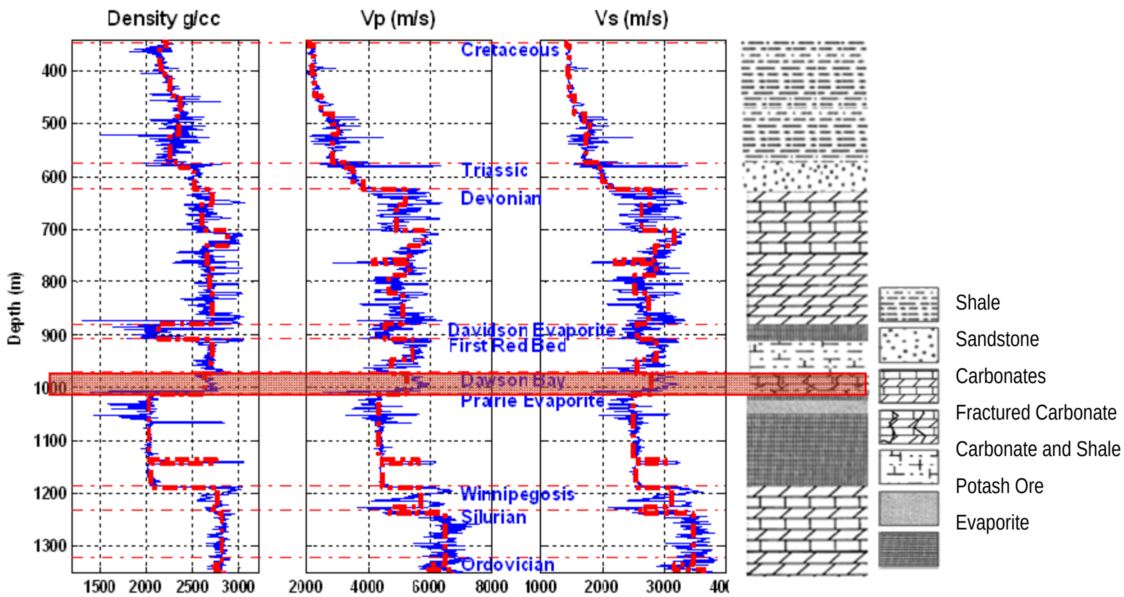

Figure 6.1 Stratigraphy chart (modified after Fuzesy, 1982) and blocked well logs. The red rectangle denotes the location of the modeled HTI layer.

Table 6.1. Rock properties of the Dawson Bay Formation, the values are averaged over the formation (coordinate used for stiffness matrix: x1 - normal direction of fracture plane (horizontal); x3 - vertical direction).

Top	970.8 m	
Thickness	40.4 m	
Fracture parameters	1% penny-shape fractures, filled by brine with Vp 1430m/s, density 1100 kg/m^3.	
	fractured	unfractured
Density	2603.9 kg/m^3	2630.2 kg/ m^3
Stiffness matrix (x10^{10} kg/m2·s)	5.610 2.354 2.354 0 0 0 2.354 6.813 2.710 0 0 0 2.354 2.710 6.813 0 0 0 0 0 0 2.052 0 0 0 0 0 0 1.243 0 0 0 0 0 0 1.243	Vp: 5184.7 m/s Vs: 2792.9 m/s

Figure 6.2 shows the interval P- and S-wave velocity models for numerical modeling. The layered models are created based on the blocked well logs. The maximum measured depth of well logs is 1378.2 m. The velocities at deeper locations than this depth are set to be equal to the velocities at 1378.2 m.

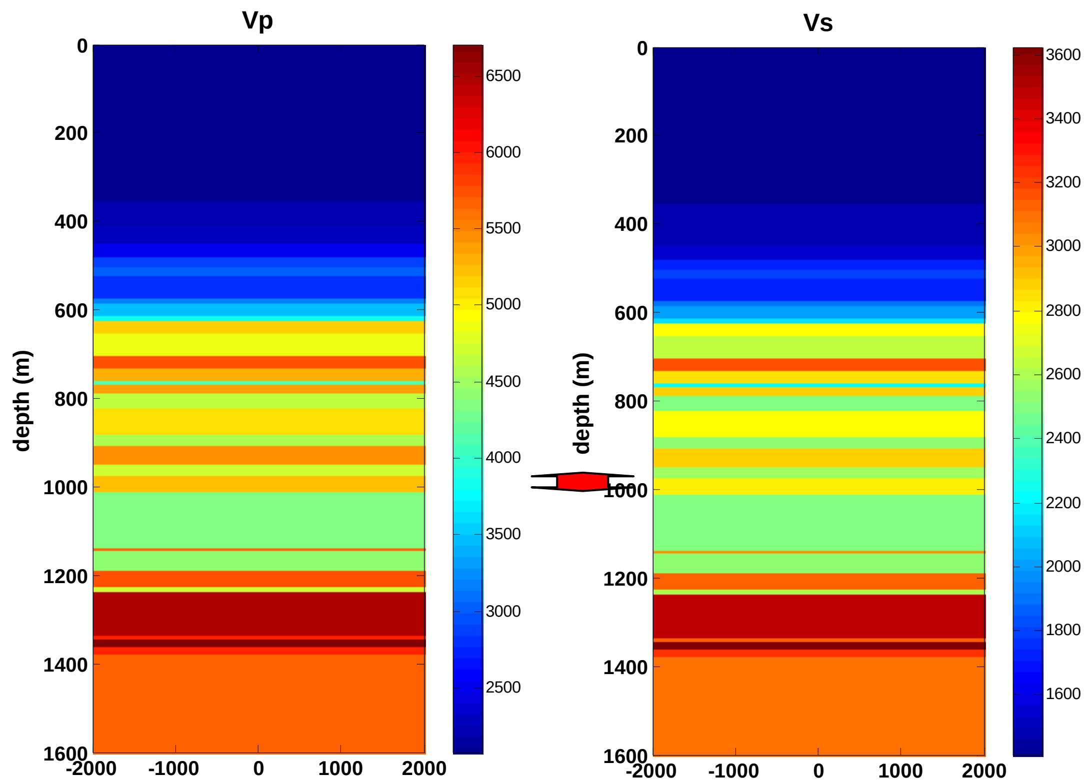

Figure 6.2 Input interval P-wave and shear-wave velocity layered models for numerical modeling. The HTI models are the same as for the isotropic model except for replacing the rock properties of the Dawson Bay Formation by values for vertically aligned fractures. The anisotropic layer (the Dawson Bay Formation) location is denoted by the red arrow.

6.1.2 Survey design and raw data analysis

An exhaustive wide azimuth survey was designed for shear-wave splitting and seismic velocity anisotropy analysis (Figure 6.4); the parameters of the survey are shown in Table 6.2. Since the earth models are laterally homogeneous, only one shot was modeled with the source location at the center of the survey. The recording coordinate used is denoted by blue arrows in Figure 6.3. X is in the direction normal to the fracture plane (isotropy axis). Y is along the fracture plane (isotropy plane). The seismic modeling was done by Dr. Jim Gaiser using the frequency-wavenumber method. 3-C data sets were modeled for both isotropic and anisotropic models.

Table 6.2 Survey design parameters for numerical modeling

Survey size	4km x 4km
Source type	Dynamite at the surface
Source location	One source at the centre of the survey
Receiver spacing	20 m
Receiver line spacing	20 m
Sample rate	2 ms
Record length	2048 ms
Modeling frequency range	2 – 110 Hz

Figure 6.4 displays azimuth and offset distribution of the survey. The offset ranges from 0 to 2824 meters. The azimuth is from 0 to 360 degrees. The number of offsets for each azimuth is relatively even with some variation, and is suitable for the shear-wave splitting and velocity anisotropy analysis described later in this report.

Figure 6.5 and Figure 6.6 show the 3-component seismic data at the selected azimuth, 0°, 45°, 90°, and 135° (negative offsets at 180°, 225°, 270°, and 315° were combined respectively) for the isotropic model and anisotropic model respectively. In the recording coordinates, x-component receives no signal at 0° and 180°, while y-component has no signal at 90° and 270° for both isotropic and anisotropic earth models. Since there is no low velocity layer at the near surface, there is P wave and shear-wave leakage on horizontal components and the vertical component respectively. Amplitude spectra were also calculated for x, y, and z components of isotropic model (Figure 6.7), the frequency ranges are quite similar for all the three components, about 10-120 Hz.

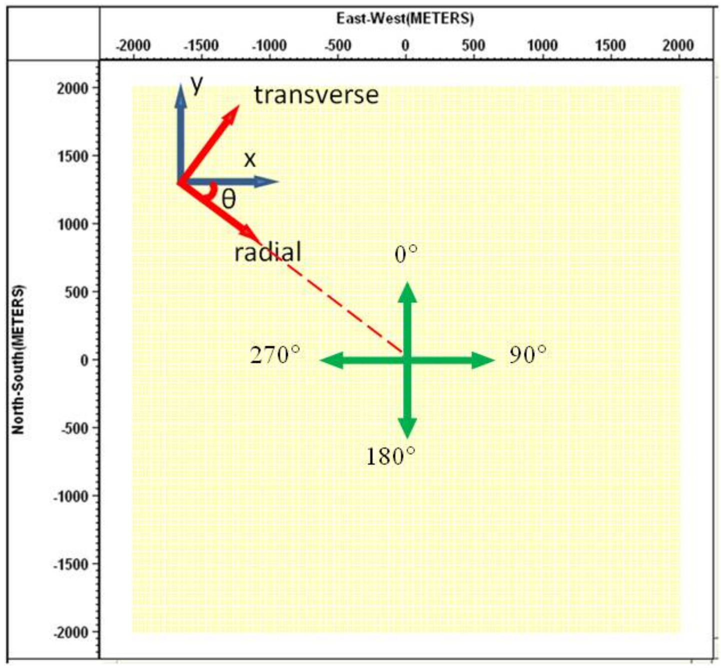

Figure 6.3 Schematic plot for coordinate system used for data recording and processing. The horizontal components were originally recorded in X and Y directions. For processing, the two components should be reoriented to radial and transverse directions. The source location is at the survey centre, red dash line denotes the direction from receiver point to source point. The azimuth used in processing is denoted by the green cross.

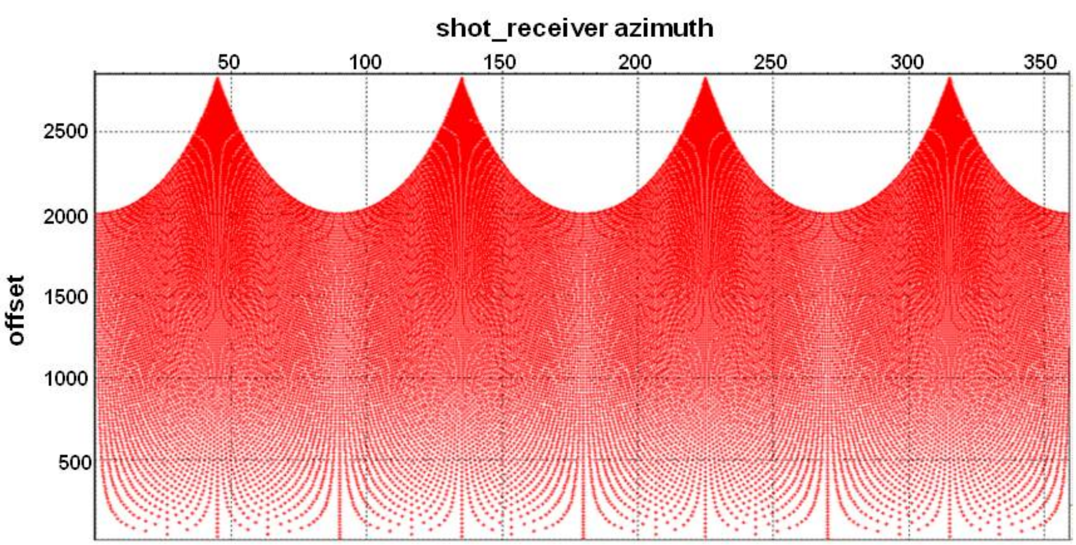

Figure 6.4 Azimuth and offset distribution of the survey.

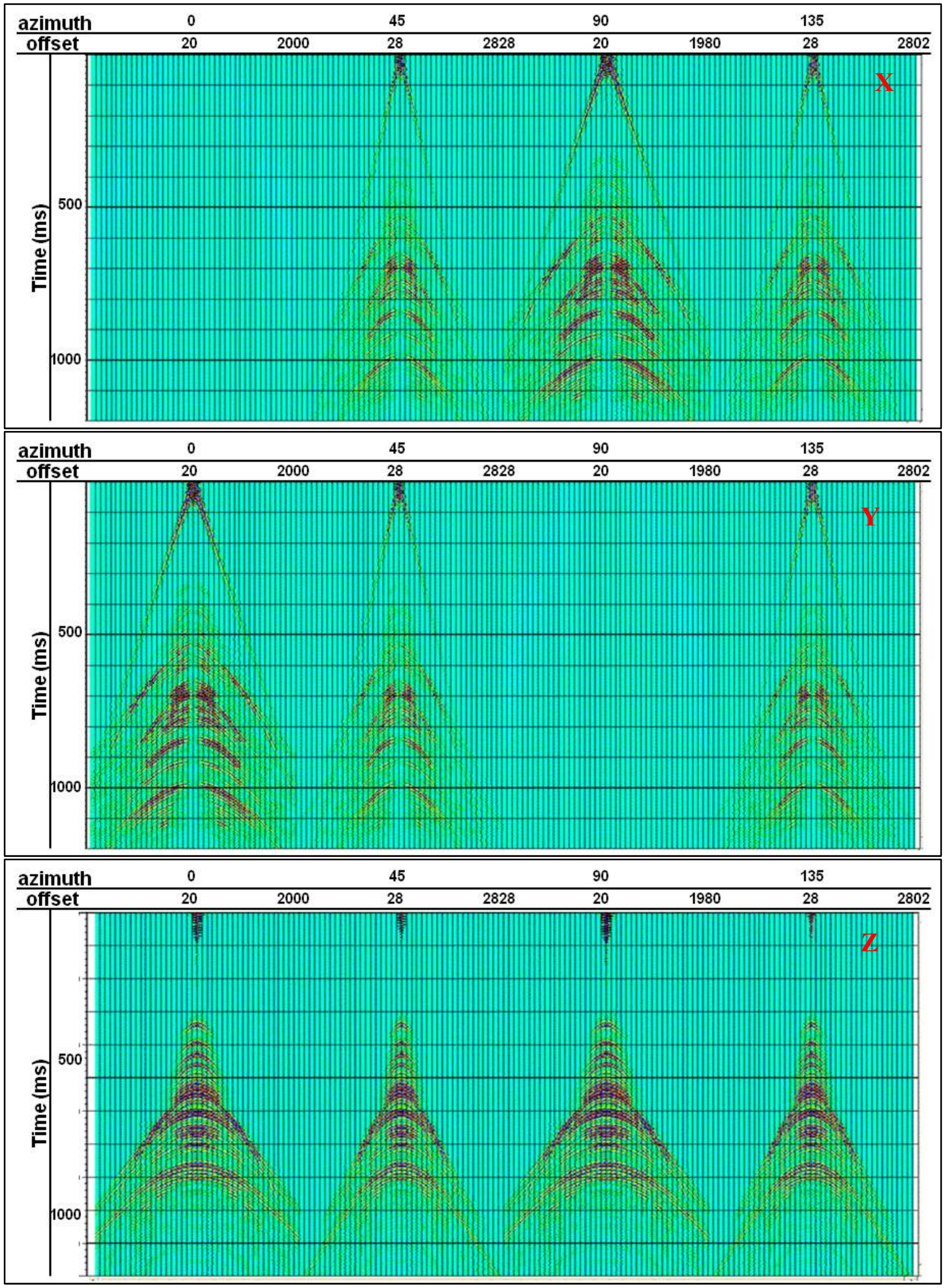

Figure 6.5 X, Y, and Z components for the isotropic earth model at azimuths of 0°, 45°, 90°, and 135°.

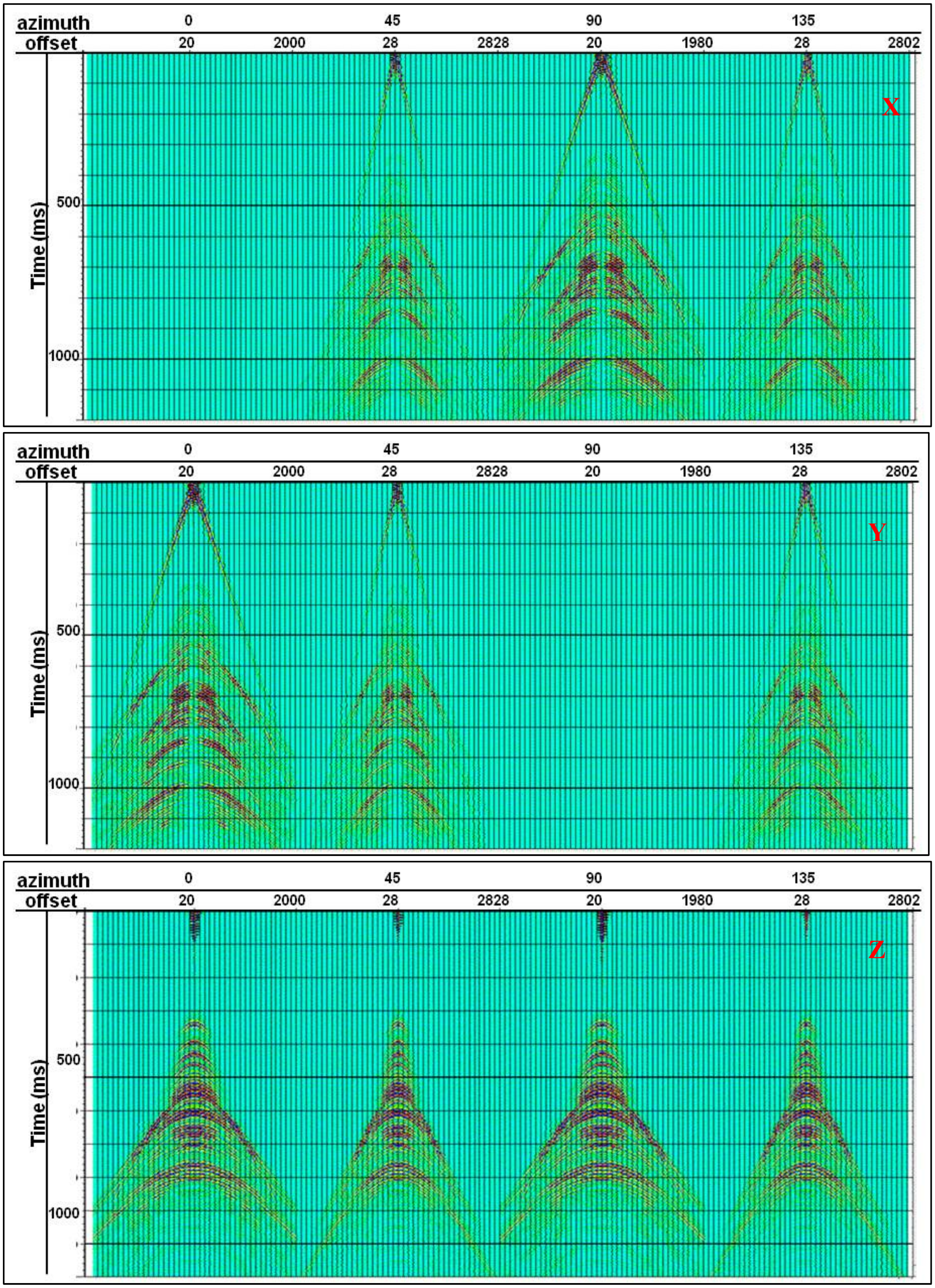

Figure 6.6 X, Y, and Z components for the anisotropic earth model at azimuths of 0°, 45°, 90°, 135°.

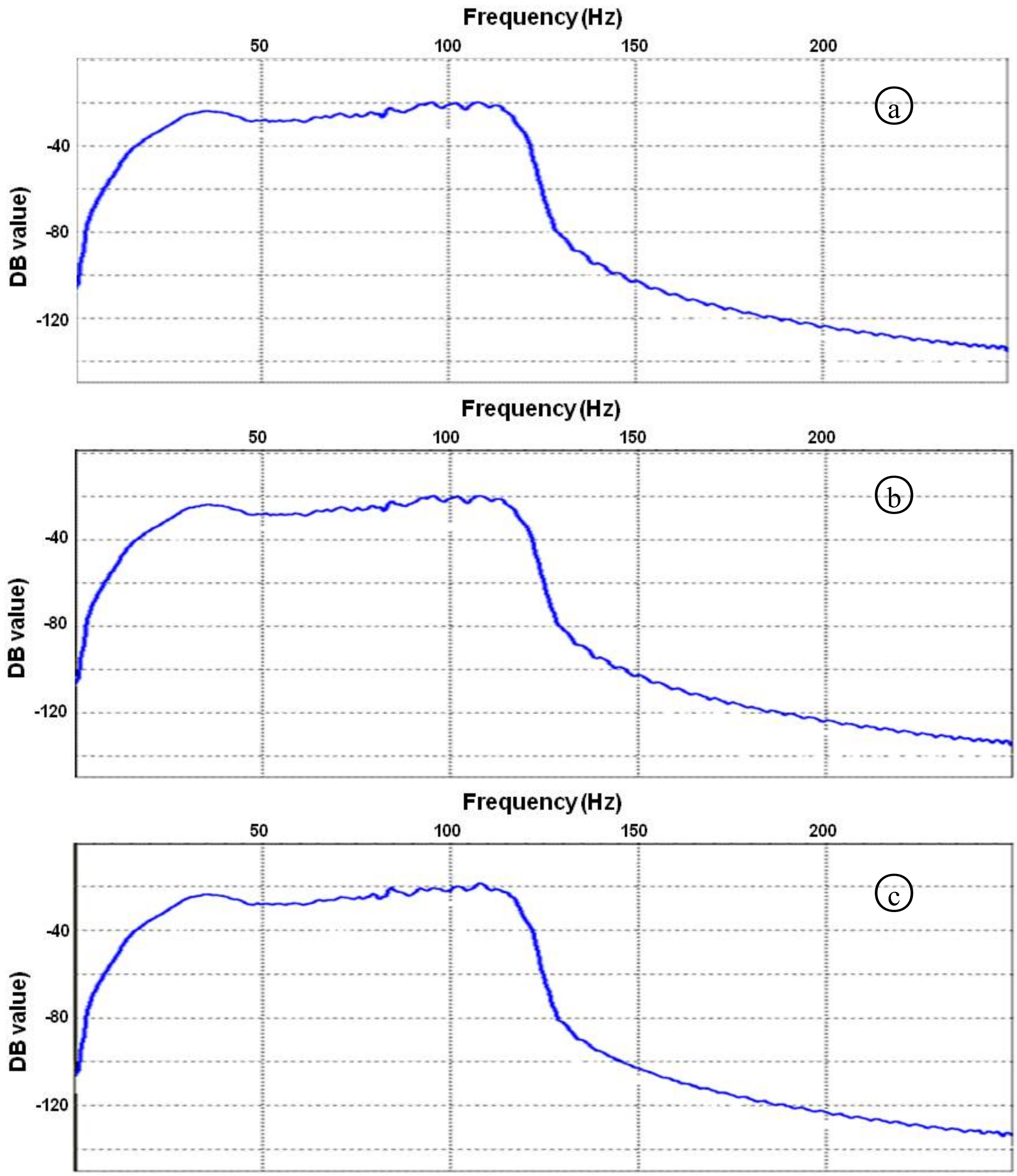

Figure 6.7 X (a), Y (b), and Z (c) components amplitude spectra for the isotropic earth model.

6.2 Seismic data processing

Table 6.3 shows the seismic processing workflow used for shear-wave splitting analysis. First, the geometry information, including source receiver locations, processing grid bin size, azimuth etc., were loaded for all the data sets.

Since the original horizontal components were recorded in the x and y directions, they were reoriented to radial and transverse directions prior to other processing steps (denoted as red arrows in Figure 6.3). Figure 6.8 and Figure 6.10 display the horizontal rotation results for isotropic and HTI earth model data. As shown in Figure 6.8, for the isotropic earth model, the shear wave energy is recorded in the radial direction (SV wave). On the transverse component, no shear wave (SH wave) energy is found. For the HTI earth model, except for the dominant SV wave recorded on the radial component, SH wave is also found below the fractured layer location (about 850ms) on the transverse component except at azimuths 0° and 90° (Figure 6.10). Figure 6.9 also displays polarity change of horizontal component between original recording coordination and rotated coordinates. On the x-component of x-direction receiver line across the source location, the polarity reverses at zero offset for both direct arrival and reflections. After horizontal rotation, the polarity is consistent across the source location on radial component for both wave types.

Table 6.3 3C seismic data processing workflow for shear-wave splitting analysis.

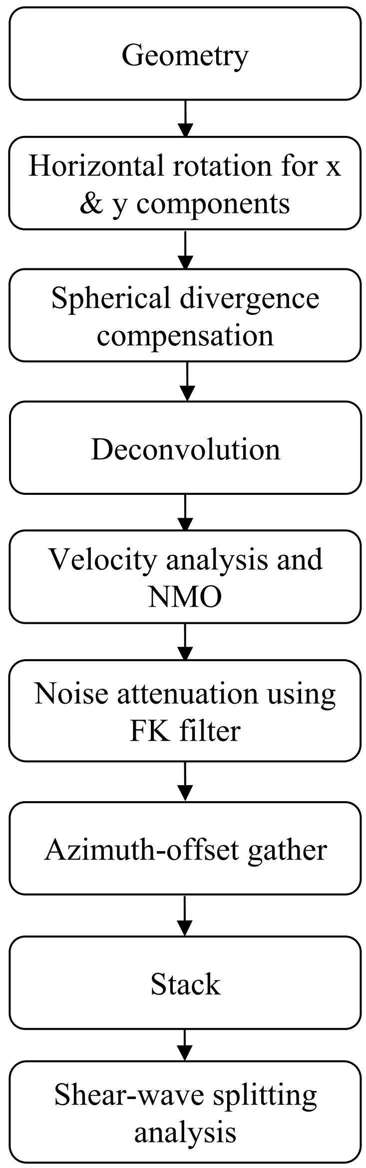

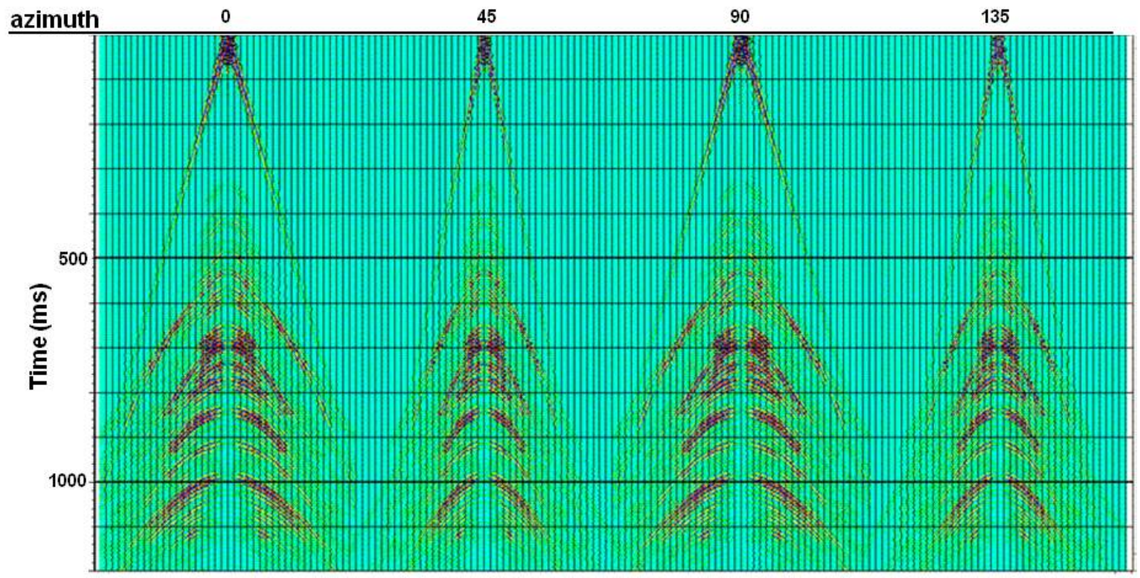

Figure 6.8 Radial component of the isotropic earth model from horizontal rotation of X and Y components (at azimuths of 0°, 45°, 90°, 135°). For laterally homogeneous isotropic media, the transverse component receives no energy.

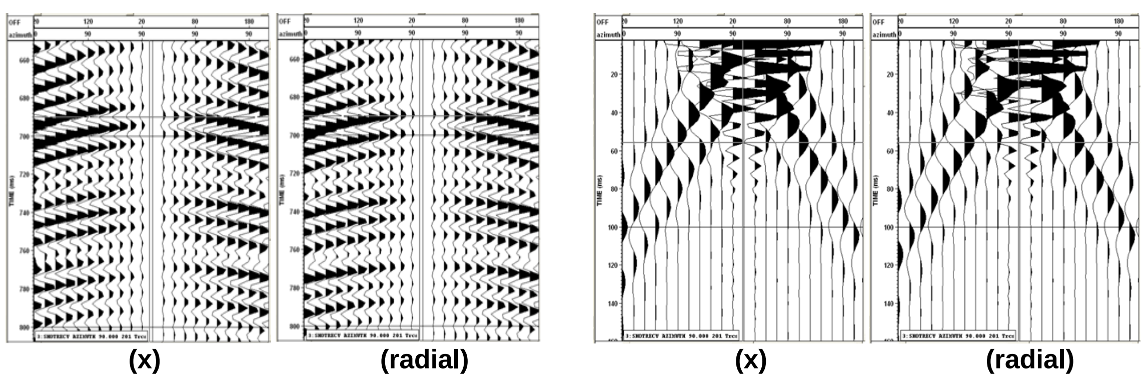

Figure 6.9 Comparison of reflection (left) and direct arrival (right) between x-component and radial component from the horizontal rotation of the isotropic model data (at azimuth of 90°). Note the polarity difference between the two data sets.

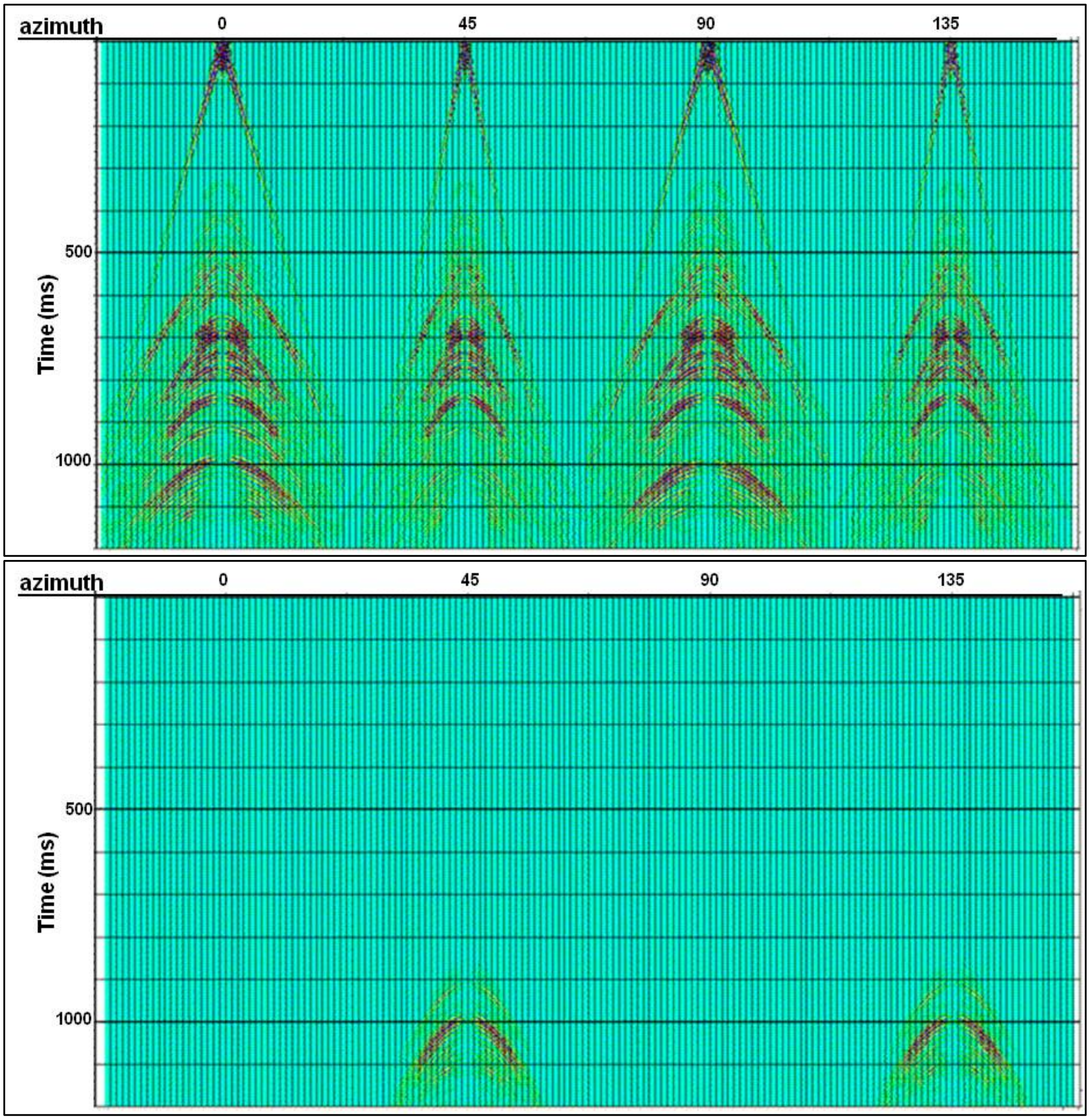

Figure 6.10 Radial (top) and transverse (bottom) components of the HTI model from the horizontal rotation of X, Y components (at azimuths of 0°, 45°, 90°, 135°).

Spherical divergence was corrected by PP and PS velocities for vertical and horizontal components, respectively. According to deconvolution test results, zero-phase deconvolution was then chosen to improve the data. Figure 6.11 shows the comparisons of a vertical component gather, autocorrelation function and amplitude spectrum at azimuth 0° before and after deconvolution of the data from the isotropic model. After deconvolution, the reflection character is clearer (Figure 6.11). From the autocorrelation function of the data, we can see that the wavelet sidelobes are suppressed and lateral coherency is improved by deconvolution. The frequency spectrum is also flattened and is more spatially coherent (Figure 6.11).

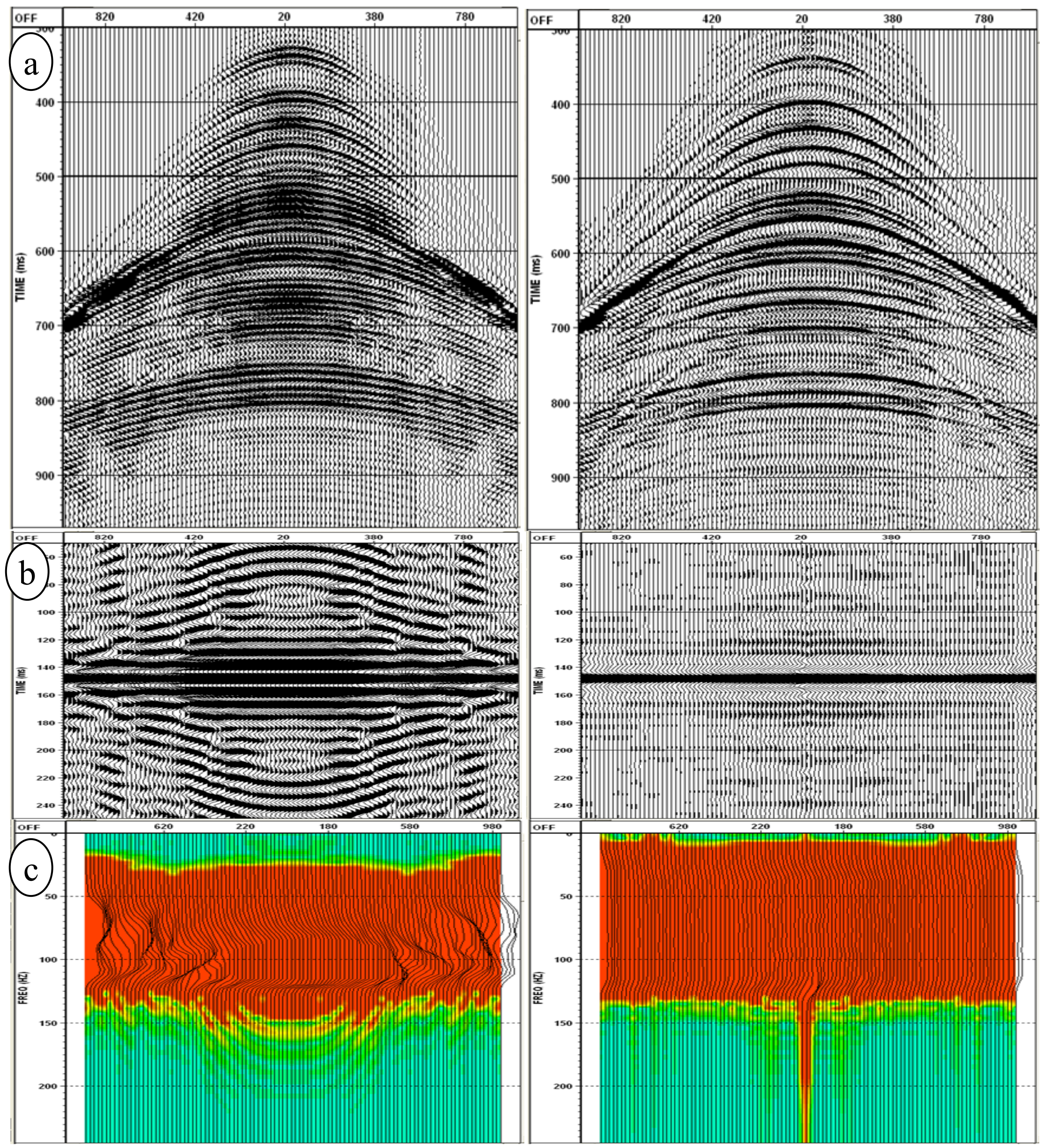

Figure 6.11 Comparison of the PP data of the isotropic earth model before (left) and after (right) deconvolution. From top to bottom: a) gathers across source point at azimuth 0°; b) autocorrelations of the gathers shown as a; and c) amplitude spectrum plots of the gathers shown as a.

Velocity analysis was performed for both PP waves and PS waves. Since both earth models are laterally homogenous, a receiver line in the x direction across the source point is considered to be a CRP gather for velocity analysis. By comparing NMO corrected gathers, velocity functions converted from velocities input for seismic modeling were adopted. Hyperbolic NMO is found to be imperfect (Figure 6.12c and Figure 6.12f), thus η parameters were picked for 4th order NMO (Figure 6.12a and Figure 6.12d). By applying 4th order NMO corrections, far-offset events are somewhat better flattened (Figure 6.12b and Figure 6.12e).

Figure 6.13 displays NMO corrected azimuth-offset gathers of the vertical component for the isotropic model and the corresponding FK spectrum. Some coherent noise can be found (Figure 6.13a). By applying an FK filter, the coherent noise is mostly attenuated (Figure 6.13c). The data was then sorted into azimuth-offset supergathers. Azimuth gathers were grouped by an azimuth increment of 6°. Within each azimuth supergather, offsets were also grouped by 40 meters panels. For seismic anisotropy analysis, the azimuth-offset supergathers were also sorted in offset-azimuth order (Figure 6.14, Figure 6.15, and Figure 6.16). For shear-wave splitting analysis, common azimuth supergathers were stacked. The vertical, radial and transverse components stack results are shown as Figure 6.19, Figure 6.20 and Figure 6.21.

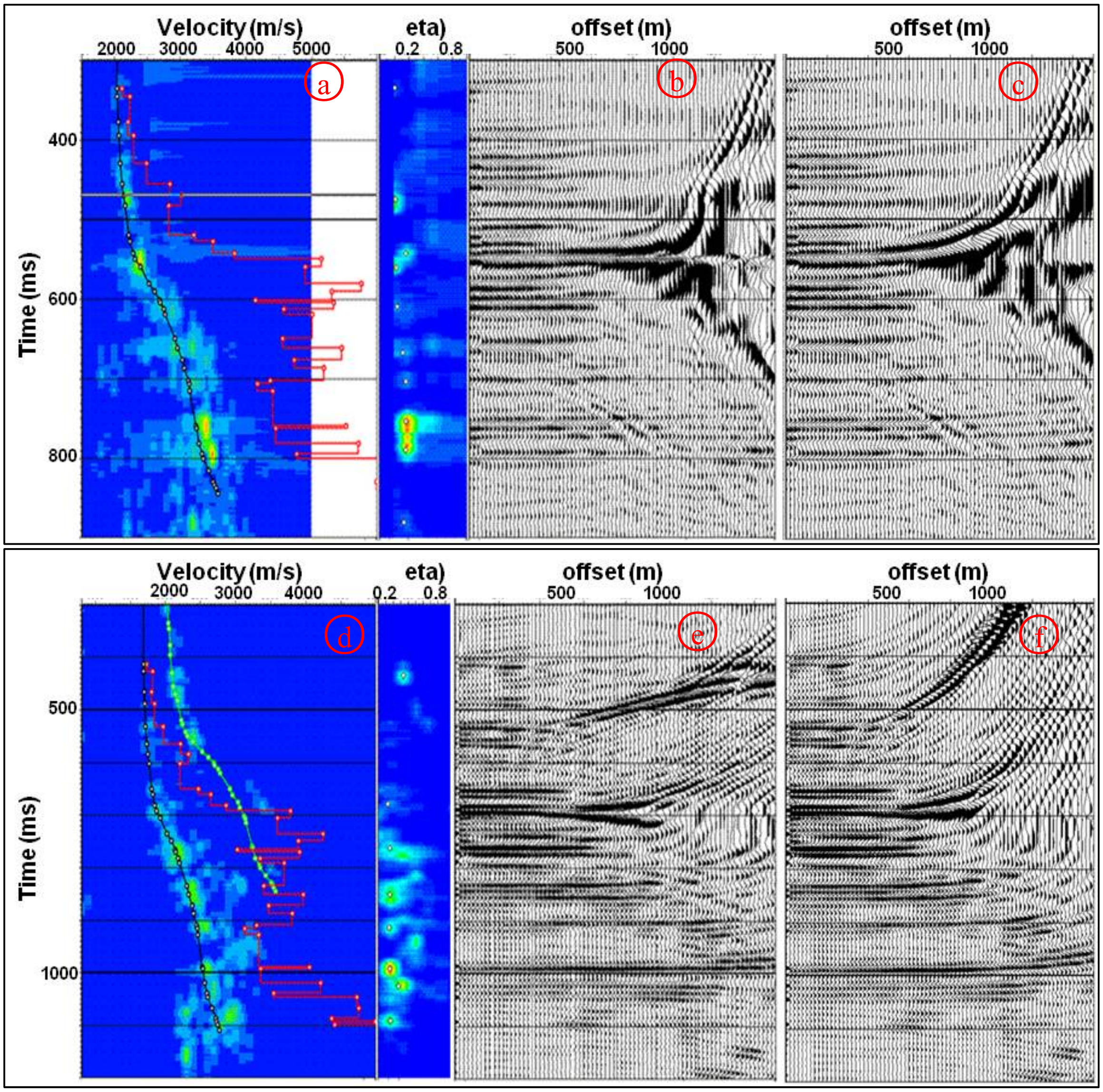

Figure 6.12 Velocity analysis for PP (top) and PS (bottom) data. From left to right: a) and d) velocity spectrum and η for 4th order moveout correction; b) and e) 4th order NMO corrected gather, and c) and f) hyperbolic NMO corrected gather. The black line in the spectrum is the RMS velocity, the red line is the interval velocity, the green line in (d) denotes the velocity picks of P waves from (a) superposed on the velocity spectrum for the PS data.

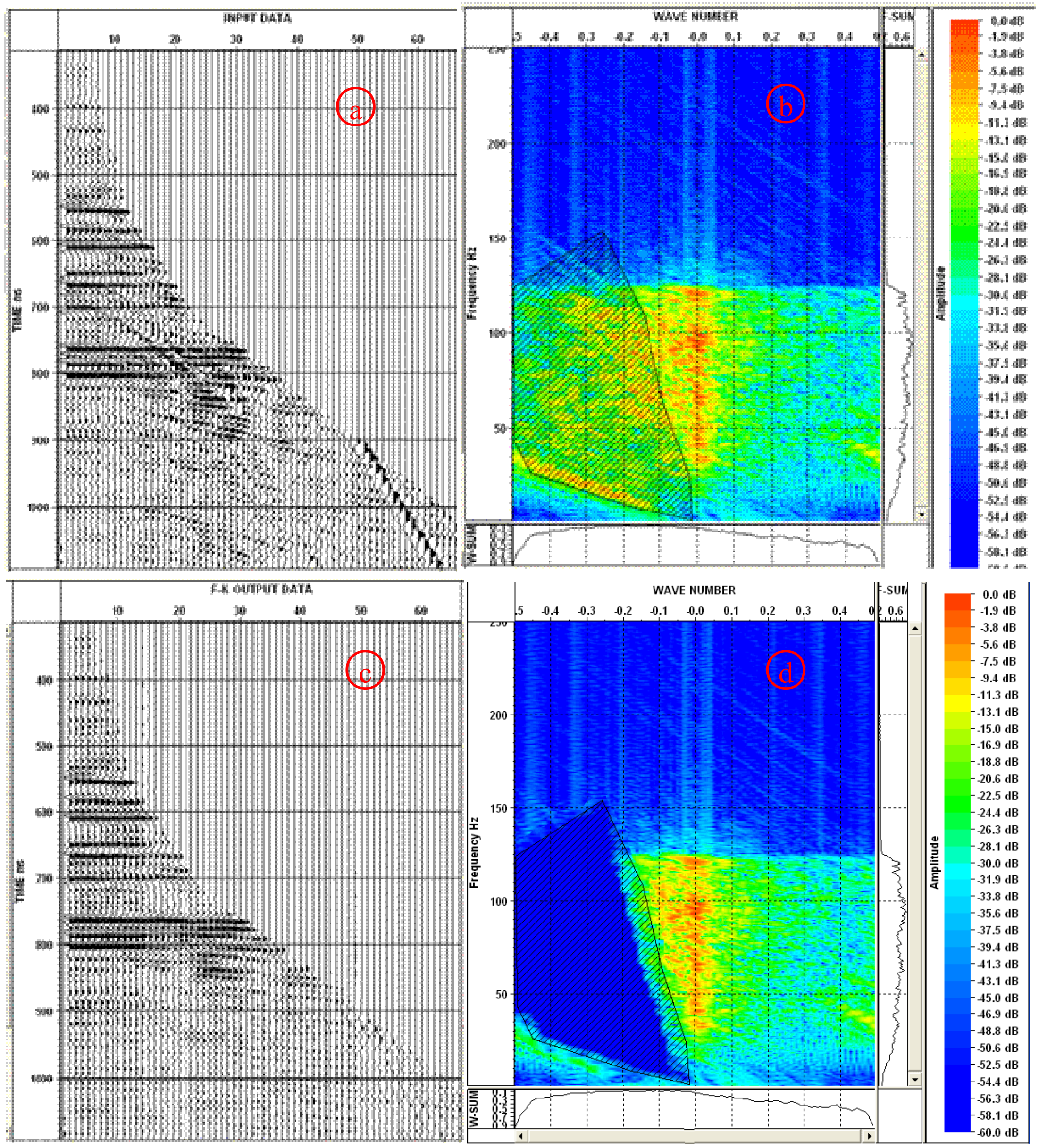

Figure 6.13 FK filtering design on vertical component azimuth gather of the isotropic model. a: the data before applying FK filter; b: FK spectrum of data in a and the designed FK filter; c: the data after applying FK filter; and d: FK spectrum of data in c.

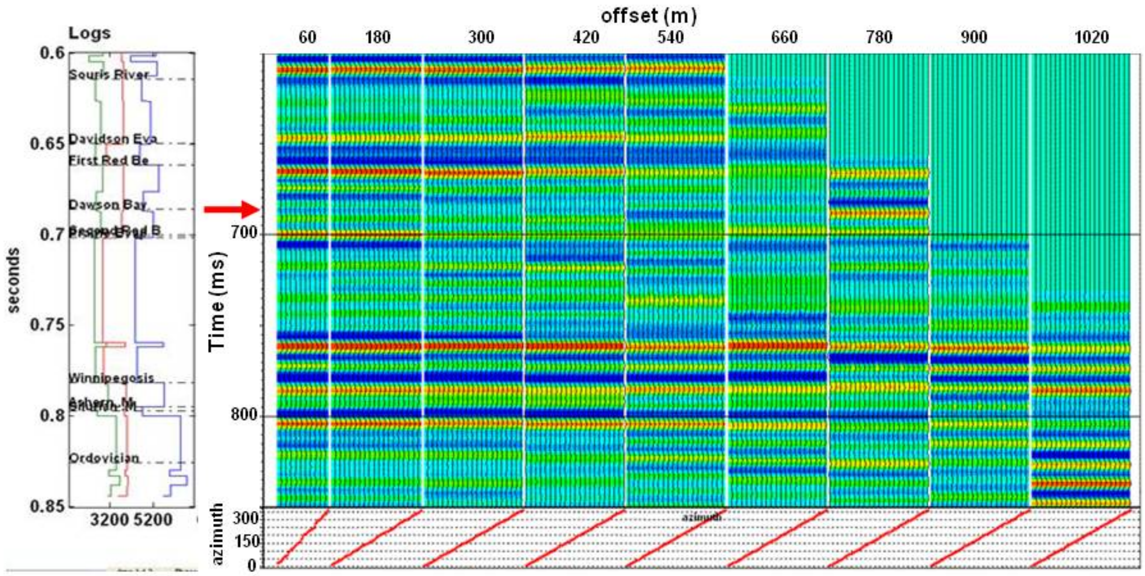

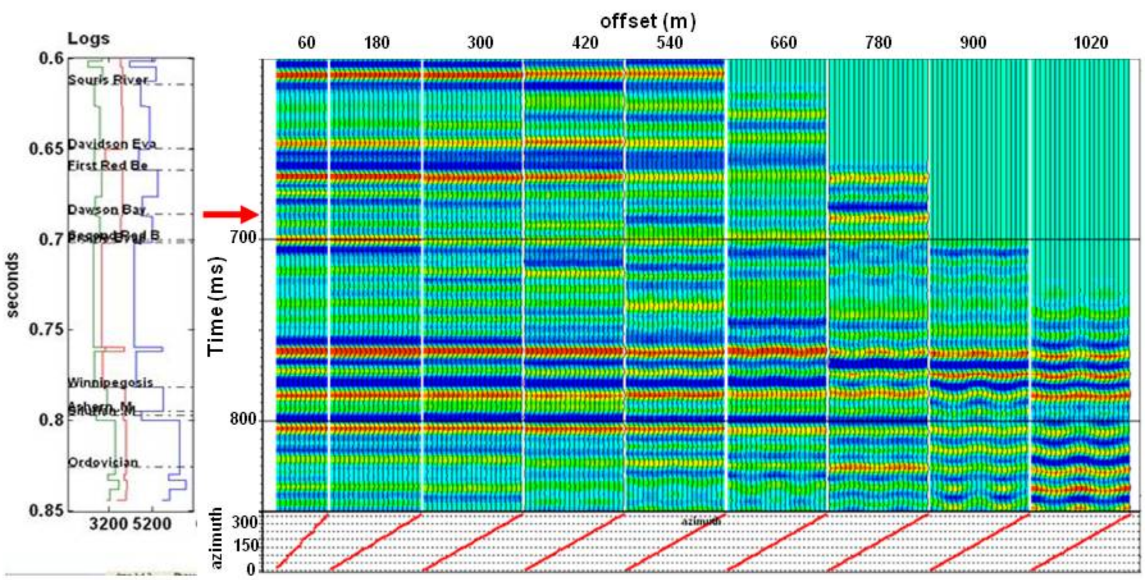

Figure 6.14 Well logs (Vp: blue; Vs: green; density: red) and offset-azimuth supergathers of the vertical component for the isotropic (top) and the HTI (bottom) earth models. The red plots at the bottom are azimuths. Common-offset gathers are separated by space and offset increases to the right.

6.3 Results and discussions

6.3.1 Velocity anisotropy

Evidence of azimuth velocity anisotropy can be seen on the offset-azimuth super-gathers of the vertical, radial and transverse components of the data (Figure 6.14, Figure

6.15 and Figure 6.16). On the vertical and radial component gathers of the isotropic model, there is no sign of azimuthal velocity variation from near to far offset (the top gathers of Figure 6.14 and Figure 6.15). On the corresponding gathers from the anisotropic model, since isotropic NMO correction was applied to the gathers, residual moveout was left on the NMO gathers. Azimuthal variation of residual moveout is noticeable on the gathers from the anisotropic model below the reflection of the top of the Dawson Bay Formation. The variation range increases with offset, the largest variation is seen at the far offset. On the far offset panels (offset > 660 m), azimuthal variation of reflection time can also be seen above the Dawson Bay Formation, it should be caused by over-NMO-corrected events (very mild mute was applied to the NMO-corrected gather). A similar phenomenon can also be observed on the gathers of the transverse component (Figure 6.16).

Based on the azimuthal super-gathers, azimuthal velocity analysis was carried out for both vertical and radial components for the anisotropic model. Figure 6.17 shows the velocity spectrum at four selected azimuths, velocity section and picked velocity plots of the vertical component focused on the fractured formation. The same plots for radial component are displayed as Figure 6.18.

The azimuthal velocity spectrum shows difference from the top of the First Red Bed Shale, at about 665 ms on vertical component data, and at 848 ms on radial component data. The stack energy peak locations of the base of the Dawson Bay (705 ms on vertical component data, 906 ms on radial component data) vary with azimuth. The Shell Lake anhydrite (762 ms on vertical component data, 984 ms on radial component data) shows smaller variation on velocity spectrum. The velocity map shows the velocity to be constant above the top of the Dawson Bay Formation. The largest variation of stack

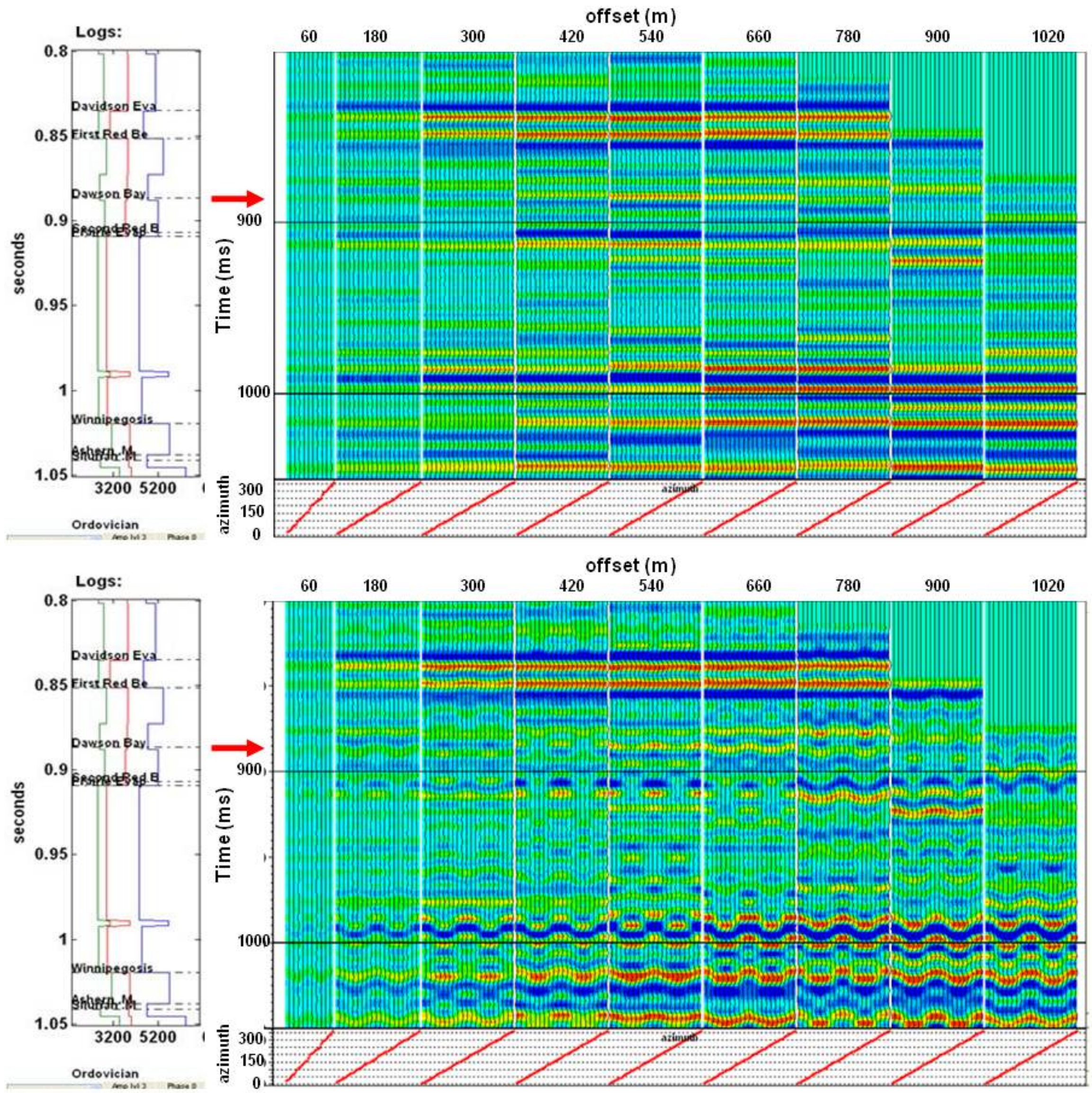

Figure 6.15 Well logs (Vp: blue; Vs: green; density: red) and offset-azimuth supergathers of the radial component for the isotropic (top) and the HTI (bottom) earth models (mild mute is applied to the gahters). The red plots at the bottom are azimuths. Common-offset gathers are separated by space, and offset increases to the right.

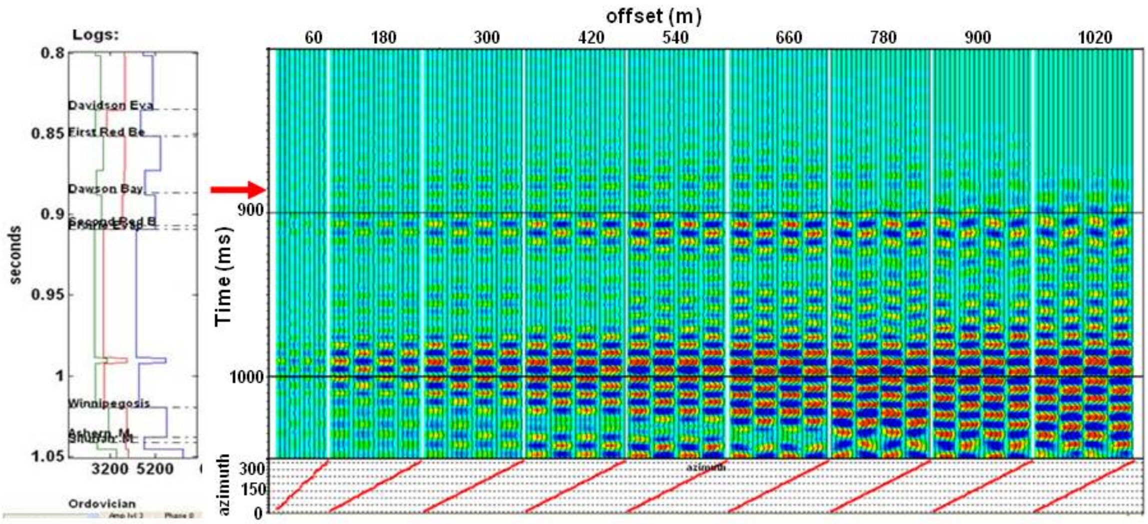

Figure 6.16 Well logs (Vp: blue; Vs: green; density: red) and offset-azimuth supergathers of the transverse component for the HTI earth model. The red plots at the bottom indicate the azimuths.

velocity with azimuth exists at the bottom of the fractured Dawson Bay. A similar observation can also be made on velocity plots for the six azimuths from 0 to 90 degree. For the P wave data, the maximum stacking velocity at the bottom of the Dawson Bay Formation is at azimuth 0°, which is parallel to the isotropy plane. The minimum stacking velocity at the base of the Dawson Bay Formation for the PS data is found to be at azimuth 45°.

6.3.2 Shear-wave splitting analysis

Figure 6.19 and Figure 6.20 show the azimuth bin stacks of vertical and radial components for both isotropic and HTI models. The stack results were also correlated to synthetic seismograms from well logs. The correlations between synthetic seismograms and azimuth bin stacks are quite good for both vertical and radial components. The four events picked (from top to bottom) are: the top of the First Red Shale (Event 1), the top of the Dawson Bay Formation (Event 2), the base of the Dawson Bay Formation (Event 3), and the top of the Shell Lake Anhydrite (Event 4). At the top of the First Red Bed

Shale, stacks of isotropic and anisotropic models are quite consistent. Below Event 1, the reflections are coherent with azimuth on stack results of the isotropic model. On the stack results of anisotropic model, however, there are variations of amplitude and time with azimuth. This is especially evident on the radial component. The differences between stack results of isotropic and anisotropic models, is the smallest at azimuth 0° and 180° (along fracture plane direction) for both vertical and radial components, while the

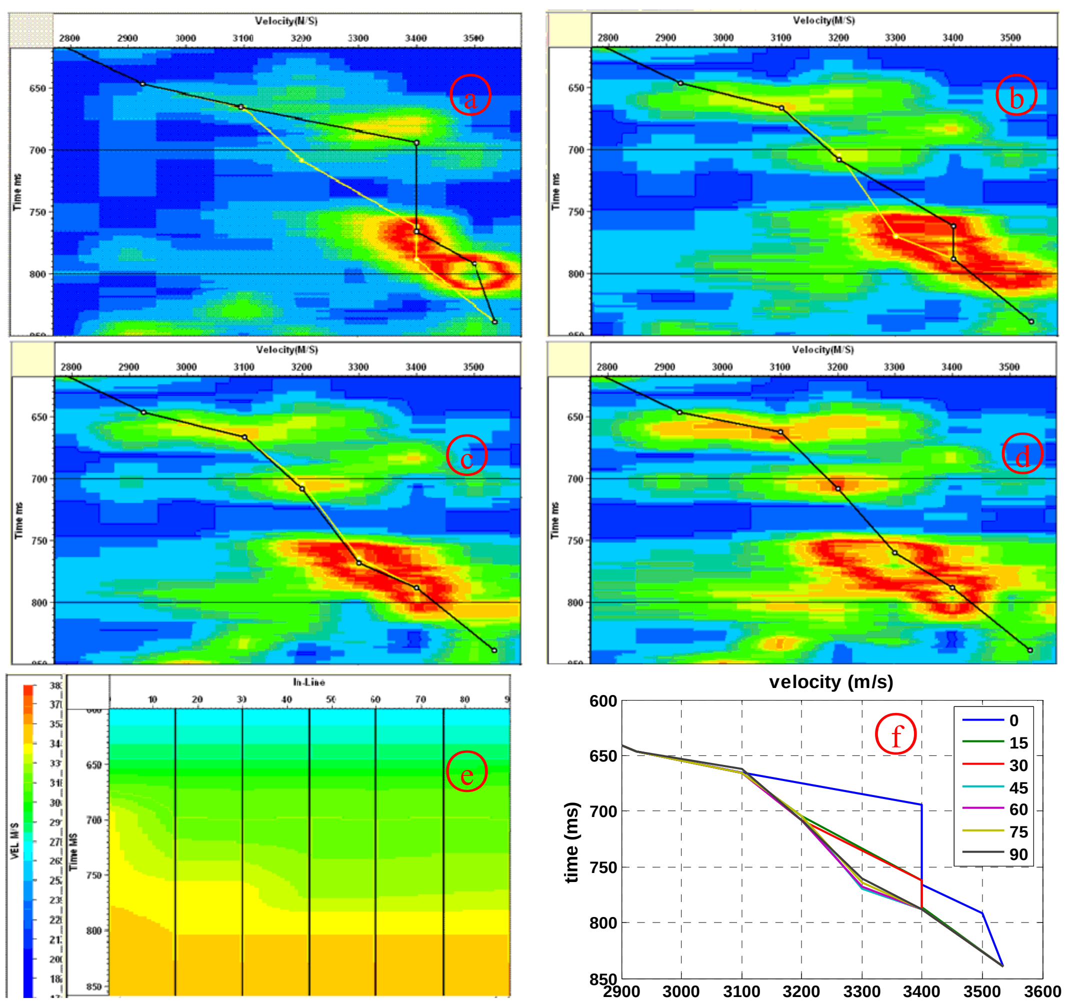

Figure 6.17 Vertical component velocity spectra (the black line denotes the velocity picks on the present spectrum, the yellow line is the picks on the adjacent spectrum) of HTI model at azimuth 0° (a), 30° (b), 60° (c), and 90° (d), stack velocity section (e) and stack velocity plots at the seven azimuths (f) from 0° to 90°.

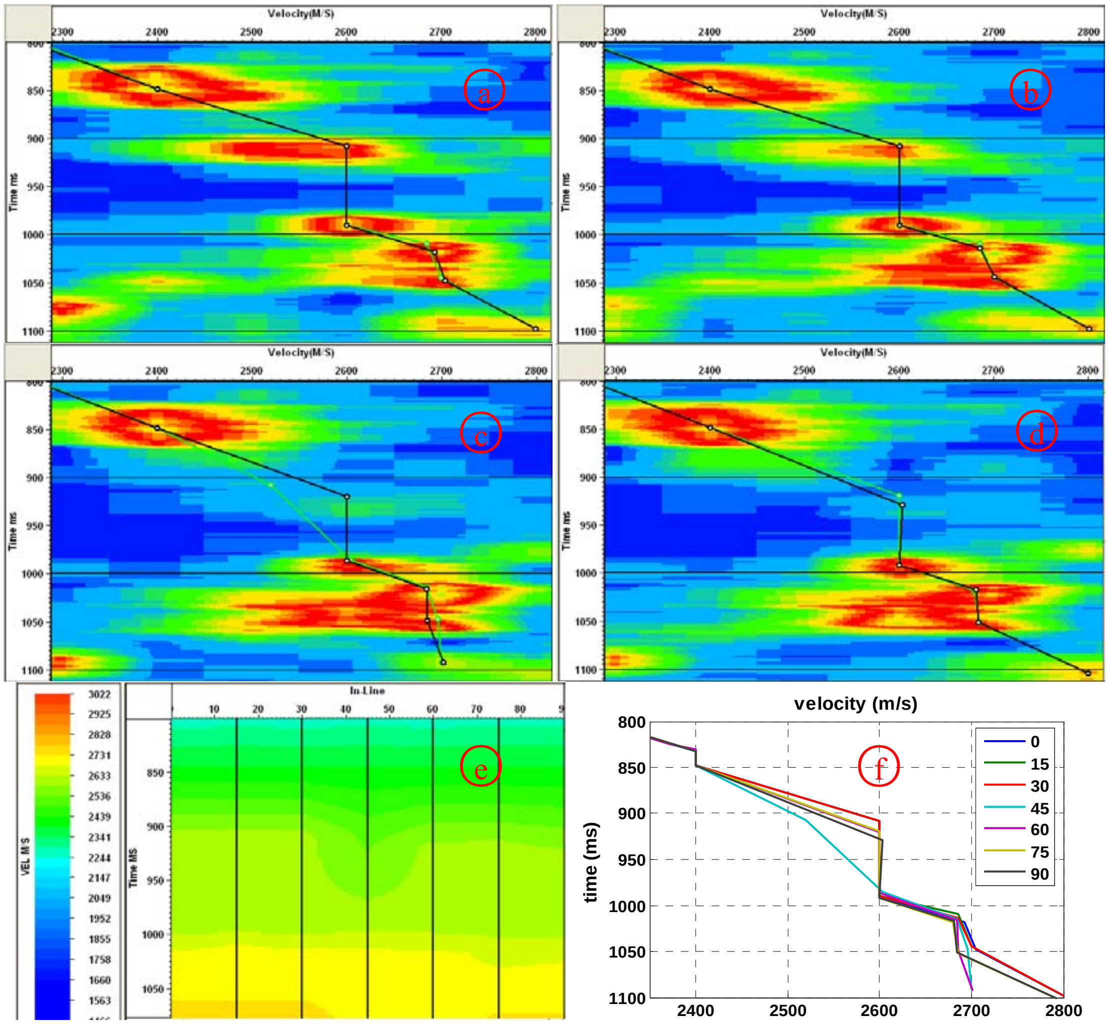

Figure 6.18 Radial component velocity spectra (the black line denotes the velocity picks on the present spectrum, the yellow line shows the picks on the adjacent spectrum) of the HTI model at azimuths 0° (a), 30° (b), 60° (c), and 90° (d), stack velocity section (e) and stack velocity plots at the seven azimuths (f) from 0° to 90°.

difference is the largest at azimuths of 90° and 270° (along the fracture normal direction). On the bin stack of transverse component (bottom of Figure 6.21), only the reflections below the top of the Dawson Bay can be seen, and no sinusoidal shape reflections time variation is found. However, polarity flip happens across 0°, 90°, 180° and 270°. From the amplitude plots of the bottom two selected reflections in Figure 6.22, the base of the Dawson Bay Formation and the top of the Shell Lake Anhydrite, we can see that amplitude crosses 0 at these four azimuths. Within each quadrant, amplitude increases with azimuth for the first 45 degrees then decreases.

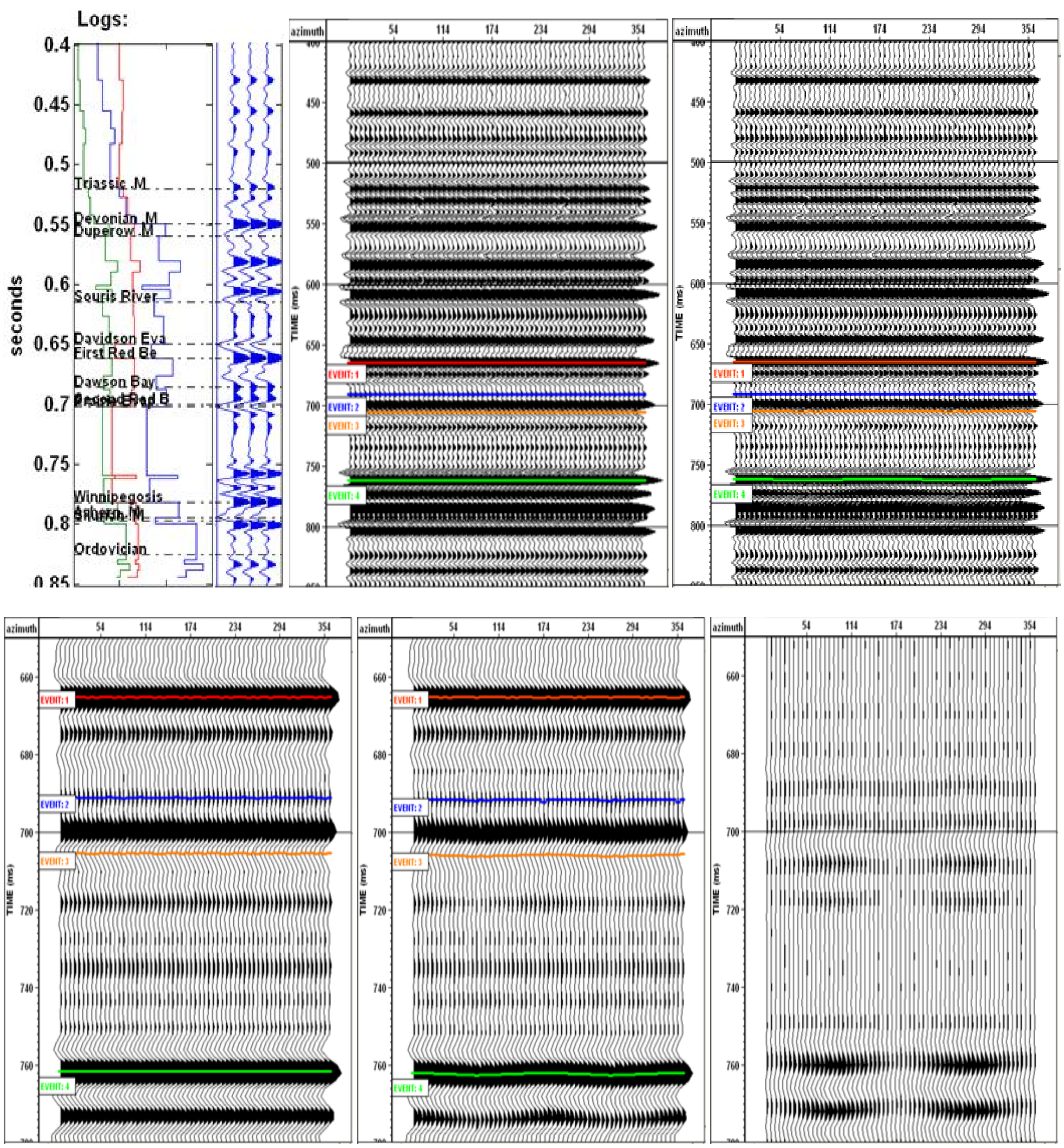

Figure 6.19 Top, from left to right: well logs (Vp: blue; Vs: green; density: red), PP synthetic seismograms (duplicated stack traces), azimuth bin stack of vertical component for isotropic earth model, and azimuth bin stack of vertical component for anisotropic earth model. Bottom, from left to right: azimuth bin stack of vertical component for isotropic (left) and anisotropic (middle) earth model, and their difference (right) focused on the fractured layer. The four events picked (from top to bottom) are the top of the First Red Shale, the top of the Dawson Bay Formation, the base of the Dawson Bay Formation, and the top of the Shell Lake Anhydrite.

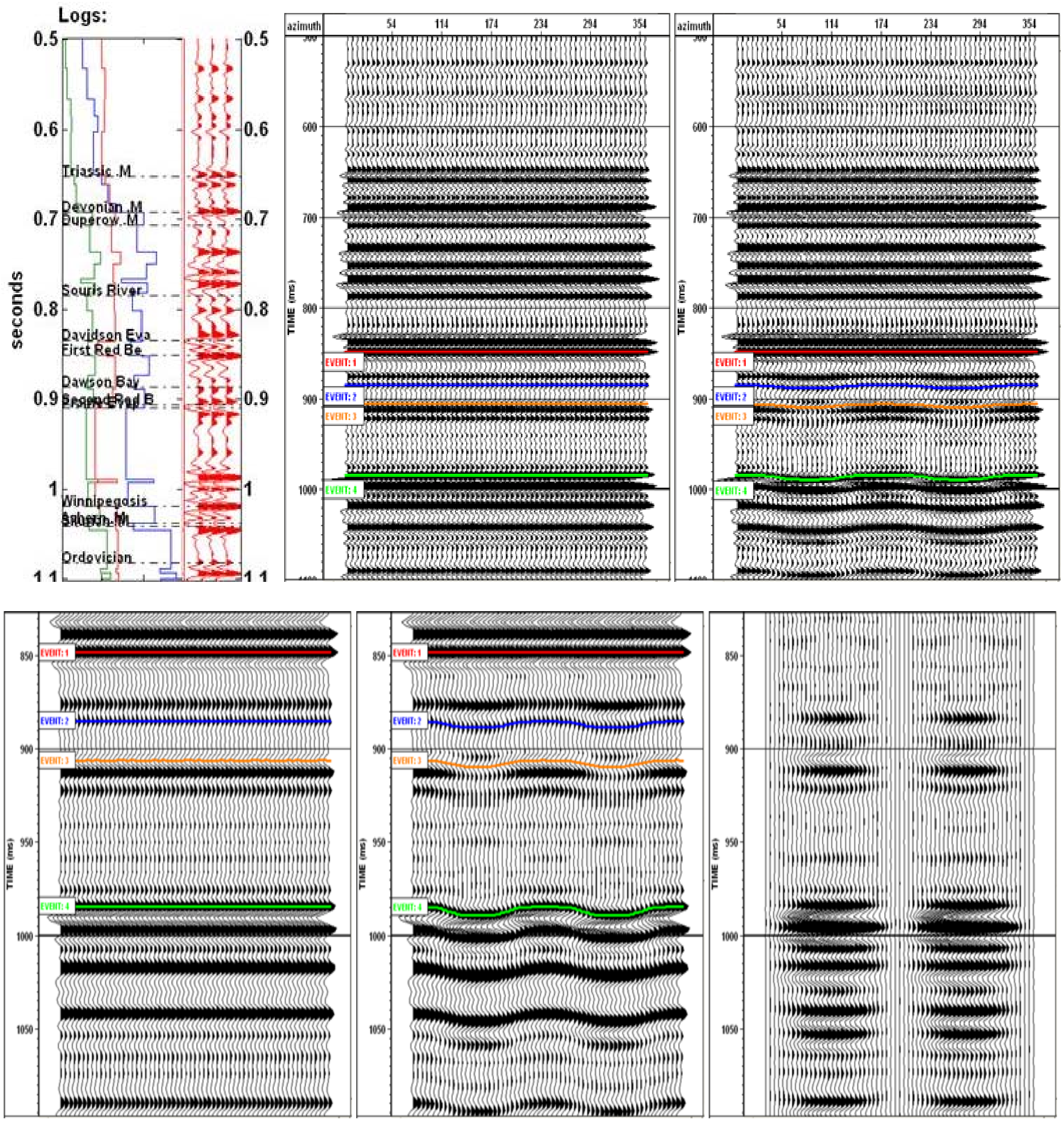

Figure 6.20 Top, from left to right: well logs (Vp: blue; Vs: green; density: red), PS synthetic seismograms (duplicated stack traces), azimuth bin stack of the radial component for the isotropic earth model, and azimuth bin stack of radial component data for the anisotropic earth model. Bottom, from left to right: azimuth bin stack of the radial component for the isotropic (left) and anisotropic (middle) earth model, and their difference (right) focused on the fractured layer. The four events picked (from top to bottom) are the top of the First Red Shale, the top of the Dawson Bay Formation, the base of the Dawson Bay Formation, and the top of the Shell Lake Anhydrite.

Figure 6.21 shows the interpretation result for the fast and slow shear-wave directions. The fast shear-wave, S1, is along 0°-180° direction, which is consistent with the fracture plane direction of the input model. The slow shear-wave orientation is along the 90°-270° direction, the direction normal to the fractures of the input model.

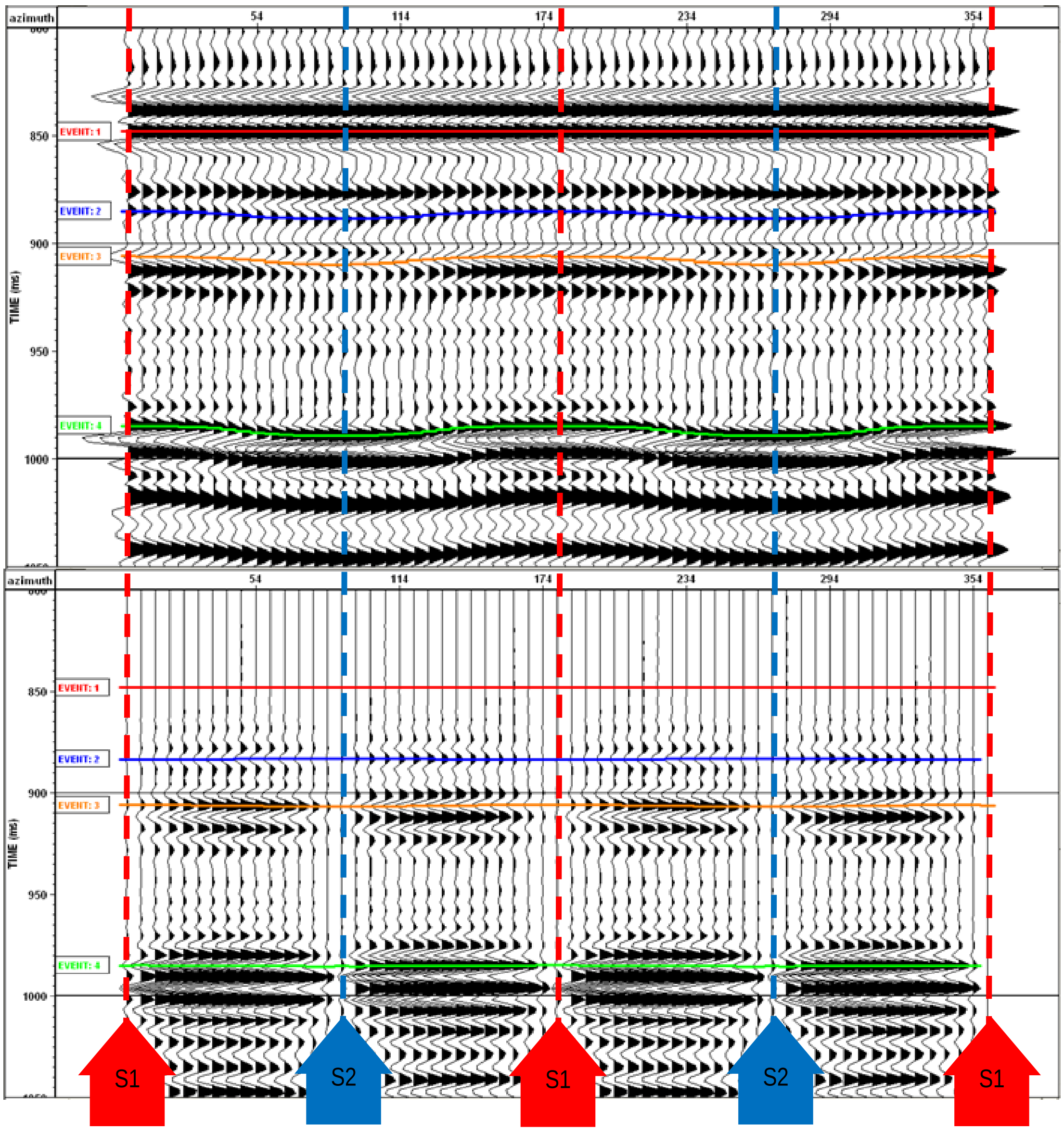

Figure 6.21 Radial (top) and transverse (bottom) component azimuth bin stacks of the fractured earth model. The red dashed lines show the fast shear-wave (S1) polarization direction, and the blue dashed lines show the slow shear-wave (S2) polarization direction. The four events picked (from top to bottom) are the top of the First Red Shale, the top of the Dawson Bay Formation, the base of the Dawson Bay Formation, and the top of the Shell Lake Anhydrite.

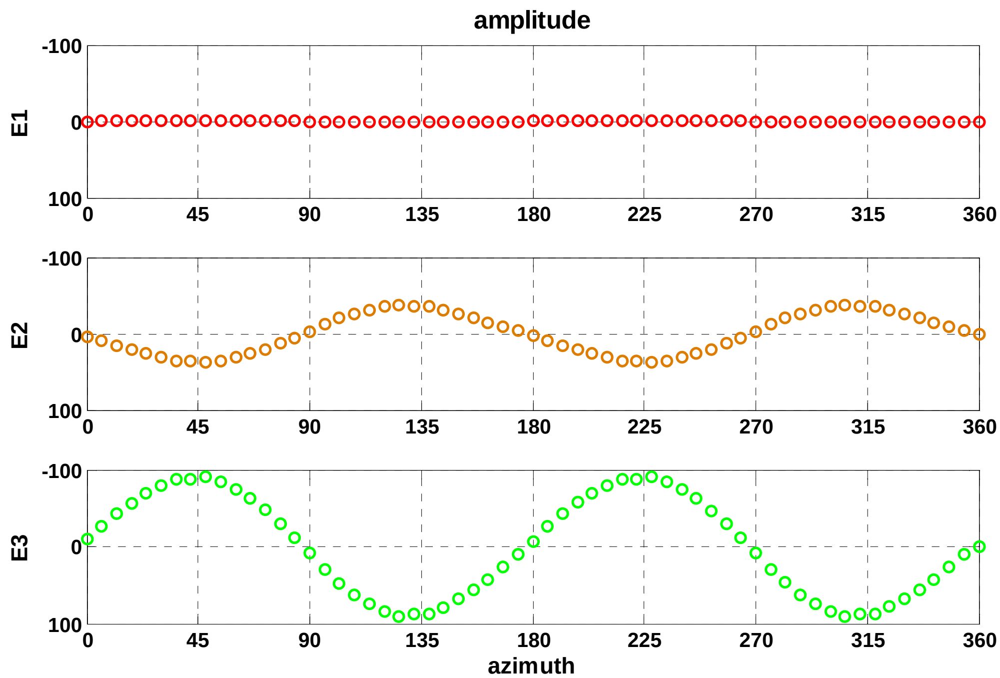

Figure 6.22 Amplitude plots of transverse component azimuth bin stack of the anisotropic model. The three events are the top of the First Red Shale (E1), the base of the Dawson Bay Formation (E2), and the top of the Shell Lake Anhydrite (E3).

Then the horizontal components were processed in S1 and S2 coordinates. The results are shown as Figure 6.23. It can be seen that there is no shear-wave splitting above the fractured layer. When the shear-wave propagates through the fractured layer, the waves split into slow and fast waves and the time shifts can be seen on azimuth stack results in the S1 and S2 directions.

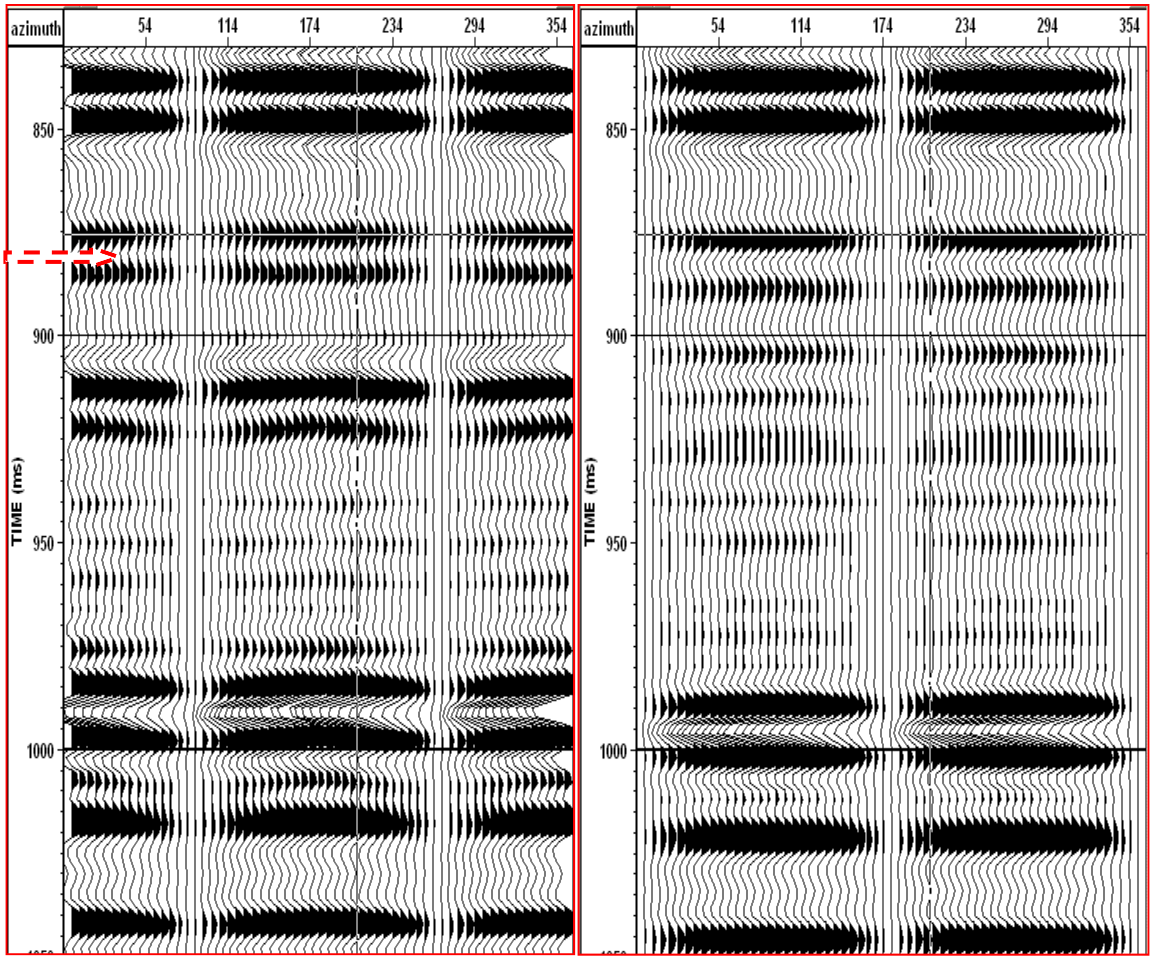

Figure 6.23 Horizontal components azimuth bin stack in S1 (left) and S2 (right) coordinates. The red arrow marks the location of the fractured layer.

6.3.3 Time-lapse attribute analysis

Time-lapse attribute analysis was performed for time and amplitude of the three picked events mentioned before, the top of the First Red Shale (E1), the base of the Dawson Bay Formation (E2), and the top of the Shell Lake Anhydrite (E3). Figure 6.24 displays the time and amplitude plots of the three events for the vertical component of isotropic and HTI models together with the corresponding differences. At the top of the First Red Bed Shale (E1), since all the overlying strata of the two models are the same and isotropic, there is almost no time shift from azimuth 0 to 360 degree. However, small amplitude difference, up to a 3.2% increase, exists at the top of this layer. At the bottom of the Dawson Bay Formation (E2), up to a 0.75ms time delay and ±3.7% amplitude change can be seen due to the fractures. Although all the formations underlying the Dawson Bay Formation are the same for the two earth models, and both are isotropic, larger time delay (up to 1.1ms) and amplitude change (up to 12.2%) are found at deeper reflections, e.g., the top of the Shell Lake Anhydrite (E3). The reason for the increases of time delay and amplitude change could be the incidence angle difference for E2 and E3 when P waves travel through the anisotropic layer.

Figure 6.25 shows the time and amplitude plots of the three events on the radial component of the isotropic and anisotropic models, together with corresponding differences. At the top of the First Red Bed Shale (E1), since all the overlying strata of the two models are same and isotropic, there is almost no time shift for azimuths from 0 to 360 degree. Similarly, a small amplitude difference, up to 2.2% increase, can also be seen at the top of the anisotropic layer on radial component. At the bottom of the Dawson Bay Formation (E2), we can see a larger time delay (up to 3.75 ms) and amplitude change (up to 46% decrease) compared with the vertical component. As seen for the vertical component, although all the formations underlying the Dawson Bay Formation are identical for the two earth models and both are isotropic, an increasing time delay (up to 4.9 ms) is found at deeper reflections, e.g., the top of the Shell Lake anhydrite (E3), and the amplitude change is up to 30%. The reason should be similar to that observed in the vertical component case.

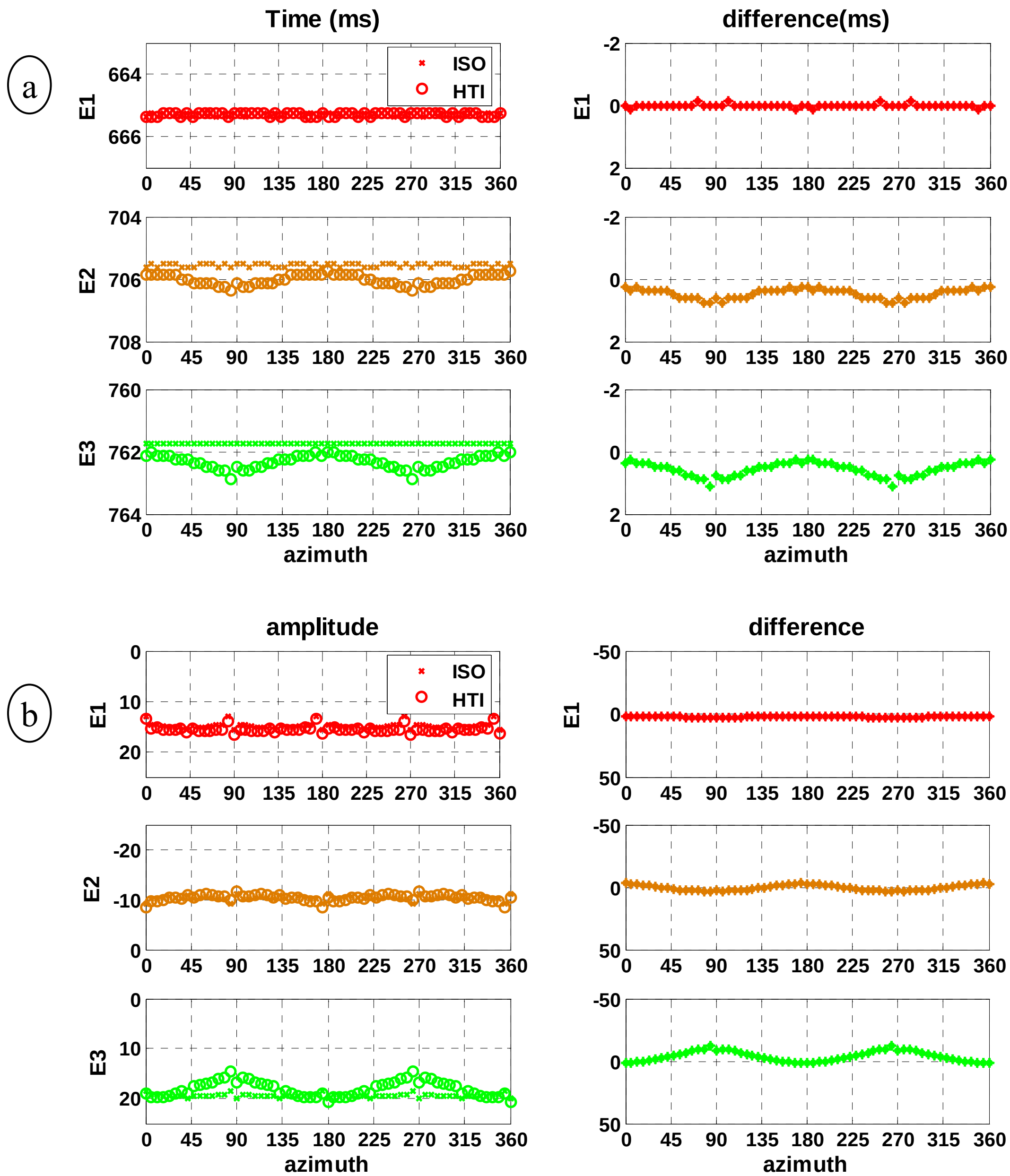

Figure 6.24 Time (a) and amplitude (b) plots of the three events on the vertical component azimuth bin stacks for the unfractured (denoted as ISO) and fractured (denoted as HTI) earth model. The amplitude differences are on a percentage scale. The three events are the top of the First Red Shale (E1), the base of the Dawson Bay Formation (E2), and the top of the Shell Lake Anhydrite (E3).

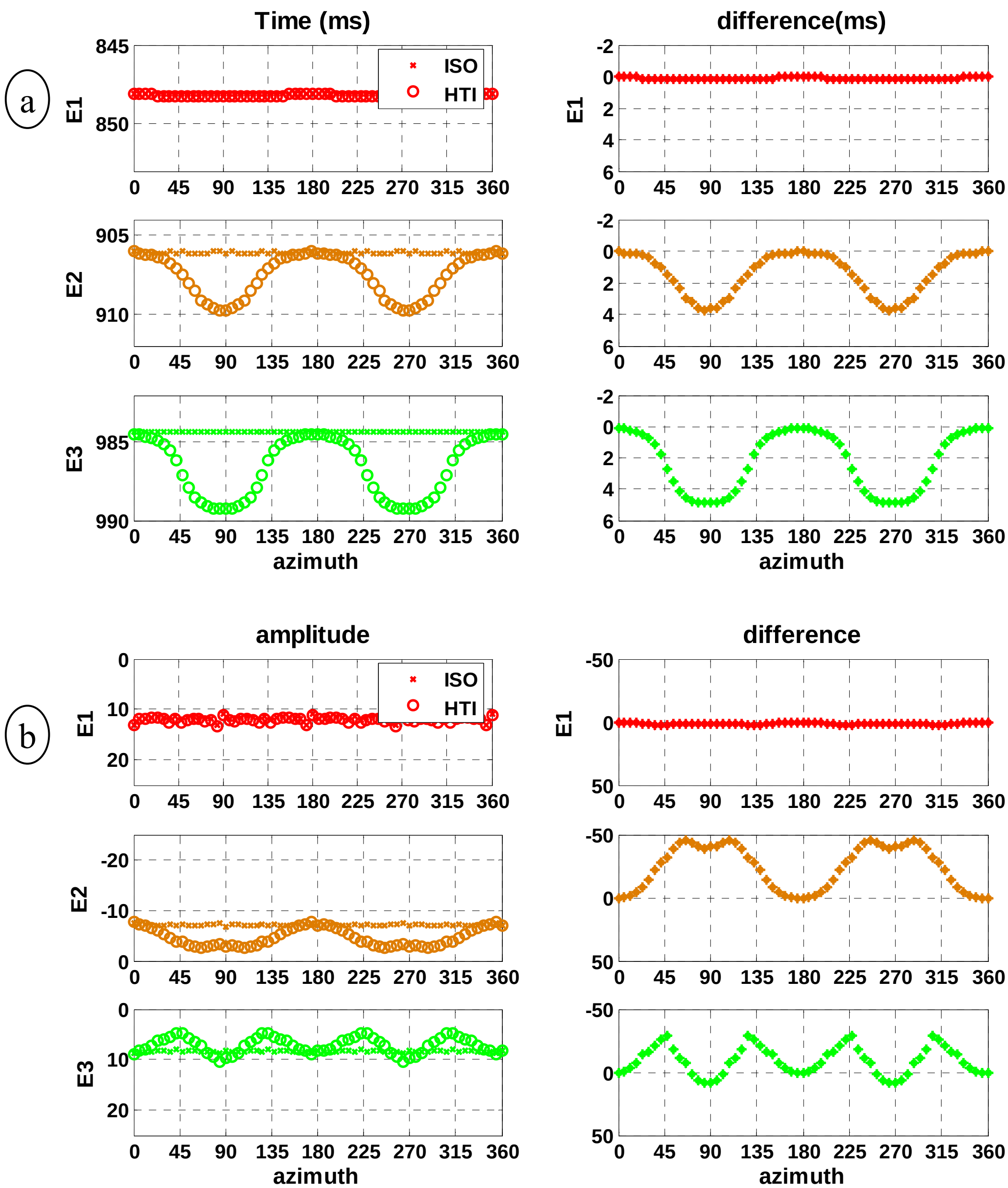

Figure 6.25 Time (a) and amplitude (b) plots of the three events on radial component azimuth bin stacks for the unfractured (denoted as ISO) and fractured (denoted as HTI) earth model. The amplitude differences are on a percentage scale. The three events are the top of the First Red Shale (E1), the base of the Dawson Bay Formation (E2), and the top of the Shell Lake Anhydrite (E3).

The resultant time shift from shear-wave splitting can be used to calculate the fracture density using a method by Tsvankin (1997). At the bottom of the fractured layer, the time shift between slow- and fast-shear waves is 3.75 ms, which is equivalent to 1.2%

porosity caused by fracture. The result is comparable to the input model value, 1% fracture porosity.

6.3.4 Discussion

The previous analysis shows that the anisotropy caused by vertically aligned fractures in the Dawson Bay Formation is evident on PP and PS data. From the offset-azimuth gathers, residual moveout can be clearly seen since only isotropic NMO is applied on the data of HTI models. We can see the proof of anisotropy, on the other side, the time shift and amplitude difference might not be the same if NMO is accurately corrected by considering anisotropy effects.

However, vertically aligned fractures in the 40 m Dawson Bay Formation can be detected by 3C seismic data. The time shift and amplitude changes are significant, especially for radial component data. The fracture orientation can also be determined by the shear-wave polarization. Thus multicomponent seismic data may be an effective way to map and monitor fractures in the Dawson Bay Formation for potash mining.

6.4 Summary

This chapter presents the processing and interpretation of seismic modeling data of the earth models generated based on well logs in a potash mining area. The goal of the work is to study the evidence of azimuthal seismic anisotropy, shear-wave splitting, and time-lapse seismic signals caused by HTI anisotropy from vertically aligned fractures in the Dawson Bay Formation. The results show that seismic velocity anisotropy can be detected by both vertical and horizontal components of the HTI earth model, it is especially evident on radial component data. Shear-wave splitting is distinctive, and the fracture orientation determined by the polarization of fast and slow shear waves is consistent with the input model. The time-shift and amplitude changes due to the anisotropic layer are also apparent on both vertical and radial component data. The time-shift on radial data is up to 5 ms at the top of the Shell Lake Anhydrite, and the amplitude change is up to 46% at the base of the Dawson Bay Formation.

Combined with the correlation results of well and surface seismic data in the previous study, this suggests that multicomponent seismic data could be interpretable in this potash area of western Canada. This also suggests that by searching for seismic anisotropy, shear-wave splitting on the multicomponent seismic data or by looking for changes in repeated seismic surveys, we may be able to detect/monitor fractures, and fracture direction as well as intensity in the Dawson Bay Formation and similar intervals can also be determined.

Chapter Seven: Conclusions and future work

7.1 Conclusions

In this dissertation, integrated petrophysical and multicomponent seismic studies were carried out for two study areas, the Ross Lake heavy oil field and a Saskatchewan potash mining site. The 3C VSP data were used for characterizing a Cretaceous age channel sand at Ross Lake. By utilizing the VSP advantages in a wave propagation study, a true reflectivity AVO gather was processed from walkaway VSP data, and seismic attenuation was also estimated for additional information in seismic interpretation. In the Saskatchewan potash mining case, rock physics, multicomponent seismic and time-lapse seismic techniques were integrated for brine inflow monitoring and prevention. The main target formation is a dolomitized carbonate unit of Devonian age with a thin shale layer at the bottom.

The 3C VSP study at Ross Lake revealed that: 1) the VSP data is valuable for providing a reliable correlation between well logs and seismic data, as well as good quality image of the rocks close to the borehole; 2) the walkaway VSP data can yield a true reflectivity offset gather for AVO analysis; 3) in situ rock properties in depth, such as seismic velocity and attenuation can be derived from VSP data; 4) an interesting correlation was found between the Q values and rock properties, such as Vp, Vs, porosity, and Vp/Vs. The relationship between Qp and clay-bound water also indicates seismic attenuation influenced by the phase of the fluid in the pore space; 5) frequency analysis on the 3C far-offset VSP data displayed that the frequency contents of PP and PS are similar near the reflectors, and the difference between the frequency of PP and PS data at some distance from the reflectors are mostly explained by attenuation.

The study using the Kuster-Toksöz and the Hudson's models for fractured/cracked media indicated that there are limitations for using the models, and the rock properties of fractured media are largely dependent on the pore shape. A small quantity of thin fractures/cracks can cause large velocity changes for various kinds of rocks.

At the Saskatchewan potash mining area, the petrophysical and seismic simulation study indicated the feasibility of using repeated multicomponent seismic to detect and monitor fractures which might pose a brine inflow problem to the mining operation. Seismic interpretation on the time-lapse 3C-3D surveys saw visible seismic signature changes similar to those on the modeling results. Based on the interpretation, three possible fractured zones were delineated. Fractured zones can also be outlined by seismic curvature attributes. From rock physics modeling results, aligned fractures in the rocks will produce velocity anisotropy. To study the evidence of azimuth seismic anisotropy, shear-wave splitting and time-lapse seismic signals caused by vertically aligned fractures, numerical seismic data were modelled. The results show detectable seismic velocity anisotropy and distinctive shear-wave splitting. From shear wave splitting, the fracture orientation and intensity can be determined. There are also detectable seismic difference attributes between unfractured and fractured models.

7.2 Future work

The well logs and the 3C VSP data of the Ross Lake oilfield provide a good opportunity to study the relationship between seismic attenuation and rock properties. However, the relationships for the channel sands are not acquired due to lack of downhole receivers beneath the reservoir. 3C surface seismic data was also acquired in the studied area. Therefore, Q values of the channel sands can be derived from the surface seismic data. Since the upper and lower sand in the studied area have similar rock properties, but saturated by oil and water, respectively, the fluid effect on the relationship is expected to be found. The processing results of horizontal radial (Hmax) and transverse (Hmin) suggest that there is possibly near-surface shear velocity anisotropy. Further analysis from multicomponent surface seismic can be done to confirm the existence of the anisotropy and then to delineate it.

The interpretation of the time-lapse 3C-3D post-stack seismic data at the Saskatchewan potash mining indicate the possibility of fractures created between 2004 and 2008 in the Dawson Bay Formation. But fracture information such as fracture intensity and fracture orientation can not be determined by post-stack seismic data. The analysis on the numerical modeling data based on the well logs suggests that such information can be acquired from velocity anisotropy and shear-wave splitting analysis. For detailed fracture description, velocity anisotropy and shear-wave splitting analysis on the field 3C-4D pre-stack seismic data should be carried out in the future.

References

Aki, K.T., and Richards, P.G., 1980, Quantitative seismology: theory and methods: Vol. 1: W.H. Freeman and Co.

Al-dossary, S., and Marfurt, K. J., 2006, 3D multispectral estimates of reflector curvature and rotation: Geophysics, **71**, 41-51.

Annan, A., Davis, J., and Gendzwill, D., 1988, Radar soundings in potash mines: Saskatchewan, Canada: Geophysics, **53**, 1556–1564.

Bale, R.A. and Stewart, R.R., 2002, The impact of attenuation on the resolution of multicomponent seismic data: CREWES Research Report, 14.

Berryman, J.G., 1980, Long-wavelength propagation in composite elastic media: Journal of the Acoustical Society of America, **68**, 1809-1831.

Best, A.l., McCann, C., and Sothcott, J., 1994, The relationships between the velocities, attenuations and petrophysical properties of reservoir sedimentary rocks: Geophysical Prospecting, **42**, l5l-l78.

Biot, M.A., 1956a, Theory of elastic waves in a fluid-saturated porous solid: I. low-frequency range: Journal of the Acoustical Society of America, **28**, 168-178.

Biot, M.A., 1956b, Theory of elastic waves in a fluid-saturated porous solid: I. higher frequency range: Journal of the Acoustical Society of America, **28**, 179-191.

Blias, E., 2007, VSP wavefield separation: wave-by-wave optimization approach: Geophysics, **72**, T47-T55.

Brown, R., and Korringa, J., 1975, On the dependence of the elastic properties of a porous rock on the compressibility of the pore fluid: Geophysics, **40**, 606-616.

Cheng, C.H., 1993, Crack models for a transversely anisotropic medium: Journal of Geophysical Research, **98**, 675-684.

Christopher, J. E., 1974, The Upper Jurassic Vanguard and Lower Cretaceous Mannville Groups of Southwestern Saskatchewan: Department of Mineral Resources: Saskatchewan Geological Survey, Sedimentary Geology Division, Report No. 151.

Coulombe, C.A., Stewart, R.R., and Jones, M.J., 1996, AVO processing and interpretation of VSP data: Canadian Journal of Exploration Geophysics, **32**, 41-62.

Crain, R., 2005, Petrophysical techniques course notes: University of Calgary.

Crampin, S., 1981, A review of wave motion in anisotropic and cracked elastic-media: Wave Motion, **3**, 343-391.

Crampin, S., 1983, Shear-wave polarizations: a plea for three-component recording: 53rd Annual International Meeting, SEG, Expanded Abstracts, 425-428.

Crampin, S., 1985, Evaluation of anisotropy by shear-wave splitting: Geophysics, **50**, 142-152.

DeMille, G., Shouldice, J.R., and Nelson, H.W., 1964, Collapse structure related to evaporites of the Prairie Formation, Saskatchewan: Geological Society of America Bulletin, **75**, 307-316.

DiSiena, J.P., Byun, B.S., Fix, J.E., and Gaiser, J.E., 1984, F-K analysis and tube wave filtering, in Toksoz, N.M. and Stewart, R.R., Eds., Vertical Seismic Profiling, Part B: Advanced Concepts: Geophysical Press.

Eso, R., Oldenburg, D., and Maxwell, M., 2006, Application of 3D electrical resistivity imaging in an underground potash mine: 76th Annual International Meeting, SEG, Expanded Abstracts, 629-632.

Fuzesy, L.M., 1982, Petrology of potash ore in the Esterhazy Member of the Middle Devonian Prairie Evaporite in southeastern Saskatchewan: Proceedings of the Fourth International Williston Basin Symposium, 67-73.

Gaiser, J., and Van Dok, R., 2002, PS-wave azimuthal anisotropy: benefits for fractured-reservoir management: 72nd Annual International Meeting, SEG, Expanded Abstracts.

Ganguly, N., Dearborn, D., Moore, M., Gordon, D., Horan, M., and Chopra, S., 2009, Application of seismic curvature attribute in the appraisal of the Tishrine-West field, North-East Syria: Recorder, **34**, 29-43.

Gassmann, F., 1951, Über die elastizität poröser medien: Vierteljahrss-chrift der Naturforschenden Gesellschaft in Zürich, **96**, 1-23. The English translation of this paper can be found at http://sepwww.stanford.edu/sep/berryman/PS/gassmann.pdf.

Gendzwill, D.J., 1969, Udergound application of seismic measurements in a Saskatchewan potash mine: Geophysics, **34**, 906-915.

Gendzwill, D. J. and Lundberg, R. M., 1989, Seismic anomalies of Saskatchewan Winnipegosis mounds: Geophysical Atlas of Western Canada Hydrocarbon Reservoirs: Canadian Society of Exploration Geophysicists.

Gupta, I. N., 1973a, Dilatancy and premonitory variations of PS travel times: Bulletin of the Seismological Society of America, **63**, 1157–1161.

———, 1973b, Premonitory variations in S-wave velocity anisotropy before earthquakes in Nevada: Science, **182**, 1129–1132.

Haase, A. B., and Stewart, R. R., 2004, Attenuation Estimates from VSP and Log Data: 74th Annual International Meeting, SEG, Expanded Abstracts, 2497-2500.

Han, D.H., and Batzle, M., 2004, Estimating shear velocity based on dry P-wave and shear modulus relationship: 74th Annual International Meeting, SEG, Expanded Abstracts.

Hamid, H., Morozov, I.B., and Kreis, L.K., 2004, Progress in seismic delineation of the southern margin of the Middle Devonian Prairie Evaporite Formation in the Elk Point Basin, south-central Saskatchewan: Summary of Investigations 2004, Volume 1: Saskatchewan Geological Survey, Sask. Industry Resources, Misc. Rep. 2004-4.1, CD-ROM, Paper A-5, 9p.

Hardage, B.A., 1983, Vertical seismic profiling: principles: Geophysical Press.

Hardage, B.A., 2001, Developments, trends and future directions in vertical seismic profiling and crosswell seismic profiling: Recorder, 72-78.

Hauge, P. S., 1981, Measurements of attenuation from vertical seismic profiles: Geophysics, **46**, 1548-1558.

Helbig, K., and Thomsen, L., 2005, 75-plus years of anisotropy in exploration and reservoir seismics: A historical review of concepts and methods: Geophysics, **70**, 9-23.

Hinds, R. C., and Kuzmiski, R.D., 1996, VSP interpretative processing: theory and practice: Society of Exploration Geophysicists.

Hinds, R. C., and Kuzmiski, R.D., 2001, VSP for the interpreter/processor for 2001 and beyond: part 1: Recorder, 84-95.

Hudson, J.A., 1980, Overall properties of a cracked solid: Math. Proc. Cambridge Philos. Soc., **88**, 371-384.

Hudson, J.A., 1981, Wave speeds and attenuation of elastic waves in material containing cracks: Geophysical Journal of the Royal Astronomical Society, **64**, 133-150.

Johnston, D.H., Toksöz, M. N., and Timur, A., 1979, Attenuation of seismic waves in dry and saturated rocks: II. Mechanisms: Geophysics, **44**, 691-711.

Klimentos T., and McCann C., 1990, Relationships among compressional wave attenuation, porosity, clay content and permeability in sandstones: Geophysics, **55**, 998-1014.

Kjartansson, E., 1979, Constant Q - wave propagation and attenuation: Journal of Geophysical Research, **84**, 4737-4748.

Koesoemadinata, A. P., and McMechan, G. A., 2001, Empirical estimation of viscoelastic seismic parameters from petrophysical properties of sandstone: Geophysics, **66**, 1457-1470.

Kuster, G.T., and Toksöz, M.N., 1974, Velocity and attenuation of seismic waves in two-phase media: Part I. theoretical formulations: Geophysics, **39**, 587-606.

Lisle, R.J., 1994, Detection of zones of abnormal strains in structures using Gaussian curvature analysis: AAPG Bulletin, **78**, 1811-1819.

Macbeth, C., 2002, Multicomponent VSP analysis for applied seismic anisotropy: Elsevier Science Ltd.

Margrave, G.F., Lawton, D.C., and Stewart, R.R., 1998, Interpreting channel sands with 3C-3D seismic data: The Leading Edge, **17**, 509-513.

Mavko, G. M., 2006, Introduction to Rock Physics course notes: Stanford University.

Mavko, G. M., and Dvorkin, J., 2005, A theoretical estimate of S-wave attenuation in sediment: 73rd Annual International Meeting, SEG, Expanded Abstract, 1470-1474.

Mavko, G.M., Mukerji, T., and Dvorkin, J., 1998, The rock physics handbook: Cambridge University Press.

Mavko, G.M., and Nur, A., 1975, Wave attenuation in partially saturated rocks: Geophysics, **44**, 161-178.

Maxwell, M., Unrau, J., Eso, R. A., Oldenburg, D.W., Song, L.P., 2005, Advancement of 2D and 3D electrical resistivity techniques for underground applications in a potash mine: 2005 International Symposium on Mine Planning and Equipment Selection, Technical Paper.

Mukerji, T., and Mavko, G., 2006, Recent advances in rock physics and fluid substitution: Recorder 2006 Special Edition, 123-127.

Pérez, M.A., Grechka, V., and Michelena, R.J., 1999, Fracture detection in a carbonate reservoir using a variety of seismic methods: Geophysics, **64**, 1266–1276.

Pesowski, M.S., and Larson, R.K., 2000, Seismic exploration methods applied to potash mining: risk analysis and mine planning: 70th Annual International Meeting, SEG, Expanded Abstracts.

Prugger, A., Nemeth, B., and Danyluk, T., 2004, Detailed 3D seismic imaging of Paleozoic karst / collapse disturbances in Saskatchewan: case study from the potash belt: 2004 Annual CSEG Meeting, CSEG, Expanded Abstracts.

Roberts, A., 2001, Curvature attributes and their application to 3D interpreted horizons: First Break, **19**, 85-99.

Slack, R.D., Ebrom, D.A., McDonald, J.A., and Tatham, R.H., 1993, Thin layers and shear-wave splitting: Geophysics, **58**, 1468-1480.

Stewart, R.R., 1984, VSP interval velocities from traveltime inversion: Geophysical Prospecting, **32**, 608-628.

Stewart, R.R., 2001, VSP: An in-depth seismic understanding: Recorder, 79-83.

Stewart, R.R, and DiSiena, J.P., 1989, The values of VSP in interpretation: The Leading Edge, **8**, 16-23.

Stewart, R.R., Huddleston, P.D., and Tze Kong Kan, 1984, Seismic versus sonic velocities: A vertical seismic profiling study: Geophysics, **49**, 1153-1168.

Tatham, R.H., Matthews, M.D., Sekharan, K.K., Wade, C.J., and Liro, L.M., 1992, A physical model study of shear-wave splitting and fracture intensity: Geophysics, **57**, 647-652.

Thomsen, L., 1986, Weak elastic anisotropy: Geophysics, **51**, 1954-1966.

Toksöz, M. N., and Johnson, D. H., 1981, Seismic wave attenuation: Society of Exploration Geophysicists.

Toksöz, M.N., and Stewart, R.R., 1984, Vertical seismic profiling: advanced concept: Geophysical Press.

Tonn, R., 1991, The determination of seismic quality factor Q from VSP data: A comparison of different computational methods: Geophysical Prospecting, **39**, 1-27.

Tsvankin, I., 1997, Reflection moveout and parameter estimation for horizontal transverse isotropy: Geophysics, **62**, 614-629.

Xu, C., and Stewart R.R, 2003, Ross Lake 3C-3D seismic survey and VSP, Saskatchewan: A preliminary interpretation: CREWES Research Report, 58, 1-12.

Verdon, J. P., Kendall, J. M., and Wüstefeld, A., 2009, Imaging fractures and sedimentary fabrics using shear wave splitting measurements made on passive seismic data: Geophysical Journal International, **179**, 1245–1254.

Verdon, J.P., Kendall1, M., and Maxwell, S.C., 2010, A comparison of passive seismic monitoring of fracture stimulation from water and CO2 injection: Geophysics, **75**, MA1–MA7.

Walsh, J.B., 1966, Seismic wave attenuation in rock due to friction: Journal of Geophysical Research, **71**, 2591-2599.

White, J.E., 1975, computed seismic speeds and attenuation in rocks with partial gas saturation: Geophysics, **40**, 224-232.

APPENDIX A: 3C orientation of VSP data

A.1 Horizontal rotation

In downhole measurement, the geophone sonde twists and the horizontal components randomly orient from depth to depth. Generally, 3C geophone does not have systems for either downhole orientation or for measuring downhole relative orientation. Thus the coherency of the seismic events of the horizontal components is very poor. Figure A.1 displays the X and Y components of vertical vibrator zero-offset (54m) VSP data. It shows that the horizontal sensors are oriented randomly. Very little coherent signal can be seen on the raw x and y data. It is necessary to orient the horizontal components to consistent directions.

The orientation of horizontal components can be determined by hodogram analysis (Hinds et al., 1996). At each depth level, the angle for the rotation is chosen using a line through the hodogram constructed using the data in a window of one period / cycle after the first arrival. Once the rotation angle is determined, the horizontal components can be rotated into two horizontal directions (Figure A.2) using equation (A-1): horizontal radial, Hmax, which is tangent to source-receiver frame, contains most of SV wave and P wave; and horizontal transverse, Hmin, which is orthogonal to source-receiver frame, containing mainly SH wave. The coordinate system of x, y, and z components at the local receiver depth along with the coordinate axis used after rotation are shown in Figure A.2.

$$\begin{pmatrix} Hmax(t) \\ Hmin(t) \end{pmatrix} = \begin{pmatrix} x(t) & y(t) \end{pmatrix} \begin{pmatrix} cos(\theta) & -sin(\theta) \\ sin(\theta) & cos(\theta) \end{pmatrix}$$

(A-1)

where,

Hmax(t), Hmin(t): horizontal radial/transverse component;

x(t), y(t): X, Y components (field record);

θ: angle between X direction and horizontal radial direction.

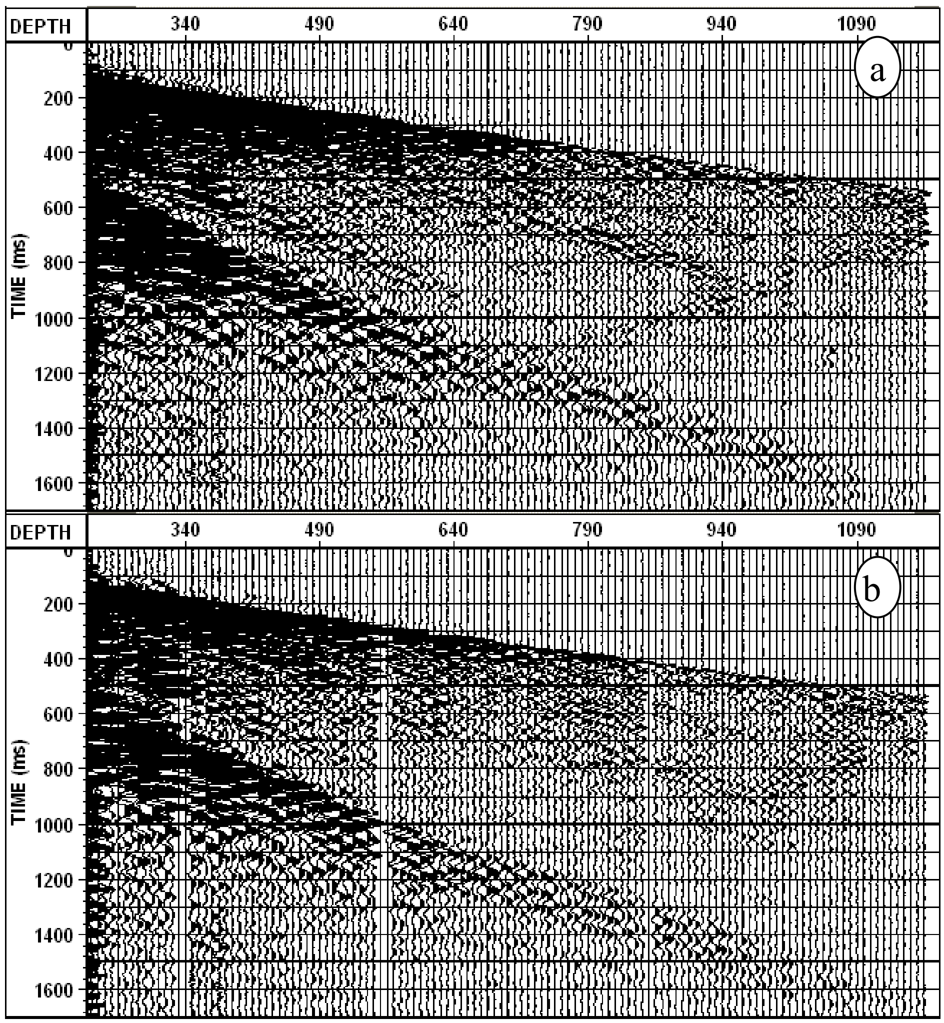

Figure A.1 X (a) and Y components (b) of vertical vibrator zero-offset VSP data (source offset 54 m). It shows that the horizontal sensors are oriented in randomly azimuth. Very little coherent signal can be seen on the raw x and y data.

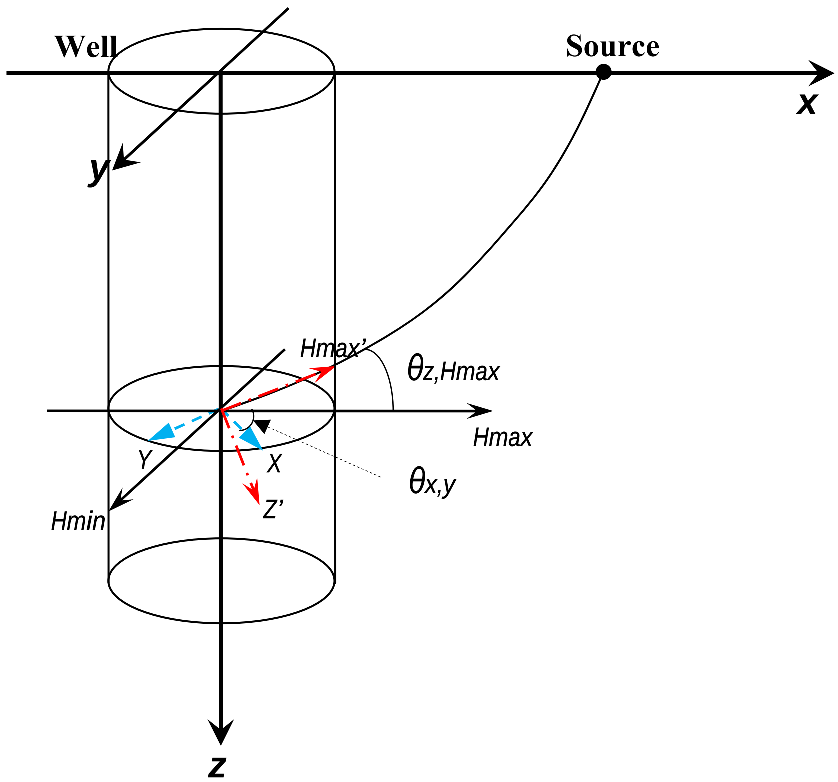

Figure A.2 The coordinate system of x, y, and z components at the local receiver depth along with the coordinate axis that will be used after rotation (after Hinds et al., 1996).

The Hmax and Hmin from rotation of X and Y components of vertical vibrator zero-offset (source offset 54 m) VSP data are shown in Figure A.3. Coherent events can be seen on the Hmax and Hmin components. Various wave types, including transmitted, reflected and direct S-waves were also recorded by horizontal receivers (refer to the wave type analysis of zero-offset VSP data in Chapter Two).

Figure A.4 displays the Hmax, and Hmin from horizontal rotation of X and Y component, and Z components of source offset 699 m VSP. On the horizontal component, transmitted, reflected and direct S-waves can be found. On the vertical component, direct and reflected P-waves can be easily spotted. Comparing with small source offset VSP data, much larger amount of direct S-waves can be seen on vertical component.

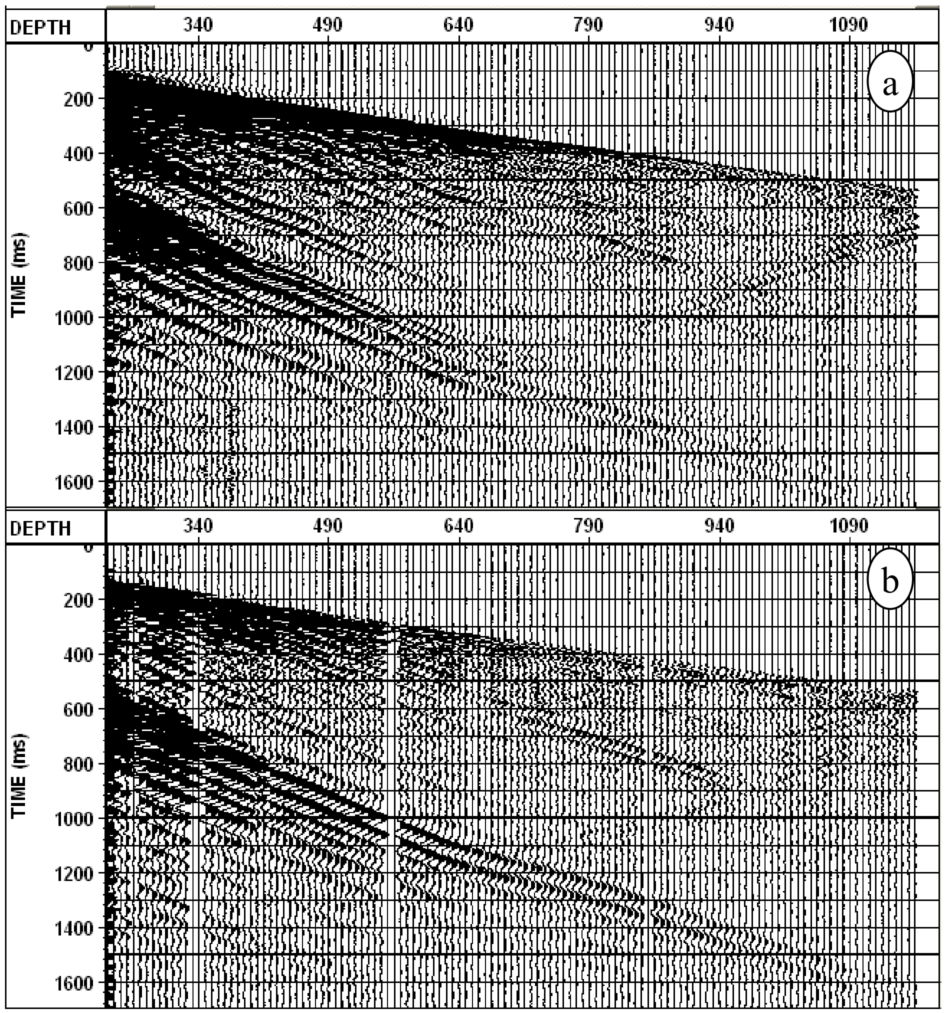

Figure A.3 Hmax (horizontal radial, a) and Hmin (horizontal transverse, b) of zero-offset VSP (offset 54m, vertical vibrator). Hmax and Hmin are from horizontal rotation of X and Y components.

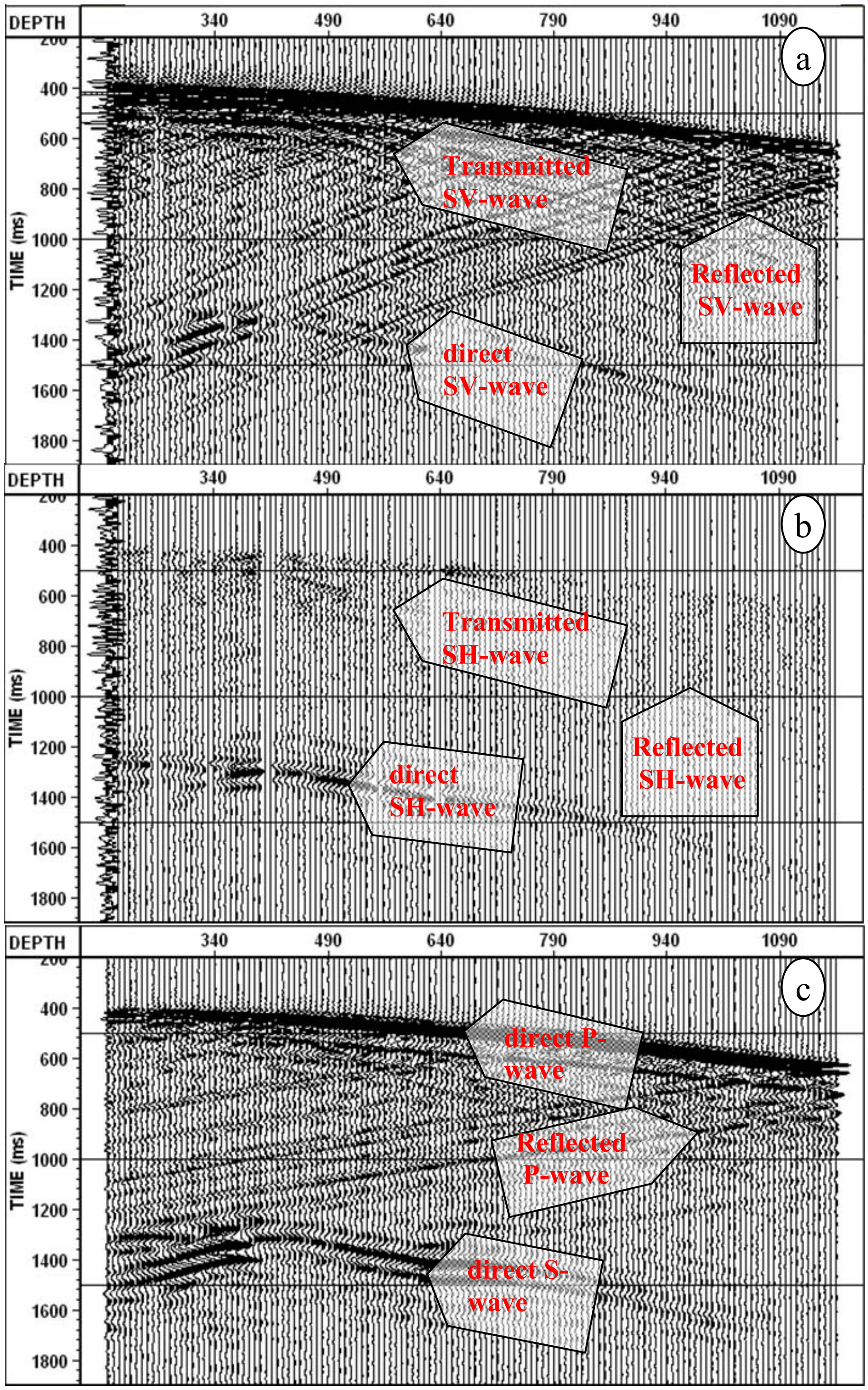

Figure A.4 Hmax (horizontal radial, a), Hmin (horizontal transverse, b), and Z (c) components of far-offset VSP (offset 699 m). Hmax and Hmin are from horizontal rotation of X and Y components.

A.2 Primary downgoing wavelet isolation

The downgoing P-waves (or SV waves) are sometimes expected to be isolated onto a single channel from the raw X, Y, and Z channels, for instance downgoing P waves are needed to design deconvolution operators. Assuming that the first-arrival wavelet is not contaminated by other wavefields such as upgoing P- and SV-events and downgoing SV-events, the primary downgoing wavelet can be isolated through two series of data rotations using hodogram analysis (Hinds et al., 1996). The first step is horizontal rotation described in A.1.The second step is to transform Hmax and Z data into Hmax' and Z' (described by Figure A.2) following a similar procedure: Hmax' is along the source-receiver direction, all the downgoing primary P-wave is redistributed to this data; Z' is orthogonal to source-receiver direction. The downgoing P-wave separated from Hmax' can then be used for deconvolution operator design or amplitude recovery.

A.3 Time-variant polarization

The incidence angles of the upgoing P-waves (or SV waves) change with increasing traveltimes at a single geophone location (Figure A.5). To separate upgoing P-wave and SV wave, a time-variant rotation is needed. A series of polarization angles for various reflections arriving on a single trace can be computed through ray-tracing using the velocity model derived from first-arrival times of zero-offset VSP data. For each trace, the upgoing P and SV waves will be separated by matrix equation (A-2) using a time-variant angle *θ(t)* (Hinds et al., 1996),

$$\begin{pmatrix} Zup''(t) \\ Hmax\_up''(t) \end{pmatrix} = \begin{pmatrix} Zup(t) & Hmax\_up(t) \end{pmatrix} \begin{pmatrix} cos(\theta(t)) & -sin(\theta(t)) \\ sin(\theta(t)) & cos(\theta(t)) \end{pmatrix}$$

(A-2)

where,

$Hmax\_up''(t)$: the component mainly contains upgoing SV wave;

$Zup''(t)$: the component mainly contains upgoing P-wave;

Zup(t), *Hmax_up(t)*: upgoing wavefield from Z and Hmax component;

θ(t): time-variant angle between Z and P-wave propagation direction.

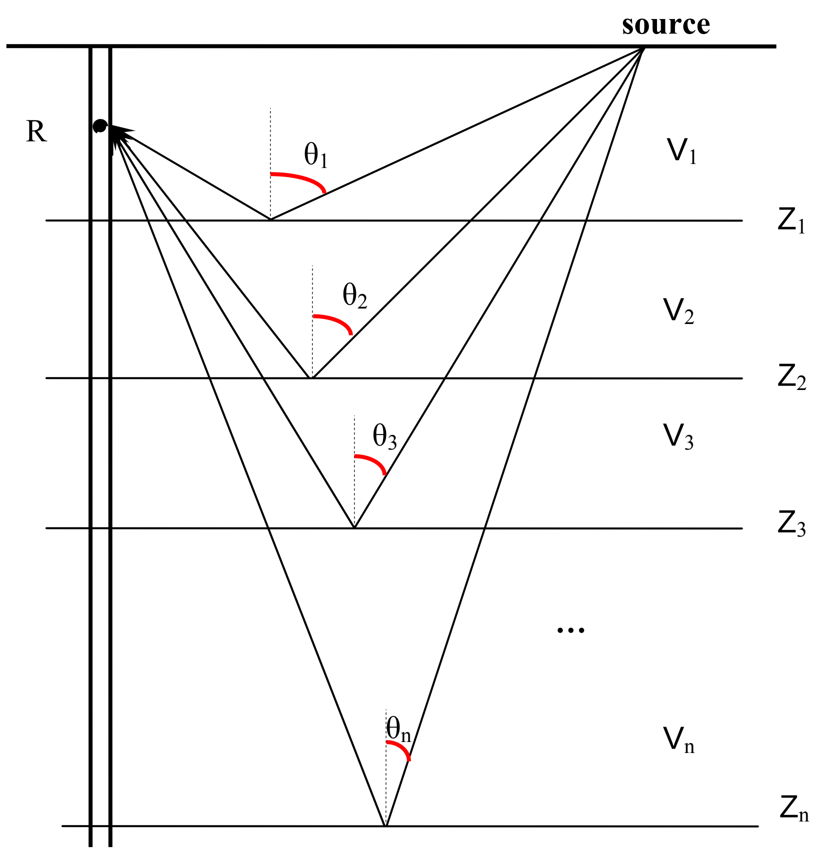

Figure A.5 Schematic diagram of time-variant polarization concept. The reflection angle for upgoing raypaths emerging at receiver R changes with depth. θ_i: the incidence angles; V_i: the layer velocities; Z_i: the layer depths; *i=1, 2, …, n*.

APPENDIX B: Linear least-square regression method for empirical relationship between Q values and rock properties

Supposing the relationship between Q values and rock properties are linear, and it can be written as:

$$a_1 * x_{11} + a_2 * x_{12} + \cdots + a_m * x_{1m} + Q_0 = Q_1$$
$$a_1 * x_{21} + a_2 * x_{22} + \cdots + a_m * x_{2m} + Q_0 = Q_2$$
$$\cdots$$
$$a_1 * x_{n1} + a_2 * x_{n2} + \cdots + a_m * x_{nm} + Q_0 = Q_n$$

(B-1)

where a_1, a_2, …, a_m are the unknown coefficients; and x_{kl} is the l^{th} rock properties at measurement depth k, $k=1, 2, \ldots, n$ is the measurement depth, $l=1, 2, \ldots, m$ is the rock properties used for Q prediction, Q_0 is a unknown constant, and Q_1, Q_2, …, Q_n are the Q values measured at each depth. Equation (B-1) can be rewritten as,

$$XA = Q$$

(B-2)

where

- $X = \begin{bmatrix} x_{11} & \cdots & x_{1m} & 1 \\ x_{21} & \cdots & x_{2m} & 1 \\ & \cdots & & \\ x_{n1} & \cdots & x_{nm} & 1 \end{bmatrix}$;
- $A=(a_1, a_2, \ldots, a_n, Q_0)'$;
- $Q=(Q_1, Q_2, \ldots, Q_n)'$;

If n is greater than the number of unknowns, then the system of equations is over-determined, and the coefficients can be solved using the least square solution of the equations. The least squares solution to the problem is a vector A, which estimates the unknown vector of coefficients. The normal equations are given by

$$(X^T X)A = X^T Q$$

(B-3)

where X^T is the transpose of the design matrix X. Solving for A,

$$A = (X^T X)^{-1} X^T Q$$

(B-4)

APPENDIX C: Crack Description

There are several parameters often used to describe simplified versions of a cracked rock:

Aspect ratio: the quantity α=b/c is called the aspect ratio.

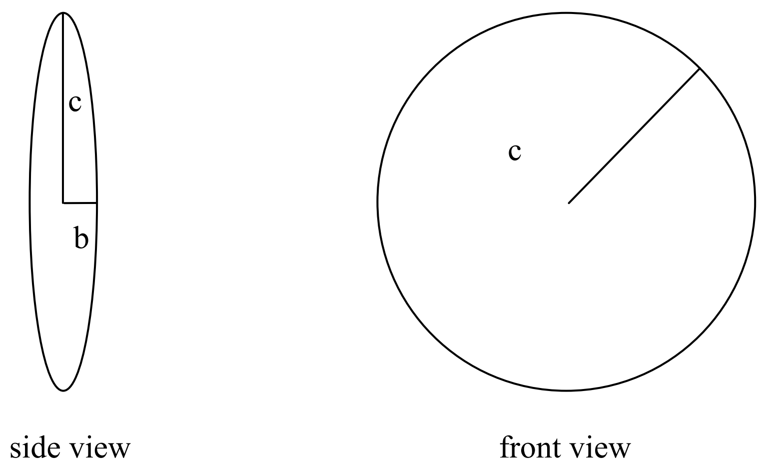

Figure C.1 The oblate spheroid is used to model a representative crack or pore, thus making the mathematics for the replacement medium tractable. This 'Hudson crack' is an ellipsoid of revolution, which a circular cross-section and a small width or thickness. The aspect ratio is defined as the ratio of half-width, b, to radius of the crack face, c (after Macbeth, 2002).

Crack density: the crack density is the number of cracks per unit volume:

$$\varepsilon = \frac{Nc^3}{V_{bulk}}$$

where

- N: number of cracks in volume V_{bulk};
- c: semi-major axis value of cracks.

If we assume a rock contains N/V_b thin oblate spheroidal cracks per unit bulk volume, each having semi-major axis and semi-minor axis $b=\alpha c$, where α is the aspect ratio, the crack porosity will be:

$$\phi = \frac{N}{V_b}\frac{4\pi c^2 b}{3} = \frac{N}{V_b}\frac{4\pi c^3 \alpha}{3}$$

where *N* is the number of cracks in volume V_b; *c*: semi-major axis value of cracks; α: aspect ratio.

Thus, crack density is:

$$\epsilon = \frac{N}{V}c^3 = \frac{3\phi}{4\pi\alpha}$$

APPENDIX D: Fluid substitution

B.1 Fluid substitution for isotropic media: Gassmann's relation

Generally, when a rock is loaded under an increment of compression, such as from a passing seismic wave, an increment of pore pressure change is reduced, which resists the compression and therefore stiffens the rock. The low-frequency Gassmann (1951) - Biot (1956) theory predicts the resulting increase in effective bulk modulus, *Ksat*, of the saturated rock through the following equation:

$$\frac{K_{sat}}{K_0 - K_{sat}} = \frac{K_{dry}}{K_0 - K_{dry}} + \frac{K_{fl}}{\varphi\left(K_0 - K_{fl}\right)}$$

$$\mu_{sat} = \mu_{dry}$$

(D-1)

B.2 Fluid substitution in anisotropic rocks: Brown and Korringa's relations (Mavko, et al., 1998)

Brown and Korringa derived theoretical formulas relating the effective moduli of an anisotropic dry rock to the effective moduli of the same rock saturated by fluid.

$$\boldsymbol{S_{ijkl}^{(dry)} - S_{ijkl}^{(saturate)} = \frac{(S_{ij\alpha\alpha}^{(dry)} - S_{ij\alpha\alpha}^{0})(S_{kl\alpha\alpha}^{(dry)} - S_{kl\alpha\alpha}^{0})}{(S_{\alpha\alpha\beta\beta}^{(dry)} - S_{\alpha\alpha\beta\beta}^{0}) + (\beta_{fl} - \beta_0)\emptyset}}$$

(D-2)

where

- $S_{ijkl}^{(dry)}$ = effective elastic compliance tensor of dry rock
- $S_{ijkl}^{(saturate)}$ = effective elastic compliance tensor of rock saturated with pore fluid
- S_{ijkl}^{0} = effective elastic compliance tensor of mineral material making up rock
- β_{fl} = compressibility of pore fluid
- β_0 = compressibility of mineral material = $S_{\alpha\alpha\beta\beta}^{0}$

- φ = porosity

There are some assumption and limitations applied to the method:

- Low frequencies
- All minerals making up rock have the same moduli
- Fluid-bearing rock is completely saturated
- For clay-filled rocks, it is often best to consider the “soft” clay to be part of the pore filling phase rather than part of the mineral matrix.
- For partially saturated rocks at sufficient low frequencies, one can usually use an effective modulus for the pore fluid that is an isostress average of the moduli of the liquid and gaseous phases:
- $\beta_{fl} = S\beta_L + (1 - S)\beta_G$

where

- β_L = the compressibility of the liquid phase
- β_G = the compressibility of the gas phase
- S = the saturation.

APPENDIX E: Hashin-Shtrikman bounds (Mavko, et al., 1998)

When the geometries of each constituent in the rock are unknown, the upper and lower bounds of effective moduli of the rock can be estimated, given the volume fraction and moduli of each constituent. When only volume fraction and elastic moduli are given for each phase in the rock, Hashin-Shtrikman bounds are the narrowest bound without knowing the geometries of the constituents. They were used to validate the modeling results. The equations can be written as:

$$K^{HS\pm} = K_1 + \frac{f_2}{(K_2 - K_1)^{-1} + f_1\left(K_1 + \frac{4}{3}\mu_1\right)^{-1}}$$

$$\boldsymbol{\mu^{HS\pm} = \mu_1 + \frac{f_2}{(\mu_2 - \mu_1)^{-1} + \frac{2f_1(K_1 + 2\mu_1)}{5\mu_1\left(K_1 + \frac{4}{3}\mu_1\right)}}}$$

(E-1)

where

- K_1, K_2 : bulk moduli of individual phases;
- μ_1, μ_2 : shear moduli of individual phases;
- f_1, f_2: volume fractions of individual phases.

The upper and lower bounds are calculated by interchanging which material is phase 1 and which is phase 2. When the stiffest material is termed 1, the upper bound will be given, otherwise, when the softest phase is termed 1, the lower bound will be calculated.

APPENDIX F: Appendix figures for the Saskatchewan potash mining

In the study mine area, wells were drilled for various purposes, especially for draining the underground water which has the potential to threaten the mining operation. For multicomponent seismic study, only one well Grout 59-1 has dipole sonic logs. However, none of the wells in the mining area was drilled deeper than the Dawson Bay Formation. Within the studied wells, the deepest well, Well A was drilled through the Ordovician formations. Although it is located some distance from the mining area, it is in the same basin as the mine and the geology is generally similar to that in the mining area. For correlating the formations underneath the Dawson Bay Formation, especially the Prairie Evaporite which includes the potash ore interval, correlation between Well A and the seismic data in the mining area was also implemented to aid the interpretation. Despite of the many kilometres distance from Well A to the seismic data, somewhat surprisingly, there is a reasonable tie with P-wave synthetic seismograms to the PP field seismic section (Figure F.1). When we tie our PS synthetic seismograms to the field PS seismic data (Figure F.2), again a believable correlation was found. We note that there is a strong Dawson Bay reflection in the PS seismic section. This bodes well for measuring changes in it. Finally, we correlate the PP and PS sections (Figure F.3).

For time-lapse 3C-3D seismic data interpretation, the time structures of the Birdbear Formation (approximately 625 m deep in Well A) and the Winnipegosis Formation (right below the Prairie Evaporite, approximately 1185 m deep in Well A) were also created on both PP and PS data (Figure F.4, Figure F.5, Figure F.6, and Figure F.7) to investigate the seismic signatures of the formation above and below the target formation. Figure F.8 shows the picking of the top and the bottom of the fracture zone on

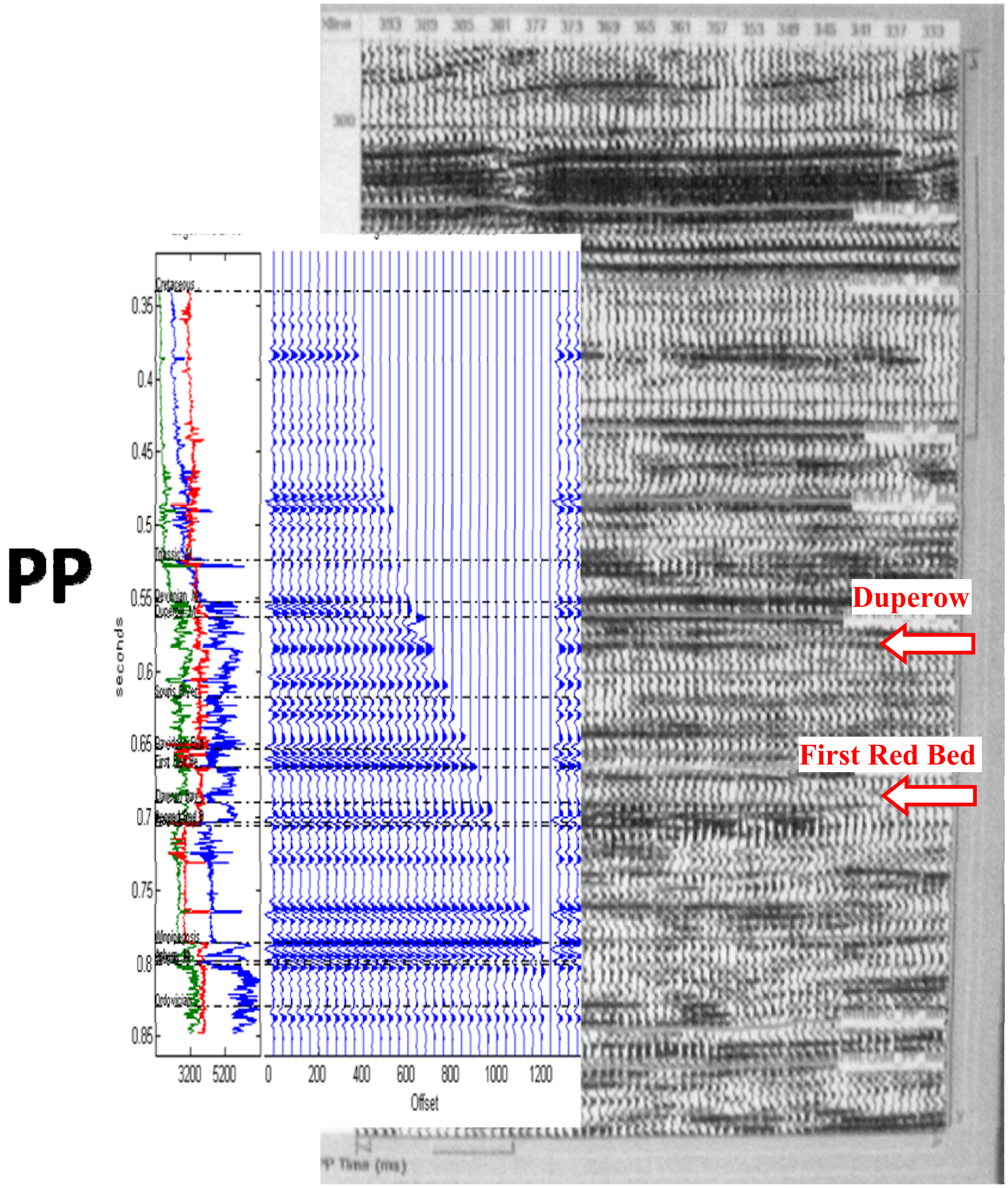

Figure F.1 Synthetic PP seismograms (blue, with well logs: shear velocity, density in red, and P velocity) of Well A and surface PP seismic data.

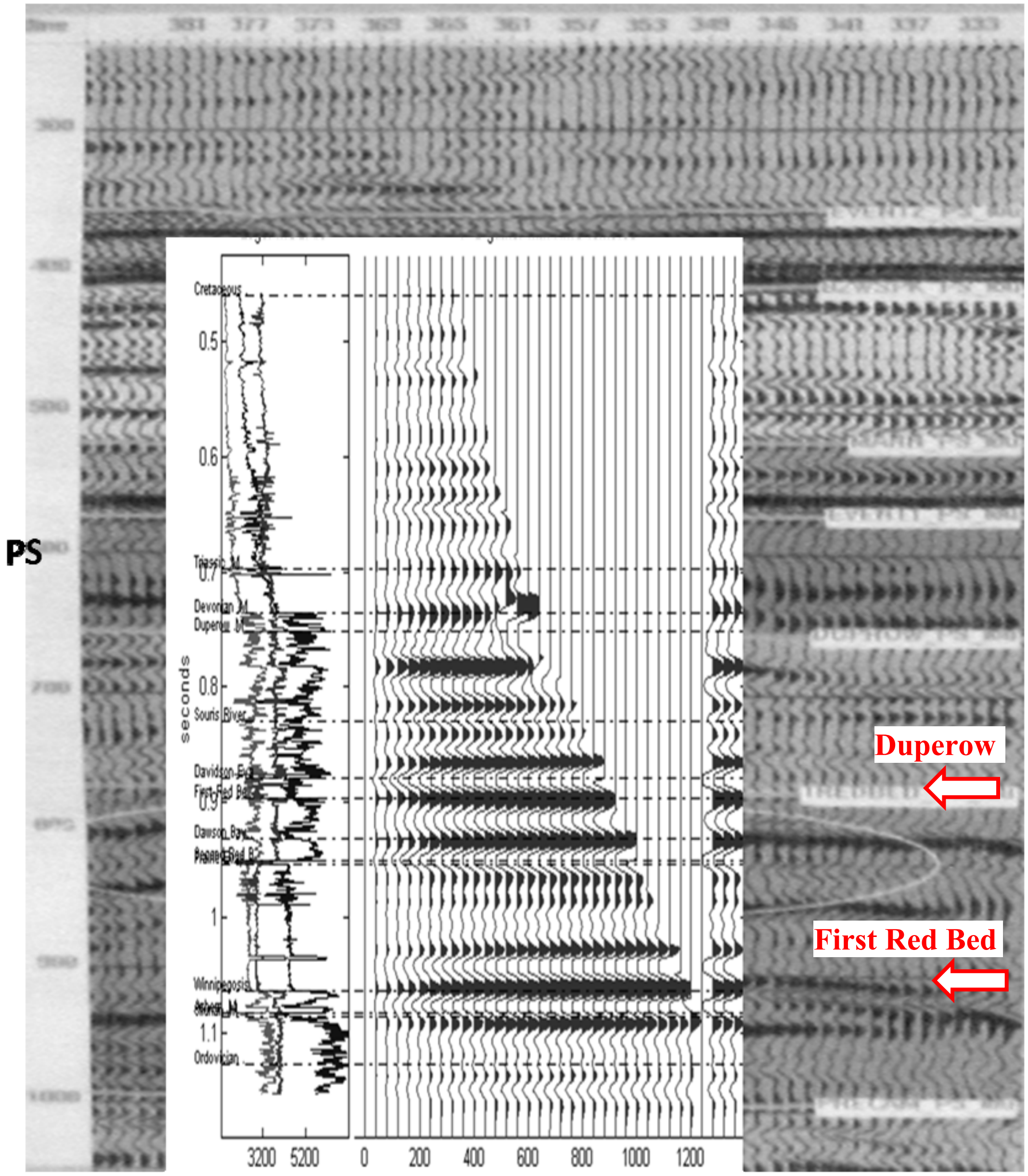

Figure F.2 Surface PS seismic data and synthetic PS seismograms (with well logs) of Well A.

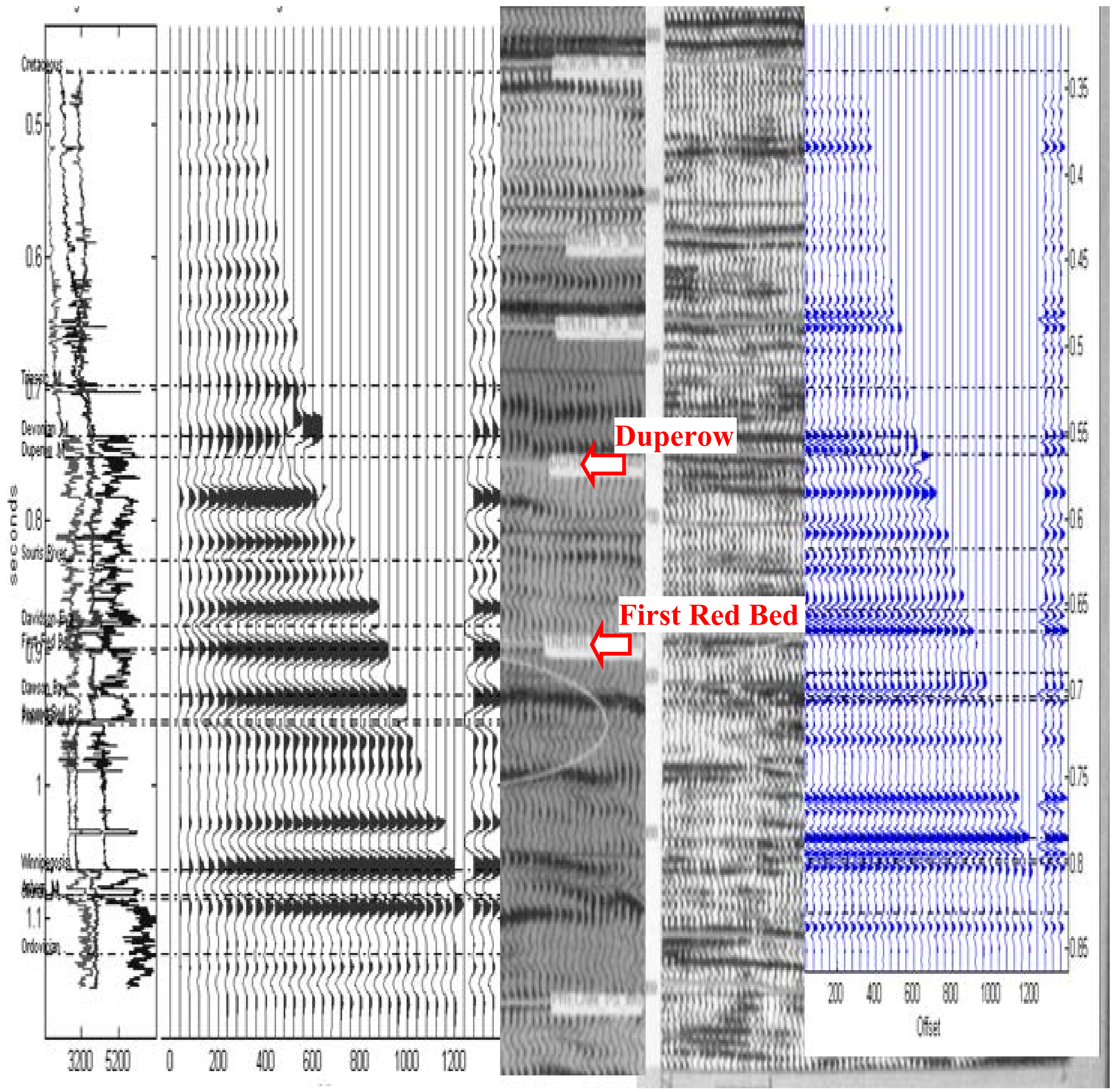

Figure F.3 Correlation of synthetic seismograms of Well A with surface seismic. From left to right: synthetic PS seismogram with well logs, PS surface seismic section, PP surface seismic section, and synthetic PP seismograms.

a line across the dipole sonic well for Vp/Vs calculation. The top of the zone can be determined by the chosen well in the mining area. However, the bottom of the zone can not be determined by the correlation between seismic data and Grout 59-1 well since the well is too shallow (only reaches the Dawson Bay Formation). The seismic signature of the bottom of the studied zone was determined from the Well A.

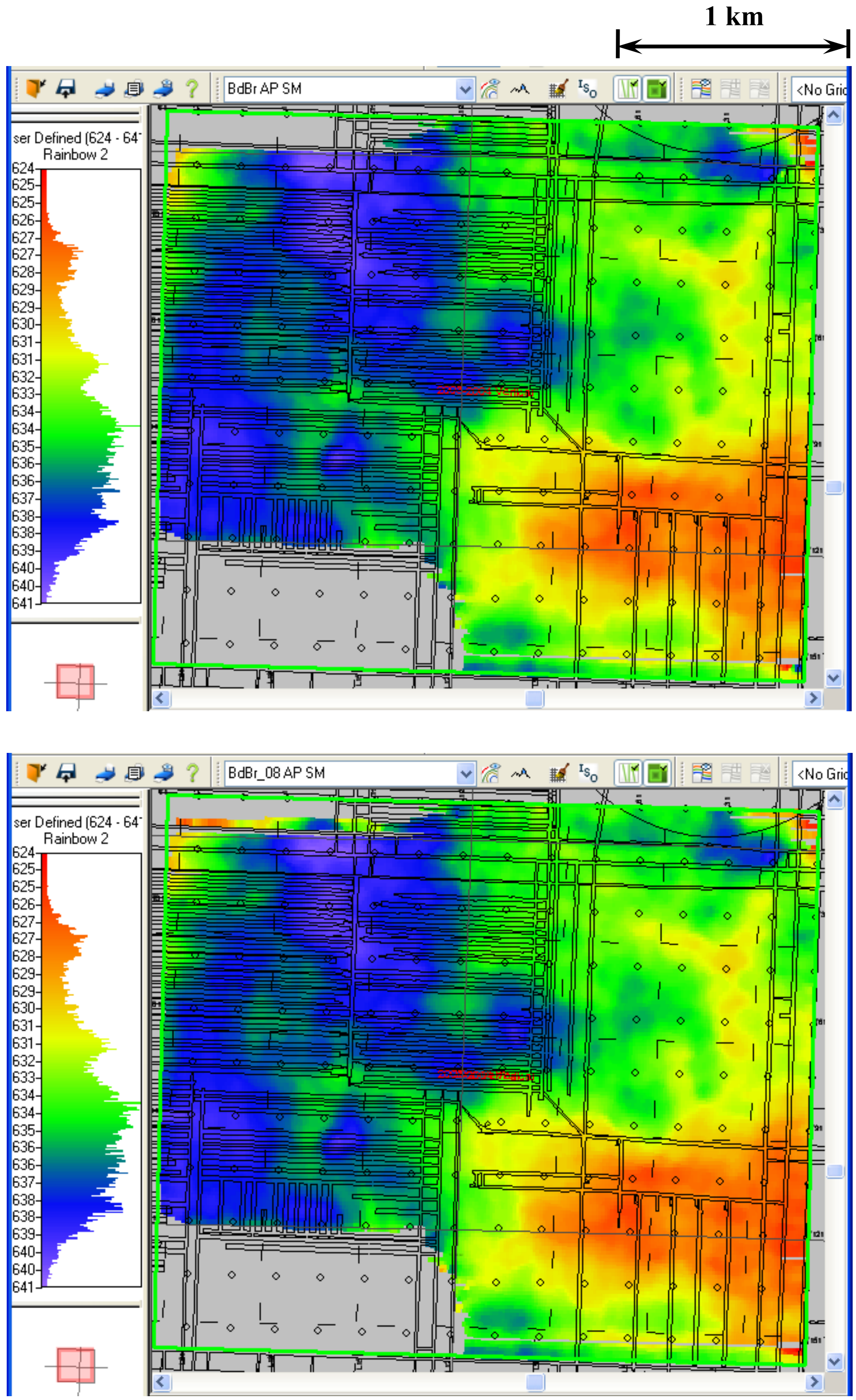

a)

b)

Figure F.4 Time structure of the top of the Birdbear Formation on the PP data, a: 2004 survey; b: 2008 survey. There is almost no time shift between the two surveys.

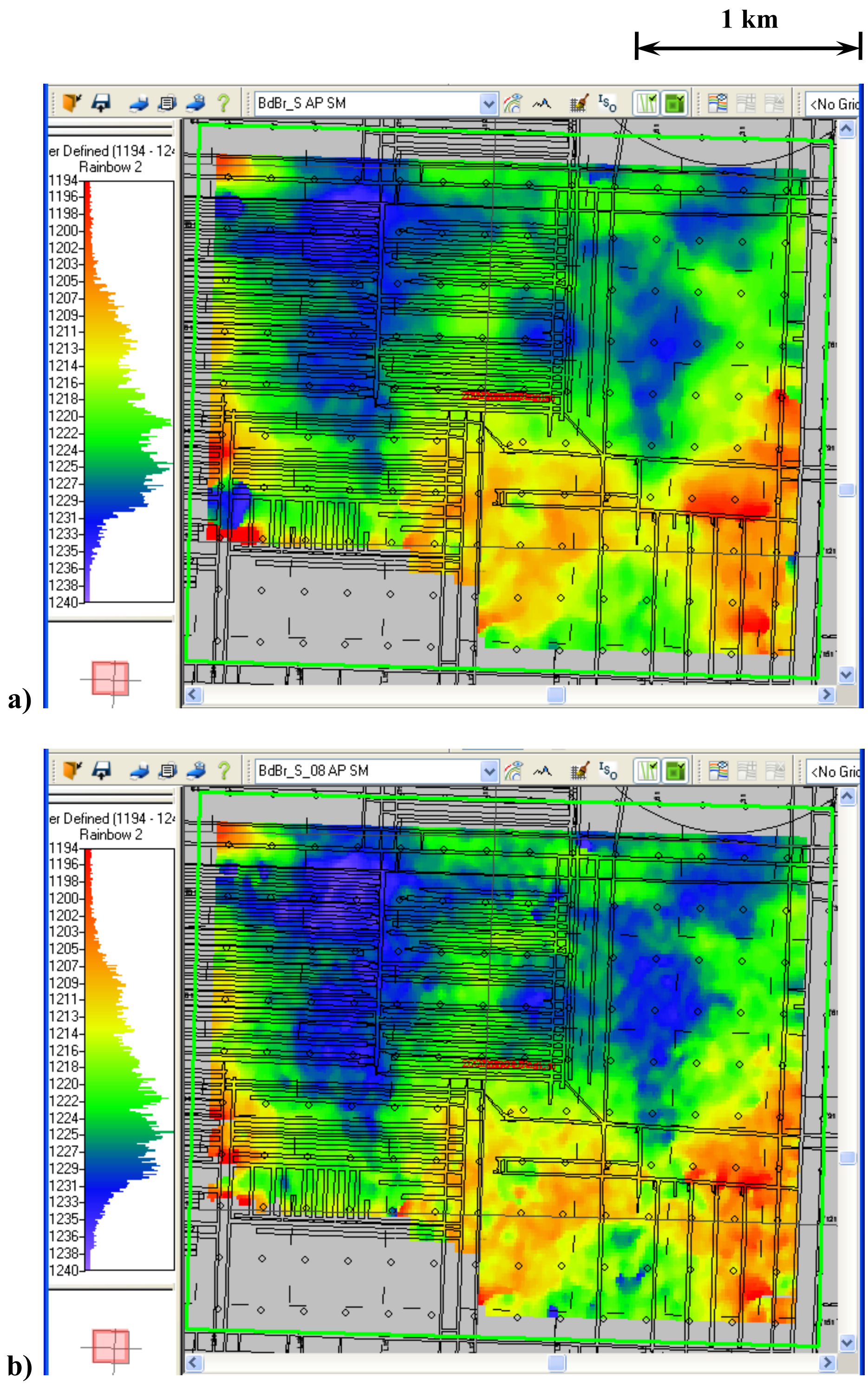

Figure F.5 Time structure of the top of the Birdbear Formation on the PS data, a: 2004 survey; b: 2008 survey. The time shift between the two surveys is fairly small. A little delay was found on 2008 survey.

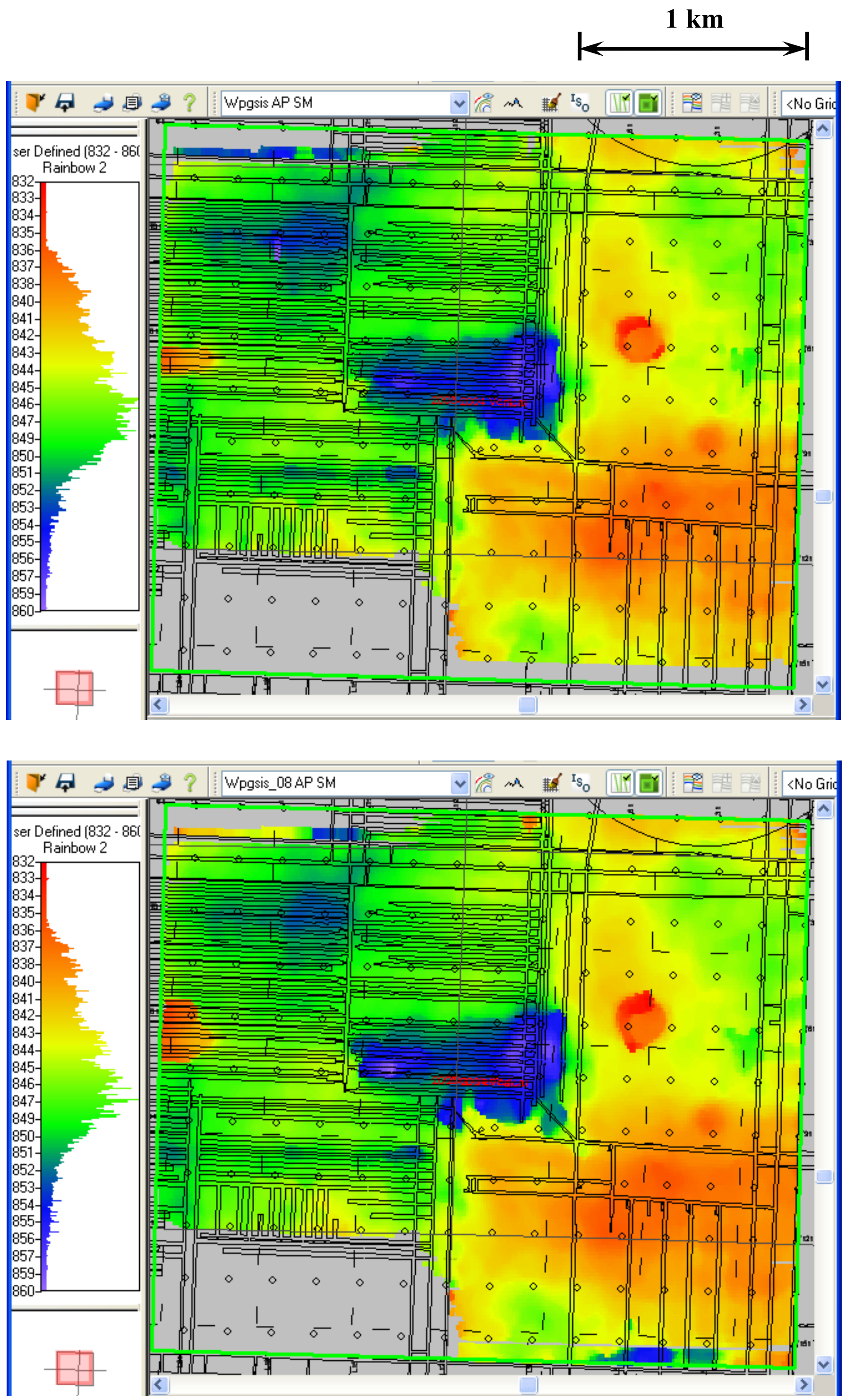

a)

b)

Figure F.6 Time structure of the top of the Winnipegosis Formation on the PP data, a: 2004 survey; b: 2008 survey. Small time delay can be found on 2008 survey, it could be attributed to fractures in the overlying formation.

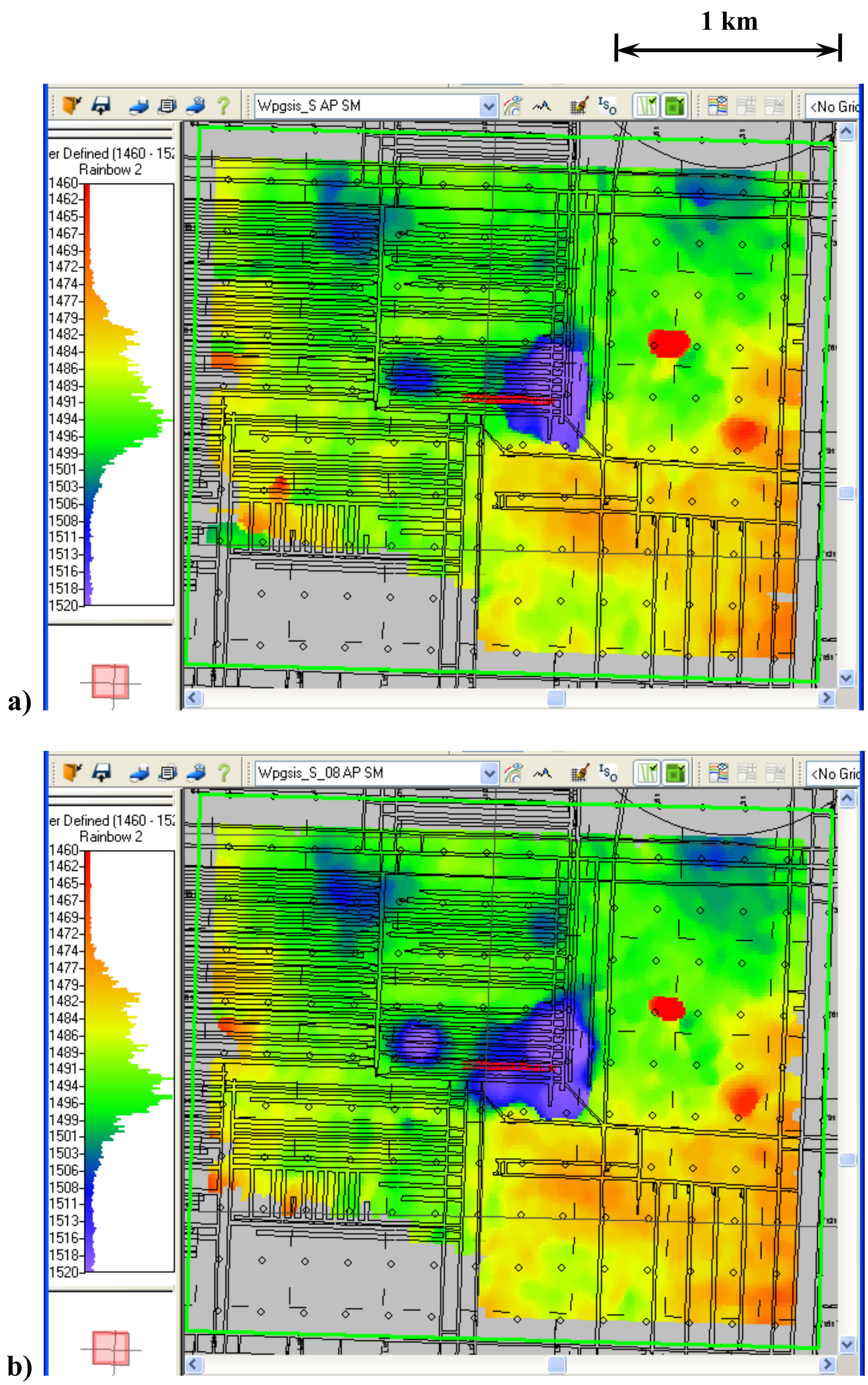

Figure F.7 Time structure of the top of the Winnipegosis Formation on the PS data, a: 2004 survey; b: 2008 survey. An obvious time delay was seen on 2008 survey, especially at the survey center, where is the trap door area. It was thought to be overlying formation fracture effects.

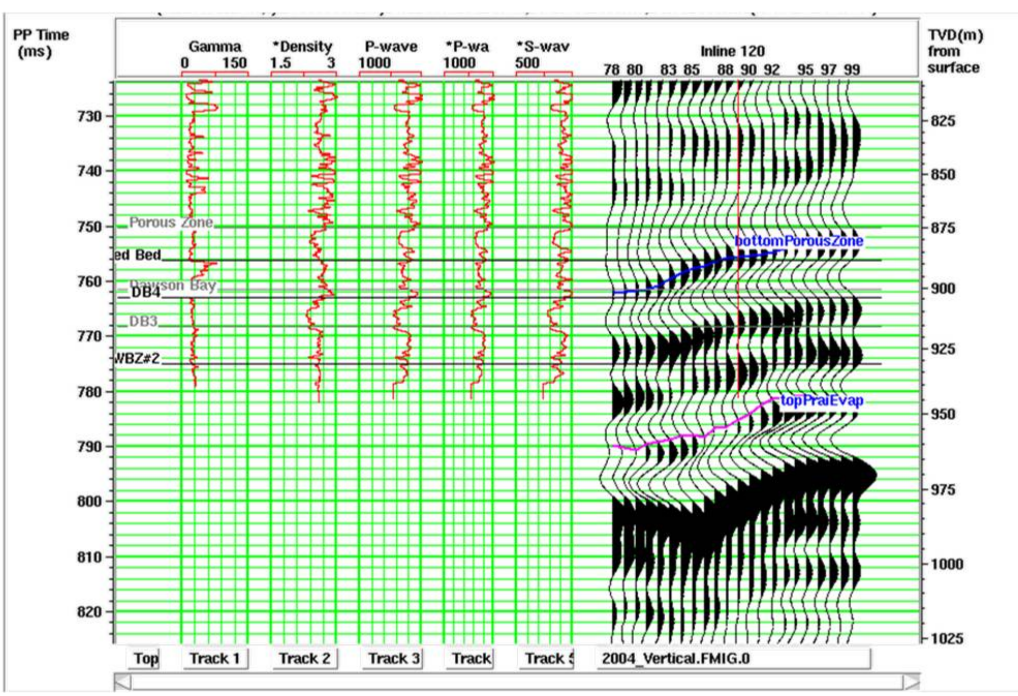

a)

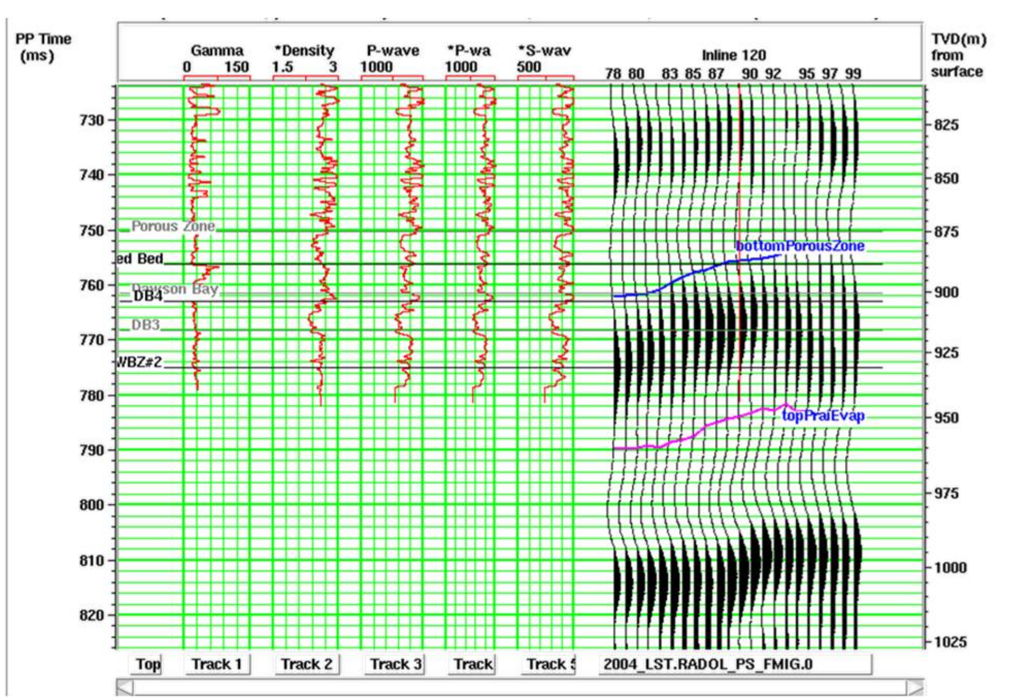

b)

Figure F.8 The bottom of the Porous Zone and the bottom of the Dawson Bay Formation pickings and the correlation with well logs. On the vertical component, the bottom of the Porous Zone is a peak, the bottom of the Dawson Bay Formation corresponds to zero-crossing point on seismic traces. On the radial component, there is no accurate picks for the two geological markers due to low resolution. Approximately they correspond to two zero-crossing points.